/N-99
71943

NASA Contractor Report 201377

National Aeronautics and Space Administration (NASA)/American Society for Engineering Education (ASEE) Summer Faculty Fellowship Program - 1995

Volume 2

William A. Hyman and Donn G. Sickorez, Editors

Grant NGT 44-001-800

August 1996

NASA Contractor Report 201377

National Aeronautics and Space Administration (NASA)/American Society for Engineering Education (ASEE) Summer Faculty Fellowship Program - 1995

Volume 2

William A. Hyman, Editor
Texas A&M University
College Station, Texas

Donn G. Sickorez, Editor
Lyndon B. Johnson Space Center
Houston, Texas

Grant NGT 44-001-800

August 1996

This publication is available from the NASA Center for AeroSpace Information,
800 Elkridge Landing Road, Linthicum Heights, MD 21090-2934, (301) 621-0390

Preface

The 1995 National Aeronautics and Space Administration (NASA)/American Society for Engineering Education (ASEE) Summer Faculty Fellowship at the Lyndon B. Johnson Space Center (JSC), including the White Sands Test Facility, was conducted by Texas A&M University and JSC. The program at JSC, as well as the programs at other NASA centers, was funded by the Education Division, Higher Education Branch, NASA Headquarters, Washington, D.C., with additional funds from the centers. The objectives of the program, which began nationally in 1964 and at JSC in 1965, are

- To further the professional knowledge of qualified engineering and science faculty members.
- To stimulate an exchange of ideas between participants and NASA.
- To enrich and refresh the research and teaching activities of the participants' institutions.
- To contribute to the research objectives of the NASA centers.

Each faculty participant spent at least 10 weeks at JSC engaged in a research project in collaboration with a NASA/JSC colleague. In addition to the faculty participants, the 1995 program included 5 students. The reports of two of the students are integral with that of the respective fellow. Three students wrote separate reports. Volume 1 contains reports 1 through 15. Volume 2 contains reports 16 through 27 and the three student reports, S-1 through S-3.

Contents

Volume 1

Contents

Volume 2

Contents

Student Papers

51-63
76305
16 P.
234347

THEORY AND ONTOLOGY FOR SHARING TEMPORAL KNOWLEDGE

Final Report
NASA/ASEE Summer Faculty Fellowship Program - 1995
Johnson Space Center

Prepared by	Rasiah Loganantharaj Ph. D.
Academic Rank:	Associate Professor
University and Department	University of Southwestern Louisiana Center for Advanced Computer Studies Lafayette, Louisiana 70504

NASA/JSC

Directorate	Engineering
Division:	Automation Robotics and Simulation
Branch:	Intelligent System Branch
JSC Colleague	Dennis G. Lawler
Date Submitted:	October 12, 1995
Contract Number:	NGT-44-001-800

ABSTRACT

Using current technology, the sharing or re-using of knowledge-bases is very difficult, if not impossible. ARPA has correctly recognized the problem and funded a knowledge sharing initiative. One of the outcomes of this project is a formal language called Knowledge Interchange Format (KIF) for representing knowledge that could be translated into other languages.

Capturing and representing design knowledge and reasoning with them have become very important for NASA who is a pioneer of innovative design of unique products. For upgrading an existing design for changing technology, needs, or requirements, it is essential to understand the design rationale, design choices, options and other relevant information associated with the design. Capturing such information and presenting them in the appropriate form are part of the ongoing Design Knowledge Capture project of NASA. The behavior of an object and various other aspects related to time are captured by the appropriate temporal knowledge. The captured design knowledge will be represented in such a way that various groups of NASA who are interested in various aspects of the design cycle should be able to access and use the design knowledge effectively. To facilitate knowledge sharing among these groups, one has to develop a very well defined ontology. *Ontology* is a specification of conceptualization. In the literature several specific domains were studied and some well defined ontologies were developed for such domains. However, very little, or no work has been done in the area of representing temporal knowledge to facilitate sharing.

During the ASEE summer program, I have investigated several temporal models and have proposed a theory for time that is flexible to accommodate the time elements, such as, points and intervals, and is capable of handling the qualitative and quantitative temporal constraints. I have also proposed a primitive temporal ontology using which other relevant temporal ontologies can be built. I have investigated various issues of sharing knowledge and have proposed a formal framework for modeling the concept of knowledge sharing. This work may be implemented and tested in the software environment supplied by Knowledge Based System, Inc.

INTRODUCTION

Representation and reasoning with time play an important role in design knowledge capture framework. The temporal knowledge could be as simple as some specific time constraints about the operation of a device, or as complicated as describing a behavior of a device. For example, the proper operating condition of a device, say a relay R_1, may be specified as: the relay must be activated with 5 units of time after the master switch is tuned on. Similarly, a complicated interaction among various devices can be elegantly specified using temporal knowledge representation.

In an established organization, such as NASA, enormous amounts of useful and critical information are accumulated over a period of time and usually are stored in some sort of electronic form in a computer. Sharing, or using such vital and important information is essential for many critical applications, such as, redesigning or maintenance of devices used in NASA space mission. Sharing of information across different platforms and different languages is a challenging problem. ARPA has initiated a project to address exactly the same problem. It is equally challenging to share the information among people of diverse backgrounds and interests. An example will be a typical NASA engineering project that typically employs a variety of different technologies and a distribution of responsibilities among the project members. In this project we study the problem and propose a practical solution.

The objectives of this research project include: (1) Propose a theory of time that is general enough to accommodate the time elements, points and intervals, and flexible enough to support qualitative and quantitative relations among the elements. (2) Develop primitive and minimal temporal ontologies from which one can build complex ontologies that are natural to the problem domain. (3) Study the problem of sharing knowledge and propose initial solutions to solve the problem.

REPRESENTATION OF TIME

Extensive works have been done on representing and reasoning with time by researchers from diverse discipline, such as, philosophy, theoretical computer science, data-base, and artificial intelligence. The approaches taken by the artificial intelligence community in representing time can be categorized broadly into event-based, or time-based. In the event-based approach, time is represented implicitly. Situation calculus is an example of the event-based approach. The order of time is implicitly represented by the corresponding events. Even though, the event-based approach has the mathematical richness of a situation calculus, and is capable of producing partial or the total ordering among the events, it may not be suitable for specifying either the duration, or the exact time of an occurrence of an event. Many of the applications relevant to NASA require that time must be represented explicitly. We, therefore, study time-based approach for representing temporal knowledge.

We will now decide on the time elements for representation. There has been a considerable amount of discussion about whether the points or the intervals should be the basis for representing temporal knowledge. McDermott [McD82] had proposed temporal knowledge representation system with time points. Allen subsequently proposed interval algebra and argued interval must be the elements of time.

In this research project, we take advantage of both the time points and the intervals. For providing equal footing for both points and intervals, we have proposed a new theory for time that integrates both the points and intervals cohesively.

Before we describe our theory of time, let us briefly introduce both the time points and the intervals.

POINTS

McDermott [McD82] introduced point temporal model for branching time. In his model the time is linear in the past while the time is branching in the future. The branching time model will be useful to studying hypothetical reasoning. Vilain et al. [VK86] has proposed point algebra for linear time. They also have proposed consistency algorithm for propagating temporal constraints.

In linear time model, if we consider a pair of time points one is either before, after or coincides with the other point. We use the notations <, >, =, to denote respectively the relations before, after and coincide. The linearity property for a pair of points t_i and t_j is formally represented as:

$$(t_i < t_j) \vee (t_i > t_j) \vee (t_i = t_j).$$

Note that exactly one relation is true between any two points.

Most of the work done in this area were concerned about propagating temporal constraints and to obtain the minimal labeled temporal constrained network. In a *minimal labeled temporal constraint network* (MLTCN) each label participates in a consistent solution of the temporal constraints. In other words, showing the availability of a MLTCN is equivalent to showing the satisfiability of the temporal constraints. VanBeek [VanB89] had shown that 4-consistency algorithm is required to obtain minimal labeled temporal constraint network for point-based representation. 4-consistency algorithm takes $O(n^4)$ time for convergence, where n is the number of nodes (time points) in the temporal constraint network.

INTERVALS

Interval is a continuous non-zero span of time. Allen [All83] has proposed interval algebra for linear time. There are thirteen relations between a pair of intervals. There relationships are, before (B), after (A), meets (M), met by (Mi) , overlaps (O), overlapped by (Oi), starts (S), started by (Si), finishes (F), finished by (Fi), overlaps (O), overlapped by (Oi), and equal (E). These relations between a pair of intervals, say I_i and I_j, can be neatly presented in a lattice form as shown in Figure 1.

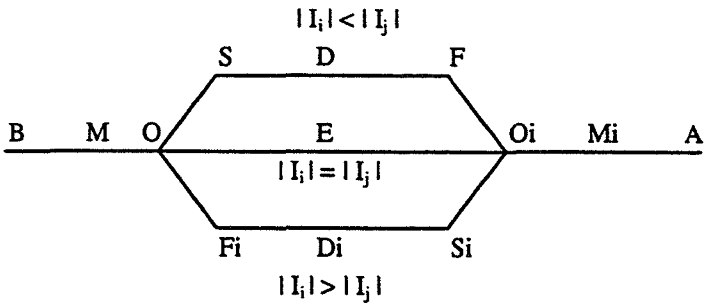

Figure 1

Where, $|I_i| < |I_j|$, $|I_i| > |I_j|$, and $|I_i| = |I_j|$ respectively indicate that the duration of I_i is less than, grater than, or equal to the duration of I_j. Allen has proposed a 3-consistency algorithm to propagate interval temporal constraints. 3-consistency of the interval constraints does not yield minimal labeled temporal constrained network. Note here that obtaining a MLTCN for interval algebra is NP-hard.

ONTOLOGY

Ontology may be thought of as a terminology for representing a conceptualization. A *conceptualization* is an agent's modeling of the objects, or the events and activities occurring in the world. We are interested in capturing events, activities and properties that varies with time. There are two different schools of thought about defining temporal ontologies. One camp believes that one must provide all the necessary ontologies with implicit or explicit semantics, while the other camp believes that one must provide only the primitive ontologies from which other ontologies could be built.

We take the second approach since, we may not know what are the possible ontologies that may be useful for different kinds of problem domains. We have witnessed numerous counter examples that can not be consistently explained by having a pre-defined set of ontologies.

In the early eighties Allen [All84] has proposed a theory for action and time using intervals. He has proposed ontologies for property, event and process. To assert that a property *p* of an object is holding during an interval *I*, Allen used an operator HOLDS(p,I). If *p* holds over an interval *I*, it must also hold over all the sub intervals of *I*. Alen has defined a stronger axiom on HOLDS: if *p* holds over an interval *I* then for every subinterval of *I* there must be at least one period within the subinterval in which *p* must be true. These properties are formally presented as follows:

$$\mathrm{HOLDS}(p,I) \leftrightarrow (\forall i \;\; \mathrm{IN}(i,I) \rightarrow \mathrm{HOLDS}(p,i))$$
$$\mathrm{HOLDS}(p,I) \leftrightarrow (\forall i \;\; \mathrm{IN}(i,I) \rightarrow (\exists s\ \mathrm{IN}(s,i) \wedge \mathrm{HOLDS}(p,s))$$

An event *e* occurring over an interval *I* is represented by OCCUR(e,I). An event occurs in the entirety of an interval, but can not occur in the subinterval. An event is formally represented as

$$\mathrm{OCCUR}(e,I) \rightarrow \neg(\exists i \ \ \mathrm{IN}(i,I) \wedge \mathrm{OCCUR}(e,i))$$

A process *e* occurring in an interval *I* is represented as OCCURRING(e,I). Allen had defined the processes as something that occurs at least once in the given interval and it is formally defined as

$$\mathrm{OCCURING}(e,I) \rightarrow \exists i \ \ \mathrm{IN}(i,I) \wedge \mathrm{OCCURING}(e,i)$$

Examples

The status of switch_1 is on over the interval *I* is represented by

HOLDS(status(switch_1, on), I)

The status of switch_1 is on in all the subintervals of *I*.

The ball changed position from *a* to *b* over the interval *I*. The ball changing position from *a* to *b* is an event and it is represented by change_pos(ball,a,b).

OCCUR(change _pos(ball,a,b),I)

Note that the ball can not change position from *a* to *b* in any subintervals of *I*.

John drank water over *I*. The process John drinking water is represented by drink(john,water).

OCCURRING(drink(john,water),I)

John drinking water is true in at least one subinterval of *I*.

Some weakness of these Ontologies

Allen's ontologies [All84] do not allow one to define precise physical phenomena such as, the status of position or motion of a continuous event at some specific instants [Gal90]. We will illustrate this with couple of examples. Consider a ball that is moving from *a* to *b* on a flat surface over an interval *I*. The ball changing position from *a* to *b* is an event and hence it is represented in Allen's ontology as OCCUR(change_pos(ball, a,b), I). Suppose we are interested in studying the relation between the location of the ball and the time. Say, the ball is at location *c* in the interval, say, *I*. Where *c* is between *a* and *b* and *i* is a subinterval of *I*. The position of the ball at *c* is a property and hence it is represented as HOLDS(position(c),i). The ball being at location *c* over an interval *i* indicates that the ball is stationary that contradicts the fact that the ball is moving.

Consider another example of throwing a ball upwards. The ball looses the velocity under gravitation during the upward movement. It momentarily comes to rest and then it increases the speed from zero in its downward movements. Let I_1 and I_2 are the intervals during which the ball is moving upward and downward respectively. The status of the ball in the interval I_1 and I_2 are respectively, moving upwards and moving downwards. In Allen's ontology they can be represented as

$$\text{HOLDS}(\text{status}(\text{ball, upwards}), I_1), \text{ and}$$
$$\text{HOLDS}(\text{status}(\text{ball, downwards}), I_2).$$

What is the status at the meeting place of I_1 and I_2? Since the status of the ball can not be both upwards and downwards at the meeting point, I_1 cannot meet with I_2. Therefore, I_1 and I_2 must be defined as open at the end, and at the beginning respectively. With this definition of the intervals we can represent the status of the ball, but we still can not represent the status of the ball as stationary at some moment since Allen's ontology does not allow us to define instant.

Theory of time by Allen and Hayes

Allen and Hayes [AH85] axiomatized time using a single relation between intervals called meets. Intervals are used as temporal elements in their theory and points were not considered at all.

The relation meets was introduced informally and it has the common-sense meaning of two objects meeting or touching each other.

The axioms of Allen and Hayes

$<M_1>$ $\forall\, i,j,k,p \in I \wedge \text{meets}(i,j) \wedge \text{meets}(i,k) \wedge \text{meets}(p,j) \rightarrow \text{meets}(p,k))$

$<M_2>$ $\forall\, i,j,k,p \in I \wedge \text{meets}(i,j) \wedge \text{meets}(k,p) \rightarrow \text{meets}(i,p)$
$\nabla \exists\, m \in I \wedge (\text{meets}(i,m) \wedge \text{meets}(m,p))$
$\nabla \exists\, n \in I \wedge (\text{meets}(k,n) \wedge \text{meets}(n,j))$

∇ denotes exclusive OR here.

$<M_3>$ $\forall\, i \in I\, \exists\, j,k \in I\, (\text{meets}(j,i) \wedge \text{meets}(i,k))$

$<M_4>$ $\forall\, j,k \in I\, (\exists\, i,p \in I\, (\text{meets}(i,j) \wedge \text{meets}(j,p) \wedge \text{meets}(i,k) \wedge \text{meets}(k,p) \rightarrow j=k)$

$<M_5>$ $\forall\, i,j \in I\, (\text{meets}(i,j) \rightarrow \exists\, k \in I\, \forall\, m,n \in I\, (\text{meets}(m,i) \wedge \text{meets}(j,n))$
$\rightarrow \text{meets}(m,k) \wedge \text{meets}(k,n))$

$<M_6>$ $\forall\, m,n \in I\, (\text{moment}(m) \wedge \text{moment}(n) \rightarrow \neg \text{meets}(m,n)$

where moment is defined by
$\forall m \in I\, (\text{moment}(m) \leftrightarrow \neg\, \exists\, i,j \in I\, (m=i+j))$

The axiom M_1 states that the meeting place of a pair of intervals is unique. The linearity of the intervals are stated by the axiom M_2

The axiom M_3 states that every interval has at least one interval preceding it and another interval succeeding it. M_4 states that the meeting place uniquely determines the intervals.

The axiom M_5 states that if two intervals, say i and j, meet then there exists another interval that is a concatenation of intervals i and j.

Axiom M_6 states that moments do not meet. Moments are special kinds of intervals that can not be decomposed, but they have other properties of intervals such as having two end points, etc.

Ma et al. [MK94] has extended Allen and Hayes theory of time by allowing time element, *I*, in Allen et al 's theory to be both time points and intervals, and restricting meets relation only to intervals. To improve the flexibility they have removed the linearity property (axiom M2) from Allen and Hayes axioms.

AXIOMS OF OUR APPROACH

We provide a theory of time with time points and intervals.

Notations:

I_s set of intervals
P_s set of points

Linearity property of time points: A pair of points is either coinciding, or one is before or after the other

$$\langle A_1\rangle\ \forall\ t_i\ t_j \in P_s \rightarrow t_i < t_j \ \vee t_i = t_j \vee t_i > t_j$$

Time span from minus infinity to plus infinity

$$\langle A_2\rangle\ \forall t\, \exists t_i\, \exists t_j\ \ t, t_i, t_j \in P_s\ \wedge\ t_i < t\ \wedge t < t_j$$

Pair of intervals meets iff they meet at a point.

$$\langle A_3\rangle\ \forall I_i\, I_j\ \in I_s\ \ I_i \{m\} I_j \leftrightarrow \exists t \in P_s\ \ I_i \{m\}\, t\ \wedge\ t\ \ \{m\}\, I_j$$

Every interval is non zero duration and has a unique pair of end points

$$\langle A_4\rangle\ \forall I_i \in I_s\ \rightarrow \exists t_b, t_e \in P_s \wedge t_b \{m\} I_i\ \wedge I_i \{m\}\, t_e\ \wedge t_b < t_e\ \ \wedge \forall t_b'\ t_e' \in P_s \\ t_b' \{m\} I_i\ \wedge I_i \{m\}\, t_e'\ \ \rightarrow t_b = t_b'\ \wedge t_e = t_e'$$

For every pair of distinct points there must be a unique interval connecting them

$$\langle A_5\rangle\ \forall t_i\, t_j \in P_s\ \ t_i\ < t_j \rightarrow \exists I \in I_s\ \ t_i\ \{m\}\, I \wedge I\ \ \{m\}\, t_j\ \wedge \forall I' \in\ I_s\ \ t_i\ \ \{m\}\, I' \wedge \\ I' \{m\}\, t_j\ \rightarrow I = I'$$

TEMPORAL ONTOLOGY

Temporal ontology should have the capability to describe any conceptualization that associates with time.

Our primitive ontology has the following syntax:

<interval | point >: <proposition | predicate | sentence >

For an interval *I* and a proposition *p, I:p* is interpreted as *p* is true for the interval *I*. Note that it does not state anything about whether *p* is true in all the sub interval or not. These properties must be specified by the user or by the ontology that uses this primitive.

Example

A pen is on the table over an interval *I*. This is a status or the property, therefore, pen on the table must be true throughout the interval, hence it is specified with the primitive as:

$$I\text{:pen\_on\_table} \leftrightarrow \forall i \in I \rightarrow i\text{:pen\_on\_table}$$

A ball moves from *a* to *b* over an interval *I*. Since the event, ball moving from *a* to *b*, cannot happen in any subinterval of *I*, it is represented with the primitive as:

$$I\text{:change\_pos(ball,a,b)} \rightarrow \neg(\exists i \in I \wedge i\text{:change\_pos(ball,a,b)})$$

The ball is at location *a* at time t_1. This representation requires that the points and intervals must be represented using end points. If we review A_5 of our theorem it asserts that a pair of end points uniquely identifies an interval, therefore, it is natural to represent an interval with a pair of end points. An interval that is closed at both end points and begins at t_b and ends at t_e is represented by $[t_b\ t_e]$. Similarly an instant t_1 can be represented as $[t_1, t_1]$. Therefore, the ball at location *a* at time t_1 is represented as

$$[t_1, t_1]\text{: location(ball, a)}$$

The ball is moving in the interval t_1 to t_2. The ball is moving throughout the interval $[t_1, t_2]$, thus it is represented as

$$[t_1, t_2]\text{: status(ball, moving)} \leftrightarrow \forall i \in [t_1, t_2] \rightarrow i\text{:status(ball, moving)}$$

Consider, for example, throwing a ball up in the air at time t_1. Suppose it reaches its highest point at t_2 and touches the ground at t_3. From the example we can state the following: the ball is moving upward from t_1 to t_2, The ball is moving downward from t_2 to t_3. The ball is stationary momentarily at t_2. There is a need to support open and closed intervals In our representation we support all variations of intervals: combinations of closed and opened at both end points.

$[t_1\ t_2)$: status(ball,upward)
$(t_2\ t_3]$: status(ball,downward)
$[t_2\ t_2]$: status(ball,stationary)

REDEFINITION OF OTHER ONTOLOGY USING OURS

Allen's ontology

Allen has defined HOLDS to represent a property is holding over a period; occur to define an event occurring over a period.

HOLDS(I,P) : P holds over all the subintervals of I.
HOLDS(I,P) $\leftrightarrow \forall \in I\ i{:}p$

occur(I,e): an event e occur in I; It can not occur in any of the subintervals of I.
occur(I,e) $\leftrightarrow I{:}e \wedge \neg \exists i \in I\ i{:}e$

occurring(I,e): a process e is occurring in I; It will occur at least one of the subinterval of I.
occurring(I,e) $\leftrightarrow \exists i \in I\ \ i{:}e$

Galton's ontology

Galton [Gal90] expanded Allen's ontology by introducing hold_at, hold_on, for specifying something is holding at , and holding within respectively

hold_at(t,P) $\leftrightarrow [t,t]{:}p$
hold_on(I,P) $\leftrightarrow\ I{:}P \wedge (\forall i \in I \rightarrow i{:}P)$

Example: Alert on Instrument Panel

Suppose the following are the instructions for the crew members about a certain alert signal on an instrument panel of a space vehicle. Following the alert, the crew must activate the battery powered backup system and then perform the specific test procedure. The crew usually respond to such alert within 5 minutes. To perform the test procedure it usually takes at least 10 minutes and at most 15 minutes. After the test procedure, the crew must enter the data interactively, and the whole procedure will take about at least 5 minutes and at most 15 minutes. At the end of data entry the computer performs diagnosis which usually takes at least 5 minutes and at most 10 minutes. The diagnosis determines the defective part. It takes at least 20 minutes and at most 30 minutes to replace the defective parts. The instruction further says that the defective part must be replaced before the battery voltage goes below 10% of its set value. The power to the backup system must be reconfigured if the defective part is not replaced when the voltage drops to 10% of its set value. It is estimated that it takes about 45 minutes for the battery to loose its charge to reach 10% drop in its voltage.

Notations

t_0 the alert starts
t_1 crew start the test procedure
t_2 test procedure completes
t_3 start entering the data
t_4 data entry completes
t_5 diagnosis starts
t_6 end of diagnosis
t_7 replacement of defective units begins
t_8 defective unit is replaced

alert starts at t_0
$[t_0, t_0]$: starts(alert)
test procedure starts at t_1
$[t_1, t_1]$: starts(test_procedure)
test procedure ends at t_2
$[t_2, t_2]$: ends(test_procedure)
test procedure is active from t_1 to t_2
$[t_1, t_2]$ status(test_procedure, active) $\rightarrow \forall i \in [t_1, t_2] \rightarrow i$: status(test_procedure, active)
entering data starts at t_3
$[t_3, t_3]$: starts(enter_data)
entering data completes at t_4
$[t_4, t_4]$: ends(enter_data)
data entry is active from t_3 to t_4.
$[t_3, t_4]$:status(data_entry, active) $\rightarrow \forall i \in [t_3, t_4] \rightarrow i$: status(data_entry, active)
diagnosis starts at t_5.
$[t_5, t_5]$: starts(diagnosis)
diagnosis ends at t_6
$[t_6, t_6]$ ends(diagnosis)
diagnosis is active from t_5 to t_6.
$[t_5, t_6]$: status(diagnosis, active) $\rightarrow \forall i \in [t_5, t_6] \rightarrow i$: status(diagnosis, active)

$0 <= t_1 - t_0 <= 5$
$10 <= t_2 - t_1 <= 15$
$5 <= t_4 - t_3 <= 15$
$5 <= t_6 - t_5 <= 10$
$20 <= t_8 - t_7 <= 30$

Assuming no delays between tasks, we have $t_2 = t_3$; $t_4 = t_5$; $t_6 = t_7$

Constraint Graphs

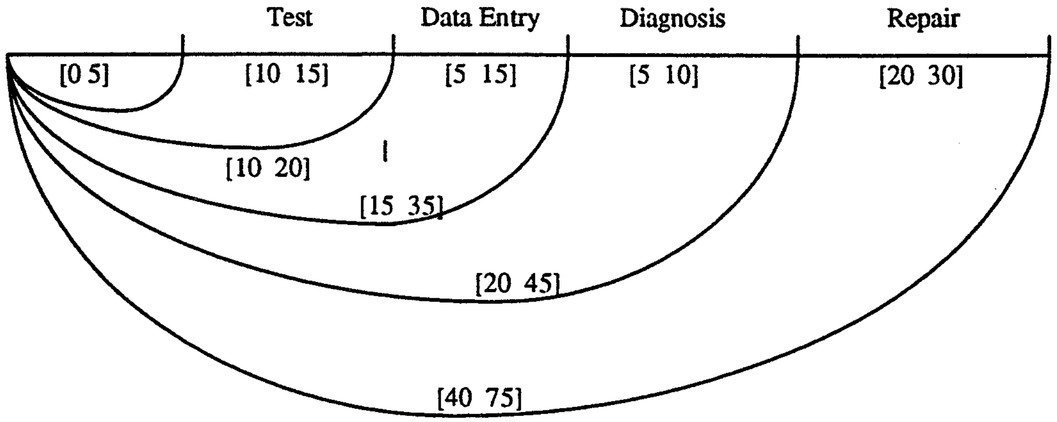

According to the specifications, the battery will rundown in 45 minutes. The propagation of the constraints indicates that the repair will be completed at least 40 minutes and it will takes at most 75 minutes in the worst case. Therefore, it is desirable to have a backup battery that will last for at least 75 minutes instead of 45 minutes. This information can be captured into the DKC framework as the rationale for having a battery that will last for at least 75 minutes.

KNOWLEDGE SHARING

Knowledge sharing, specially the one that is stored in the electronic form, has tremendous advantages some of which include minimization of effort in recreating the same or the similar information, enable one to build a much larger and comprehensive systems using the existing knowledge and thereby minimizing the overall costs. Sharing the information from one system to another is very challenging because of incompatibility between the systems, representational formats, or languages. Realizing the enormous amount of advantages of sharing the knowledge and the formidable challenges, the ARPA has initiated a knowledge sharing effort at Stanford University and the University of Southern California. The major theme of the ARPA initiative is the research and development of technology for reusing an existing knowledge base or information.

We take a complementary view of sharing knowledge. We focus on the concept of sharing information among the people with different, or diverse backgrounds. An example will be a typical NASA engineering project that typically employs a variety of different technologies and a distribution of responsibilities amongst the project members (software design, mechanical design, financial analysis, etc.). Suppose, two people or agents are communicating together. For them to understand the communication they must use the ontology that is understood by each other precisely, otherwise they may not understand each other. Similarly, to share the information stored in a computer either the users must understand the ontology of which it is communicating to them, or the computer must understand the ontology of the user. Pre-defining the commonly used ontology for many domains makes it easier and possible for agents to use or access and share knowledge. While such approaches for knowledge sharing are very useful for common objects, domains, or concepts, they tend to hinder creativity, or to increase the human errors in specialized areas or domains. An alternative approach to knowledge sharing without sacrificing the agent's own ontology is called view-point.

VIEW-POINT

We propose an alternative approach to achieve knowledge sharing without sacrificing the agent's own ontology. View-point is commonly understood as one's perspective or conceptualization. Two view-points of the same object from different agents may not be identical.

Example

Consider a design of a device. Project manager is concerned with the overall cost of the unit while the design engineers are concerned with modeling the expected behavior, realizing it while satisfying most of the important design constraints which include the total weight of the unit. The engineer who is responsible for SMR&QA is concerned about the reliability of the device, backup redundant units, the ease of replacement of the defective units, etc. The production manager is concerned with materials, capacity of the plant, subcontracting or to develop in house, etc..

The differences between views can be attributed to the following factors: Different agents are interested in different aspects or features of the same object; therefore they see or view the object differently. Different agents have different conceptualizations of the same object; worse yet, they may use different ontologies to describe the same feature of an object.

To study and understand the problem, we have formalized the notion of point-of-view. Let O be an object in the world. An object can be concrete, or abstract, primitive, or composite, or it can even be fictional. Suppose there are two agents L and M. Let O_L, andO_M be respectively the L's and M's conceptualization of O. If I_L, and I_M respectively be the interpretation of the agents L and M then we have $I_L(O) = O_L$, and $I_M(O) = O_M$. If the agents, L and M, understand or know each other's interpretation then they can understand each other's conceptualization of the objects. For any meaningful communications we need to add function constants and relation constants. In such expanded environment the agents must understand the semantics of the function and the relation constants. In order to achieve such understanding the agent must know the other agent's believes and knowledge that is not feasible. Therefore, we provide a restricted version of multiple view-points by making the interpretation of all the constant to be public, and defining all the functional and relational constants in terms of some well known public ontology

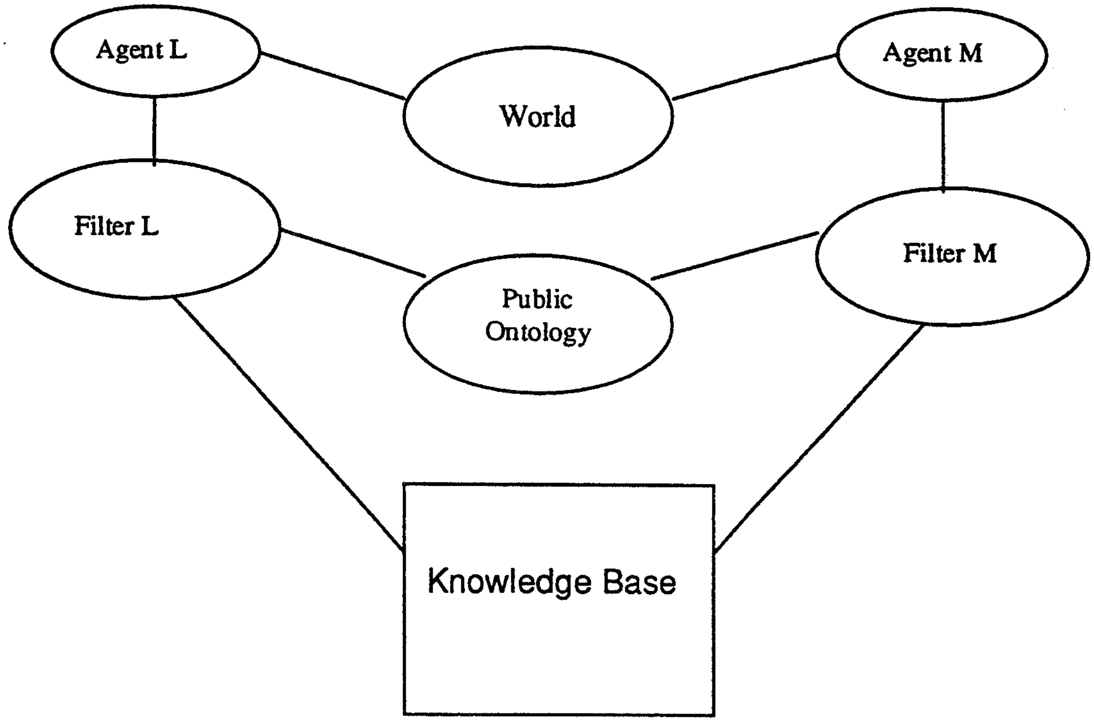

Our solution for sharing knowledge or information is shown in the above diagram.

SUMMARY AND CONCLUSION

We have investigated several temporal models for the purpose of using it to capture the temporal knowledge associated with devices and their behaviors. For an excellent survey on temporal knowledge representation and reasoning, refer to Hayes' [Hay95] recent work. We established the following desirable properties for the temporal representation: representation of explicit time, supporting time points and intervals, representation of qualitative and quantitative constraints. The temporal ontology should be minimal and primitive so as to support any complex ontologies that may be built from the primitive. We were unable to find any previous work that meets our requirements. We, therefore, developed a new theory for time that integrates time points and intervals. We have also proposed a primitive temporal ontology from which any complex ontologies can be built. We have shown that other ontologies can be rewritten using our ontology. Our theory of time subsumes theories of time of Allen and Hayes, and Ma et al's.

In this project we have also investigated the notion of knowledge sharing among various groups of people with diverse backgrounds and needs, and responsibilities. We have proposed a practical framework for sharing knowledge.

For future work we propose the following investigations: (1) temporal constraint propagation and implementation, (2) feasibility study and other issues on knowledge sharing.

REFERENCE

[All83] J. F. Allen, Maintaining Knowledge about Temporal Intervals, in *Communications of ACM*, Vol. 26, No. 11, pp 832-843, 1983

[All84] J. F. Allen, Towards a General Theory of Action and Time, in *Artificial intelligence*, Vol. 23, No. 1, pp 123-154, 1984

[AH85] J. F. Allen and P. J. Hayes, A Common Sense Theory of Time, in *the Proceedings of IJCAI 1985*, pp 528-531, 1985

[Gal90] A. Galton, A Critical Examination of Allen's Theory of Action and Time, in *Artificial Intelligence*, Vol. 42, pp 159-188, 1990

[Hay95] P. Hayes, A Catalog of Temporal Theories, *Report*, unpublished, 1995.

[MK94] J. Ma, and D. Knight, A General Theory of Time, in *The Computer Journal*, Vol. 37, No. 2, 1994

[McD82] D. McDermott, A temporal Logic for Reasoning About Process and Plans, *Cognitive Science* 6, pp 101-155, 1982

[VanB89] P. van Beek, Approximation Algorithms for Temporal Reasoning, in *the Proceedings of IJCAI 1989*, pp 1291-1296, 1989.

[VK86] M. Vilain and H. Kautz, Constraint Propagation algorithm for Temporal Reasoning, in the *Proceedings of AAAI-86*, pp 377-382, 1986.

52-51
76307
12P.

EVALUATION OF AUTOMATED YEAST IDENTIFICATION SYSTEM

234348

Final Report
NASA/ASEE Summer Faculty Fellowship Program - 1995
Johnson Space Center

Prepared By:	Michael R. McGinnis, Ph.D.
Academic Rank:	Professor
University & Department:	University of Texas Medical Branch Department of Pathology Galveston, TX 77555-0609

ORG. NA
FIN: JCS.

NASA/JSC

Directorate:	Space and Life Sciences
Division:	Medical Sciences
Branch:	Biomedical Laboratories
JSC Colleague:	Duane L. Pierson, Ph.D.
Date Submitted:	August 10, 1995
Contract Number:	NGT-44-001-800

ABSTRACT

One hundred and nine teleomorphic and anamorphic yeast isolates representing approximately 30 taxa were used to evaluate the accuracy of the Biolog yeast identification system. Isolates derived from nomenclatural types, environmental, and clinical isolates of known identity were tested in the Biolog system. Of the isolates tested, 81 were in the Biolog database. The system correctly identified 40, incorrectly identified 29, and was unable to identify 12. Of the 28 isolates not in the database, 18 were given names, whereas 10 were not. The Biolog yeast identification system is inadequate for the identification of yeasts originating from the environment during space program activities.

INTRODUCTION

A ground-based automated system is needed for the identification of environmental yeasts recovered from the space shuttle, MIR, and crew members. There is a pressing need to have the capability to identify a broad spectrum of yeasts in an efficient and timely manner. The identity of environmentally important yeasts has a major impact upon accessing environmental issues and crew health.

Biolog Inc. (Hayward, CA) has recently introduced an automated system designed to identify 267 species of environmental yeasts. Using 94 biochemical tests contained in a microtiter plate, a computer and microtiter plate reader, the system can identify yeast isolates based upon their metabolic ability to utilize or oxidize different carbon sources within 24 to 72 hours. Owing to the design of the automated Biology system, it's methodology may lend itself to evaluating various disinfectants for clearing the environment of yeasts and moulds.

The purpose of this investigation was to determine the accuracy of the Biolog yeast identification system for identifying clinically and environmentally important yeasts.

MATERIALS AND METHODS

Ascomycetous and basidiomycetous yeasts of known identity (Table 1) having JSC, UTMB, ATCC, and CBS accession numbers originating from environmental and clinical sources were grown on Sabouraud glucose agar at 25°C. Subcultures were made onto Biolog Universal Yeast Agar (BUY agar, Biolog, Inc., Haywood,CA) and then incubated 48-72 hrs at 25°C. Yeast cells were harvested with a sterile cotton swab and placed into 50 ml sterile distilled water. The suspensions were adjusted to between 62 and 68.5% T at 590 nm using a spectrophotometer. The % T range was determined by using Biolog yeast turbidity standards. The suspensions were dispensed using an 8-channel repeating pipetter. 100 μl was dispensed to each well of the Biology YT MicroPlates, after which they were placed in an incubator at 25°C. Each plate was read at 24, 48, and 72 hrs using the MicroLog 3 automated MicroStation System consisting of a reading device, computer, and software release 3.50.

RESULTS

After each reading was made, the goodness of match of the unknown isolate to the data contained within the computer database was determined. A similarity index of greater than 0.75 at 24 hrs, or greater than 0.50 at 48 and 72 hrs was considered to be an acceptable identification by the system (Table 1). Only the identifications at 72 hrs were used in this study because some isolates with subsequent periods of incubation changed their identifications from correct to incorrect, whereas others changed from incorrect to correct.

Seventy-six isolates included in the database resulted in 40 correct identifications, 29 incorrect identifications, and 12 no identifications. For the 28 isolates not inluded in the database, 18 were given incorrect identifications, whereas 10 were not identified.

DISCUSSION

Yeast identification systems must be able to accurately identify isolates included in their databases and exclude, without identifying, isolates not in their databases. Systems should provide timely identifications at a reasonable cost.

A major short coming of the Biolog system, as well as other commercial systems, is that they exclusively rely upon the ability of a yeast to assimilate or oxidize different carbon sources. Owing to the fact that morphology is a component of the description of yeast taxa, this must be considered when attempting to identify an unknown isolate. The omission of morphologic data can contribute significantly to erroneous identifications.

When considering isolates contained with the Biolog database, 40 (49.4%) were correctly identified, 29 (35.8%) were incorrectly identified, and 12 (14.8%) were not identified because the biocodes could not be matched in the Biolog database. If isolates not in the database are considered, as well as those being force-fitted into an identification, the accuracy of the Biolog system for yeast identification becomes 36.7%.

It is unfortunate that the Biolog system has no mechanism to exclude isolates whose identity and biocode are not contained within the database. This is also a problem with other systems such as Vitek and API 20C. The use of morhpology would enhance the ability of these systems not only to exclude taxa, but to more accurately identify ones contained in their databases.

In contemporary mycology, the holomorphic concept is being strongly endorsed. Because many potential users of the Biolog system may not be aware of teleomorph-anamorph connections, the use of teleomorph names for many of the taxa without a cross-referenced list of teleomorph-anamorph connections creates confusion. Many of the isolates to be identified are recovered only as anamorphs. This means that most individuals will be familiar with anamorphic names rather than teleomorphic names being applied to the whole fungus.

CONCLUSIONS

The accuracy of the Biolog System for the identification of environmental yeasts is unsatisfactory. Until the database for the system is revised, the system has only limited epidemiologic application.

Table 1.- Yeast taxa and their identification at 24, 48, and 72 hours.

Name	JSC	24 hr	48 hr	72 hr
Candida albicans	1	none	*Hyphopichia burtonii*	*Candida albicans*
Candida krusei	2	none	none	*Issatchenkia scutulata*
Candida tropicalis	3	*Candida tropicalis*	none	*Candida albicans*
Candida kefyr	4	*Kluyveromyces marxianus*	*Kluyveromyces marxianus*	*Kluyveromyces marxianus*
Candida guilliermondii	5	none	none	*Pichia guilliermondii*
Torulopsis glabrata	6	none	*Pichia trehalophila*	*Candida glabrata*
Cryptococcus neoformans	7	none	*Yarrowia lipolytica*	none
Saccharomyces cerevisiae	8	*Saccharomyces cerevisiae*	*Saccharomyces cerevisiae*	*Saccharomyces cerevisiae*
Lodderomyces elongisporus	9	none	*Lodderomyces elongisporus*	none
Bullera alba	10	*Cryptococcus* sp.	*Bulleromyces albus*	*Bulleromyces albus*
Debaryomyces maramus	11	none	*Debaryomyces maramus*	*Debaryomyces maramus*
Kluyveromyces marxianus	12	none	*Kluyveromyces marxianus*	*Kluyveromyces marxianus*
Kluyveromyces marxianus	13	*Kluyveromyces marxianus*	*Kluyveromyces marxianus*	*Kluyveromyces marxianus*
Kluyveromyces marxianus	14	*Kluyveromyces marxianus*	*Kluyveromyces marxianus*	*Kluyveromyces marxianus*
Pichia ohmeri	15	none	*Pichia* sp.	*Pichia membranaefaciens*
Pichia membranaefaciens	16	*Pichia ohmeri*	*Pichia ohmeri*	*Pichia ohmeri*
Issatchenkia orientalis	17	none	*Issatchenkia orientalis*	*Candida sorboxylosa*
Pichia guilliermondii	18	none	*Kluyveromyces thermotolerans*	*Saccharomyces cerevisiae*

Table 1.- Yeast taxa and their identification at 24, 48, and 72 hours.

Name	JSC	24 hr	48 hr	72 hr
Hansenula californica	19	none	none	*Candida incommunis*
Hansenula anomala	20	none	*Hyphopichia burtonii*	none
Torulopsis maris	21	*Candida* sp.	*Candida maris*	*Candida maris*
Torulopsis glabrata	22	none	*Pichia trehalophila*	*Candida glabrata*
Torulopsis candida	23	none	*Debaryomyces hansenii*	*Pichia guilliermondii*
Sporobolomyces salmonicolor	24	none	*Sporidiobolus johnsonii*	*Sporidiobolus johnsonii*
Saccharomyces cerevisiae	25	*Saccharomyces cerevisiae*	*Saccharomyces cerevisiae*	*Saccharomyces cerevisiae*
Saccharomyces cerevisiae	26	none	*Zygosaccharomyces* sp.	*Zygosaccharomyces* sp.
Rhodotorula minuta	27	none	*Rhodotorula aurantiaca*	none
Rhodotorula aurantiaca	28	none	*Candida* sp.	*Rhodotorula aurantiaca*
Rhodotorula rubra	29	none	none	none
Candida norvegensis	30	none	*Candida incommunis*	*Pichia norvegensis*
Candida ciferrii	31	none	*Geotrichum terrestre*	*Stephanoascus ciferrii*
Candida utilis	32	none	*Pichia jadinii*	*Pichia jadinii*
Candida humicola	33	none	none	*Cryptococcus* sp.
Cryptococcus albidus	34	*Cryptococcus* sp.	*Cryptococcus albidus*	*Cryptococcus albidus*
Cryptococcus ater	35	none	none	*Cryptococcus albidus*
Blastoschizomyces capitatus	36	none	*Galactomyces geotrichum*	*Galactomyces geotrichum*

Table 1.- Yeast taxa and their identification at 24, 48, and 72 hours.

Name	JSC	24 hr	48 hr	72 hr
Blastoschizomyces capitatus	37	none	none	*Galactomyces geotrichum*
Blastoschizomyces capitatus	38	*Candida pararugosa*	*Schizoblastosporon starkeyi*	*Dipodascus ovetensis*
Blastoschizomyces capitatus	39	none	*Galactomyces geotrichum*	*Galactomyces geotrichum*
Blastoschizomyces capitatus	40	none	*Galactomyces geotrichum*	*Galactomyces geotrichum*
Blastoschizomyces capitatus	41	none	none	none
Filobasidium capsuligenum	42	none	*Hyphopichia burtonii*	*Cryptococcus terreus*
Pichia farinosa	43	*Pichia* sp.	none	*Pichia farinosa/musicola*
Candida intermedia	44	none	none	*Pichia mexicana*
Torulospora rosei	45	none	none	*Schizosaccharomyces pombe*
Candida stellatoidea	46	none	none	none
Candida ravautii	47	none	none	none
Candida membranaefaciens	48	none	none	*Candida parapsilosis*
Candida humicola	50	*Trichosporon beigelii*	*Candida glaebosa*	*Cryptococcus terreus*
Torulopsis candida	51	none	none	*Saccharomyces ludwigii*
Torulopsis candida	52	none	none	none
Pichia ohmeri	53	none	*Candida parapsilosis*	*Candida parapsilosis*
Trichosporon beigelii	54	none	*Rhodotorula aurantiaca*	none
Candida lusitaniae	55	*Clavispora lusitaniae*	*Clavispora lusitaniae*	*Clavispora lusitaniae*

Table 1.- Yeast taxa and their identification at 24, 48, and 72 hours.

Name	JSC	24 hr	48 hr	72 hr
Candida stellatoidea	56	*Candida* sp.	*Hyphopichia burtonii*	none
Torulopsis candida	57	*Debaryomyces hansenii*	*Candida salmanticensis*	none
Torulopsis candida	58	*Candida edax*	*Debaryomyces hansenii*	*Trichosporon beigelli*
Candida utilis	59	none	none	none
Hyphozyma variabiles	60	*Cryptococcus luteolus*	*Rhodotorula aurantiaca*	*Pichia mexicana*
Hansenula fabianii	61	none	*Hyphopichia burtonii*	*Pichia onychis*
Torulospora rosei	62	none	none	*Torulaspora globosa*
Blastoschizomyces capitatus	63	none	none	none
Candida kefyr	64	*Kluyveromyces marxianus*	*Kluyveromyces marxianus*	*Kluyveromyces marxianus*
Trichosporon beigelii	65	none	*Rhodotorula acheniorum*	*Rhodotorula acheniorum*
Cryptococcus ater	66	none	none	none
Torulopsis magnoliae	67	none	*Candida magnoliae*	*Candida magnoliae*
Haneniospora uvarum	68	none	*Hanseniaspora guilliermondii/ uvarum/valb*	*Hanseniaspora guilliermondii/ uvarum/valb*
Candida lusitanae	69	none	*Kluyveromyces lodderae*	*Kluyveromyces lodderae*
Candida krusei	70	none	none	none
Candida humicola	71	none	*Rhodotorula aurantiaca*	*Rhodotorula aurantiaca*
Trichosporon beigelii	72	*Trichosporon beigelii*	*Rhodotorula acheniorum*	none
Candida diddensiae	73	none	*Dekkera bruxellensis*	none

Table 1.- Yeast taxa and their identification at 24, 48, and 72 hours.

Name	JSC	24 hr	48 hr	72 hr
Metschnikowia pulcherrima	74	none	*Candida sorboxylosa*	*Candida sorboxylosa*
Candida albicans	75	*Pichia stipitis*	*Hyphopichia burtonii*	*Hyphopichia burtonii*
Candida albicans	76	none	*Hyphopichia burtonii*	none
Candida albicans	77	none	*Candida albicans*	*Candida albicans*
Candida albicans	78	none	*Candida albicans*	*Candida albicans*
Candida albicans	79	*Candida* sp.	*Candida albicans*	*Candida albicans*
Candida lusitaniae	80	none	*Candida parapsilosis*	*Candida parapsilosis*
Candida lusitaniae	81	none	*Candida parapsilosis*	*Candida parapsilosis*
Candida lusitaniae	82	none	*Clavispora lusitaniae*	*Clavispora lusitaniae*
Candida lusitaniae	83	none	*Clavispora lusitaniae*	*Clavispora lusitaniae*
Candida krusei	84	none	*Issatchenkia orientalis*	*Issatchenkia orientalis*
Candida krusei	85	none	*Candida sorboxylosa*	*Candida sorboxylosa*
Candida krusei	86	none	*Issatchenkia orientalis*	*Issatchenkia orientalis*
Candida krusei	87	none	*Issatchenkia orientalis*	*Issatchenkia orientalis*
Saccharomyces cerevisiae	88	*Saccharomyces boulardii*	*Saccharomyces boulardii*	*Saccharomyces boulardii*
Candida parapsilosis	89	none	*Candida parapsilosis*	*Candida parapsilosis*
Candida parapsilosis	90	none	*Candida parapsilosis*	*Candida parapsilosis*
Candida parapsilosis	91	none	*Candida parapsilosis*	*Candida parapsilosis*

Table 1.- Yeast taxa and their identification at 24, 48, and 72 hours.

Name	JSC	24 hr	48 hr	72 hr
Candida parapsilosis	92	none	*Candida parapsilosis*	*Candida parapsilosis*
Candida parapsilosis	93	none	*Saccharomyces dairensis*	*Pichia mexicana*
Torulopsis glabrata	94	none	*Candida parapsilosis*	*Candida parapsilosis*
Candida tropicalis	95	none	*Candida parapsilosis*	*Candida tropicalis*
Cryptococcus neoformans	96	none	*Candida albicans*	*Candida albicans*
Cryptococcus neoformans	97	none	none	*Filobasidiella neoformans* var. *neoformans*
Blastoschizomyces capitatum	98	none	*Schizoblastosporon starkeyi*	none
Candida paratropicalis	99	none	*Hypopichia burtonii*	*Cryptococcus terreus*
Candida rugosa	100	*Candida rugosa*	*Candida rugosa*	*Candida rugosa*
Torulopsis candida	101	*Pichia ohmeri*	*Pichia ohmeri*	*Pichia ohmeri*
Torulopsis candida	102	none	none	none
Torulopsis candida	103	none	*Pichia ohmeri*	*Pichia ohmeri*
Candida krusei	104	none	*Issatchenkia orientalis*	*Issatchenkia* sp.
Candida kefyr	105	none	none	*Pichia guilliermondii*
Candida kefyr	106	none	*Guilliermondella selenospora*	none
Candida geochares	136	none	*Candida geochares*	*Candida geochares*
Yamadazyma haplophilia	138	none	none	*Candida parapsilosis*
Cryptococcus laurentii	157	*Cryptococcus laurentii*	*Cryptococcus luteolus*	*Cryptococcus luteolus*

Table 1.- Yeast taxa and their identification at 24, 48, and 72 hours.

Name	JSC	24 hr	48 hr	72 hr
Candida albicans	158	none	*Candida albicans*	*Candida albicans*

53-54
76300
12P.
237349

A HUMAN FACTORS ANALYSIS OF EVA TIME REQUIREMENTS

Final Report
NASA/ASEE Summer Faculty Fellowship Program -- 1995
Johnson Space Center

Prepared By:	Dennis W. Pate
Academic Rank:	Lecturer
University & Department:	Texas A&M University Engineering Technology Department College Station, TX 77843

NASA/JSC

Directorate:	Safety, Reliability, and Quality Assurance
Division:	Flight Systems Safety and Mission Assurance
Branch:	Analysis and Risk Assessment
JSC Colleague:	Dr. Richard P. Heydorn
Date Submitted:	August 8, 1995
Contract Number:	NGT-44-001-800

ABSTRACT

Human Factors Engineering (HFE), also known as Ergonomics, is a discipline whose goal is to engineer a safer, more efficient interface between humans and machines. HFE makes use of a wide range of tools and techniques to fulfill this goal. One of these tools is known as motion and time study, a technique used to develop time standards for given tasks. A human factors motion and time study was initiated with the goal of developing a database of EVA task times and a method of utilizing the database to predict how long an EVA should take. Initial development relied on the EVA activities performed during the STS-61 mission (Hubble repair). The first step of the analysis was to become familiar with EVAs and with the previous studies and documents produced on EVAs. After reviewing these documents, an initial set of task primitives and task time modifiers was developed. Videotaped footage of STS-61 EVAs were analyzed using these primitives and task time modifiers. Data for two entire EVA missions and portions of several others, each with two EVA astronauts, was collected for analysis. Feedback from the analysis of the data will be used to further refine the primitives and task time modifiers used. Analysis of variance techniques for categorical data will be used to determine which factors may, individually or by interactions, effect the primitive times and how much of an effect they have.

INTRODUCTION

International Space Station Alpha (ISSA) will require unique procedures in the construction and maintenance of the facility. Never before has mankind endeavored such an engineering and construction feat in such an alien environment. Many of these procedures will require extravehicular activity (EVA) time. There have been several major studies performed to determine the amount of EVA time required in the construction phase of ISSA and in the operational phase (required maintenance). Many of the studies indicate EVA time will be a major issue.

For ease of maintenance, ISSA is being designed with components, orbital replacement units (ORUs), that are replaceable by astronauts performing EVAs or using remote manipulator systems. Both require the expenditure of valuable astronaut time. Tools are currently being developed to better predict the likely failure rate of the ORUs. The number of ORU failures will determine the number of EVAs required. Early studies to determine the amount of EVA time required to replace the ORUs have varied greatly in their designs and in their findings. The variations between the studies is a direct result of the different methods people use to determine EVA time requirements. Currently, shuttle EVA timelines are developed by people with years of experience in the area of EVAs using their judgment to determine how the EVA should be conducted and how long it should take. These estimates are further refined by hours of practice by the astronauts who will perform the EVA. A large portion of shuttle EVA timelines attributed to overhead factors. The overhead is the non-productive time expended during an EVA mission. Planners regularly add between ten and thirty percent extra time to an EVA to account for individual differences and unexpected events. Even with this additional time, timelines are rarely met. This uncertainty in time makes predictions of future EVA time requirements difficult. To aid in more accurately predicting the amount of EVA time required for a given task, a human factors analysis of EVAs was initiated. This paper will present the considerations that went into the human factors analysis of the EVA time requirements, the state of the current analysis of the Hubble mission, and the planned future activities.

DISCUSSION

Motion and Time Studies

Motion and time studies involve observing a task, whether real time or recorded, and timing how long it takes to perform the basic movements of the task (known as "task primitives" in the EVA realm). The task primitives used in industry have undergone close to one hundred years of refinement. Frank and Lillian Gilbreth were among the first people to perform motion and time studies on industrial activities. They developed a set of task primitives, known as Therbligs, that could be used to describe all the task performed by a worker. The Therbligs are divided into productive and non-productive activities. This distinction allows the analyst to identify and eliminate waste within an operation. The primitives are useful both in the analysis and in the planning stages of a task. In planning, databases containing the standard times allowed for the various task primitives from prior motion and time studies can be used to predict how long a task should take. These predicted times can be adjusted for worker specific traits as well as environmental factors. Factors such as training, physical abilities, and motivation may have large effects on the times.

The unique environment of EVA precludes using the Therbligs in the analysis of EVAs. The EMU the astronaut wears prevents viewing many of the visual queues an analyst of this system requires to determine what is going on. For this reason, the basic system was modified to accommodate the EVA environment.

EVA Timeline Resources

A review of the NASA document database was conducted to locate EVA related materials that may have contained information useful in the development of the modified motion and time study system. The EVA documents were reviewed to determine their exact content. None of the documents located were a complete source of EVA timelining information, however, some did contain a few task primitives with their associated times as well as some general guidelines to be considered when developing a timeline. The main source of EVA information is the experience and intuition of the people working in the EVA area. Unfortunately, much of this experience and knowledge has yet to be collected into a single common EVA reference resource.

The Fisher-Price study, *Space Station Freedom External Maintenance Task Team: Final Report,* was one of the most comprehensive studies of EVA activities conducted to date. A motion and time study of task primitives performed in prior EVA missions and WETF training sessions was conducted as part of the study to determine how long it would take to perform certain key task. The task primitives were used to predict how long EVA maintenance missions would take. This study did not address the issue of task time modifiers effecting the task times.

The MOD training library contains two volumes of an EVA training manual entitled *EVA Lessons Learned.* The manuals contain observations from all of the past EVA missions and also includes a listing of EVA task primitives; however, the task primitives are taken directly from the Fisher-Price study.

Post-flight analysis of each mission are also available. These report how much time the major task required, but do not report the data at the task primitive level. They do provided a means of identifying the EVAs that did not meet the planned mission time. These could then be reviewed to determine what factors may have effected the times.

A copy of a post-flight EVA analysis report of STS-51A was obtained from the EVA office. The report included comparisons between task times in the WETF and the inflight task times. The report also contained a listing of task primitives and their associated times. Some of the primitives included a general observation of possible task time modifiers.

Task Primitives

The Therbligs used in the traditional motion and time study were used as a starting point in developing the task primitives used in the EVA analysis. The following is adapted from Niebel:

A. Effective
    1. Physical basic division
        a. Reach
        b. Move
        c. Grasp
        d. Release
        e. Pre-position
    2. Objective basic division
        a. Use
        b. Assemble
        c. Disassemble
B. Ineffective
    1. Mental of semimental basic division
        a. Search
        b. Select
        c. Position
        d. Inspect
        e. Plan
    2. Delay
        a. Unavoidable delay
        b. Avoidable delay
        c. Rest to overcome fatigue
        d. Hold

Some of the Therbligs rely on being able to determine where the subjects gaze is. This is not possible when viewing an astronaut within an EMU. The gold visor obscures their face during the day and the poor lighting and reflections obscure their face during the night. This also hinders determining what activities may be going on during a delay. Times when the astronaut are eating, drinking, or resting cannot be distinguished from each other. The following is a list of the task primitives used in the initial study along with a brief description of the primitives:

- Adjust - the action of modifying a setting of a tool, PFR, or MFR
- Assemble - the action that occurs when two or more components are joined together.
- Delay - any time during which no work is occurring.
- Disassemble - the action that occurs when two or more components are taken apart.
- Grasp - the action of closing the fingers around an object.

- Hold - the action of supporting an object that is not being (dis)assembled or transported.
- Inspect - the action of visually checking an object to determine something about it.
- Operate - the action that occurs when work is being performed with a tool.
- Plan - the action of deciding what operation or task is to occur next.
- Position - the action of properly orienting and aligning an object.
- Reach - the action of moving a hand to or from an object.
- Rotate - the action of moving a PFR or MFR about its axis.
- Search - the action of locating an object.
- Select - the action of selecting one object from among a large number of objects.
- Tether - any action involving the use of a tether.
- Transfer - the action of transporting an object that is within the grasp on the astronaut.
- Translate - the action of moving from one position to another.
- Translate command - the action of communicating the desired RMS translation the IV RMS operator.
- Verify - the required action of checking with the IV operators to ensure the proper tool setting or procedure.
- Wait - a delay due to someone else.

The task are further divided into different classes (e.g. Translate: manual, Translate: RMS, Tether: select, Tether: open, etc.) Further refinement of the primitives will likely become necessary as the analysis of the Hubble mission continues.

Task Time Modifiers

To increase the power in predicting how long an EVA will take, one must have an understanding of the factors that may have an effect on the task times and what the effect will be. A list of factors effecting EVA times was developed from reviewing the lessons learned documents and other resources. Factors from the human factors field were added to these to develop the initial list used in the data collection and analysis of STS-61 (Hubble). In reviewing the EVA documents, the times given for the few task primitives listed were averages of observed times from past missions. The times did not include information on how to adjust the base task time for possible task time modifiers. Timeliners know from experience that task performed while free-floating will take longer than task performed while within a foot restraint

The astronaut performing the EVA is one of the largest sources of possible task time modifiers in the EVA system. The anthropometry (physical attributes) of the individual, their training, motivation, prior EVA experience, and mental ability will all have an effect on their ability to perform an EVA task. A female who is in the 5th percentile strengthwise (i.e. given all the females in a population, 95 percent of the females will be stronger) will have different capabilities than a 95th male. There will be individual differences in stature, stamina, and strength. The intrinsic characteristics of the individual must be considered when predicting the time required to perform an EVA.

Related to this would be the posture the astronaut is in while performing the task. Some postures are biomechanically superior to others. Task times will be effected if the astronaut is in a twisted, extended, or otherwise contorted posture.

Another astronaut dependent factor would be the case of side dominance. Everyone has a dominant or preferred side (e.g. left or right). Task performed with the dominant side will be faster, more powerful, and more precise than those performed with the non-dominate side.

When analyzing a task time, one must consider the previous task(s) performed by the astronaut and the stamina of the astronaut. If the astronaut has just finished a labor intensive task or has been waiting on a reply from mission control, they may require more time to perform the next task. The longer they are into the mission, the more likely they are to slow down. The slow down may be offset, though, by the motivation factor. If the astronauts are behind on their schedule, they may push themselves at a faster pace than they normally work at.

The amount of training and the type of training an EVA astronaut receives will also effect the EVA time. Space station EVAs will not be practiced to the same degree shuttle EVAs are practiced due to time and monetary constraints. The effect the difference in training will have must be considered when predicting the time future EVAs will require. Ideally, a person should be trained until they reach the asymptote of their learning curve. This is the point where further training has no effect on the time required to perform the task. The training should continue till just prior to the mission. The longer the interval between their training and the actual performance of the task, the longer the inflight task time will take due to recall and relearning. The STS-61 EVA missions were the most highly trained for EVA missions to date. This must be considered when including the data from this mission with the data from other missions. This mission also included many astronauts with prior EVA experience. This would increase the confidence of the astronaut as well as increase the value of the training they received prior to the mission. One must also be aware of the possible negative results of training; that is, actual task will require more time than the same task performed during training due to learning the wrong methods. An example of this would be material positioning task learned in the WETF. In the WETF, the water provides a damping action to the positioning task making it easier to stop the load than in orbit, yet it requires more force to start the object into motion. Another effect of training in the WETF leading to negative training is the pain induced by floating upside down. When the astronaut is upside down, their weight is supported by their collar bones resting on the bearing ring in the collar of the EMU. This leads astronauts to practice in a predominately heads-up manner. When in space, they may experiment with a heads-down attitude leading to a change in the planned activities and times.

The external lighting environment during the EVA will also effect some of the task times. When in sunlight, visual task will be performed with greater ease. When out of the sunlight, lighting deficiencies become apparent and visual task will be hampered by the low light levels within the payload bay. During STS-61, the EVA astronauts required the IV crew to shine a flashlight through the orbiter window to provide more lighting for the task. Lighting induced psychological effects on the astronauts will also be possible. Some of the astronauts have commented that it is unsettling when you are on the RMS arm above the shuttle at night and everything except the shuttle is pitch black.

The thermal environment is also a function of the day and night conditions and will have an effect on the task times. During the night, the temperature will drop. As the temperature drops, the extremities, namely the fingers and hand, will cool at a faster rate than the bodies core. Conductive cooling that occurs while handling materials during the night can be severe enough to cause frostbite. Even a moderate cooling of the hands will cause a loss in the dexterity of the hands leading to an increase in the task times and an increased risk of accidents. Time will also be required to allow for the astronauts to put on a pair of protective thermal mittens. The thermal mittens may no longer be required when the actively heated EVA gloves are manifested on futures flights. The changing thermal environment can also cause equipment problems. PFRs may become difficult to ingress during the day when the boots and the PFR are thermally expanded. During the viewing of the Hubble mission, one of the astronauts had difficulty in ingressing a PFR attached to Hubble. The other astronaut had to interrupt their work to assist the ingress. In another incident, the astronaut could only ingress their right foot. Thermal vacuum chamber testing has helped to reduce the occurrence of thermal expansion and contraction problems, but they still need to be considered.

The restraint of the astronaut will also effect the time required to perform a task. A firmly restrained astronaut will be faster than one who is performing a task while free-floating. Task performed in these two different conditions must be differentiated.

The metabolic load the astronaut is under will also impact the task times. If an astronaut is under a heavy metabolic load, they will be producing large amounts of heat and CO_2 that must be removed from the EMU system. If they operate beyond the ability of the system, their body will respond by slowing them down to reduce the metabolic heat load and CO_2.

Some of the task times will be subject to task modifiers unique to the task. While translating, factors such as encumbrance and obstacles must be considered. Direction of travel may also be important when looking at such things as rotational movements, and positioning task.

Interruption in the EVA activities can have a negative impact on task times. Story Musgrave describes EVA as a type of ballet. This is a useful and appropriate analogy to many task. Once you start the EVA/ballet, you enter a routine where everything starts to flow and your thinking about the entire EVA/ballet as a whole, not just the next move. Whenever you interrupt the EVA/ballet, it will take some time to again get into the routine.

Data Collection

Videotapes of the entire STS-61 mission were obtained for analysis. These tapes included both onboard video (video recorded on tape recorders in the orbiter) and downlink video (video transmitted to mission control). Ideally the videotape to be analyzed included both the audio track and a time encoding. The audiotrack helped to determine the exact activity the astronaut was performing and determine what the pauses were for. Little useful information can be collected in the absence of the audio track. An essential tool used in conjunction with the audiotrack is the EVA timeline contained in the Flight Data File for the mission. The timeline allows one to know what is going on in the video and what operations are taking place. This also allows the analyst to know when the mission is deviating from the planned mission. The time encoding allows for the easy analysis of the time required to perform a task. It is possible to collect useful information in the absence of the encoding by using a stop watch to time the activities. This is cumbersome and does not allow for the slow motion analysis that is sometimes required to get a precise time.

The downlink video had a lower resolution than the onboard video, however, many of the onboard videos lacked either the audio tracks or time encoding. Initial data collection was performed using the downlink footage. This footage was taped in the order of the EVA missions and more attention had been paid to the focusing of the cameras on the activities that were being performed. Onboard videos were used to supplement the downlink videos when the astronauts were out of view in the downlink footage or the downlink was lost due to the lack of complete TDRS coverage. Even when making use of the two video sources, gaps in the coverage of a given EVA mission still exist.

The resolution and lighting of the videotapes is a problem in performing the motion and time study. At times the video image flares to white when the camera is over exposed with light and at times it fades to black when the light level drops on the camera is under exposed.

A studio quality tape player was used to play the tapes. The recorder allowed the speed of the tape to be controlled without a loss in the resolution of the image. This allowed speeding through portions of the video where there was no activity and slowing down for portions where there was a lot of activities occurring requiring close observation.

A spreadsheet to record the data was created using Microsoft Excel. The spreadsheet had space for the following information to be collected:

- Reference number within the data base
- Astronaut performing the task
- Planned time of the task
- Actual time of the task
- Timeline procedure from the Flight Data File
- Task primitive

- Task class of the primitive
- Task description containing supplemental information
- Starting time of the task
- Stopping time of the task
- Elapsed time of the task
- Hand used for the task (left, right, both)
- The task
  - Direction (CW, CCW, left, right, etc.)
  - Value (ft, revolutions, etc.)
  - Encumbrance
  - Obstacles
  - Rate (ft/sec, rev/sec, etc.)
- View
- Light (day, night, helmet lights, helmet and spot, etc.)
- Restraint (free, holding with left hand / right hand, PFR, MFR, etc.)
- Posture (neutral, twisted, hunched forward, etc.)
- Metabolic rate
- Errors committed
- Comments

This information will allow for the analysis of the times required for the task primitives and for analyzing the effects of the possible task modifiers. The database will be modified to reflect any lessons learned from the initial data collection performed on the Hubble EVAs.

Analysis

Analysis of the data collected on from STS-61 is currently in progress. Most of the analysis will be performed using the PC SAS statistical package. The following section presents an example of the analysis currently performed. The task primitive being analyzed is the "Rotate MFR" primitive. The data set is comprised of information collected from two different astronauts, EV1 and EV2. Table 1 presents the results of performing t-tests comparing the rotation rates of EV1 to EV2. None of the results are significantly different, but we can discern some qualitative differences between the two astronauts in reviewing the comments section of the data. In clockwise rotations, EV1 was large enough in stature to be physically capable of reaching around and grabbing the PWS and pulling himself around. EV2 had to rely on inertia to rotate around due to a small physical stature preventing the ability to reach around and grab the PWS. This is reflected in the t-value. The larger mass of EV1 also allowed him to have a greater rotational inertia when rotating without the aid of the stanchion.

Table 1. T-test comparing EV times.

EV1 to EV2	t_0=	df=
CW to CW	0.296282	49
CCW to CCW	0.112795	38
CW to CCW	0.05151	37
CCW to CW	0.362592	50

Future Plans

Analysis of the currently collected data will continue. This will provide an insight into how the different task primitives should be handled and what types of adjustments will have to be made. Any necessary refinements to the system will also be made at this time. After the refinements are made, the remaining EVAs from STS-61 will be analyzed to build up the database. Data will also be collected from the WETF training sessions with the hope of determining the correlation factors between WETF times and flight times.

ACRONYMS

EMU	extravehicular mobility unit
EVA	extravehicular activity
ISSA	International Space Station Alpha
MFR	manipulator foot restraint
PFR	portable foot restraint
PWS	portable work stanchion
RMS	remote manipulator system
TDRS	tracking and data relay satellite
WETF	weightless environment trainer

REFERENCES

Fisher, William F., Price, Charles R., *Space Station Freedom External Maintenance Task Team, Final Report*, vol. I, parts 1-2, July 1990, NASA

Niebel, Benjamin W., *Motion and Time Study*, 8th ed., Homewood, Il.:Irwin, 1988.

NASA, *EVA Lessons Learned*, vol. I, October 1994.

NASA, *EVA Lessons Learned*, vol. II, October 1994.

NASA, *STS-61 Flight Data File*

NASA, *STS-61 Videotape Scenelist*, JSC-25945-61

STABLE ISOTOPE ANALYSIS OF MOLECULAR OXYGEN FROM SILICATES AND OXIDES USING CO_2 LASER EXTRACTION

54-25
76312
10P.
234350

Final Report
NASA/ASEE Summer Faculty Fellowship Program – 1995
Johnson Space Center

Prepared by:	Eugene Perry, PhD.
Academic Rank:	Professor
University and Department:	Northern Illinois University Department of Geology DeKalb, IL 60115
NASA/JSC	
Directorate:	Space and Life Sciences
Division:	Earth Science and Solar System Exploration
Branch:	Planetary Science
JSC Colleague:	Everett K. Gibson, Jr.
Date Submitted:	September 8, 1995
Contract Number:	NGT-44-001-800

Abstract

A laser-excited system for determination of the oxygen isotope composition of small quantities of silicate and oxide minerals was constructed and tested at JSC. This device is the first reported to use a commercially available helium cryostat to transfer and purify oxygen gas quantitatively within the system. The system uses oxygen gas instead of the conventional CO_2 for mass spectrometer analyses. This modification of technique permits determination of all three stable oxygen isotopes, an essential requirement for oxygen isotope analysis of meteoritic material. Tests of the system included analysis of standard silicate materials NBS 28 and UWMG2 garnet, six SNC meteorites, and inclusions and chondrules from the Allende meteorite. Calibration with terrestrial standards was excellent. Meteorite values are close to published values and show no evidence of terrestrial oxygen contamination. The one limitation observed is that, in some runs on fine-grained SNC matrix material, sample results were affected by other samples in the sample holder within the reaction chamber. This reemphasizes the need for special precautions in dealing with fine-grained, reactive samples. Performance of the JSC instrument compares favorably with that of any other instrument currently producing published oxygen isotope data.

Introduction

Oxygen isotope analysis of silicates and oxides, a technique developed by Silverman, 1951; Taylor and Epstein, 1962; and Clayton and Mayeda, 1963, has provided a wealth of information in igneous and metamorphic petrology, geochemistry of mineral deposits, meteoritics, and other fields. Interest in transport phenomena and nucleosynthetic processes has driven efforts to analyze small samples, leading to development of laser-fluorination devices that quantitatively release oxygen from milligram amounts of material. (Sharp, 1992). In most cases, the method of choice has been to liberate oxygen using a fluorinating agent such as fluorine gas (Taylor and Epstein, 1962) or bromine pentafluoride (Clayton and Mayeda, 1963) and convert the oxygen gas produced to CO_2, which is then analyzed mass spectrometrically.

Laser fluorination differs from conventional fluorination in that the fluorination system is attached directly to a mass spectrometer for "real time" analysis; and fluorination occurs in a small chamber in which laser energy is focussed on the sample so that the containment vessel is not exposed to the fluorinating agent at high temperature. The reason that most analysts convert oxygen to CO_2 before analysis is that CO_2 can be readily pumped and concentrated in liquid nitrogen cold traps whereas oxygen cannot. A particular disadvantage of performing isotopic analysis of oxygen using CO_2 gas is that ^{13}C (abundance approximately 1.1%) is collected in the mass spectrometer at nominal mass 45 ($^{13}C^{16}O^{16}O$) and masks isotopic variations in ^{17}O ($^{12}C^{17}O^{16}O$), which has an abundance of approximately .0375%. This does not pose a problem for analysis of terrestrial samples, which are isotopically homogeneous, that is, they show only chemical variations so that $^{17}O/^{16}O$ is always proportional to $^{18}O/^{16}O$. In contrast, the ability to analyze only abundances of ^{16}O and ^{18}O poses an unsatisfactory limitation on meteorite studies because meteorites are isotopically inhomogeneous, and this inhomogeneity offers critically important information about the origin of the solar system (Clayton 1993).

In collaboration with C. S. Romanek and R. A. Socki, I have developed and tested an apparatus for laser-excited mass spectrometric analysis of molecular oxygen in silicates and oxides in the stable isotope laboratory of Everett Gibson. The fluorination line is shown in Figure 1. A 25 watt CO_2 laser is used to heat the sample within a reaction chamber in the presence of a strong fluorinating agent. This procedure releases oxygen gas quantitatively from silicates and/or oxides by replacing it with a stronger oxidizing agent: fluorine. For example:

$$5SiO_2 + 4BrF_5 = 5SiF_4 + 2Br_2 + 5O_2$$

BrF_5 required in the reaction chamber (Fig. 1, RC) is fed into the system through the detachable cylinder R. After fluorination takes place in RC, a mixture of gases is present in the system, including O_2, excess BrF_5, SiF_4, Br_2, F_2, and trace gases. BrF_5, SiF_4, Br_2, and some trace gases are removed in a cold trap (T1) maintained at the temperature of liquid nitrogen. To the right of this trap, gas should be relatively free of strong oxidizing substances except sample oxygen. Some F_2 is carried over, and this is removed by reaction with KBr present in the vacuum line as indicated. The reaction involved:

$$F_2 + 2KBr = 2KF + Br_2$$

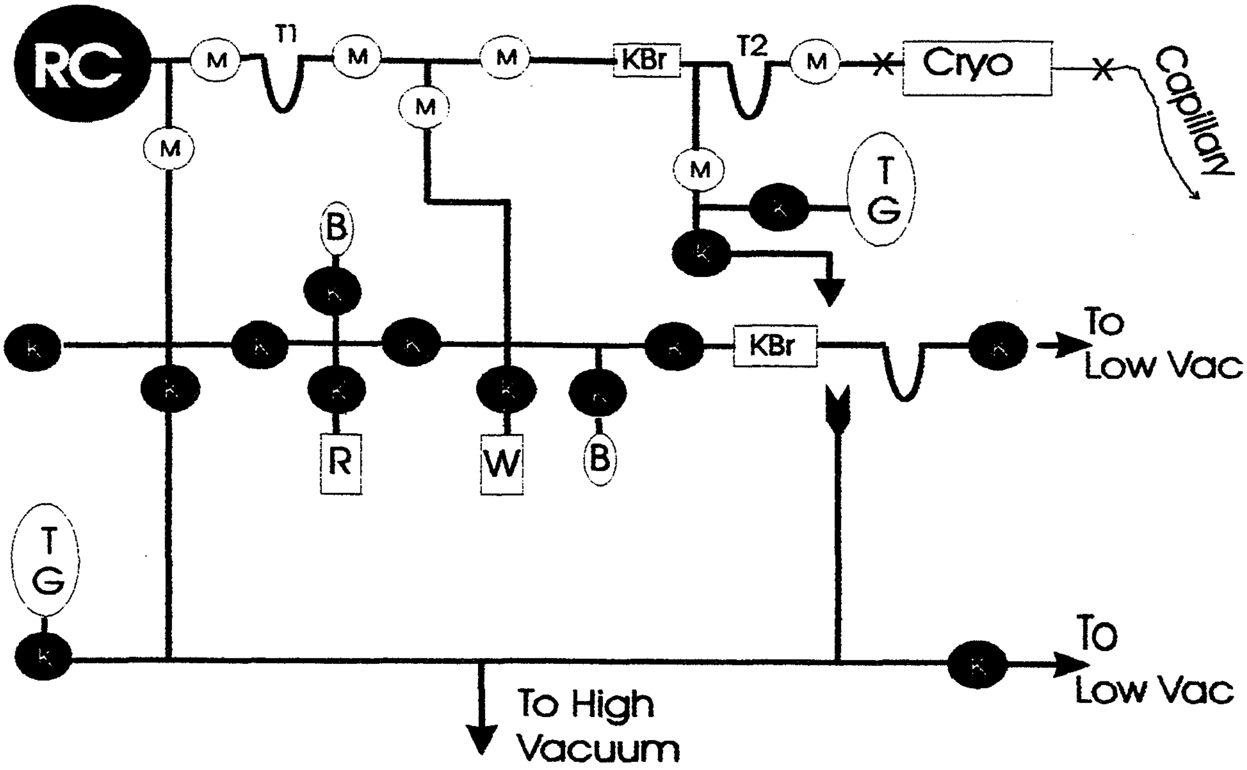

Figure 1.- Schematic of laser excitation system. RC: Reaction Chamber; Cryo: Helium Cryotrap; M:All-Metal Valves; K: Valves with Kel-F seats; KBr: KBr Traps for Fluorine; R: BrF_5 Reservoir; W: Waste collector; B: Bourdon Gauge: TG: Thermocouple Gauge.

produces Br_2 which is trapped in a second liquid nitrogen trap (T2). No Br_2, F_2, BrF_5, or H_2O should ever be allowed to pass beyond this trap. The gases Br_2, SiF_4, and excess BrF_5 are removed from the system by trapping them with liquid nitrogen in the cylinder labelled W.

An essential sample pretreatment step is to begin with one or more short (5 to 20 minute) fluorinations. This is because water vapor reacts to form HF, which is more corrosive than fluorine to 316SS tubing, copper gaskets and particularly BaF_2 windows:

$$5H_2O + 2BrF_5 = 10HF + Br_2 + {}^5/_2O_2.$$

As the reaction indicates, water vapor is also a serious analytical contaminant.

The unique feature of the JSC system is that it uses a comercially available helium cryostat to collect oxygen gas for analysis. Oxygen is frozen out very effectively below 37° K, whereas Br_2 and BrF_5 remain frozen at 100° K. The troublesome trace gas NF_3 (which has a breakdown fragment at mass 33 that interferes with ^{17}O measurements) remains frozen at 100° K. Thus, the procedure that has been developed is to cool the cryostat to 35° K, trap the sample in the cryostat and then raise the temperature to 100° K and release the collected sample, through a capillary leak, into a mass spectrometer (MAT 251).

The reason for building this system is to examine meteorites, particularly the SNC ("martian") meteorites. This type of analysis is a challenging task that has been accomplished by few laboratories in the world. Meteorite data that I collected is given in Table 1 and plotted in Figure 2. Units are $\delta^{18}O$ and $\delta^{17}O$ defined as permil (‰) variations from a standard: SMOW.

$$\delta^{18}O = 1000x[(^{18}O/^{16}O)_{Sample} - (^{18}O/^{16}O)_{SMOW}]/(^{18}O/^{16}O)_{SMOW}$$

$$\delta^{17}O = 1000x[(^{17}O/^{16}O)_{Sample} - (^{17}O/^{16}O)_{SMOW}]/(^{17}O/^{16}O)_{SMOW}.$$

For all terrestrial samples, to a good approximation,

$$\delta^{17}O = 0.52\delta^{18}O.$$

This is the equation for the "Terrestrial Fractionation line" shown in Figures 2 and 4, and it is the locus of oxygen isotope composition of all terrestrial oxygen reservoirs accessible to direct human observation (except the upper atmosphere). The implication is that these reservoirs are all well mixed. The sample analyses in Table I include two well-established terrestrial standards, NBS 28 quartz and UWMG 2 garnet. They also include meteorite material that spans over half the known variation in oxygen isotope composition of silicate minerals of the solar system. These constitute an excellent test of the capabilities of the JSC system. As Figure 3 shows, JSC data are consistent with accepted values for the some of the most diverse samples, inclusions in the carbonaceous chondrite meteorite Allende. The correlation of JSC values with "accepted" values reported by Clayton et al (1977) is excellent; there is no evidence of contamination with terrestrial oxygen.

Data for SNC ("martian") meteorites, plotted in Figure 4, show both the power and one of the limitations of the laser excitation method.The oxygen isotope composition of SNC samples plots on a line similar to, but distinctly displaced from, terrestrial samples as is shown in the figure. The least square regression line ($r^2 = .938$) through my data is:

$$\delta^{17}O = 0.50\delta^{18}O + 0.47.$$

The regression line through published analyses is:

$$\delta^{17}O = 0.53\delta^{18}O + 0.25.$$

Within the range of values of interest, these two equations are nearly identical, and there is little or no evidence of terrestrial contamination during an extremely humid summer.

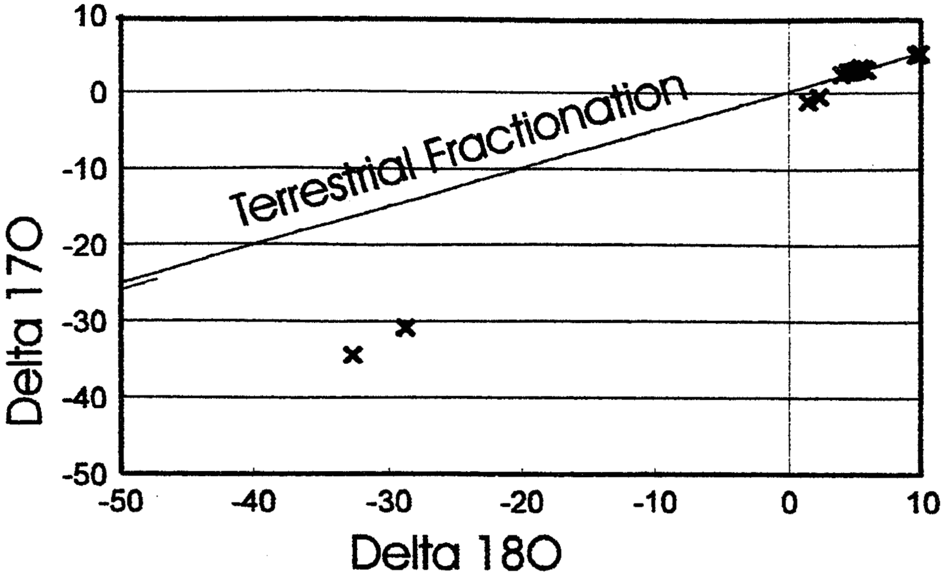

Figure 2.- Data generated with the JSC laser-excited system. Meteorite data diverge widely from terrestrial data. (Terrestrial samples from whatever source lie on the line labelled "terrestrial fractionation.")

Table 1.-

Sample	Run #	$\delta^{17}O_{machine}$	$\delta^{18}O_{machine}$	$\delta^{17}O_{SMOW}$	$\delta^{18}O_{SMOW}$
NBS28	110	-8.42	-17.21	4.94	9.53
NBS28	111	-8.4	-17.22	4.96	9.52
NBS28	112	-8.32	-17	5.04	9.74
NBS28	114	-8.25	-16.97	5.11	9.77
Chassigny	115	-10.89	-22.68	2.44	3.91
LaFayette	116	-10.43	-21.56	2.91	5.06
79001B	118	-10.62	-21.97	2.71	4.64
Zagami	119	-10.6	-22	2.73	4.61
79001A	120	-10.53	-21.94	2.80	4.67
Chassigny	122	-10.59	-22.25	2.74	4.35
Chassigny	123	-10.57	-21.92	2.76	4.69
Chassigny	124	-10.45	-21.73	2.89	4.88
LaFayette	125	-10.35	-21.5	2.99	5.12
LaFayette	126	-10.06	-21.29	3.28	5.34
Allende Chondrule	128	-13.76	-24.31	-0.47	2.23
Allende Chondrule	129	-14.4	-25.1	-1.12	1.42
Allende Pink Inclusion	131	-47.25	-58.3	-34.41	-32.68
Allende Pink Inclusion	132	-43.71	-54.51	-30.82	-28.79
UWMG 2	133	-10.25	-20.95	3.09	5.69
UWMG 2	134	-10.31	-20.87	3.03	5.77
UWMG 2	135	-10.34	-20.92	3.00	5.72

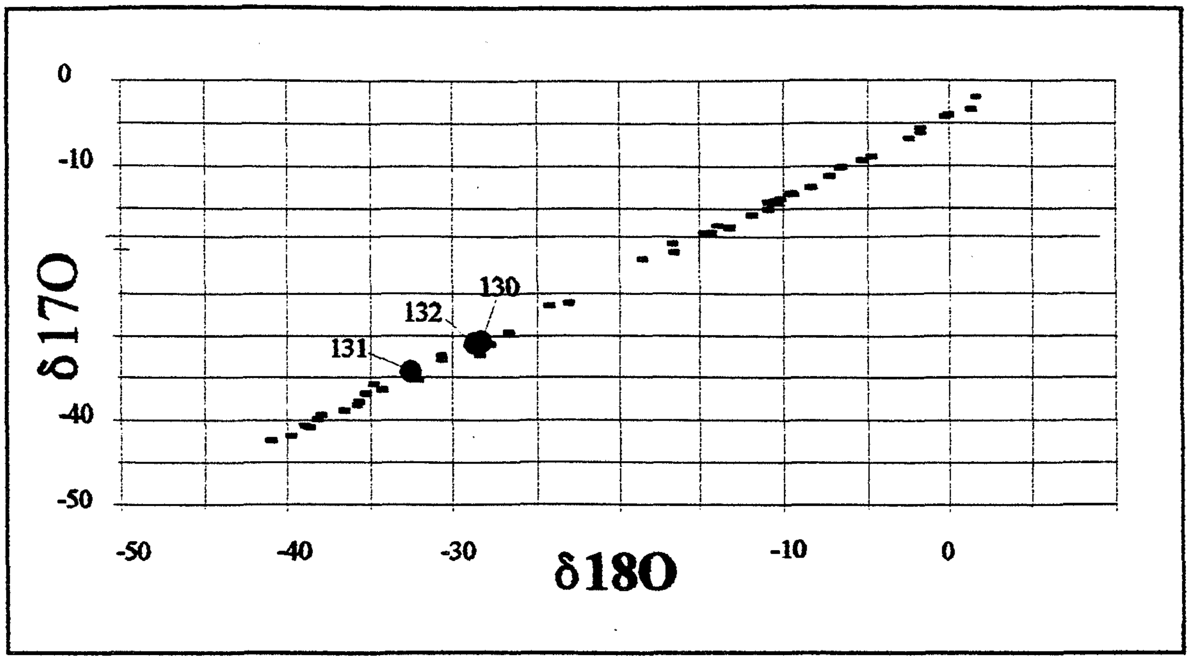

Figure 3.- Allende inclusion data. JSC data superimposed on literature data

The system limitation mentioned above shows up in repeat analyses of samples Chassigny and Lafayette. Although terrestrial contamination was not a problem, reproducibility of individual sample isotope compositions is not as good as predicted. Evaluation of the data strongly suggest that these samples (which are composed of extremely fine-grained and reactive material) contaminated each other within the sample chamber (where multiple samples were placed awaiting reaction). Clearly, with fine-grained meteorite samples special precautions will be required to obtain reproducible results.

The analyses reported here were of a size to produce 15 micromoles or more of oxygen gas. This is a normal sample size for laser analysis, but it does not challenge the limits of small sample analysis. The idea behind this choice of sample size was to test the precision of the system before attempting to work with extremely small samples. Some considerably smaller samples (about 5 micromoles of oxygen) were run in a small secondary cryotrap. Preliminary results from these runs indicate that samples significantly smaller than those reported on here can be analyzed using the JSC instrument. This contrasts with devices using CO_2 conversion to produce samples for introduction into the mass spectrometer. These CO_2 systems may be unable to analyze relatively small samples because of the increased importance of carbon monoxide production at very low pressure.

Early results of the work reported here will be presentedat the 1995 annual meeting of the Geological Society of America (Romanek et al, 1995). A more detailed report (Perry, Romanek, Socki, and Gibson) is in preparation.

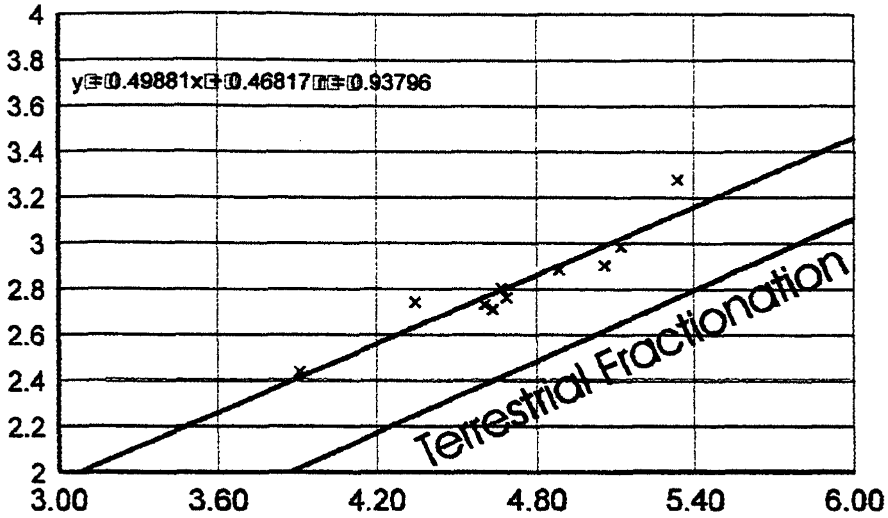

Figure 4.- SNC ("martian") meteorites. These are tightly grouped and fall slightly above the terrestrial fractionation line on a three isotope plot.

Conclusions

A system for laser excitation of oxygen in silicateand oxide minerals has been designed, built, and tested. This system incorporates a new design that depends on a helium cryostat to freeze oxygen and to release it into a mass spectrometer under precisely controlled conditions. Analyses of meteorites and terrestrial oxygen isotope standards indicate that the system is capable of precise analyses of small samples and that its performance compares favorably with that of any system currently in operation.

Bibliography

Clayton, R. N. (1993) Oxygen isotopes in meteorites. Ann Rev Earth Planet Sci **21**, pp.115-149.

Clayton, R. N. , N. Onuma, L. Grossman, and T. K. Mayeda (1977) Distribution of the pre-solar component in Allende and other carbonaceous chondrites. EPSL **34**, pp. 209-224.

Clayton, R. N,. and T. K. Mayeda (1963) The use of bromine pentafluoride in the extraction of oxygen from oxides and silicates for isotopic analysis. Geochim et Cosmochim Acta 27, p. 43.

Romanek, C. S., E. C. Perry, R. A. Socki, and E. K. Gibson, Jr. (1995) Stable isotope analysis of diatomic oxygen from quartz. To be presented at the annual national meeting of GSA, New Orleans, 1995.

Sharp, Z. D. (1992) In-situ laser microprobe techniques for stable isotope analysis. Chem Geol **101**, pp. 3-19.

Silverman, S. R. (1951) The isotope geology of oxygen. Geo et Cosmo Chim Acta **2**, pp. 26-42.

Taylor, H. P., Jr. and S. Epstein (1962) Relationship between O^{18}/O^{16} ratios in coexisting minerals of igneous and metamorphic rocks. GSA Bull **73**, pp. 461-480.

ILIAD TESTING; AND A KALMAN FILTER FOR 3-D POSE ESTIMATION

S5-82
76323
234351
14P.

Final Report
NASA/ASEE Summer Faculty Fellowship Program-1995
Johnson Space Center

Prepared By:	Albert O. Richardson, Ph.D
Academic Rank:	Professor
University & Department	California State Univ., Chico Dept. of Electrical & Computer Engineering Chico, California, 95929-0888
NASA/JSC	
Directorate:	Information Systems
Division:	Technology Systems
Branch:	Client/Server
Date Submitted:	8/10/95
Contract Number:	NGT-44-001-800

ABSTRACT

This report presents the results of a two-part project. The first part presents results of performance assessment tests on an Internet Library Information Assembly Data Base(ILIAD). It was found that ILIAD performed best when queries were short(one-to-three keywords), and were made up of rare, unambiguous words. In such cases as many as 64% of the typically 25 returned documents were found to be relevant. It was also found that a query format that was not so rigid with respect to spelling errors and punctuation marks would be more user-friendly.

The second part of the report shows the design of a Kalman Filter for estimating motion parameters of a three dimensional object from sequences of noisy data derived from two-dimensional pictures. Given six measured deviation values representing X, Y, Z, pitch, yaw, and roll, twelve parameters were estimated comprising the six deviations and their time rate of change. Values for the state transition matrix, the observation matrix, the system noise covariance matrix, and the observation noise covariance matrix were determined. A simple way of initilizing the error covariance matrix was pointed out.

INTRODUCTION

A two-part project was undertaken. For the first part, some tests were performed on ILIAD(Internet Library Information Assembly Data Base)[1] in order to assess its performance, user-friendliness, and to develop some insight into the search technique utilized by ILIAD. For the second project, A Kalman Filter was designed for estimating a rigid body's motion parameters from noisy images. The ILIAD tests will be describe first, followed by the Kalman Filter Design.

THE ILIAD TESTS

Introduction.

ILIAD, which is an Internet-based information search and retrieval system with a built-in intelligent agent, was designed and implemented, at the NASA Johnson Space Center, by the Client Server Branch of the Information Systems Directorate. It was designed as an intelligent data base primarily to serve K-12 teachers. In operation, a teacher sends a "query", made up of key words, to ILIAD, via electronic mail(e-mail). ILIAD uses the key words to search the Internet for documents whose contents deal with the subject matter represented by the key words. The entire contents of these documents are sent, by e-mail, to the person who sent the query.

It must be emphasized, that apart from the tests described here, the designers of ILIAD performed their own series of tests. What is reported here is, for the most part, the result of the author's tests. Although these tests are not comprehensive, their value lies in the fact, that they provide a sense of how well ILIAD is working---more than thirty queries were generated and sent by the author---, and help point to some of the issues that must be addressed in any future systematic testing of, and improvements upon, ILIAD. The queries employed dealt with subject matter that the author was interested in.

Testing Procedure:

The testing process comprised the following:

1. Develop a series of queries spanning a variety of subject areas.
2. Send queries to ILIAD.
3. Observe simplicity/complexity of query submission and response.
4. Examine ILIAD responses, noting:
    a) Response Time.
    b) Relevance of Returned Documents.
5. Select a few representative queries and the corresponding returned documents.
6. Examine these documents in detail with respect to:
    a) Ratio of relevant versus non-relevant documents
    b) Choice of words or terminology and the relevance of returned documents.

b) ILIAD's relevance criteria versus query submitter's relevance criteria:

--- "Key words search" or "Key phrases" search?

RESULTS AND DISCUSSION.

Query Format, Simplicity And User Friendliness.

The author found the query format and ILIAD acknowledgements to be quite simple and user-friendly. The user only needs to type in the following:

*TeacherEmail: the user's actual email is typed here.
*VolumeLevel: type in here, low, medium, or high, to indicate amount of materials desired.
*?Q1: actual query key words are typed in here.

Problems arise only when the user is careless in typing in the required items in the exact format specified. This would typically be in the form of typographical errors, ommisions, and incorrect cases(upper case or lower case) for characters. Although, it has been pointed out that most email systems have spell checkers, rejection of queries by ILIAD due to incorrect formats could be a source of frustration for teachers, many of whom may be in a hurry to squeeze in some information retrieval activity among their daily busy schedule.

Upon the author's recommendations, the ILIAD designers have implemented changes that make ILIAD no longer rigidly sensitive to spelling errors and innocuous characters like spaces and commas.

ILIAD Response Time And Relevance Of Returned Documents.

When a query was sent, ILIAD first acknowledged receipt of the query within a minute. The documents themselves were received within one to two hours.

More than thirty queries were sbmitted. These dealt with a variety of subject areas including technology, science, government, history, and ancient architecture. Some representative queries were: "parallel processing", "genetic algorithms", "intelligent robots", "fuzzy logic", "microprocessors microcontrollers", "wavelets", "European Economic Community", and " Egyptian Pyramids". Most of the documents returned in response to these queries were found to be very relevant. However, documents returned in response to queries like: "Microsoft Corporation", "wavelets communication", "volcano eruptions Africa", were not particularly relevant. More on that later, under the section on "Key words search" or "Key phrases search".

Detailed Results Of Some Queries.

Shown below is a tabulation of the details of six queries.

Query #	Query	# Of Docs.	# Docs. Relv.	% Docs. Relv.
1	parallel processing	25	10	40%
2	intelligent robots	25	12	48%
3.	wavelets	25	16	64%
4.	Airbus Consortium	25	0	0%

5.	wavelet communications	25	< 5	<20%
6.	microprocessors	25	>15	>60%

Key Word Choice And Relevance Of Returned Documents.

The data shown above, together with other observed results, would seem to indicate that the ideal query would be a one word query where that single word does not find usage in many different applications and contexts. For example, the query "wavelet" produces a high percentage of relevant documents(64%), whereas the query "Airbus Consortium" produces a low percentage of relevant documents(0%)! Although the term, "Airbus" generally refers to the model name of the airplane manufactured by the European Airbus Industries Inc., the term "Consortium" has such widespread usage, that ILIAD found lots of documents describing consortiums that had nothing to do with the Airbus Industries of Europe.

"Key Words" Or "Key Phrases" Search?

ILIAD uses the WAIS(Wide Area Information Server)[2] package developed at Thinking Machines Corporation, Cambridge, Massachusetts. In his paper entitled, " Massively Parallel Information Retriever for Wide Area Information Servers", Craig Stanfill of Thinking Machines Corporation refers to the way in which WAIS treats the query thus: [3]

" Queries consist of short natural language phrases, such as 'Corazon Aquino and the Philippine Election'. Each phrase is broken into primitive components such as 'Corazon Aquino,' and 'Philippine Election,' and each component is assigned a numerical weight with rare(i.e. more specific)terms assigned higher value. The documents are then ranked from highest to lowest, and the best matches presented to the user."

The author has not been able to assess how efficiently WAIS does this weight assignment in favor of 'rare terms', but in the case of the query "wavelet communication"--communication, meaning information transmission in an engineering context--, the term 'communication' must not have been assigned a small enough weighting, because too many documents containing only the word 'communication'(within a non-engineering context), and without the word 'wavelet', were returned by ILIAD. A higher percentage of relevant documents would result if WAIS did indeed search for the ocurrences of the whole phrase representing the key words. Alternatively, a more stringent assignment of weighting in favor of rare terms, so that the word 'communication' would be recognized as an everyday word , and therefore should be assigned a very low weighting wherever it occurs alone.

KALMAN FILTER DESIGN

Introduction.

The second project involved the design of a Kalman filter for estimating motion parameters of a three dimensional body from a sequence of two dimensional images. Geometrical techniques had been used by Jodi Seaborn and Robert Goode of ER4 to obtain measured values of the object's center coordinates, X,Y,Z, as well as the pitch, roll, and yaw, as determined from at least three image corresponding points on the object and on the two-dimensional picture.[4] The idea is to use the Kalman filter to estimate these parameters in addition to their time rates of change.

System Modeling, Determining The State Transition Matrix[5,6,].

The object to be tracked can be modelled by the state equations

$$x(k+1) = \Phi x(k) + u(k) \qquad (1)$$

where

$$x(k) = \begin{array}{c} X(k) \\ X(k) \\ Y(k) \\ Y(k) \\ Z(k) \\ Z(k) \\ \alpha(k) \\ \alpha(k) \\ \beta(k) \\ \beta(k) \\ \chi(k) \\ \chi(k) \end{array}$$

$$= \begin{bmatrix} X-deviation \\ X-rate \\ Y-deviation \\ Y-rate \\ Z-deviation \\ Z-rate \\ pitch-deviation \\ pitch-rate \\ yaw-deviation \\ yaw-rate \\ roll-deviation \\ roll-rate \end{bmatrix}$$

Assume an object being tracked is at coordinates X'+$X(k)$, Y'+$Y(k)$, Z'+$Z(k)$, $\mathrm{A}+\alpha(k),\mathrm{B}+\beta(k),\mathrm{X}+\chi(k)$, at time k, and at coordinates X'+$X(k+1)$, Y'+$Y(k+1)$,Z'+$Z(k+1)$, $\mathrm{A}+\alpha(k+1),\mathrm{B}+\beta(k+1),\mathrm{X}+\chi(k+1)$, at time $k+1$, T seconds later. "T" represents the time spacing between two successive two dimensional still images taken by a camera of the moving object. We are interested in estimating these linear and angular deviations and their rates, which are assumed to be statistically random with zero-mean values.

To a first approximation, if the object is moving at velocities, or rates, given by $\dot{X}(k),\dot{Y}(k),\dot{Z}(k),\dot{\alpha}(k),\dot{\beta}(k),\dot{\chi}(k)$, and T is not too large, then considering, for example, the Z coordinate, we have

$$Z(k+1)=Z(k)+T\dot{Z}(k) \quad \text{......................................}(2)$$

which is an example of a "deviation equation".

Similarly, considering the acceleration $u(k)$, we have

$$Tu(k)=\dot{Z}(k+1)-\dot{Z}(k) \quad \text{......................................}(3)$$

which is the "acceleration equation". Assuming that $u(k)$ is a zero-mean, stationary white noise process, the acceleration is, on the average, zero and uncorrelated between intervals, $E[u(k+1)u(k)]=0$, but it has some variance $E\left[u^2(k)\right]=\sigma_u^2$. Such accelerations could be caused by short term irregularities in external influences on the object. The quantity $u_3(k)=Tu(k)$ is also a white noise process, and therefore the acceleration equation for the coordinate Z, can be written as

$$\dot{Z}(k+1)=\dot{Z}(k)+u_3(k) \text{..}(4)$$

The complete set of range/bearing and acceleration equations for the twelve parameters are:

$$\begin{aligned}
X(k+1) &= X(k)+T\dot{X}(k)\\
\dot{X}(k+1) &= \dot{X}(k)+u_1\\
Y(k+1) &= Y(k)+T\dot{Y}(k)\\
\dot{Y}(k+1) &= \dot{Y}(k)+u_2\\
Z(k+1) &= Z(k)+T\dot{Z}(k)\\
\dot{Z}(k+1) &= \dot{Z}(k)+u_3\\
\alpha(k+1) &= \alpha(k)+T\dot{\alpha}(k)\\
\dot{\alpha}(k+1) &= \dot{\alpha}(k)+u_4\\
\beta(k+1) &= \beta(k)+T\dot{\beta}\\
\dot{\beta}(k+1) &= \dot{\beta}(k)+u_5\\
\chi(k+1) &= \chi(k)+T\dot{\chi}\\
\dot{\chi}(k+1) &= \dot{\chi}(k)+u_6
\end{aligned} \qquad \text{..................................(5)}$$

$$u(k)=\begin{bmatrix} u_1(k)\\ u_2(k)\\ u_3(k)\\ u_4(k)\\ u_5(k)\\ u_6(k)\end{bmatrix}=\begin{bmatrix} X-acceleration\\ Y-acceleration\\ Z-acceleration\\ pitch-acceleration\\ yaw-acceleration\\ roll-acceleration\end{bmatrix} \text{..... between time k and k+1}$$

The complete state equation for the system is given by

$$\begin{bmatrix} \chi_1(k+1)\\ \chi_2(k+1)\\ \chi_3(k+1)\\ \chi_4(k+1)\\ \chi_5(k+1)\\ \chi_6(k+1)\\ \chi_7(k+1)\\ \chi_8(k+1)\\ \chi_9(k+1)\\ \chi_{10}(k+1)\\ \chi_{11}(k+1)\\ \chi_{12}(k+1)\end{bmatrix}=\begin{bmatrix}
1 & T & 0 & 0 & 0 & 0 & 0 & 0 & 0 & 0 & 0 & 0\\
0 & 1 & 0 & 0 & 0 & 0 & 0 & 0 & 0 & 0 & 0 & 0\\
0 & 0 & 1 & T & 0 & 0 & 0 & 0 & 0 & 0 & 0 & 0\\
0 & 0 & 0 & 1 & 0 & 0 & 0 & 0 & 0 & 0 & 0 & 0\\
0 & 0 & 0 & 0 & 1 & T & 0 & 0 & 0 & 0 & 0 & 0\\
0 & 0 & 0 & 0 & 0 & 1 & 0 & 0 & 0 & 0 & 0 & 0\\
0 & 0 & 0 & 0 & 0 & 0 & 1 & T & 0 & 0 & 0 & 0\\
0 & 0 & 0 & 0 & 0 & 0 & 0 & 1 & 0 & 0 & 0 & 0\\
0 & 0 & 0 & 0 & 0 & 0 & 0 & 0 & 1 & T & 0 & 0\\
0 & 0 & 0 & 0 & 0 & 0 & 0 & 0 & 0 & 1 & 0 & 0\\
0 & 0 & 0 & 0 & 0 & 0 & 0 & 0 & 0 & 0 & 1 & T\\
0 & 0 & 0 & 0 & 0 & 0 & 0 & 0 & 0 & 0 & 0 & 1
\end{bmatrix}\begin{bmatrix} \chi_1(k)\\ \chi_2(k)\\ \chi_3(k)\\ \chi_4(k)\\ \chi_5(k)\\ \chi_6(k)\\ \chi_7(k)\\ \chi_8(k)\\ \chi_9(k)\\ \chi_{10}(k)\\ \chi_{11}(k)\\ \chi_{12}(k)\end{bmatrix}+\begin{bmatrix} 0\\ u_1(k)\\ 0\\ u_2(k)\\ 0\\ u_3(k)\\ 0\\ u_4(k)\\ 0\\ u_5(k)\\ 0\\ u_6(k)\end{bmatrix} \text{..(6)}$$

The measured data(the six motion parameters) are assumed to be noisy, and are modelled thus:

$$\left.\begin{array}{l} y_1(k) = x_1(k) + v_1(k) \\ y_2(k) = x_3(k) + v_2(k) \\ y_3(k) = x_5(k) + v_3(k) \\ y_4(k) = x_7(k) + v_4(k) \cdots \\ y_5(k) = x_9(k) + v_5(k) \\ y_6(k) = x_{11}(k) + v_6 \end{array}\right\} \begin{array}{l} X - deviation \\ Y - deviation \\ Z - deviation \\ pitch - deviation \\ yaw - deviation \\ roll - deviation \end{array} \qquad \cdots\cdots\cdots\cdots(7)$$

Therefore, the data vector can be written as:

$$\begin{bmatrix} y_1(k) \\ y_2(k) \\ y_3(k) \\ y_4(k) \\ y_5(k) \\ y_6(k) \end{bmatrix} = \begin{bmatrix} 1 & 0 & 0 & 0 & 0 & 0 & 0 & 0 & 0 & 0 & 0 & 0 \\ 0 & 0 & 1 & 0 & 0 & 0 & 0 & 0 & 0 & 0 & 0 & 0 \\ 0 & 0 & 0 & 0 & 1 & 0 & 0 & 0 & 0 & 0 & 0 & 0 \\ 0 & 0 & 0 & 0 & 0 & 0 & 1 & 0 & 0 & 0 & 0 & 0 \\ 0 & 0 & 0 & 0 & 0 & 0 & 0 & 0 & 1 & 0 & 0 & 0 \\ 0 & 0 & 0 & 0 & 0 & 0 & 0 & 0 & 0 & 0 & 1 & 0 \end{bmatrix} \begin{bmatrix} x_1(k) \\ x_2(k) \\ x_3(k) \\ x_4(k) \\ x_5(k) \\ x_6(k) \\ x_7(k) \\ x_8(k) \\ x_9(k) \\ x_{10}(k) \\ x_{11}(k) \\ x_{12}(k) \end{bmatrix} + \begin{bmatrix} v_1(k) \\ v_2(k) \\ v_3(k) \\ v_4(k) \\ v_5(k) \\ v_6(k) \end{bmatrix} \cdots(8)$$

In terms of vector formulation, the two vector equations representing the system and measurement models are:

$$\begin{array}{r} x(k+1) = \Phi(k)x(k) + u(k) \\ y(k) = H(k)x(k) + v(k) \end{array} \qquad \cdots\cdots\cdots\cdots(9)$$

$$\Phi = \begin{bmatrix} 1 & T & 0 & 0 & 0 & 0 & 0 & 0 & 0 & 0 & 0 & 0 \\ 0 & 1 & 0 & 0 & 0 & 0 & 0 & 0 & 0 & 0 & 0 & 0 \\ 0 & 0 & 1 & T & 0 & 0 & 0 & 0 & 0 & 0 & 0 & 0 \\ 0 & 0 & 0 & 1 & 0 & 0 & 0 & 0 & 0 & 0 & 0 & 0 \\ 0 & 0 & 0 & 0 & 1 & T & 0 & 0 & 0 & 0 & 0 & 0 \\ 0 & 0 & 0 & 0 & 0 & 1 & 0 & 0 & 0 & 0 & 0 & 0 \\ 0 & 0 & 0 & 0 & 0 & 0 & 1 & T & 0 & 0 & 0 & 0 \\ 0 & 0 & 0 & 0 & 0 & 0 & 0 & 1 & 0 & 0 & 0 & 0 \\ 0 & 0 & 0 & 0 & 0 & 0 & 0 & 0 & 1 & T & 0 & 0 \\ 0 & 0 & 0 & 0 & 0 & 0 & 0 & 0 & 0 & 1 & 0 & 0 \\ 0 & 0 & 0 & 0 & 0 & 0 & 0 & 0 & 0 & 0 & 1 & T \\ 0 & 0 & 0 & 0 & 0 & 0 & 0 & 0 & 0 & 0 & 0 & 1 \end{bmatrix} = \text{state transition matrix}$$

$$H = \begin{bmatrix} 1 & 0 & 0 & 0 & 0 & 0 & 0 & 0 & 0 & 0 & 0 & 0 \\ 0 & 0 & 1 & 0 & 0 & 0 & 0 & 0 & 0 & 0 & 0 & 0 \\ 0 & 0 & 0 & 0 & 1 & 0 & 0 & 0 & 0 & 0 & 0 & 0 \\ 0 & 0 & 0 & 0 & 0 & 0 & 1 & 0 & 0 & 0 & 0 & 0 \\ 0 & 0 & 0 & 0 & 0 & 0 & 0 & 0 & 1 & 0 & 0 & 0 \\ 0 & 0 & 0 & 0 & 0 & 0 & 0 & 0 & 0 & 0 & 1 & 0 \end{bmatrix}$$

is the observation matrix.

The additive noise, v(k), is usually assumed to be Gaussian with zero-mean and variances $\sigma_X^2(k)$, $\sigma_Y^2(k)$, $\sigma_Z^2(k)$, $\sigma_\alpha^2(k)$, $\sigma_\beta^2(k)$, $\sigma_\chi^2(k)$.

The next step is to formulate noise covariance matrix Q for the system, and R for the measurement model.

Since we are assuming there is no correlation between noise processes, either in the case of system noise processes, or in the measurement noise processes, the off-diagonal terms of both the observation noise covariance matrix, R, and the system noise covariance matrix, Q, are all zero.

For the measurement model, the noise covariance matrix is given by

$$R(k) = E[v(k)v^T(k)] = \begin{bmatrix} \sigma_X^2(k) & 0 & 0 & 0 & 0 & 0 \\ 0 & \sigma_Y^2(k) & 0 & 0 & 0 & 0 \\ 0 & 0 & \sigma_Z^2(k) & 0 & 0 & 0 \\ 0 & 0 & 0 & \sigma_\alpha^2(k) & 0 & 0 \\ 0 & 0 & 0 & 0 & \alpha_\beta^2(k) & 0 \\ 0 & 0 & 0 & 0 & 0 & \sigma_\chi^2(k) \end{bmatrix} \quad \text{...(10)}$$

and the system noise covariance matrix is, for this case, given by

$$Q(k)=E[u(k)u^T(k)]=\begin{bmatrix}0&0&0&0&0&0&0&0&0&0&0&0\\0&\sigma_1^2&0&0&0&0&0&0&0&0&0&0\\0&0&0&0&0&0&0&0&0&0&0&0\\0&0&0&\sigma_2^2&0&0&0&0&0&0&0&0\\0&0&0&0&0&0&0&0&0&0&0&0\\0&0&0&0&0&\sigma_3^2&0&0&0&0&0&0\\0&0&0&0&0&0&0&0&0&0&0&0\\0&0&0&0&0&0&0&\sigma_4^2&0&0&0&0\\0&0&0&0&0&0&0&0&0&0&0&0\\0&0&0&0&0&0&0&0&0&\sigma_5^2&0&0\\0&0&0&0&0&0&0&0&0&0&0&0\\0&0&0&0&0&0&0&0&0&0&0&\sigma_6^2\end{bmatrix} \quad \text{...(11)}$$

where

$\sigma_1^2=E(u_1^2),\ \sigma_2^2=E(u_2^2),\ \sigma_3^2=E(u_3^2),\ \sigma_4^2=E(u_4^2),\ \sigma_5^2=E(u_5^2),\ \sigma_6^2=E(u_6^2).$

are the variances of T times the linear and angular accelerations respectively.

Specific values must be substituted for those variances in order to define the Kalman filter numerically. One way to proceed is to assume that the probability density function(p.d.f) for each of the six accelerations is uniform and equal to p(u)=1/2M, between limits +M and -M. The variance then is $\sigma_u^2=M^2/3$.

Therefore, the six variances for the system noise covariance matrix are:

$$\begin{aligned}\sigma_1^2&=\sigma_2^2=\sigma_3^2=T^2\sigma_u^2\\ \sigma_4^2&=\sigma_1^2/Y'^2\\ \sigma_5^2&=\sigma_1^2/X'^2\\ \sigma_6^2&=\sigma_1^2/R^2\end{aligned} \quad \text{......................(12)}$$

where X',Y' is the average X, Y coordinates , R is the radial distance of the image corresponding points, all taken with respect to the center of the object.

One other covariance matrix must be determined. This is the "error covariance matrix", P. It is the mean-square errors of all the estimates over their actual values. Its vector form is:

$$P(k)=E[e(k)e^T(k)] \quad \text{...(13)}$$

For twelve signals, we have a 12x12 martix, thus:

$$P(k) = \begin{bmatrix} E[e_1^2(k)] & E[e_1(k)e_2(k)] & \cdots\cdots\cdots & & E[e_1(k)e_{12}(k)] \\ \cdot & E[e_2^2(k)] & \cdots & & \cdot \\ \cdot & \cdot & & & \cdot \\ \cdot & \cdot & \cdot & & \cdot \\ & & & & \\ & & & & \\ \cdot & & & \cdot & \cdot \\ \cdot & & & \cdot\;\cdot & \cdot \\ E[e_{12}(k)e_1(k)] & \cdot & \cdot & & E[e_{12}^2(k)] \end{bmatrix}$$

....(14)

The Kalman Filter And The Computational Process.
A form of the Kalman Filter equations suitable for numerical computation is indicated below.

Estimator:

$\hat{x}(k) = \Phi\hat{x}(k-1)\mathrm{H} + K(k)[y(k) - \mathrm{H}\Phi\hat{x}(k-1)]$

Filter – gain:

$K(k) = P_1(k)\mathrm{H}^T[\mathrm{H}P_1(k)\mathrm{H}^T + R(k)]^{-1}$

where..... $P_1(k) = \Phi P(k-1)\Phi^T + Q(k-1)$ ....(15)

Error...covariance..matrix:

$P(k) = P_1(k) - K(k)\mathrm{H}(k)P_1(k).$

To start Kalman processing we have to initialize the gain matrix K(k). For this purpose, the error covariance matrix P(k) has to be specified in some way. A reasonable initialization can be established using a sequence of two cosecutive measurements, in this case, two consecutive images. This is meaningful in situations where actual initial deviation values are known.This will give six linear and angular deviations at time k=1, and six linear and angular deviations at time k=2. From these twelve measurement data, and using the group of deviations and accelerations equations provided earlier, estimates of all twelve parameters at time K=2, can be generated . From this, the error covariance matrix at time k=2 can be computed, seeing that

$$P(2) = E\{[x(2) - \hat{x}(2)][x(2) - \hat{x}(2)]^T\}$$

From P(2), the Kalman Predictor gain K(3) can be calculated, from which, estimates at time k=3 can be generated. Such computational approach will lead to computation, in a sequential fashion, of estimates at times K=4, 5, 6,....etc.

An alternative initialization approach is to initialize the error covariance matrix is by making it a diagonal matrix with variance values of 1. In essence, we overestimate the error covariance. Its only effect is to slow down the convergence of the filter. The filter itself builds up the covariance matrix, just as it buids up the gain.

REFERENCES

1. M.E. Rorvig, M.W. Hutchison, R.O. Shelton, S.L. Smith, and M.E. Yazbeck, "An Intelligent Agent for the K-12 Educational Community", In The Proceedings, Advanced Digital Libraries Conference, Edited By Nabil Adam, Springer Verlag, New York, N.Y. 1995, pp. 121-132.
2. WAIS Documentation, 1992, Thinking Machines Corp., Cambridge, Mass.
3. C. Stanfill, "Massively Parallel Information Retrieval for Wide Area Information Servers", Thinking Machines Corp. Report, 1991.
4. J. Seaborn and R. Goode, Report On Pose Estimation Of 3-D Objects, NASA, JSC Report, ER4, June, 1995.
5. S.M. Bozic, *Digital And Kalman Filters*, 2nd. Ed., Wiley, 1994.
6. T. J. Broida and R. Chellappa, "Estimation Of Object Motion Parameters From Noisy Images", IEEE Trans. PAMI, Vol. PAMI-8, NO.1, 1986, pp. 90-99

56-34

76315

16P

Feasibility Study of Velocity and Temperature Measurements of an Arcjet Flow Using Laser Resonance Doppler Velocimetric (LRDV) Technique

234352

Final Report
NASA/ASEE Summer Faculty Program - 1995
Johnson Space Center

Prepared By:	Mohammad A. Rob
Academic Rank:	Assistant Professor
University & Department:	University of Houston-Clear Lake Division of Natural Sciences Houston, Texas 77058
NASA/JSC	
Directorate:	Engineering
Division:	Aeroscience and Flight Mechanics
Branch:	Aeroscience
JSC Colleague:	Carl D. Scott
Date Submitted:	August 10, 1995
Contract Number:	NGT-44-001-800

ABSTRACT

Thermal protection system (TPS) materials are used in space vehicles to shield from high heating environment encountered during their atmospheric reentry.[1] Arcjet wind tunnels are used to simulate the flowfield encountered by the spacecrafts, and are used for testing TPS materials. How well these tests simulate the actual heating environment encountered by space vehicles depends on the characteristics of the simulated flow. The flow characterization requires the determination of temperature, concentration, and velocity of the various atomic and molecular species present in the flow. However, determining these parameters requires a complex set of both analytical and experimental procedures. The ability to properly simulate the flight environment is directly related to the accuracy with which these techniques can be used to define the arcjet flow.

Laser resonance Doppler velocimetric (LRDV) technique can be used to accurately determine the velocity and temperature of a gaseous species.[2,3] In this technique, the medium is probed with a laser beam that is in resonance with an absorbing transition of the species. The absorption lineshape is Doppler-shifted due to the flow velocity of the species, and the frequency-shift is detected as the variation in intensity of the fluorescence emitted by the species. Thus a measurement of the Doppler shift and the width of a spectral line can give both the temperature and the velocity of the flowfield.

This summer, our project was to make a feasibility study to set up an experimental arrangement for the laser resonance Doppler velocimetric technique using a ring dye laser. Experiments required troubleshooting, cleaning, testing, and alignment of two lasers and several diagnostics instruments. All instruments and lasers necessary for the project worked well, but the output power of the broadband fundamental dye laser was limited to about 20 mW. This was quite low as compared to that necessary to obtain second harmonic oscillation at 327.49 nm for the LRDV studies. Further optimization of the dye laser optical elements is necessary before it can be used for the experiment, which requires narrowband (about 20 Mhz) laser operation.

BACKGROUND

Introduction

Thermal protection system (TPS) materials are used in space vehicles to shield from high heating environment encountered during their atmospheric reentry.[1] Arcjet wind tunnels are used to simulate the flowfield encountered by the spacecrafts, and are used for testing TPS materials. How well these tests simulate the actual heating environment encountered by space vehicles depends on the characteristics of the simulated flow. The flow characterization requires the determination of temperature, concentration, and velocity of the various atomic and molecular species present in the flow. However, determining these parameters requires a complex set of both analytical and experimental procedures. The ability to properly simulate the flight environment is directly related to the accuracy with which these techniques can be used to define the arcjet flow.

Laser resonance Doppler velocimetric (LRDV) technique can be used to accurately determine the velocity and temperature of a gaseous species.[2,3] In this technique, the medium is probed with a laser beam that is in resonance with an absorbing transition of the species. The absorption lineshape is Doppler-shifted due to the flow velocity of the species, and the frequency-shift is detected as the variation in intensity of the fluorescence emitted by the species.

Theoretical

The shift in the absorption line center is given by[2]

$$w_s = w_o \left(1 \pm \frac{\vec{v}}{c} \right) \qquad (1)$$

where w_s is the shifted absorption frequency, w_o is the absorption frequency at rest, $\vec{v}$ is the velocity of the absorber with respect to the direction of the light propagation vector, and c is the speed of light. In a gas with a random velocity distribution, the lineshape arising due to Doppler broadening is:

$$I(w) = I_o \exp\left[-4ln2\left(\frac{w-w_o}{\Delta w_D}\right)^2\right] \tag{2}$$

where Δw_D is the characteristic Doppler width and is given by

$$\Delta w_D = \frac{w_o}{c}(8RT\ ln2/M)^{1/2} \tag{3}$$

where R is the universal gas constant, T is the temperature, and M is the molecular weight of the gaseous species.

Under most practical arcjet flow measurement conditions the Doppler effect provides a major contribution to the linewidth than the natural and collisional broadening. Thus, in principle, measurement of the Doppler shift and the width of a spectral line can give both the temperature and the velocity of the flowfield.

Copper Atom as a Probing Species

The anode of the dc arc column of the arcjet is made of copper and the sputtered copper in the flow field is found to be sufficient to carry out LRDV studies. The spectroscopy of atomic copper makes it an ideal candidate for flow velocity and temperature measurements. The ground state of the Cu atom is the $^2S_{1/2}$ state. The optically allowed absorptive transitions to the energy states $^2P_{3/2}$ and $^2P_{1/2}$ occur at wavelengths 324.85 and 327.49 nm respectively. Radiative decay from the $^2P_{3/2}$, $^2P_{1/2}$ states to the metastable states $^2D_{5/2}$, $^2D_{3/2}$ gives emissions at 510.70 and 578.37 nm respectively. This is illustrated in an energy level diagram in Fig.1. Doppler width and frequency shift measurements may be accomplished by exciting the ^2P-^2S transtition with a narrow band dye laser and scanning the frequency of the dye laser to find the line center and width. The fluorescence emitted from the ^2P state is proportional to the fraction of the excitation beam absorbed. But the analysis of the lineshape is complicated by the hyperfine splitting of the energy levels. The problem can be simplified by exciting only the $^2P_{1/2}$ - $^2S_{1/2}$ at 327.49 nm, where only two hyperfine components in each level are involved. In this case, only the $^2P_{1/2}$ - $^2D_{3/2}$ emission line at 578.37 nm is observed. A more detailed energy level diagram for these transitions is shown in Fig.2.

Arepalli et al.[3] demonstrated the feasibility of the LRDV technique using a pulsed dye laser and a heated cell containing copper vapor as the absorbing medium. The accuracy of velocity and temperature measurements of the flow field can be improved by using a narrowband pump laser such as a ring dye laser that can be used to resolve the hyperfine splitting in the Cu atom spectral lines mentioned above. This summer, our project was to make a feasibility study to set up an experimental arrangements for the laser resonance Doppler velocimetric technique using a ring dye laser.

EXPERIMENTAL

The objective of the project was to set-up the ring dye laser at the excitation wavelength of 327.49 nm as required for the Cu atom study and characterize its frequency bandwidth. The experiment could be divided into several parts: (i) troubleshooting, and setting up the pump argon ion laser, (ii) troubleshooting, cleaning, and setting up the dye circulator for the dye laser, (iii) mixing of DCM dye with benzyl alcohol to obtain oscillation at the frequency-doubled wavelength of 327.49 nm, (iv) alignment and optimization of the dye laser without the inracavity elements to obtain broadband emission at the fundamental wavelength around 655 nm, (v) optimization of the dye laser output with intracavity etalons and tuning elements to obtain narrow bandwidth and second harmonic oscillation at the required 327.49 nm, (vi) troubleshooting and setting up the spectrum analyzer with a HeNe laser, and finally (vii) characterize the dye laser oscillation bandwidth using the spectrum analyzer. Some parts of the experiments went well in the limited time of the summer program. Others need to be continued. They are described below.

Setting Up the Argon Ion Laser

The argon ion laser was not in operational condition, and it was found that the water flow control switch was not working. A new flow switch was purchased and it was installed in a separate socket, so that it can be changed easily in the future. This was not possible before. With this simple change, the laser was found to be operational with an output power of more than 6W (multi-wavelength operation), which was necessary for the dye laser pumping.

Setting Up the Dye Circulator

First, the old Rhodamine 6G dye mix was poured out safely and the dye circulator was cleaned as per standard operating procudure ES4-SOP-ARMSEF-129.0. Then it was circulated several times with methanol and ethylene glycol until no trace of old dye was present. The dye jet at the laser head was also cleaned so that a thin ribbon like flow was present at the jet. For the new dye solution, 2 grams of DCM was mixed with 400 ml of benzyl alcohol and the mixture was vigorusly mixed for about an hour in a soner bath. Most of the mixture was poured in the circulator for dye pumping. The leftover would be added later to optimize dye laser output power.

Oscillation of Dye Laser Without the Intracavity Optical Elements

First, the dye laser oscillation was tried without the complex intracavity optical elements as per procedure described in the operation manual of the ring dye laser (Coherent 699-05 ring dye laser). These elements include, nonlinear crystal for second harmonic generation, birefringent filter for frequency tuning, and a cascade of etalons for extreme narrow band operation. See Fig.3 for details. For initial alignment of the laser, the pump argon ion laser was used at a low power (about 500 mW). The experimental arrangement is shown in Fig.4. After several foldings through high reflecting mirrors, the pump beam passed through the optic axis of the dye laser and on to the pump mirror of the dye laser. See fig.3(b). The dye circulator was turned on and the dye flow was set at 40 psi. Fluorescence emitted from the dye was used to line up the three cavity mirrors of the ring dye laser. Two counterpropagating beams of the ring were overlapped at the output coupler. The spots were further lined-up on a distant screen from the output coupler. The laser was found to be oscillating after several trials, specially after adjusting the output coupler and the pump mirror horizontal and vertical adjustments. The output power was limited to about 20 mW. This was very low compared to the manufactered suggested power level of 300 mW. Note that we needed high power in the fundamental wavelength so that the power in the frequency-doubled wavelength would be few milliwatts, which would be sufficient for LRDV studies. But after many many tries, no further improvement in the output power of the laser was observed.

Testing of the Spectrum Analyzer

Even though the frequency-doubled output of the dye laser could not be tested for spectral analysis, but we have tested the responsivity of the spectrum analyzer using a HeNe laser as a narrowband source. The experimental arrangement is shown in Fig. 5(a). Laser beam was focused on to the spectrum analyzer (a confocal Fabry-Perot cavity) using a mode matching lens (f = 50 cm). The output from the spectrum analyzer was directed to an oscilloscope. To study sepectral output of the laser, the spectrum analyzer was sweeped using an external sweeping generator at a sweep frequency of about 25 Hz. Figure 5(b) shows a reproduction of the oscilloscope trace observed for such a sweep. Figure shows two complete sweeps over the gain bandwidth of the laser. From the knowledge of the free-spectral range of the spectral analyzer (6 Ghz), a cavity mode spacing of 780 MHz was measured for the HeNe laser. This is equivalent to a laser cavity length of 20 cm, which was exactly measured for the laser cavity used in the experiment. Note, the neighbouring low intensity modes, at a separation of 45 MHz from the peak cavity modes, are due to transverse modes of the laser. From the figure it should be clear that the resolution of the spectrum analyzer is better than 22 MHz.

CONCLUSION

We made a fesibility study to set up a high resolution laser resonance Doppler velocimentric (LRDV) experiment to study velocity and temperature of the folowfiled of an arcjet. Experiment required troubleshooting, cleaning, testing, and alignment of two lasers and several other diagnostics instruments. All instruments and lasers necessary for the project worked well, but the output power of the fundamental dye laser wavelength was limited to about 20 mW. This was quite low as compared to that necessary to obtain second harmonic oscillation at 327.49 nm for the LRDV studies. Further optimization of the dye laser output power is necessary before it can be used for the experiment.

ACKNOWLEDGEMENT

I would like to take this opportunity to thank NASA/ASEE Summer Faculty Fellowship Program for proving us an opportunity to work at NASA. I sincerely thank Carl D. Scott of Johnson Space Center for providing the opportunity to work on this project. I am also indebted to Sivaram Arepalli for his expert experimental support without which I could not have been completed this project. Finally, I wish to thank all NASA and contract personnel of the arcjet facility who made my short research period very pleasant.

REFERENCES

1. C. D. Scott, "Survey of Measurements of Flow Properties in Arcjets," Journal of Thermophysics and Heat Transfer, Vol.7, No.1, 1993

2. W.J. Marinelli, W.J. Kessler, M.G. Allen, S.J. Davis, S. Arepalli, and C.D. Scott, "Copper Atom Based Measurements of Velocity and Turbulence in Arc Jet Flows," AIAA-91-0358, 29th Aerospace Science Meeting, January 7-10, 1991, Reno, Nevada.

3. S. Arepalli, E. H. Yuen, and C. D. Scott, "Application of Laser Induced Fluorescence for Flow Diagnostics in Arc jets," AIAA-90-1763, AIAA/ASME 5th Joint Thermophysics and Heat Transfer Conference, Seattle, WA, June 18-20 (1990).

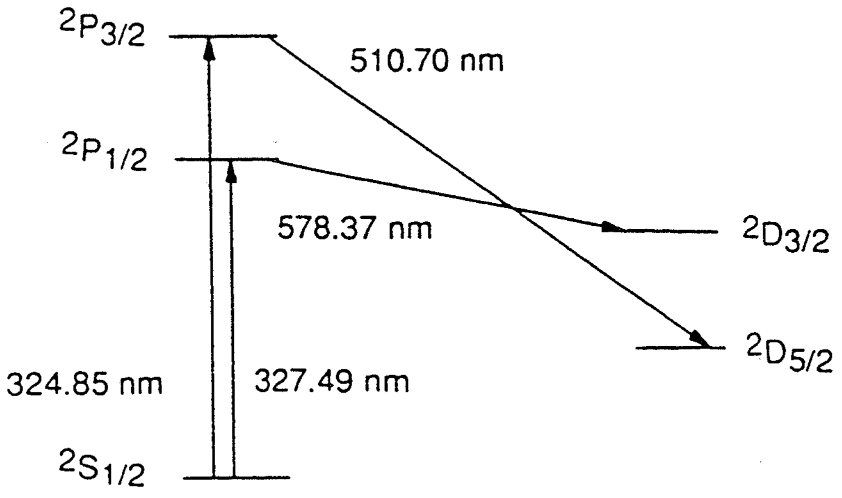

Figure 1. Energy Level Diagram Showing the Excitation from the Ground State of Cu to the Excited $^2P_{1/2}$, $^2P_{3/2}$ States and Fluorescence to the $^2D_{5/2}$, $^2D_{3/2}$ States

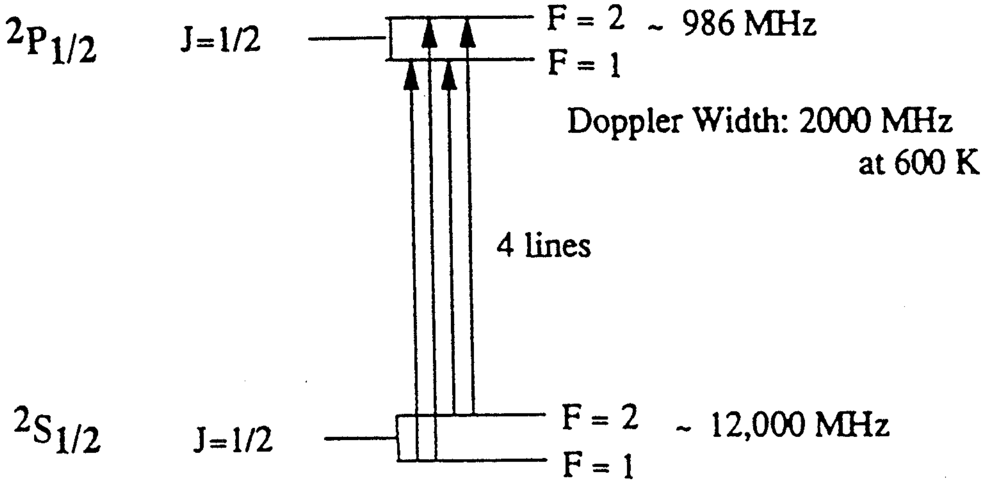

Figure 2. Detailed Level Diagram of the $^2P_{1/2}$ - $^2S_{1/2}$ Transition Indicating the Hyperfine Splittings (F sublevels)

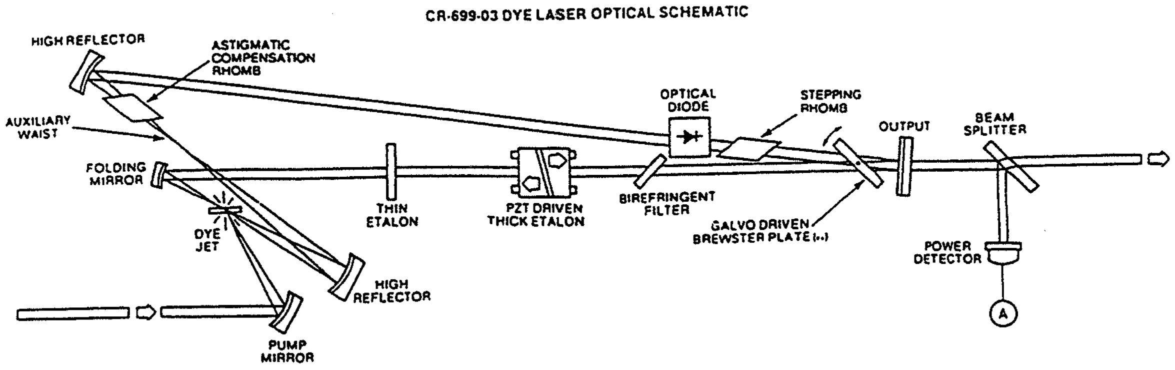

Fig. 3(a). Optical schematic of the dye laser with all optical elements.

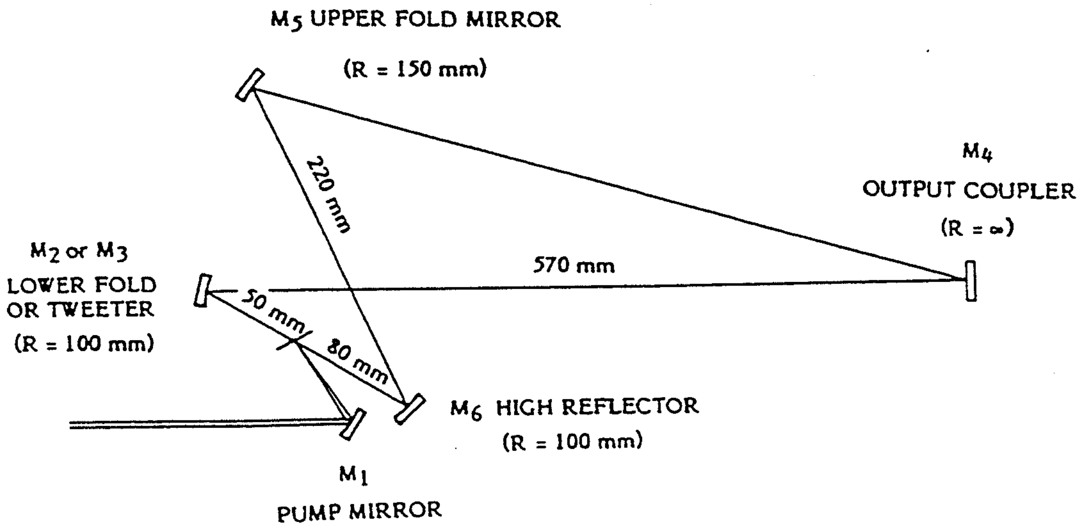

Fig. 3(b) Dye laser optical schematic without the tuning elements.

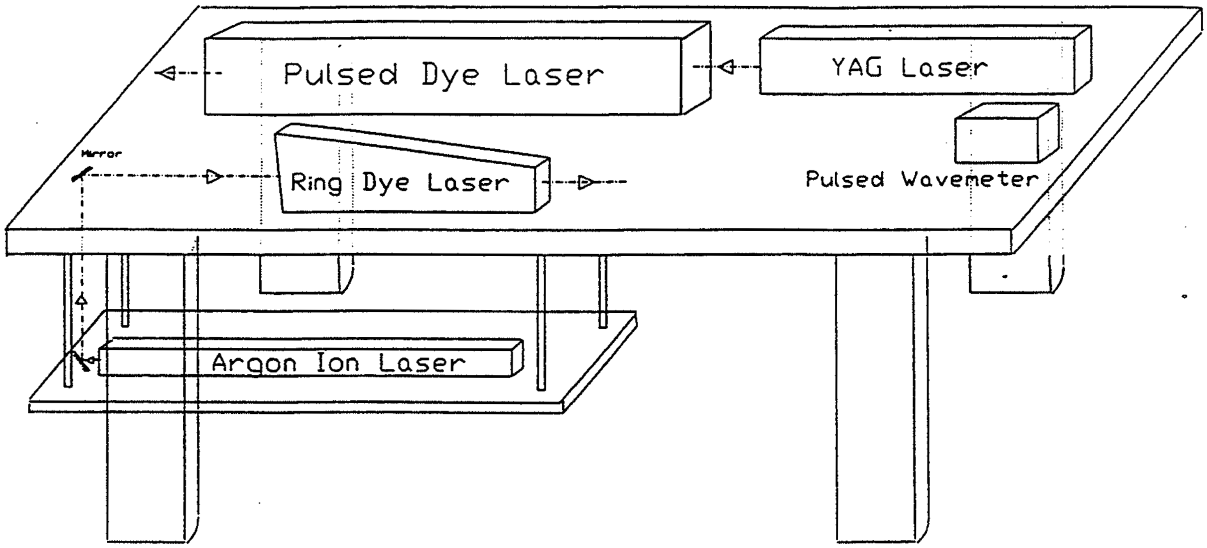

Fig.4. Dye laser pumping arrangement using an argon ion laser.

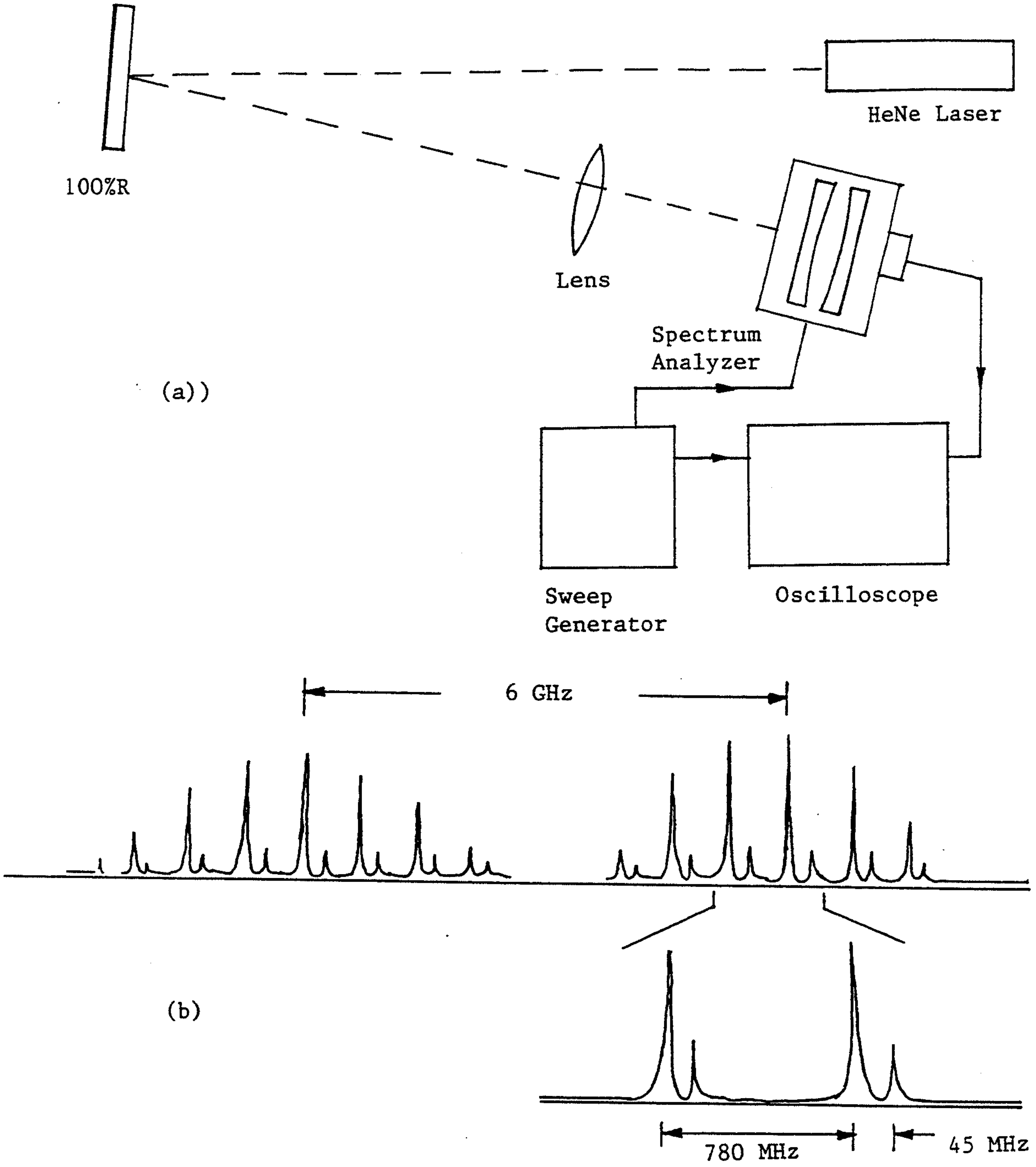

Fig.5. (a) Experimental arrangement to study resolution of the spectrum analyzer,
(b) HeNe laser emission spectra over two free-spectral range of the spectrum analyzer.

DESIGN AND IMPLEMENTATION OF A WINDOWS NT NETWORK TO SUPPORT CNC ACTIVITIES

Final Report
NASA/ASEE Summer Faculty Fellowship Program--1995
Johnson Space Center

Prepared By:	**Charles A. Shearrow, Ph.D.**
Academic Rank:	**Assistant Professor**
University & Department	**Ohio Northern University** **Department of Technology** **Ada, Ohio 45810**
NASA/JSC	
Directorate:	**Engineering**
Division:	**Manufacturing, Materials, & Processes Technology Division**
Branch:	**Manufacturing Process Development**
JSC Colleague:	**Charles L. Salkowski**
Date Submitted:	**August 3, 1995**
Contract Number:	**NGT-44-001-800**

Abstract

The Manufacturing, Materials, & Processes Technology Division is undergoing dramatic changes to bring it's manufacturing practices current with today's technological revolution. The Division is developing computer automated design and computer automated manufacturing (CAD/CAM) abilities. The development of resource tracking is underway in the form of an accounting software package called Infisy. These two efforts will bring the division into the 1980's in relationship to manufacturing processes. Computer integrated manufacturing (CIM) is the final phase of change to be implemented. This document is a qualitative study and application of a CIM application capable of finishing the changes necessary to bring the manufacturing practices into the 1990's. The documentation provided in this qualitative research effort includes discovery of the current status of manufacturing in the Manufacturing, Materials, & Processes Technology Division including the software, hardware, network and mode of operation. The proposed direction of research included a network design, computers to be used, software to be used, machine to computer connections, estimate a timeline for implementation, and a cost estimate. Recommendation for the division's improvement include action to be taken, software to utilize and computer configurations.

Introduction

The Manufacturing, Materials, & Processes Technology Division is undergoing dramatic changes to bring it's manufacturing practices current with today's technological revolution. The Division is developing computer automated design and computer automated manufacturing (CAD/CAM) abilities. The development of resource tracking is underway in the form of an accounting software package called Infisy. These two efforts will bring the division into the 1980's in relationship to manufacturing processes. Computer integrated manufacturing (CIM) is the final phase of change to be implemented. This document is a qualitative study and application of a CIM application capable of finishing the changes necessary to bring the manufacturing practices into the 1990's.

Current status of Manufacturing in EM at JSC

Software:

The current major software packages used by EM include Infisy, Pro/Engineer, Unigraphics, and AutoCAD13. Infisy is being implemented to collect manufacturing and administrative data for accountability. Pro/Engineer is being used for CAD drawings and design analysis. Unigraphics is being used to convert drawings into NC programs. AutoCAD13 was used to convert drawings that have come into the division from AutoCAD users. There is no software being used to integrate the operation of the manufacturing operation.

Hardware:

The hardware can be divided into the two categories of machines on the production floor and the computers available to service the machines. All but one of the numerically controlled machines are network ready and can be linked to the network with minimal effort. The older Mazak machining center will need an adapter to allow the delivery of NC files. This can be accomplished with and after market adapter. Other than the NT server there are no computers on the production floor to start building a computer integrated manufacturing system (CIM).

Network:

The network in building ten is incomplete for CIM use. It is being used to support a few computers that are used primarily for computer automated manufacturing (CAM) and administrative needs. The existing network has been planned to be expanded to better serve the building. Once the expansion is complete there will have to be an additional expansion to support a fully integrated manufacturing operation.

The extent of use of the existing network cabling between buildings nine and ten and within building ten is as follows. A four strand fiber cable exists between the two buildings with only two strands being used. At this time this part of the net may be adequate but it may be necessary to use the other two fibers to isolate the graphics terminals and their heavy traffic from the general network traffic. It is estimated that under non-graphic communications modes the network is functioning at about 10% capacity but when the graphics stations are transmitting this usage increases to 50%. This is not a problem with the current status of the two buildings but if CIM is implemented then network use will have to be reevaluated. Within building ten the network use consists of the graphic stations (4) and a few management stations (3). The initial expansion of the network will connect electronics on the second level and a few other work stations to the NT servers.

Mode of operation:

The present mode of manufacturing operation can be dated back to the 1970's. Brining the CAD/CAM and Infisy applications on line will bring the manufacturing facilities up to the 1980's. This mode of operation still is not what is required of manufacturing operations that are going to compete in the late 1990's and into the years beyond. To become a competitive operation EM must show accountability for all of its inputs, processes, and outputs.

Proposed Action

Network design:

A plan for the expanded network in building ten will be proposed to serve as a file transfer system for implementing CIM. This plan will include the wiring consisting of fiber-optics, thinnet wire and twisted pair. Hardware included in the plan will include bridges, hubs, and the server.

Computers:

Existing micro-computers will be configured and tested to bring a basic CIM operation into a functioning state. The computers will be tested at varying stages of computing power. The varying powers will include the speed of the computer, size of the random access memory (RAM) and the size of the existing hard drive (HD). A minimum configuration that is acceptable for the CIM operation will be recorded so surplus computers can be recycled at NASA-JSC.

Software:

Commercially available software will be evaluated to determine if the software is suitable for the needs of EM implementing CIM. Once a software package has been identified it will be tested for compatibility with the machines, computers and the network. A recommendation for the software will be recorded.

Machine to computer connections:

Connections for common types of machines will be tested. This will ensure ease of instillation for the cabling between the computers and the machines.

Time Line:

A timeline will be developed taking into consideration the funding of a grant to continue this work for the 1995-96 academic year, without the grant being funded and a planned return for next summer as a visiting faculty member.

Cost Estimate:

A cost estimate for the software, software instillation, and training will be included. Not included in this estimate will be the cost of the extended network, computers for upgrading the CIM system, possible other needed software, and small items.

Network Design

There is a need to locate bridges and hubs for security and isolation of the network failure. If there is a failure of a workstation or a machine it could threaten the integrity of the network. The first step is to locate the primary domain controller (PDC) and the backup domain controller (BDC) behind bridges to isolate them from potential problems, provide security and additionally limit the excess data flow which can slow down network operations dramatically. Once the computers are isolated the building should be zoned into five zones so network or hardware problems can further be isolated. Additional fiber should be run between the domain controllers and the bridges to eliminate electrical interference and loss of digital signal within building ten. See figure 1 for machine zoning and placement of the bridges and hubs.

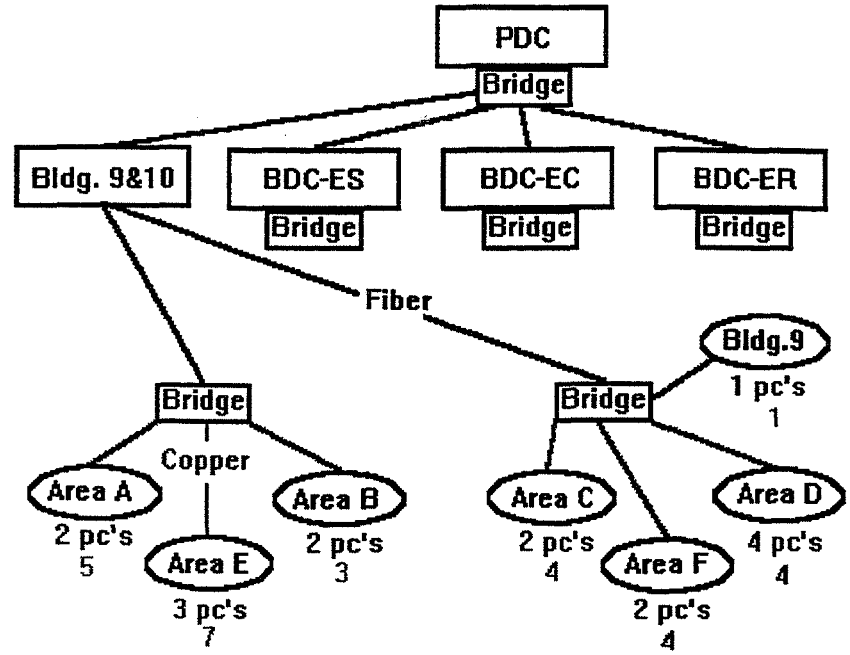

Figure 1

The large boxes represent the PDC and BDC's. The red boxes represent the proposed bridges for net isolation and security. The connecting net is represented by blue and green lines that represent fiber optics and twisted pairs of copper wire respectively. The ovals with letters in them represent the isolated areas or machine zones and/or hubs. The purple text are the numbers of computers needed on the floor and the light blue color text represents the number of machines in each zone.

Justification for zoning the machines is to limit the network damage in case of catastrophic failure that could happen in a machine, computer, or the net connecting the machine or the PC running the machine. To strategically place the bridges and hubs so they can economically facilitate the distribution of data it will be necessary to divide Building ten into six zones and one zone for building nine's model shop. The zones will create areas in which similar data and file size can be transferred. These zones are depicted in figure 2. Note that Building 9 is to the bottom of figure 2.

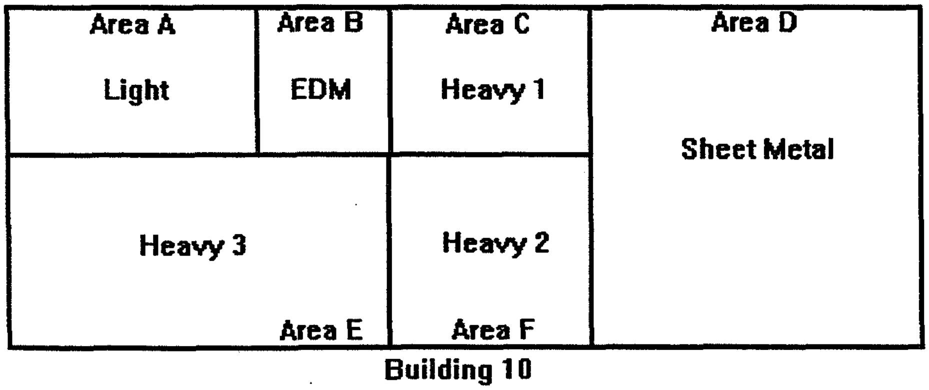

Figure 2

Area A includes vertical milling machines. Area B contains the EDM machines and one tape punch machine. Area C contains the Mazak SV-25, Mazak SlantTurn, and the two Hurco BMC 50's.

Area D contains all the "sheet" type equipment. Area E contains the Hurco's with tool changers. Area F contains the larger machining centers. Note that the PDC and BDC will be housed in area F room 135.

Feasibility and number of workstations on the production floor.

The reason for placing work stations on the facility floor is to perform two functions related to the inevitable transformation to CIM technology. The first function is to deliver NC programs to the supported machines. The second function of the stations will be to support production data collection and delivery of this data to the PDC. The final implementation of the NT work station is to limit the use of the PC's to manufacturing processes directly related to CIM only.

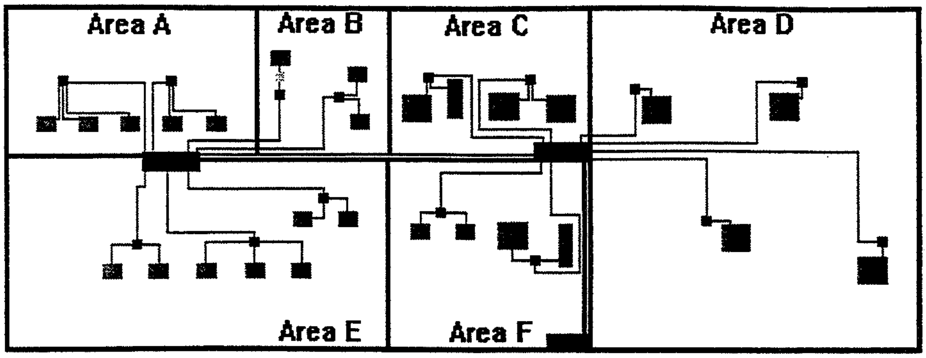

Building 10

The blue lines represent the locations of fiber for data transfer. The green lines are copper wire used to finish the connection. The red boxes represent the bridges used for isolation of the zones. The blue boxes represent the machines to be networked. The purple boxes represent the PC's.

Computers

Acquisition:

The acquisition of computers from surplus and redistribution (S&R) was done with great care. A bootable disk was built that would supply the DOS programs of f-disk, memory check, scandisk, and Microsoft diagnostics. This disk was built on a 3.5" disk but computers that booted to the 5.25" disk had to have the drives switched for testing. Monitors were acquired in excess of the number of computers. This was due to the loss of monitors during the burn in period of two days. Keyboard to be used by these computers must have the special function keys across the top of the keyboard. The keyboards with the special function keys along the left side will not function with the 386 computers. All disks involved with the configuration of these computers should be locked and the anti-virus program should be loaded second after DOS is loaded.

Configuration options:

The varying "powers" of computers will include the speed of the computer, size of the RAM and the size of the existing HD. A minimum configuration for CIMNET was reported so computers can be recycled at NASA-JSC. The computers available at this point pose several identifiable road blocks to implementing the basic components of a CIM operation. The computers available are 386sx's running at 6 to 20 MHz. This is not a problem for NC file transfer but is a problem for collecting, displaying and processing other data. The HD on these computers will limit the amount and type of software to be placed on the computers. Because of these limitations four models will be built and tested. Four models will use the 386's and one will be a 486 using NT as its platform. CIMNET software will be used because they support DOS only, Windows For Workgroups (WFW), and NT stations. Two versions of the software have been acquired for testing. One that supports the DOS application (DNCJunior) and one that supports WFW and NT (DNCplus).

Model 1: 1355807

A 386sx with a 20meg hard drive, 5 meg. RAM will be equipped with DOS and the CIMNET DNC junior software. This model is expected to save the most room on the small hard drives but **will not be user friendly**. Once the software is configured the setup will under go testing to determined usability. It will also be noted that this machine will not support a good link to the net and will not provide the feedback and accountability needed.

Model 2: CPU: 1242161 Monitor: 1009326

A 386sx with a 80meg hard drive, 4 meg. of RAM will be equipped with DOS, WFW, Anti-various and the CIM software. This model is expected to save the most room on the small hard drives. Once the software is configured the setup will be moved to B10 to under go testing on a group of different machine brands and types. It will also be noted that this machine will support net connectivity and the feedback needed for accountability.

Model 3: CPU: 1356026 Monitor: 1009323

A 386sx with a 40meg hard drive will be equipped with DOS, WFW, Anti-various and the CIM software. This model is expected be the model implemented until proper PC's can be purchased. Once the software is configured the setup will be moved to B10 where it will be tested on a group of different machine brands and types. It will also be noted that this machine will support net connectivity and the feedback needed for accountability.

Model 4: CPU: 1297775 Monitor: G042811

A 386sx with a 80meg hard drive, 4 meg. of RAM will be equipped with DOS, WFW, Anti-various and the CIM software. This model is expected be the model implemented until proper PC's can be purchased. Once the software is configured and the software stripped the setup will be moved to B10 where it will be tested on a group of different machine brands and types. This machine will support net connectivity and the feedback needed for accountability. The bar-code reader will be installed and tested for practicability.

Model 5: 1354925

A 486sx with a 212meg hard drive 8 meg. RAM will be equipped with NT and the CIM software. This model is expected be the model implemented when proper PC's can be purchased. Once the software is configured and the software user limits have been developed then setup will be moved to B10 where it will be tested on a group of different machine brands and types. This machine will support the ultimate net connectivity and the feedback needed for accountability. The bar-code reader will be installed and tested for practicability.

Computer Testing Results

The testing for model one was as expected. The computer could use the software but was not user friendly. Because of the non-user friendly aspects of the software further discovery was not warranted. The testing on models two through four was successful. It didn't matter what the speed or size of the hard drive was the CIM and network software functioned correctly. It was found that the amount of random access memory has to be over four meg. and preferably over five meg. to run the CIM software tested. The fifth model was not constructed and tested due to a lack of time. The following page contains the computers identification tags and how they are configured.

Computer Tracking

Shearrow	Identification Numbers			Computer Characteristics			Software Installed			Software Installed			Service Performed		
7/8/95	CPU	CRT	Key	Hard	RAM	Mhz	DOS	WFW	Anti.	Mouse	CIM	Psdwd	Scan	Defrag	Mem
Del 320	1242161	1009326	00103	20/	4	20	6.2	3.11	X	Win	X	EM3	X	X	X
Del 320	1356026	1009323	02674	40/	4	20	6.2	3.11	X	Win	X	EM3	X	X	+2meg
Del 310	1297775	G042811	02311	80/	4	12	6.2	3.11	X	Win	X	EM3	X	X	X
Del 320	1355807	G97359	00928	20/13	5	20	6.2	3.11	X	Win	X	EM3	X	X	X
Del 310	1293406	G97328		80/53	4	12	6.2	3.11	X	Win	No	No	X	X	X
Del 310	1449068	G97350		80/58	4	12	6.2	3.11	X	Win	No	EM3	X	X	X
Del 310	1242180	G97304		80/58	4	12	6.2	3.11	X	Win	No	No	X	X	X
Del 310	1242036	1293311		40/8.2	4	20	6.2	3.11	X	Win	No	EM3	X	X	X
Unisys	G26371	G97354	00609	80/26	5	16	6.2	3.11	X		No	EM3	X	X	X
Del 310	1352113	1009269	00104	80/58	4	20	6.2	3.11	X	Win	No	EM3	X	X	X
Unisys	G25350	1009320	02791	33/8	3	16	6.2	3.11	X	Win	No	EM3	X	X	X
Unisys	G98598	G97302	01134	42/8	5	16	6.2	3.11	X	Win	No	EM3	X	X	X

Notes:

G26371 has no extra Com ports and will need a bus mouse.
G25350 has no extra Com ports and will need a bus mouse.
G98598 has no extra Com ports and will need a bus mouse.

Software Comparison

There were three manufactures of CIM software selected for evaluation. The three manufactures selected were INTERCIM based in Minneapolis, Minnesota; CINNET is produced by J.N.L Industries based in Robesonia, Pennsylvania; and CADCAM Integration based in Woburn, Massachusetts. The comparison was based on the common features of the software's and the unique features offered by each company. Selection of a software to test was based on the software's compatibility with the needs of EM at NASA-JSC.

Common features of the software include NC file transfer to and from the machine. The transfer also includes the software's ability to drip feed a machine a file that is larger than the machines memory without interruption. All the software's ultimately support the concept of a paperless exchange of information on the production floor. The information on the production floor that becomes paperless are tool lists, setup instructions, NC programs and part display images by item managed file systems. The three companies did support their software with training and technical support. The machine operator does have the ability to edit the NC program and redline changes on the drawing at the computer. Databases are used by all three software's to compile information on program files, drawing files, tool lists, and images of parts to be produced. Administratively the benefits of the CIM software's is the ability to track work in progress, statistical analysis on processes, generation of activity reports, and produce accountability for work completed.

Unique features of CIMNET include the following options. Hot keys are offered to speed up the work at the hub (computer) next to the machine. CIMNET is completely ISO9000 compatible and uses password authentication for file access. The machine operator can view the files being transferred when the transfer is active. Anyone using CIMNET can view side by side the NC program that was fed to the machine tool and the program that was up linked back into CIMNET. The most unique feature that CIMNET offers is the ability to archive machine tool setups with audio and video. This can be done if a part is to be made in the future. The machinist can record the setup procedure and it can be down loaded in the form of audio and as many as 32 digital pictures.

Unique features of INTERCIM include such options as machine operator hot keys to speed computer operations and the ability of the operator to see the file transfer as it is happening. The rest of INTERCIM's options were covered under common features of the CIM software.

Unique features of the CAD/CAM software is that it is ISO9000 compatible and it does offer password security. The rest of CAD/CAM's options were covered under common features of the CIM software.

Software Comparison for CIM Application

Shearrow		File Transfer			Paper on Floor			Menu Options				Other		On The Floor			On The Floor		
7/7/95	Name	To	From	Drip Feed	Prg.	Tool List	Pict. Any	Win	Hot Key	Edit	Help Scrn.	train.	ISO	edit	See trns	File Com	Pass- word	File S/S	Red Line
	FTP	X	X			X	X					DOS/ NT		DOS					
CIMNET	DNC Jr.	X	X	X		X	X	X	X	X	X	DOS/ NT	X	X		X	X		
CIMNET	DNC+	X	X	X				X	X	X	X	Some	X	X	X	X	X	X	X
CIMNET	DNC+/w Lite	X	X	X				X	X	X	X	Yes	X	X	X	X	X	X	X
CIMNET	DNC+/w Fldrs	X	X	X				X	X	X	X	Yes	X	X	X	X	X	X	X
InterCIM	F-net Entry	X	X	X		X	X	X			X	Yes				X			X
InterCIM	F-net Inter.	X	X	X				X		X	X	Yes		X		X			X
InterCIM	F-net Advncd	X	X	X				X	X	X	X	Yes		X	X	X			X
CAD/CAM	DNC500	X	X	X		X	X			X	X		X	X					
CAD/CAM	DNC500/w Cell	X	X	X				X		X	X	Yes	X	X			X		
CAD/CAM	DNCII	X	X	X				X		X	X	Yes	X	X			X		X

Name: Software's name.

File Transfer:
To: Moves files to the server.
From: Moves files from the server.
Drip Feed: Moves NC programs as needed.

Paper on Floor:
Program: NC program in written form.
Tool List: List of tools need for the job.
Pict. Any: Images supported at workstation.

Menu Options:
Win: Functions in Windows 3.1 or 3.11
Hot Key: Is the menu accessible by short cuts.
Edit: Can the program be edited.
Help Scrn: Are there help screens available.

Other:
Train: Is there training necessary to run the system.
ISO: Is the software ISO9000.

On The Floor:
Edit: Editing at the workstation.
See Trns: Observation of file transfers.
File Com: Comparison of files and flagging.
Password: Station and file password authentication.
File S/S: File comparison side by side.
Red Line: Operator notes on drawings or pictures.

Software Comparison for CIM Application

Shearrow		Other			Use of Database			Administrative			Setup Information			Computer Requirements		
7/7/95	Name	Tech Supp	View Grph	Item Mang. File	Program files	Drawing files	Tool files	WIP Track	Stats.	Activity Reports	Audio Setup	Pict. Setup	Audit Setup	HD meg.	RAM meg.	CHIP
	FTP													40	2	286sx
CIMNET	DNC Jr.	X												40	4	386sx
CIMNET	DNC+	X	X											40	4	386sx
CIMNET	DNC+/w Lite	X	X	X	DBIV	DBIV	DBIV	X						200+	8	486dx
CIMNET	DNC+/w Fldrs	X	X	X	DBIV	DBIV	DBIV	X	X	X	X	X	X	200+	16	486dx /586
InterCIM	F-net Entry	X	X		X	X	X							100	4	386sx
InterCIM	F-net Inter.	X	X		X	X	X	X						200+	6	486dx
InterCIM	F-net Advncd	X	X	X	X	X	X	X	X	X				200+	16	486dx /586
CAD/CAM	DNC500	X												40	4	386sx
CAD/CAM	DNC500/w Cell	X	X		X		X			X				40	8	486dx
CAD/CAM	DNCII	X	X	X	X	X	X	X	X	X				200+	16	486dx /586

Other:
Tech Supp: Technical support for the software.
View Grph: Graphics viewed at the workstation.
Item Mang. File: Files managed by software.

Use of Database:
Program files: Files stored and tracked.
Drawing files: Drawings stored and tracked.
Tool Files: Tooling lists stored and tracked.

Administrative:
WIP Track: Work in progress tracking.
Stats: Statistical analysis of the operation.
Activity Reports: Generation of activity reports.

Setup Information:
Audio Setup: Audio recording of the procedure.
Pict. Setup: Deliver setup pictures at the workstation.
Audit Setup: Track the setup progress via remote.

Computer Requirements:
HD meg.: Size of the hard drive in the workstation.
RAM: Size of the RAM to be available.
Chip: Type of processor classification.

Machine to Computer Connections

There are two common machines used on the production floor in building ten. The first is the MAZAK which can be connected with a 25 pin shielded cable that has the following pin configuration.

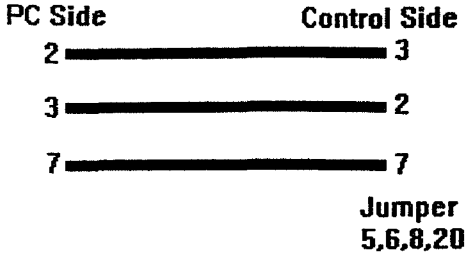

The second most common machine on the production floor are the Hurco milling machines. They can be connected from the computer to the machine with the following pin configuration. It must be noted that one end of the shielded cable must be 25 pin and the other end going into the machine is 9 pin.

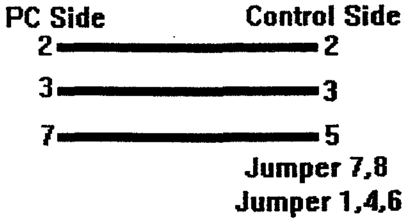

Time Line

Two timelines for implementation of the CIM application have been constructed. The first timeline takes into consideration a grant to continue the development of the CIM application at NASA-JSC during the 1995 academic year. This timeline is considerably shorter that the second time line which was constructed without a grant to continue the work on the CIM application during the accademic year. The second timeline also depends on NASA personnel to do the final phase of implementation.

With A Grant

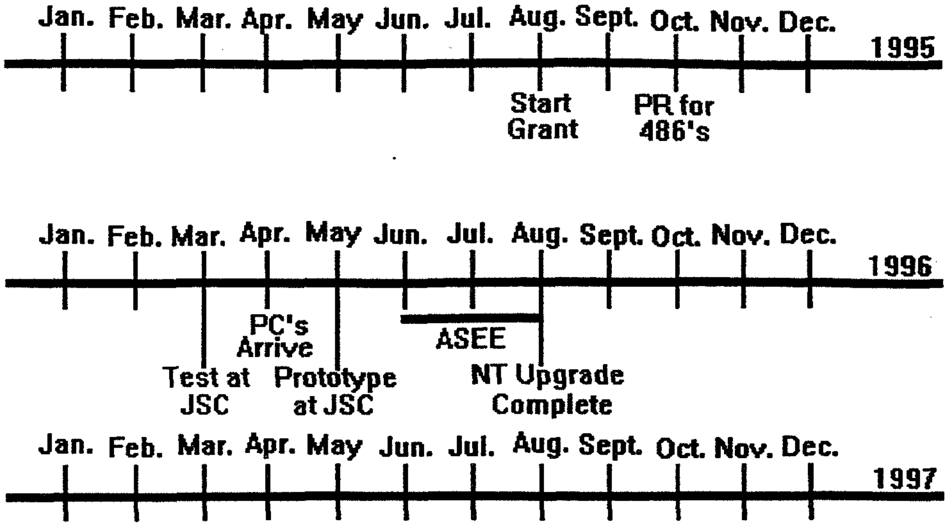

Without A Grant

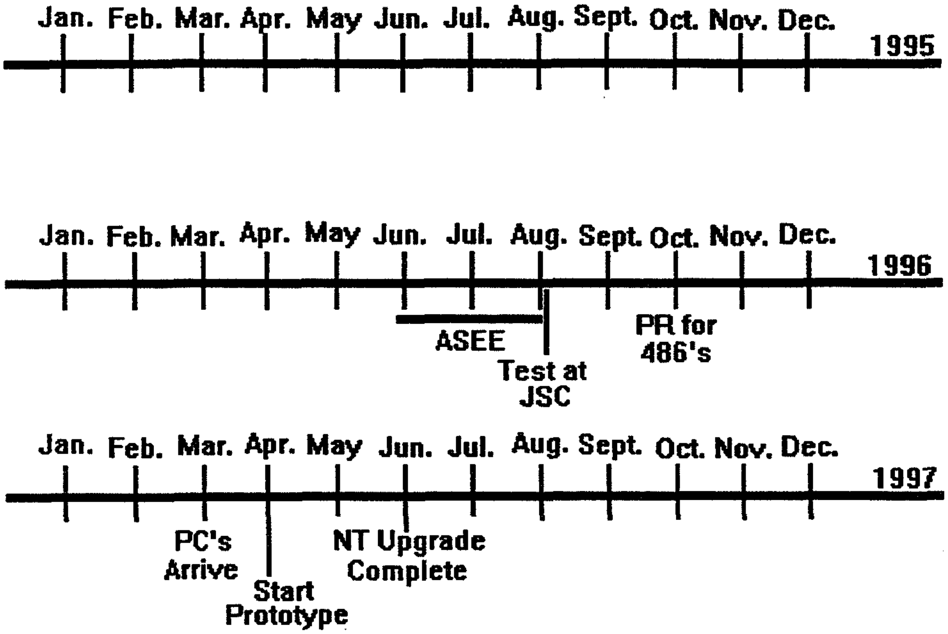

In comparing of the two time lines it can be seen that with a grant from NASA it will be possible to bring the CIM technology on line a year before it could be brought on line by doing it in house. Another advantage of using the grant to get the work done is that there are fewer NASA employee hours related to the project and less disturbance to production activities.

Cost Estimate

The estimate for the cost of the software can be broken into two main sections consisting of expenses during this fiscal year and expenses during the 1996 fiscal year. During this year the estimated cost of the CIM software is $16,795.00. This price includes installation of the CIMNET software, training of EM's personnel, and a one year maintenance contract on the software for a 20 concurrent users license. To upgrade the software during the 1996 fiscal year bringing on line all the options needed to fully automate this CIM operation an additional $32,300.00 will have to be spent. This final step will include managerial reports, statistical evaluation of the facilities functions, job tracking, and tool monitoring. There is no cost estimate for the upgrade computers due to the rapid changes in computer prices.

Recommendations

1. Build the network recommended in building 10 that will support connectivity between machines and the NT server.
2. Purchase and implement the CIMNET software (DNC+ w/Folders Lite) and select and configure recycled computers from R&U.
3. Develop a limited NT workstation for the production floor limiting the use of the computers to business only.
4. Integrate the CIMNET software (DNC+ w/Folders Lite) with the NT workstation and test the configuration to insure computability before disrupting production.
5. Replace the 386sx computers with 486dx computers running at 66Mhz or faster. The RAM in the replacement computers must be at least 16 meg. The HD should not be any smaller than 500Meg. with a built in video 1Meg. memory.
6. Install an additional 7 computers so each machine has its own computer. This should eliminate any waiting that could occur during peak use times.

58-52
76318
14p.
234354

DEXTROAMPHETAMINE: A PHARMACOLOGIC COUNTERMEASURE FOR SPACE MOTION SICKNESS AND ORTHOSTATIC DYSFUNCTION

Final Report
NASA/ASEE Summer Faculty Fellowship Program--1995
Johnson Space Center

Prepared By:	L. Dale Snow, Ph.D.
Academic Rank:	Professor
College and Department:	Louisiana Tech University Biochemistry Program College of Engineering and Sciences Ruston, Louisiana 71272

NASA/JSC

Directorate:	Space and Life Science
Division:	Medical Sciences Division
Branch:	Biomedical Operations and Research Branch
JSC Colleague:	Lakshmi Putcha
Date Submitted:	August 4, 1995
Contract Number:	NGT-44-001-800

ABSTRACT

Dextroamphetamine has potential as a pharmacologic agent for the alleviation of two common health effects associated with microgravity. As an adjuvant to space motion sickness (SMS) medication, dextroamphetamine can enhance treatment efficacy by reducing undesirable central nervous system (CNS) side effects of SMS medications. Secondly, dextroamphetamine may be useful for the prevention of symptoms of post-mission orthostatic intolerance caused by cardiovascular deconditioning during spaceflight.

There is interest in developing an intranasal delivery form of dextroamphetamine for use as a countermeasure in microgravity conditions. Development of this dosage form will require an analytical detection method with sensitivity in the low ng range (1 to 100 ng/mL). During the 1995 Summer Faculty Fellowship Program, two analytical methods were developed and evaluated for their suitability as quantitative procedures for dextroamphetamine in studies of product stability, bioavailability assessment, and pharmacokinetic evaluation. In developing some of the analytical methods, β-phenylethylamine, a primary amine structurally similar to dextroamphetamine, was used.

The first analytical procedure to be evaluated involved hexane extraction and subsequent fluorescamine labeling of β-phenylethylamine. Assay standard curves were linear from 0.025 to 10 μg/mL. The lower limit of detection was 0.1 μg/mL. When serum was spiked with drug and extracted with hexane, the standard curve was linear in the 1.0 to 10.0 μg/mL range. The lower limit of detection was 1.0 μg/mL. The recovery of drug was 55 percent. The fluorescamine assay had insufficient sensitivity for quantitation of β-phenylethylamine at the levels which would occur in serum or saliva. However, this method would be amenable to measuring β-phenylethylamine or dextroamphetamine in urine where higher drug concentrations are observed.

The second analytical procedure to be evaluated involved quantitation of dextroamphetamine by an enzyme-linked immunosorbent assay (ELISA). The primary antibody was a purified, monoclonal antibody (mouse) to dextroamphetamine. The secondary antibody was sheep anti-mouse IgG conjugated with horse radish peroxidase (HRP). The HRP activity was determined by measuring A490 with a microplate reader.

For spiked human serum, the ELISA assay standard curves were linear from 50 to 1000 ng/mL. The lower limit of detection was 100 ng/mL. The sensitivity of the ELISA procedure was comparable to the combined extraction and fluorescamine-labeling procedures. The ELISA assay had insufficient sensitivity for quantitation of dextroamphetamine at the levels which would occur in serum or saliva. However, if the ELISA procedure is coupled with an organic solvent extraction procedure or with a membrane ultrafiltration concentration procedure, the combined procedures may prove adequate for measurement of dextroamphetamine in serum or saliva. This possibility will be investigated in future experiments at Louisiana Tech University.

INTRODUCTION

Dextroamphetamine as a countermeasure

A common health effect of space flight is motion sickness which presents severe operational decrements during early flight days (1,2). The choice treatment for this flight specific illness is administration of promethazine intramuscularly (3). Unfortunately, promethazine has side effects that can affect alertness and performance. Dextroamphetamine (Dexdrine) given in conjunction with an antimotion sickness drug such as promethazine or scopolamine has been shown to enhance the effectiveness and reduce intensity of side effects (4). Furthermore, dextroamphetamine has been shown to reduce the risk and be beneficial for treatment of vasodepressor syncope (5).

Physiologic changes of the GI function, symptoms of motion sickness, and other related GI disturbances render oral administration of medications a undesirable option for the effective treatment of these disturbances during space flight (6). There is interest in examining the bioavailability and effectiveness of an intranasal dosage form of dextroamphetamine in conjunction with promethazine. The goal is to develop noninvasive methods of pharmacologic treatment to provide safe, effective medications in space, as well as to offer these methods for the general benefit of clinical populations.

During the 1995 Summer Faculty Fellowship Program, the feasibility of developing an intranasal formulation of dextroamphetamine was examined. Development of this dosage form will require an analytical method suitable for conducting product stability studies, bioavailability assessment, and pharmacokinetic evaluation. Two existing assays for dextroamphetamine analysis, fluorometric assay and enzyme-linked immunosorbent assay (ELISA), were modified and compared.

Ultimately, the analytical methodology developed during this Summer Faculty Program will be used to compare the bioavailability and pharmacodynamics of two dosage forms of dextroamphetamine. Concentrations of parent drug and metabolites will be measured in blood, saliva, and urine after intranasal (IN) and oral (IM) administration. Pharmacokinetics and bioavailability will be estimated, and pharmacodynamics will be assessed. The analytical methodology developed during the Summer Faculty Program in conjunction with the ongoing research at the Johnson Space Center may ultimately provide a new dosage form for dextroamphetamine and may contribute to applications of the drug dextroamphetamine in space flight.

Pharmacologic background

Dextroamphetamine is a non-catecholamine, sympathomimetic amine with CNS stimulant activity and is used chiefly for its CNS effects. D-Amphetamine exerts most of its CNS effects by releasing biogenic amines from their storage sites in the nerve terminals. The alerting effect of amphetamine, its anorectic effect, and at least a component of its locomotor-stimulating action are presumably mediated by release of norepinephrine from central noradrenergic neurons (7).

Following an oral dose, dextroamphetamine is completely absorbed within 3 hours. It is widely distributed in the body with high concentrations in the brain. Therapeutic blood levels range from 50 to 10 ng/mL (7). In a pharmacokinetic study in humans, ingestion of 10 mg dextroamphetamine produced an average peak blood level of 29.2 ng/mL at 2 hours post-administration (8). The average half-life was 10.25 hours. The average urinary recovery was 45% in 48 hours. Ingestion of a sustained release capsule containing 15 mg produced a peak blood level at 8 to 10 hours post-administration with peak urinary recovery at 12 to 24 hours. The dextroamphetamine volume of distribution was 270 liters/70 kg. The plasma protein binding of dextroamphetamine at concentrations of 10 and 100 ng/mL was 16% bound (9).

Urinary excretion of the unchanged drug is pH dependent (10). Urinary acidification to pH < 5.6 yields a plasma half-life of 7 to 8 hrs. Urinary alkalinization increases half-life ranging from 18.6 to 33.6 hours. For every one unit increase in urinary pH, there is an average 7 hour increase in plasma half-life. Proportionality between blood and urine data allowed an estimate of 120 mL/min for the apparent renal clearance of amphetamine.

METHODS

Materials

A purified monoclonal antibody against dextroamphetamine was purchased from Biodesign International. Dextroamphetamine standard (1 mg/mL in methanol) was purchased from Sigma Chemical Company. For fluorescamine labeling experiments, β-phenylethylamine, a drug structurally similar to dextroamphetamine, was used as a drug standard for assay development.

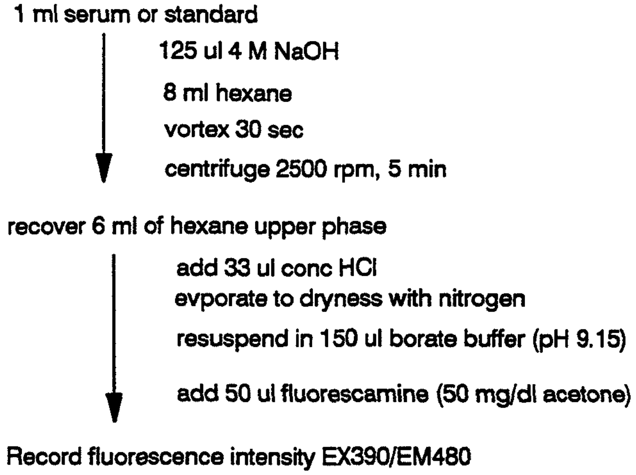

Figure 1.- Steps in the extraction and labeling procedure for fluorescamine assay of beta-phenylethylamine.

Extraction of β-phenylethylamine

Aliquots of β-phenylethylamine standard or serum spiked with β-phenylethylamine were prepared with a final volume of 1.0 mL in 4 inch culture tubes. Assay mixtures received 0.125 mL of 4 N NaOH and were extracted with 8 mL hexane by vortexing for 30 sec. After centrifugation at 2,500 rpm for 5 min, the upper organic phase was recovered and evaporated to dryness by passing a stream of nitrogen over the sample. The dry residue was used for fluorescamine labeling.

Fluorescamine labeling of β-phenylethylamine

All samples to be labeled with fluorescamine were brought to a final volume of 0.15 mL with 0.1 M sodium borate buffer (pH 9.15). Each sample received 0.05 mL of fluorescamine reagent (50 mg fluorescamine/100 mL of acetone). In preliminary experiments, an additional 2.3 mL of 0.1 M borate buffer (pH 9.15) was added and fluorescence intensity was measured in a 3 mL cuvette using a fluorimeter. Excitation was at 390 nm with a bandwidth of 10 nm, and emission was measured at 480 nm with a bandwidth of 20 nm. Alternatively, the undiluted fluorescamine-labeled samples were drawn into Hoefer TKO capillary tubes, and the fluorescence intensity was measured in a Hoefer TKO capillary cuvette.

Immunoassay of dextroamphetamine

Dextroamphetamine standards with concentrations of 0, 10, 50, 100, 500, and 1000 ng/mL were prepared in either 20 mM potassium phosphate, 150 mM NaCl, pH 7.2 (PBS) or pooled human serum. Triplicate aliquots (50 μL) of standards were dispensed into Immulon 96-well microtiter plates and incubated over night at room temperature. The plates were washed with five changes of Dulbecco' phosphate-buffered saline (D-PBS) containing 1 mM magnesium chloride, 1 mM calcium chloride, 20 mM potassium phosphate, and 150 mM NaCl (pH 7.2) over a 20-minute period. For 1 hr at 37°C, wells of plates were blocked with 150 μL of Blocking Buffer containing 4% bovine serum albumin (BSA) and 4% heat-inactivated sheep serum in calcium- and magnesium-free PBS, pH 7.2 (CMF-PBS). Blocking Buffer was removed, and wells were washed five times with Wash Buffer containing 0.05% Tween 20 in D-PBS (pH 7.2). Wash Buffer was removed, and primary antibody (mouse monoclonal anti-dextroamphetamine) was added in 50 μL of Antibody Blocking Buffer containing 1% BSA and 1% HISS in calcium-magnesium-free PBS (pH 7.2). Plates containing primary antibody were incubated for 2 hr at 37°C, and wells were washed five times with Wash Buffer. Wash Buffer was removed, and secondary antibody (horse radish peroxidase conjugated sheep anti-mouse antibody) was added in 50 μL of Antibody Blocking Buffer. Plates containing secondary antibody were incubated for 1 hr at 37°C, and wells were washed five times with Wash Buffer. Wash Buffer was removed, and each well received 150 μL of Chromagen Reaction Buffer containing 9.25 mM o-phenylenediamine, 0.2 mg% hydrogen peroxide in 70 mM sodium citrate (pH 6.0). Reaction time was 1 hr, and the reaction was stopped by addition of 150 μL of 2 M sulfuric acid. Absorbance was measured at 490 nm with a plate reader.

RESULTS AND DISCUSSION

Calibration of spectrofluorimeter with riboflavin

To calibrate the spectrofluorimeter for use in fluorescence measurements, a riboflavin standard curve was prepared, and native fluorescence was measured. Concentrations of standards ranged from 0.4 to 40 ng/mL. Samples volumes were 2.5 mL, and fluorescence intensity was determined in a 3 mL cuvette with 1 cm light path. By performing excitation and emission scans, the optimum wavelengths for detection of native fluorescence were excitation at 425 nm and emission at 530 nm. The standard curve was linear from 0.4 to 30 ng/mL (data not shown).

Labeling of β-phenylethylamine with fluorescamine

Ten β-phenylethylamine standards with 0.15 mL volume in 0.1 M borate buffer (pH 9.15) were prepared. The standard concentrations ranged from 0.01 μg to 100 μg per tube. A 0.05 mL solution of fluorescamine reagent was added to each tube. The mixtures were further diluted with 2.3 mL of borate buffer, and fluorescence intensity was measured in a 3 mL cuvette with 1 cm light path. By performing excitation and emission scans, the optimum wavelengths for detection of fluorescamine-labeled β-phenylethylamine were excitation at 390 nm with a bandwidth of 10 nm and emission at 480 nm with a band width of 20 nm. The standard curve was linear from 0.05 to 10 μg per tube (data not shown).

Percent recovery of β-phenylethylamine from serum

Water or serum was spiked with 0, 1, 5, or 10 μg of β-phenylethylamine. The samples were extracted and labeled with fluorescamine. The fluorescence intensity was determined using a 3 mL cuvette. A set of standards which was not extracted was also assayed so that recovery could be estimated (Fig. 2). The recovery of β-phenylethylamine from water was 80%, while the recovery from serum was 55%.

Requirement of acid addition before evaporation to dryness

The fluorescamine labeling reaction is strongly pH dependent with a pH maximum of 8.0 to 9.5. The extraction procedure includes the addition of 33 μl of concentrated HCl to the hexane aliquot before evaporation to dryness. To determine if the addition of HCl to the hexane extract before evaporation was essential to the labeling reaction, water and serum standards of β-phenylethylamine were prepared and extracted. The organic phase was evaporated to dryness either with or without the 33 μl concentrated HCl addition. After labeling, fluorescence intensity was determined using a 3 mL cuvette. When acid was added before evaporation, the recovery of β-phenylethylamine was 80% from water and 55% from serum (Fig. 3). When acid addition was omitted, recoveries from water and serum were 20% and 15%, respectively (Fig. 3). Addition of concentrated HCl was required for successful labeling of β-phenylethylamine.

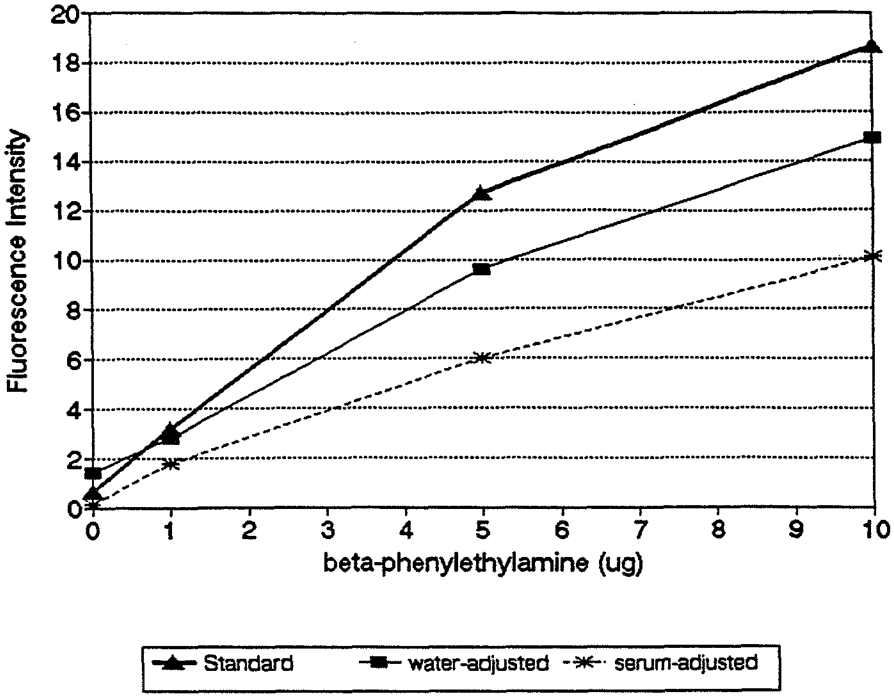

Figure 2.- Fluorescamine labeling of beta-phenylethylamine after extraction from water or serum

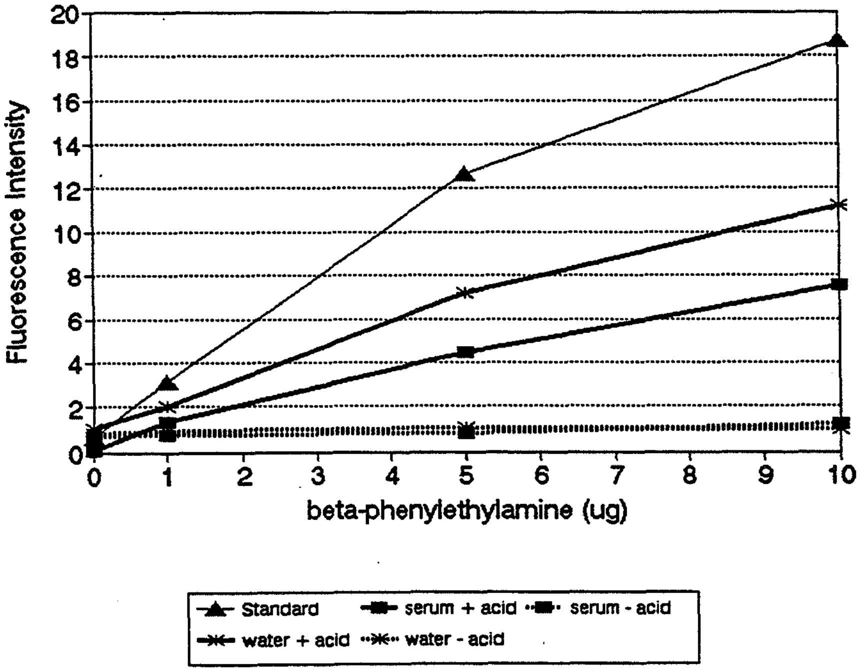

Figure 3.- Effect HCl addtion on recovery and labeling of beta-phenylethylamine in the fluorescamine assay.

In another experiment, the amount of concentrated HCl added to the hexane extract before evaporation was doubled to 66 μl. The percent recovery for both water and serum samples was unchanged by doubling the HCl addition (data not shown). The results suggest that HCl addition is required and that 33 to 66 μl of concentrated HCl is an adequate addition to support subsequent fluorescamine labeling.

Effect of mechanical mixing on drug extraction

The effect of prolonged mechanical mixing on drug recovery was examined. Spiked water and serum samples were extracted by either 30 min rotation on a clinical mixing table or by 30 sec vortexing by hand. The percent recovery for both water and serum samples was unchanged by 30 min agitation versus simple vortexing. This demonstrates that the more elaborate extraction procedure is not required (Data not shown).

Use of capillary cuvette to measure fluorescence intensity

The use of a 3 mL quartz cuvette for measuring fluorescence intensity necessitated the dilution of the 0.2 mL labeling mixture to 2.5 mL. To avoid this dilution, a Hoefer TKO capillary cuvette and TKO quartz capillary tubes were employed to measure the fluorescence intensity of undiluted 0.2 mL samples after labeling. For a 10 μg/mL standard, the fluorescence intensity for the diluted 2.5 mL samples and undiluted 0.2 mL samples were 21 and 98, respectively (Fig. 4). For all subsequent assays, the capillary cuvette was employed, and dilution of labeled samples was avoided.

To further examine the utility of the capillary cuvette, serum samples were spiked with β-pheynylethylamine to create a standard curve ranging from 0.01 to 1 μg/mL. Samples were extracted with hexane. After labeling with fluorescamine, the fluorescence intensity was determined using the capillary cuvette. A standard curve of β-phenylethylamine in water was also prepared and labeled without extraction. The standard curve for unextracted samples was linear from 0.025 to 1 μg. The lower limit of detection was 0.025 to 0.1 μg (Fig. 5). Although unextracted aqueous samples could readily be assayed in the 0.1 to 1 μg range, recoveries for extracted serum samples were low, and quantitation was not possible from serum. The fluorescence intensity of extracted serum samples was only slightly higher than blanks. The capillary cuvette method increased the fluorescence intensity of samples, but the sensitivity of the method was not improved by this technique.

Time dependence of fluorescamine labeling

The labeling of primary amines with fluorescamine is both pH and time dependent. Several 10 μg samples of β-phenylethylamine were prepared and labeled for different times ranging from 5 to 30 min. The extent of labeling was unchanged throughout the time interval examined and did not increase for incubations as long as either 2 or 3 hr (data not shown).

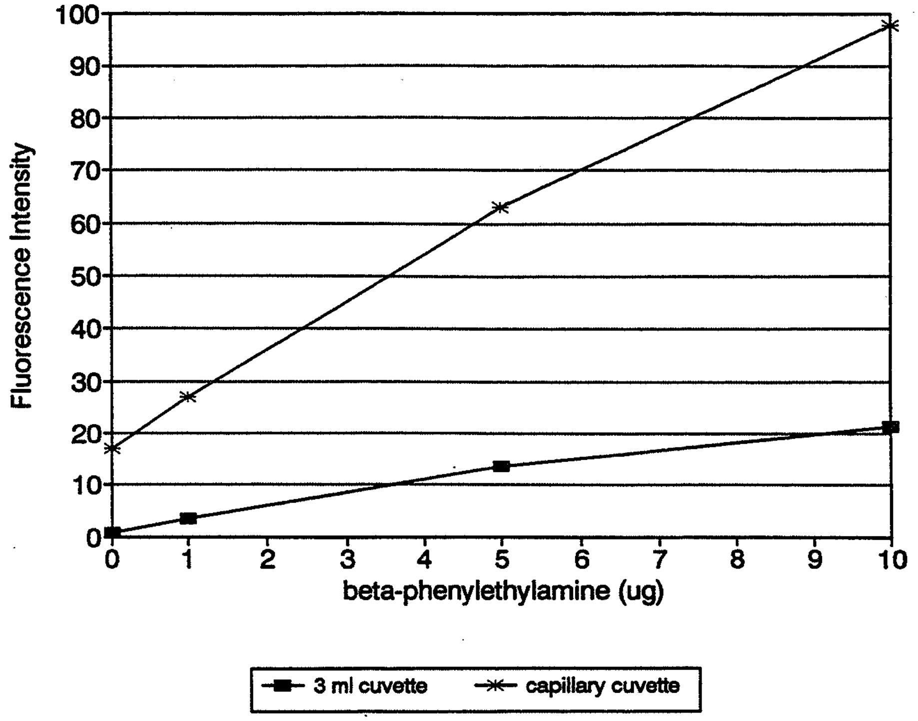

Figure 4.- Quantitation of fluorescamine labeled beta-phenylethylamine using a capillary cuvette and a 3 ml cuvette.

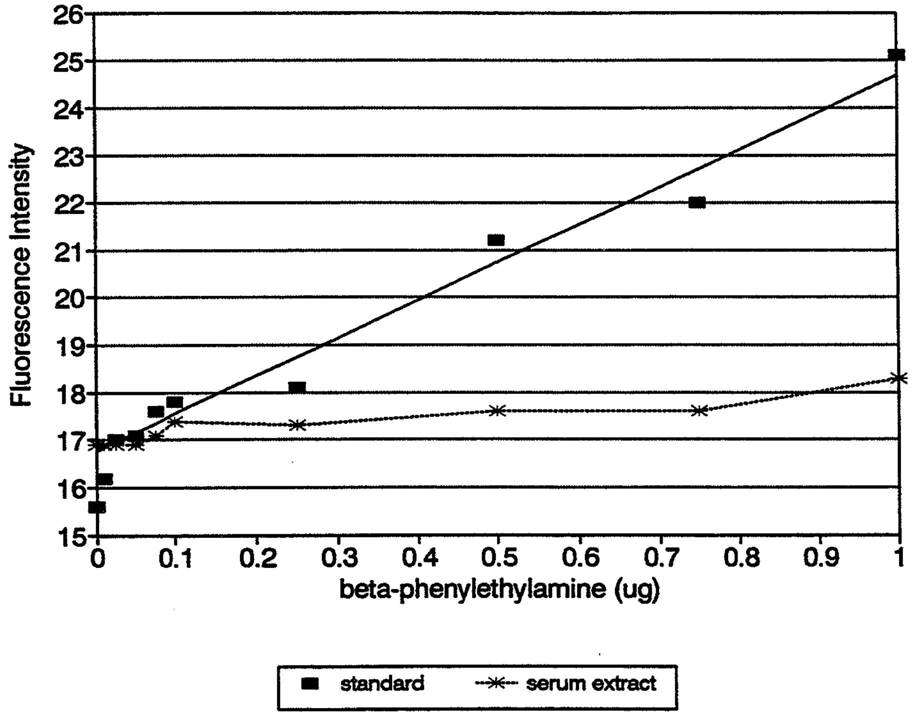

Figure 5.- Capillary cuvette measurement of fluorescamine-labeled beta-phenylethylamine in standards or in serum extract.

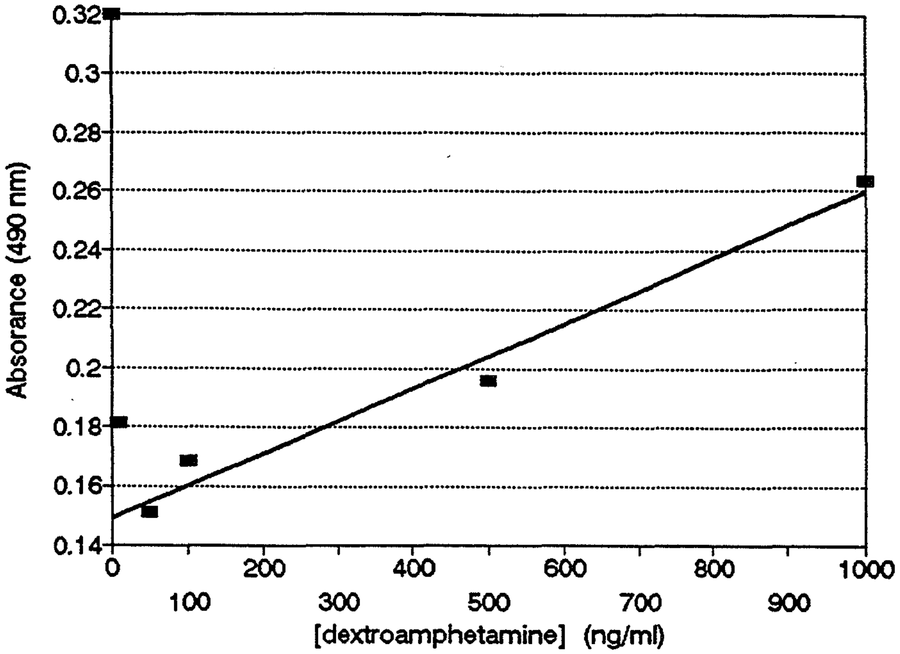

Figure 6.- ELISA standard curve of dextroamphetamine in human serum.

Enzyme-linked immunosorbent assay of dextroamphetamine

Enzyme-linked immunsorbent assays (ELISA) have been used to measure ng and pg quantities of proteins, peptides, and drugs in biological specimens. A purified, monoclonal antibody to dextroamphetamine was purchased and used to measure dextroamphetamine in spiked human serum. As shown in Fig. 6, a linear standard curve was obtained in the range of 50 to 1000 ng/mL. The lower limit for dextroamphetamine detection in spiked human serum was 100 ng/mL.

The lower limit for detection of dextroamphetamine by ELISA was similar to the lower limit for dextroamphetamine detection by the fluorescamine labeling procedure. However, the ELISA procedure involved the detection of dextroamphetamine in only 50 μl of serum, whereas the fluorescamine procedure involved extraction and assay of dextroamphetamine from 1 mL of serum.

It is anticipated that much lower limits of detection could be obtained by the ELISA procedure if serum dextroamphetamine samples could be concentrated before analysis. Concentration of serum dextroamphetamine samples could be accomplished by either extraction with organic solvents or by membrane ultrafiltration coupled with Speed-Vac solvent evaporation. Studies of the utility of these concentration procedures for enhancing ELISA measurement of dextroamphetamine will be continued in the Biochemistry Program at Louisiana Tech University.

CONCLUSIONS

Primary amines such as β-phenylethylamine were readily extracted from alkalinized serum by hexane. Recoveries ranged from as high as 80% for aqueous solutions of the amine to about 50% for spiked serum samples.

Hexane extraction of β-phenylethylamine followed by covalent labeling of the primary amine with fluorescamine was a viable analytical procedure for quantitation. Assay standard curves were linear from 0.025 to 10 μg/mL. The lower limit of detection was 0.1 μg/mL for aqueous solutions of the amine and 1.0 μg/mL for spiked serum.

The fluorescamine assay had insufficient sensitivity for quantitation of β-phenylethylamine at the levels which would occur in serum or saliva. However, this method would be amenable to measuring β-phenylethylamine or dextroamphetamine in urine where higher drug concentrations are observed.

The enzyme-linked immunosorbent assay (ELISA) procedure proved to be a viable analytical method for determination of dextroamphetamine. The primary antibody was a purified, monoclonal antibody (mouse) to dextroamphetamine, and the secondary antibody was sheep anti-mouse IgG conjugated with horse radish peroxidase (HRP). For spiked human serum, the ELISA assay standard curves were linear from 50 to 1000 ng/mL. The lower limit of detection was 100 ng/mL.

The sensitivity of the ELISA procedure was comparable to the sensitivity of the combined hexane extraction/fluorescamine-labeling procedures. The ELISA assay had insufficient sensitivity for quantitation of dextroamphetamine at the levels which would occur in serum or saliva. However, if the ELISA procedure is coupled with an organic solvent extraction procedure or with a membrane ultrafiltration concentration procedure, the combined procedures may prove adequate for measurement of dextroamphetamine in serum or saliva. This possibility will be investigated in future future experiments at Louisiana Tech University.

REFERENCES

(1) J. R. Davis, J. M. Vanderploeg, P. A. Santy, R. T. Jennings and D. F. Stewart (1988) Space motion sickness during 24 flights of the Space Shuttle. Aviat. Space Environ. Med. **59**, 1185.

(2) M. F. Reschke, D. L. Harm, D. E. Parker, G. R. Sandoz, J. L. Homic, and J. M. Vanderploeg (1994) Neurophysiologic aspects: space motion sickness. In: A. E. Nicogossian, S. L. Pool and C. L. Huntoon, eds. Space Physiology and Medicine. 3rd ed. Philadelphia: Lea & Febiger, p. 228.

(3) J. R. Davis, R. T. Jennings, B. G. Beck, and J. P. Bagian (1993) Treatment efficacy of intramuscular promethazine for space motion sickness. Aviat. Space Environ. Med. **64**, 230.

(4) C. D. Wood, J. J. Stewart, M. J. Wood, J. E. Manno, B. R. Manno and M. E. Mims (1990) Therapeutic effects of antimotion sickness medications on the secondary symptoms of motion sickness. Aviat. Space Environ. Med. **61**, 157.

(5) A. Susmano, A. S. Volgman and T. A. Buckingham (1993) Beneficial effects of dextro-amphetamine in the treatment of vasodepressor syncope. PACE Pacing Clin. Electrophysiol. **16**, 1235.

(6) L. Putcha and N. M. Cintron (1991) Pharmacokinetic consequences of space flight. Ann. New York Acad. Sci. **618**, 615.

(7) B. B. Hoffman and R. J. Lefkowitz (1990) Catecholamines and sympathomimetic drugs. In Goodman and Gilman's The Pharmacologic Basis of Therapeutics. 8th edition. A. G. Gilman, T. W. Rall, A. S. Nies, and P. Taylor (editors) Pergamon Press, New York, pg. 210.

(8) M. Rowland (1969) Amphetamine blood and urine levels in man. J. Pharm. Sci. **58**, 508.

(9) S. K. Wan, S. B. Matin, and D. L. Azarnoff (1978) Kinetics, salivary excretion of amphetamine isomers, and effect of urinary pH. Clin. Pharmacol. Ther. **23**, 585.

(10) A. M. Asatoor, B. R. Galman, J. R. Johnson and M. D. Milne (1965) The excretion of dexamphetamine and its derivatives. Br. J. Pharmacol. **24**, 293.

59-46

76320

DETECTING THE DYNAMICAL STATE OF THE ATMOSPHERE FROM THE ORBITAL DECAY OF THE ODERACS SPHERES

16P.

034355

Final Report

NASA/ASEE Summer Faculty Fellowship Program - 1995

Johnson Space Center

Prepared By:	Arjun Tan
Academic Rank:	Professor
College & Department:	Alabama A & M University Department of Physics Normal, Alabama 35762

NASA/JSC

Directorate:	Space and Life Sciences Directorate
Division:	Solar System Exploration Division
Branch:	Space Science Branch
JSC Colleague:	Gautam D. Badhwar
Date Submitted:	August 11, 1995
Contract Number:	NGT 44-001-800

ABSTRACT

The orbital decay curve of a satellite having constant cross-sectional area and in circular orbit can furnish valuable information regarding the dynamical state of the atmosphere. It is shown that a rectilinear decay curve having constant downward slope (zero curvature) should indicate that the atmosphere was undergoing compression during that period. A decay curve having concavity upwards (positive curvature) will strongly indicate that the atmosphere was in a contracting phase. A decay curve with downward concavity (negative curvature) may indicate an expanding, a stationary or a contracting atmosphere. This theory, when applied to the orbital decay of the Orbital Debris Radar Calibration Spheres (ODERACS) satellites, indicates that during the period from Day 90 through Day 240 in the year 1994, the atmosphere was very definitely in a compression mode. During this period, ODERACS Sphere 1 faced nearly constant densities while Sphere 6 actually encountered progressively smaller air densities as they descended. The atmospheric scale height as calculated from the orbital data of Spheres 1 and 6 diminished steadily during the same period. It is shown that Spheres 1 and 6 descended faster and slower, respectively, than the level of constant air density equal to 5×10^{-12} kg/m^3. During a brief period from Day 240 through Day 290, the atmosphere reversed to a strongly expanding mode. Thereafter, the atmosphere reverted back to a compression mode from Day 290 through Day 390, 1994.

INTRODUCTION

The orbital decay of artificial Earth satellites have provided valuable information regarding atmospheric densities, temperature and other parameters upon which most atmospheric models are now based. Further, specific information can be extracted from satellite orbits which are nearly circular. For example, Tobiska, et al. (1987) developed a 10.7 cm solar flux model for sunspot cycle 22 from the observed decay of the Solar Mesosphere Exposure Satellite, whereas Badhwar (1990) determined the exospheric temperature during the same cycle from the orbital decay of the Long Duration Exposure Facility Satellite.

This study analyzes the orbital decay of the Orbital Debris Radar Calibration Spheres (ODERACS) satellites, which were deployed on 9 February 1994 from the Space Shuttle Discovery into nearly circular orbits of 352 x 347 km (The ODERACS News Roundup, February 1994). The ODERACS consisted of six perfectly spherical metallic satellites: two 4"-diameter Aluminum spheres; two 2"-diameter Stainless Steel spheres; and two 6"-diameter Aluminum spheres. One sphere of each category had a smooth surface and the other was sandblasted. The smooth Aluminum spheres were also chrome-plated. On account of the perfectly spherical shapes, the cross-sectional areas of the ODERACS were constants and accurately known.

The present study analyzes the orbital decay of satellites having constant cross-sectional areas and in nearly circular orbits. Special attention is focussed on the significance of the slope and curvature of the orbital decay curve and their implications on the dynamic state of the atmosphere. Particular emphasis is given to finding the signatures of atmospheric compression. The theory is applied to the orbital decay of the ODERACS satellites. It is shown that from Day 90 through Day 240 during the year 1994, the atmosphere was in a compression phase.

THEORY

The theory of orbital decay is well documented in the literature. The rate of change of the semi-major axis of a satellite of mass m is given by (cf. King-Hele, 1964)

$$\dot{a} = - \frac{C_D a^2 A \rho v^3}{\mu m} , \qquad (1)$$

where C_D is the drag coefficient, A the cross-sectional area of the satellite, v its velocity, ρ the density of the ambient air and μ the gravitational parameter of the Earth. The dot represents total differentation with respect to time. Equation (1) can be employed to calculate the density of the ambient air if the cross-sectional area of the satellite is accurately known (cf. Tobiska, et al., 1987).

For a circular orbit, we have

$$v^2 = \frac{\mu}{a} , \tag{2}$$

so that Eq. (1) takes a simpler form (cf. Badhwar, 1990)

$$\dot{a} = - \frac{C_D \, A \, a \, \rho \, v}{m} . \tag{3}$$

Since atmospheric drag reduces the eccentricity of elliptic orbits, an initially circular orbit remains circular (cf. King-Hele, 1964). For circular orbits, $a = r_o + z$, where r_o is the reference radius of the Earth and z can be taken as the mean altitude of the satellite. $\dot{a}$ is geometrically equal to the slope of the tangent to the decay curve on a plot of the semi-major axis a (or z for that matter) versus time.

As a satellite in a circular orbit descends in the atmosphere, it normally faces greater and greater atmospheric densities. The slope of the decay curve becomes progressively steeper and the curve becomes concave downwards, as a general rule. However, if a decay curve is straight over a considerable period of time, then $\ddot{a}$ is zero over that period. In that case, the variation of density encountered by the satellite as a function of z is obtained from Eqs. (3) and (2):

$$\rho \propto \left(1 + \frac{z}{r_o} \right)^{-\frac{1}{2}} . \tag{4}$$

If the satellite descends from an altitude z_1 (corresponding density ρ_1) to an altitude z_2 (corresponding density ρ_2), then

$$\rho_1 = c \left(1 + \frac{z_1}{r_o} \right)^{-\frac{1}{2}} , \tag{5}$$

and

$$\rho_2 = c \left(1 + \frac{z_2}{r_o} \right)^{-\frac{1}{2}} , \tag{6}$$

c being the constant of proportionality. Dividing (6) by (5), expanding and retaining first order terms only, we have

$$\frac{\rho_2}{\rho_1} \cong 1 + \frac{z_1 - z_2}{2 \, r_o} . \tag{7}$$

Since $z_1 - z_2$ is positive, the density increases as the satellite descends. However, as $(z_1 - z_2)/r_o$ is small, the increase is a slowly varying function of the altitude drop $z_1 - z_2$.

This increase may now be compared with the natural increase in density encountered by an object descending through a stationary atmosphere. In the altitude range of low-Earth-orbit satellites, the atmospheric density decreases exponentially with height, with a scale height of H between 30 and 50 km (cf. King-Hele, 1964):

$$\rho = \rho_o e^{-\frac{z}{H}} . \tag{8}$$

Here ρ_o is the density at a reference base level. If the object descends between altitude z_1 (corresponding density ρ_1) and altitude z_2 (corresponding density ρ_2), then

$$\rho_1 = \rho_o e^{-\frac{z_1}{H}} , \tag{9}$$

and

$$\rho_2 = \rho_o e^{-\frac{z_2}{H}} . \tag{10}$$

Dividing (10) by (9), expanding and retaining first order terms only,

$$\frac{\rho_2}{\rho_1} \cong 1 + \frac{z_1 - z_2}{H} . \tag{11}$$

Since $r_o >> H$, the density change in (11) is much greater than that given by Eq. (7). In other words, a rectilinear decay curve requires that the satellite face smaller densities than it would normally face in descending through a stationary atmosphere. This is possible only if densities decreased naturally as the satellite descended, i.e., if the atmosphere was undergoing compression during the descent.

If a decay curve possesses positive curvature over a considerable length of time, i.e., it exhibits concavity upwards (second derivative $\ddot{a} > 0$), then logically, the satellite is progressively facing even smaller densities than in a rectilinear decay. This, then signifies that the atmosphere was contracting at an even faster rate. To sum up, a decay curve that is straight or concave upwards indicates atmospheric compression. Decay curves which are concave downwards ($\ddot{a} > 0$), on the other hand, include all three possibilities of expanding, stationary or contracting atmospheres.

We now look into the significance of the second derivative $\ddot{a}$. Taking logarithm of Eq. (3) and differentiating with respect to time, we have

$$\frac{\ddot{a}}{\dot{a}} = \frac{\dot{a}}{a} + \frac{\dot{\rho}}{\rho} + \frac{\dot{V}}{V} . \tag{12}$$

Likewise, from Eq. (2)

$$\frac{\dot{V}}{V} = - \frac{\dot{a}}{2\,a} . \tag{13}$$

Combining (12) and (13) gives

$$\frac{\dot{\rho}}{\rho} = \frac{\ddot{a}}{\dot{a}} - \frac{\dot{a}}{2\,a} \ . \tag{14}$$

Geometrically speaking, $\ddot{a}$ determines the curvature of the decay curve: a positive curvature ($\ddot{a} > 0$) denotes concavity upwards, whereas a negative curvature ($\ddot{a} < 0$) denotes concavity downwards. The radius of curvature is given by the expression

$$R = \frac{(1 + \dot{a}^2)^{3/2}}{\ddot{a}} \ . \tag{15}$$

Substituting in Eq. (14), we get

$$\frac{\dot{\rho}}{\rho} = \frac{(1 + \dot{a}^2)^{3/2}}{\dot{a}\ R} - \frac{\dot{a}}{2\,a} \ . \tag{16}$$

For small but finite intervals, the left hand side of Eq. (16) can be taken as $\Delta\rho/\rho/\Delta t$, which represents the relative change in air density $\Delta\rho/\rho$ encountered by the satellite during a time interval Δt as it descends in the atmosphere. The second term on the right hand side is actually positive since $\dot{a} < 0$. The first term on the right is positive for negative curvature ($R < 0$, downward concavity) and negative for positive curvature ($R > 0$, upward concavity). Depending on the magnitude of R, the second term can dominate the first to determine the outcome of the left hand side. If the left hand side is negative, this means that the satellite is actually facing smaller densities as it descends. That occurs when

$$R < \frac{2\,a}{\dot{a}^2}\,(1 + \dot{a}^2)^{3/2} \ . \tag{17}$$

This is possible when the atmosphere is contracting at a faster rate than the rate of descent of the satellite. If the left hand side of Eq. (16) is positive, that merely indicates that the satellite is facing greater densities during descent. The atmosphere may even be contracting at the same time, but the satellite must be descending at a rate faster than the atmospheric contraction in the last case.

RESULTS AND DISCUSSIONS

This study analyzes the orbital decay of ODEARCS Spheres 1 and 6. Sphere 1 was a 4"-diameter chrome-plated Aluminum sphere having a mass of 1.488 kg, whereas Sphere 6 was a 6"-diameter sand-blasted Aluminum sphere of mass 5.000 kg. It was shown that chrome-plating Aluminum increased the drag coefficient by 8%, whereas sand-blasting increased it by 9% (Tan and Badhwar, 1995). However, since this difference is not significant, the traditional value of 2.2 for C_D was assumed for both spheres (cf. Cook, 1965).

Figure 1 (from The ODERACS News Roundup, December 1994; The ODERACS News Roundup, February, 1995) shows the relative orbital decay (mean altitude vs. time) of the ODERACS Spheres 1 and 6. The decay curve of Sphere 1

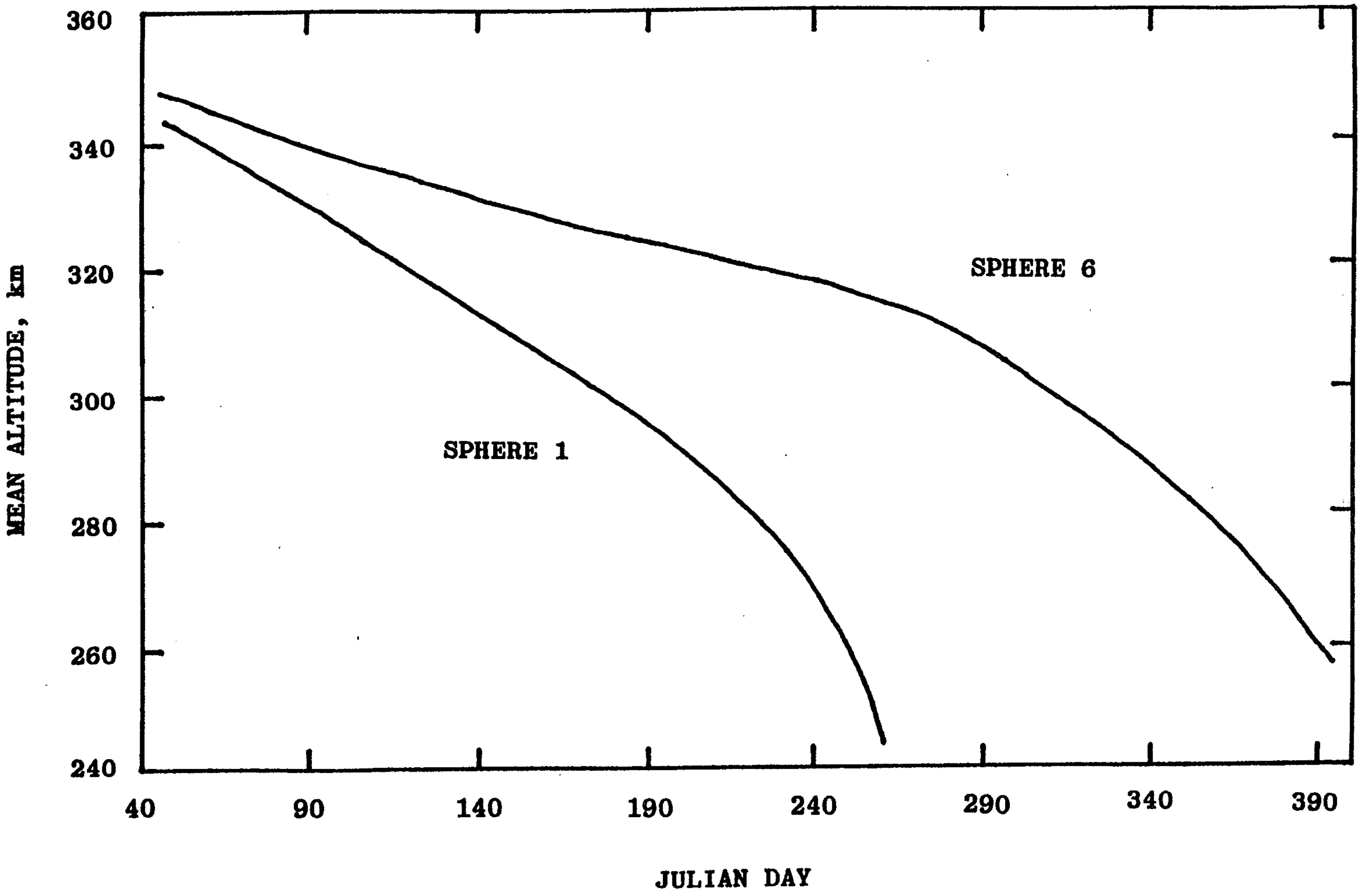

Fig. 1. Orbital Decay Curves (Mean Altitude vs. Day of Year) of ODERACS Spheres 1 and 6.

through Day 190, 1994 was almost straight with a slight concavity downwards. However, the most striking feauture lies on the decay curve of Sphere 6. Through Day 240, the curve exhibits a definite concavity upwards. According to our earlier analysis, this is the interval during which a compression of the atmosphere must have taken place.

The atmospheric densities encountered by ODERACS Spheres 1 and 6 were calculated at intervals of 50 days using Eq. (3) and entered in Tables I and II respectively. Sphere 1 had a greater rate of decay and consequently a shorter lifetime in the atmosphere owing to its larger area-to-mass ratio (A/m). It is remarkable that despite the drop of altitude of over 50 km in 150 days, the densities encountered by Sphere 1 in its early days remained nearly the same. Normally, there would have been a 3-fold increase in the density if the atmospheric conditions had remained the same (cf. U.S. Standard Atmosphere, 1976). This suggests that the atmosphere was undergoing compression during the same period.

A more definite proof of this compression comes from Table II. Through Day 240, Sphere 6 had actually encountered progressively smaller densities as it descended, which means that condition (17) must have been met during this period. In accordance with our earlier analysis, this confirms the fact that the atmosphere had contracted at a rate faster than the rate of descent of Sphere 6. The density encountered by the sphere decreased at an average rate of about 1.9% per 10 days. This rate of decrease can also be calculated from Eq. (16) and Fig. 2. The decay curve through Day 240 is nearly circular. The radius of curvature is estimated from a least-square fit circle and converted to proper units. The rate of relative decrease in density turns out to be 2.2% per 10 days, which fairly agrees with the earlier figure.

Next, since Spheres 1 and 6 descended over different altitudes at the same time, it is possible to calculate the average scale height of the atmosphere over the altitude range under consideration. Assuming an average scale height H, the densities ρ_1 at altitude z_1 (Sphere 1) and ρ_2 at altitude z_2 (Sphere 6) can be taken as those given by Eqs. (9) and (10) respectively. Here ρ_0 is the density at a base level, where fluctuations due to solar 10.7 cm flux are a minimum. This level occurs at about 100 km (cf. U.S. Standard Atmosphere, 1976), which is well below the altitude range of interest. Eliminating ρ_0 from Eqs. (9) and (10), we get

$$H = \frac{z_1 - z_2}{\ln \frac{\rho_2}{\rho_1}} . \tag{18}$$

The scale heights calculated from Eq. (18) using the data from Tables I and II are entered in Table III. It is interesting to note that there is a continuous decrease in the scale height during this period which cannot be accounted for by the much smaller normal decrease over the

Table I. Atmospheric Densities Encountered by Sphere 1

Julian Day	z, km	a, km	v, km/s	$\dot{a}$, 10^{-3}m/s	ρ, 10^{-12}kg/m^3
90	330.2	6708.3	7.708	3.90	6.29
140	313.3	6691.5	7.718	4.29	6.93
190	293.5	6671.7	7.730	5.36	8.67
240	267.2	6643.3	7.745	8.58	13.91

Table II. Atmospheric Densities Encountered by Sphere 6

Julian Day	z, km	a, km	v, km/s	$\dot{a}$, 10^{-3}m/s	ρ, 10^{-12}kg/m^3
90	339.8	6718.0	7.703	2.11	5.08
140	331.5	6709.6	7.708	1.84	4.43
190	324.3	6702.4	7.712	1.65	3.98
240	317.6	6695.7	7.716	1.51	3.65
290	307.4	6685.6	7.721	3.78	9.13
340	287.6	6665.7	7.733	5.15	12.44
390	259.4	6637.6	7.775	8.04	19.42

Table III. Atmospheric Scale Heights

Julian Day	z_1, km	z_2, km	ρ_1, 10^{-12}kg/m^3	ρ_2, 10^{-12}kg/m^3	H, km
90	330.2	339.8	6.291	5.079	45.0
140	313.3	331.5	6.929	4.429	40.6
190	293.5	324.3	8.674	3.977	39.4
240	267.2	317.6	13.910	3.651	37.7

same altitude range. This provides further evidence that from Day 90 through Day 240 during the year 1994, the atmosphere was in a compression mode.

Finally, it would be instructive to calculate the rate of contraction of the atmosphere during Days 90 through 240, 1994. One must bear in mind that the contraction rate would depend on the density level, but this dependence would be slight over the altitude range under consideration. We can calculate the altitude z corresponding to a certain density ρ from Eq. (8). Eliminating ρ_0 between (8) and (9) or (10), we get

$$z = -H \ln \left(\frac{\rho}{\rho_1} e^{-\frac{z_1}{H}}\right) = -H \ln \left(\frac{\rho}{\rho_2} e^{-\frac{z_2}{H}}\right) . \tag{19}$$

The levels of constant density equal to 5×10^{-12} kg/m^3 are calculated using Eq. (19) and plotted in Fig. 3 along with the altitudes of descent of Spheres 1 and 6. The figure shows that this level descended steadily at a rate of approximately 2.3 km per 10 days. The figure further verifies our earlier findings that Sphere 1 and Sphere 6 descended faster and slower, respectively, than this level of constant density. Consequently, Sphere 6 encountered smaller densities while Sphere 1 encountered greater densities even as the atmosphere itself was undergoing compression at the same time.

This entire analysis could not be extended beyond Day 240, for Sphere 1 had deorbited on Day 275 (The ODERACS News Roundup, December 1994) and we cannot calculate the scale height from the orbital data of Sphere 6 alone. However, we can still determine the dynamical state of the atmosphere subsequent to Day 240 as follows. If ρ_1 is the density at altitude z_1, we can calculate the density ρ_2 at a lower altitude z_2 if the satellite descended in a stationary atmosphere by assuming a constant plausible scale height H. From Eqs. (9) and (10)

$$\rho_2 = \rho_1 e^{\frac{z_1 - z_2}{H}} . \tag{20}$$

If Sphere 6 had descended from 317.6 km to 307.4 km between Day 240 to Day 290 (cf. Table II) in a stationary atmosphere, then the density at the latter height would range from 4.58×10^{-12} kg/m^3 to 5.13×10^{-12} kg/m^3 corresponding to scale heights between 45 km and 30 km. Since this range of density is only about half of the observed density (9.13×10^{-12} kg/m^3), the satellite had actually encountered far greater densities than it would have in a stationary atmosphere. This necessarily means that the atmosphere was in an expansion mode from Day 240 to Day 290. Similar analyses carried out between Day 290 and Day 340 and between Day 340 and Day 390 indicate that the atmosphere had reverted to a compression mode during both of these periods. In summation, the atmosphere was in a compression mode from Day 90 through Day 140

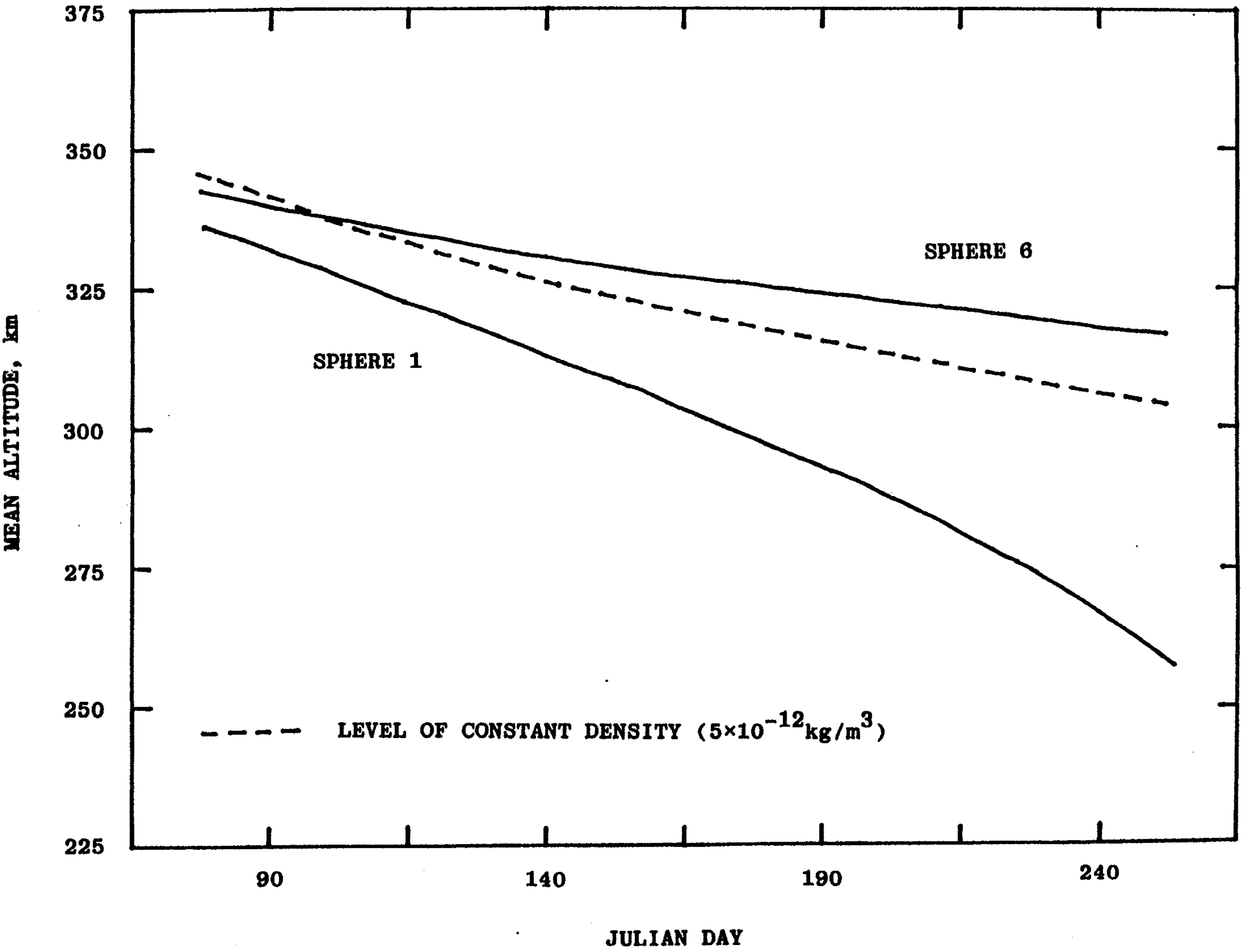

Fig. 2. Altitudinal descent of ODERACS Spheres 1 and 6 and atmospheric level of constant density

followed by an expansion mode from Day 240 through Day 290 and finally, another compression mode from Day 290 through Day 390 during the year 1994.

CONCLUSIONS

The following conclusions are drawn from the analysis of the orbital decay of satellites in circular orbits.
(1) A rectilinear decay curve (zero curvature) indicates atmospheric compression.
(2) A decay curve with concavity upwards (positive curvature) strongly indicates atmospheric contraction.
(3) A decay curve with downward concavity (negative curvature) may indicate expanding, stationary or contracting atmospheres.
(4) Throughout the period from Day 90 through Day 240 during the year 1994, the atmosphere was in a compression mode.
(5) During this period, ODERACS Sphere 1 faced nearly constant densities while Sphere 6 actually encountered progressively smaller densities as they descended.
(6) The atmospheric scale height diminished steadily during the same period.
(7) During a brief period from Day 240 to Day 290, the atmosphere reversed to a strongly expanding mode.
(8) The atmosphere reverted back to a compression mode from Day 290 through Day 390, 1994.

REFERENCES

G. D. Badhwar, Exospheric Temperatures During Solar Cycle 22, J. Astronaut. Sci., 38, 369-375 (1990).

G. E. Cook, Satellite Drag Coefficients, Planet. Space Sci., 13, 929-945 (1965).

D. King-Hele, Theory of Satellite Orbits in an Atmosphere, Butterworths, London (1964).

The ODERACS News Roundup, No. 1, NASA Johnson Space Center (February 1994).

The ODERACS News Roundup, No. 15, NASA Johnson Space Center (December 1994).

The ODERACS News Roundup, No. 16, NASA Johnson Space Center (February 1995).

A. Tan and G. D. Badhwar, Drag Coefficients, Atmospheric Parameters and Solar Flux from the Orbital Decay of the ODERACS Spheres, Bull. Am. Phys. Soc., 40, 1011 (1995).

W. K. Tobiska, R. D. Culp and C. A. Barth, Predicted Solar Cycle 22 10.7 cm Flux and Satellite Orbit Decay, J. Astronaut. Sci., 35, 419-433 (1987).

U.S. Standard Atmosphere, NASA, NOAA, USAF, Washington (1976).

Proportional and Scale Change Models to Project Failures of Mechanical Components with Applications to Space Station

50-18
76322
234357
12P.

Final Report
NASA/ASEE Summer Faculty Fellowship Program - 1995
Johnson Space Center

Prepared By:	Vidya S. Taneja
Academic Rank:	Professor
University & Department:	Western Illinois University Department of Mathematics Macomb, IL. 61455

NASA/JSC

Directorate:	Safety, Reliability, and Quality Assurance
Division:	Flight System Safety and Mission Assurance
Branch:	Analysis and Risk Assessment
JSC Colleague:	Richard P. Heydorn
Date Submitted:	August 4, 1995
Contract Number:	NGT - 44 - 001 - 800

ABSTRACT

In this paper we develop the mathematical theory of proportional and scale change models to perform reliability analysis. The results obtained will be applied for the reaction Control System (RCS) thruster valves on an orbiter. With the advent of extended EVA's associated with PROX OPS (ISSA & MIR), and docking, the loss of a thruster valve now takes on an expanded safety significance. Previous studies assume a homogeneous population of components with each component having the same failure rate. However, as various components experience different stresses and are exposed to different environments, their failure rates change with time.

In this paper we model the reliability of a thruster valves by treating these valves as a censored repairable system. The model for each valve will take the form of a nonhomogeneous process with the intensity function that is either treated as a proportional hazard model, or a scale change random effects hazard model. Each component has an associated z, an independent realization of the random variable Z from a distribution G(z). This unobserved quantity z can be used to describe heterogeneity systematically.

For various models methods for estimating the model parameters using censored data will be developed. Available field data (from previously flown flights) is from non-renewable systems. The estimated failure rate using such data will need to be modified for renewable systems such as thruster valve.

INTRODUCTION

In this paper we develop the mathematical theory of proportional and scale change models to perform reliability analysis. The results obtained will be applied for the Reaction Control System (RCS) thruster valves on a space vehicle. With the advent of extended EVA's associated with PROX OPS (ISSA & MIR), and docking to space station, the loss of a thruster valve now takes on an expanded safety significance. RCS thruster valves are installed on the orbiter at 38 locations, 14 in front (Forward) and 24 in the rear (Aft), 12 on each side. At each location there is a fuel valve and an oxidizer valve. Thus there are a total of 76 valves on an orbiter. These inlet valves can leak due to various reasons. These include the shrinkage of the teflon seal due to extreme weather conditions, reduction in the teflon seal height above the seal retainer, and contamination deposits between the valve seat and poppet face. The mixing of moist air and residual oxidizer (N_2O_4) form metallic nitrates. It is believed that the metallic nitrates cause deposits to build up in the valves.

The orbiter thruster valves have at least three failures modes. These are: (1) Nitrate build up so that the valve will not open (FAIL-OFF/CLOSED); (2) Nitrate deposits on the seat causes leaks and the valve will not close (FAIL-OFF/OPEN); and (3) Spontaneous leaks (FAIL OFF/LEAKS). The number of times a valve is opened or closed provide an indication of the amount of fluid flow which may be related to the contamination failure mechanism. Also, the amount of fluid each valve is subjected to varies substantially from each location. In the past several studies have been done in an attempt to estimate valve reliability. Studies done at Rockwell Aerospace have used cycle time as the casual variable, while studies done at JSC have used soak time as the casual variable. Only one variable was used in both of these studies since standard statistical computer models treat only one variable. In this paper we develop new statistical theory based on both variables. Also, previous studies assume a homogeneous population of components with each component having the same failure rate. However, as various components experience different stresses and are exposed to different environments, their failure rates can change across the population of components. Techniques which ignore the heterogeneity can result in incorrect estimates of failure distributions.

We propose to model the reliability of the thruster valves by treating these valves as a censored repairable system. The system is repairable since valves that either leak or stick are removed, repaired and placed back in operation. Censoring occurs whenever the time-to-failure records are terminated before each valve has had a chance to fail. The model for each valve will take the form of a nonhomogeneous process with the intensity function that is either treated as a proportional hazard model, or a scale change random effects hazard model.

The proportional hazard function model will assume that the time the valve is soaked in the oxidizer prior to failure is the primary variable that describes the base hazard function and that the cycle time, and perhaps other variables, adjust this hazard. The scale change random effects model will also assume that there is a soak-time-hazard function for each valve, but in this case cycle time and other variables will be used to randomly scale the soak time.

Thus for a given $Z=z$, the cumulative hazard function for proportional change and scale change models are given respectively by,

$$H(t / Z=z) = z\,H(t), \quad \text{and} \quad H(t / Z=z) = H(zt),$$

where H(t) is an unobserved cumulative baseline hazard function. Thus each component has an associated z, an independent realization of the random variable Z from a distribution G(z). This unobserved quantity z can be used to describe heterogeneity systematically. This variable z may represent environmental influences on different components, effects of microgravity, effect of location of components on the orbiter, and various other risk factors.

For each of these models methods for estimating the model parameter using censored field data will be developed. The model which appears to best forecast failures of the Orbiter's RCS thruster valves will then be selected as the appropriate model.

To estimate the component life for components on a space vehicle (such as ISSA), one needs to understand the mechanism that cause the failures of the components and component types. Ideally each component with a different vintage should be put on test under environmental and operational conditions identical to those under which it is to be operated, and time to failure be observed. This experiment needs to be repeated a number of times to get a reasonable size statistical sample. However it is not possible to conduct meaningful life tests on earth because of not being able to replicate the proper stress environment and also because of cost. Thus, the only available data on failure of components in microgravity is the field data obtained from previously flown spacecraft's. This data needs to be adjusted because:

1. The available data is from non-renewable systems, i.e., a failed component is not replaced. The failure rate distributions estimated using such data will need to be modified for renewable systems such as ISSA.

2. Previous studies use the field data collected from sixties, seventies and eighties, and conclude that design and environment are the main contributors to failure. Assuming that how to design and knowledge about environment has improved substantially since sixties, this data need to be examined carefully.

MIXTURE MODELS UNDER HETEROGENEITY

It is generally accepted that the lifetime of electronic components can be described by an exponential probability distribution, that is,

$$f(t) = \lambda . e^{-\lambda t}, t \geq 0, \lambda > 0 \qquad (1)$$

where λ is a parameter which is the hazard rate. This model assumes constant failure rate for each component. However, in most cases the failure rate-age characteristic may rise or fall in addition to remaining constant. A probability distribution which can represent any form of failure rate-age curve is the Weibull distribution. The probability density function of this distribution is given by

$$f(t) = \frac{\beta}{\eta}\left(\frac{t}{\eta}\right)^{\beta-1} \cdot e^{-\left(\frac{t}{\eta}\right)^{\beta}} \quad , \quad t \geq 0, \beta, \eta > 0 \qquad (2)$$

Exponential distribution (1) is a special case when $\beta = 1$. The cumulative distribution function, survival function S(t), and hazard function are given respectively by

$$F(t) = 1 - e^{-\left(\frac{t}{\eta}\right)^{\beta}}; S(t) = 1 - F(t); and h(t) = \frac{\beta}{\eta}\left(\frac{t}{\eta}\right)^{\beta-1}$$

These models assume a homogeneous population of components with each component having the same failure rate. However, as various components on the orbiter are exposed to different environments and experience different stresses, their failure rates can change across the population of component types. In this paper we develop proportional and scale change models when the life-time distribution is given by (2). The failure model for each component will take the form of a non-homogeneous process with intensity function that is either treated as a proportional hazard model, or a scale change random effects hazard model.

Proportional Hazard Model

Under this model the lifetime of a component, T, has the cumulative hazard function, $H(t / Z=z) = z H(t)$, where H(t) is an unobserved baseline cumulative hazard function, the same for each component. Each component has an associated z, an independent realization of a r.v. Z from a distribution G(z). This variable z (possibly a vector) can represent environmental influences on different components, effects of microgravity, effects of location on the orbiter, and various other risks factors. This unobserved quantity z can be used to describe heterogeneity systematically.

Case I:

Let $g(z) = \frac{\lambda}{\Gamma(r)}(\lambda.z)^{r-1}e^{-\lambda z}, z \geq 0, \lambda.,.r > 0$, then, (3)

$$\mathbf{S(t) = E_z\, S(t/Z=z)} = \int_0^\infty e^{-\lambda(\frac{t}{\eta})^\beta} \frac{\lambda}{\Gamma(r)}(\lambda \cdot z)^{r-1}e^{-\lambda z}dz$$

$$= \frac{\lambda^r}{\left[\lambda + (\frac{t}{\eta})^\beta\right]^r},$$

and,

$$\mathbf{h(t)} = -\frac{d}{dt}\log S(t) = \frac{r}{\eta}\frac{\beta(\frac{t}{\eta})^{\beta-1}}{\lambda + (\frac{t}{\eta})^\beta} \tag{4}$$

when $t=\eta$, the characteristic life is given by ,

$$h(t) = \frac{r}{\eta}\frac{\beta}{\eta+1}$$

We note from (4) that for given r, $\beta, \eta, \lambda,$, h(t) $\mapsto 0$ as t gets large.

Case II:

Let $g(z) = 1, \; 0 < z < 1.$ (5)

In this case,

$$S(t) = \frac{1-e^{-(\frac{t}{t\eta})^\beta}}{(\frac{t}{\eta})^\beta} \; ; \; \text{and } h(t) = \frac{\beta}{t} - \frac{\beta.(\frac{t}{\eta})^{\beta-1}.e^{-(\frac{t}{\eta})^\beta}}{1-e^{-(\frac{t}{\eta})^\beta}}. \tag{6}$$

We note that h(t)$\mapsto 0$ as t gets large.

Case III: Let g(z) be a 2 -point distribution, i.e.

$$P(Z=z_1) = p \; ; \; P(Z= z_2) = 1-p \tag{7}$$

then,

$$S(t) = p\; e^{-z_1.(t/\eta)^\beta} + (1-p)\,.\, e^{-z_2.(\frac{t}{\eta})^\beta}.$$

The expression for the hazard rate, h(t) , is lenghty, but can be obtained easily. Also, it can be shown that h(t) $\mapsto 0$, as t gets large.

Scale change Hazard Models

Under the scale cahnge hazard model the lifetime, T, has the cumulative hazard function, H(t / Z=z) = H(zt), where H(t) is an unobserved baseline hazard function, the same for all components. In this case,

$$S(t / Z=z) \;=\; e^{-H(zt)} \qquad \text{and} \qquad S(t) \;=\; \int_0^\infty e^{-H(zt)}\, dG(z), \tag{8}$$

Case I:

Let Z has the gamma distribution given by (3), then from (8)

$$S(t) \;=\; \int_0^\infty e^{-z^\beta (\frac{t}{\eta})^\beta} \cdot \tfrac{\lambda}{\Gamma(r)} (\lambda \cdot z)^{r-1} e^{-\lambda z} dz, \quad \text{and } h(t) = -\tfrac{d}{dt} \log S(t) \text{ can be computed and}$$

the resulting integral can be evaluated numerically.

Case II:

Let Z has the Weibull distribution given by (2) with η replaced by δ. In this case,

$$S(t) = \frac{1}{\delta^\beta \left[(\frac{t}{\eta})^\beta + (\frac{1}{\delta})^\beta \right]}, \quad \text{and } \; h(t) = \frac{\frac{\beta}{\eta} (\frac{t}{\eta})^{\beta-1}}{(\frac{t}{\eta})^\beta + (\frac{1}{\delta})^\beta} \tag{9}$$

we note that h(t) $\mapsto$ 0 as t gets large.

Case III:

Let Z has the uniform distribution given by (5). In this case,

$$S(t) \;=\; \int_0^1 e^{-z^\beta (\frac{t}{\eta})^\beta} dz, \; \text{and} \quad h(t) \;=\; \tfrac{1}{t} \left[1 - \frac{e^{-(\frac{t}{\eta})^\beta}}{S(t)} \right]. \tag{10}$$

S(t) needs to be evaluated numerically. It can be shown that h(t) $\mapsto$ 0 as t gets large.

Case IV:

Let Z has the 2-point distribution given by (7). In this case

$$h(t) \;=\; \beta \cdot t^{\beta-1} \left[p {z_1}^\beta e^{-{z_1}^\beta (\frac{t}{\eta})^\beta} + (1-p) {z_2}^\beta e^{-{z_2}^\beta (\frac{t}{\eta})^\beta} \right], \tag{11}$$

Where $z_1 . z_2$ are particular values of Z. It is clear from (11) that h(t) $\rightarrow$ 0 as t gets large.

A Regression Model

Assume that for a given value z of a random variable Z, the regression of logT on log z is linear, that is,

$$\log T = \log a + b \log z + \log \varepsilon \tag{12}$$

where a is a constant. From (12) $T = a\, z^{b} \varepsilon$, $S(t/z) = P(T > t/z) = P(\varepsilon > \frac{t}{a z^{b}} /z)$, and

$$S(t) = \int P(\varepsilon > \tfrac{t}{a \cdot z^{b}}) \cdot g(z) dz, \tag{13}$$

where g(z) is the density of Z. This integral can be evaluated either analytically or numerically depending on the form of the densities of ε and z. Assuming ε has a Weibull (β, η) distribution, the survival function S(t) is given by,

$$S(t) = \int e^{-(\frac{t}{\eta a \cdot z^{b}})^{\beta}} g(z)\, dz = \int e^{-\Psi(z) \cdot H(t)} g(z) dz,$$

where g(z) is the density of z, $\Psi(z)$ is a function of z only, and H(t) does not depend on z. We note that both proportional hazard and scale change hazard models are special cases, when $\Psi(z) = z$, and $\Psi(z) = z^{\beta}$ respectively.

Case 1:

Let $g(z) = \frac{\phi^{\lambda}}{\Gamma(\lambda)} \cdot (\frac{1}{z})^{\lambda+1} e^{-\frac{\phi}{z}}$ (inverted gamma). In this case survival function S(t) is given by

$$S(t) = \frac{\phi^{\lambda}}{\Gamma(\lambda)} \int_{0}^{\infty} e^{-\left[(\frac{t}{a\eta z^{b}})^{\beta} + \frac{\phi}{z}\right]} (\tfrac{1}{z})^{\lambda+1} dz \tag{14}$$

This integral can be evaluated numerically. In a special case when $b\beta = 1$, the expression in (14) can be simplified, that is,

$$S(t) = \left(\frac{\phi \cdot \mu}{t^{\frac{1}{b}} + \phi \cdot \mu \alpha} \right)^{\lambda}$$, where $\mu = (a\eta)^{\frac{1}{b}}$. From this, we get

$$h(t) = \frac{\lambda \cdot t^{\frac{1}{b}-1}}{b(t^{\frac{1}{b}} + \phi \cdot \mu)}, \tag{15}$$

which approaches zero as t gets large

Case II:
If $\log\varepsilon$ is distributed as a $n(0, \sigma^2)$, then ε has the lognormal distribution. In this case,

$$S(t/z) = P(T > t/z) = P(\varepsilon > \tfrac{t}{az^b} / z)$$

$$= 1 - \Phi\left[\tfrac{1}{\sigma}(\log t - \log a - b\log z)\right],$$

where $\Phi(z)$ is the distribution function of the standard normal, and we get

$$S(t) = \int_0^\infty\int_0^\infty \frac{1}{\sqrt{2\pi}\cdot\sigma(x + \log\frac{t}{a\cdot z^b})} e^{-\frac{1}{2\sigma^2}(\log(x+\log\frac{t}{az^b}))^2} g(z) \quad dx\, dz, \qquad (16)$$

where $x = \varepsilon - \log\frac{t}{a\cdot z^b}$. This integral can be computed numerically, and then h(t) can be computed.

Applications to RCS Thruster Valves

As stated in the introduction, previous studies to estimate the reliability of a RCS thruster valve use either cycle time or soak time as the casual variable. It is quite possible that each of these two variables has a substantial effect on the valve contamination mechanism. It is also possible that other factors such as, location of valve on the orbiter, also contribute to failure mechanism. A preliminary analysis using logistic function can be used to decide which of the two independent variables has major effect on the contamination failure mechanism.. Let S denote the Soak time and C denote the cycle time, and define P(s,c) denote the probability of a valve failure for a given S=s and C=c.

The logistic regression model assumes that the log(odds) is a linear function of independent variables. This procedure can be performed as follows:

Step 1.
Use data to fit 3 logistic functions independently:

$$\log(p(s,c) / (1-p(s,c))) = \alpha + \beta s + \phi c \qquad (17)$$

$$\log(p(s) / (1-p(s))) = \alpha + \beta s \qquad (18)$$

$$\log(p(c) / (1-p(c))) = \alpha + \phi c \qquad (19)$$

Step 2
For each model compute the lack of fit statistic G^2 (with corresponding d.f.)
Denote G^2 by G_i^2 for model (16+i), i= 1, 2, 3

Step 3

3a. If G_2^2 gives a good fit, then soak time is important independent variable

3b If G_3^2 gives a good fit, then cycle time is important independent variable

Step 4

4a. To test the hypothesis of 'no cycle time effect'
compute $G_2^2 - G_1^2$ [increase in G^2 in using model (18) instead of (17)]. This difference is asymptotically distributed chi-squared with 1 d.f.

4b. To test for ' no soak time effect' compute $G_3^2 - G_1^2$, again this difference is asymptotically distributed chi-squared with 1 d.f.

Step 5

If both hypotheses in step 4a and 4b are rejected and G_1^2 indicates a good fit, then we conclude that both independent variables are contributing to failure.

For the remainder of this section, let the variable T denote the Soak time and the variable Z denote the cycle time. Various models developed in this report can be used to estimate the reliability of RCS thruster valves. In particular, if T is weibull and z has a gamma distribution, then the hazard rate is given by equation (4).

As mentioned before, with the advent of extended EVA's and docking, a growing interest in the field performance of RCS thruster valves has developed. The reliability and safety requirements for the space shuttle program, have emphasized the need for adequate statistical methods for obtaining reliable safety guarantees. To achieve this objective, we need reliable sample data from various RCS thruster valves systems. Available field failure data on these valves is from a number of individual systems, each characterized by a serial number. The system may be put into, or taken out of, operation at different times. For each thruster valve, its (censored) life history which contains the following information is available:

- The time when the valve was put into operation.
- The location of the valve on the orbiter.
- New or flushed valve
- The time when the valve failed.
- The time periods when the system was temporarily put out of operation (down periods).

The location information is necessary if the objective is to find a location (or locations) on the orbiter where valves are more likely to fail.

The Maximum Likelihood procedure is a powerful method of estimating parameters in statistics. However, due to censoring, the likelihood function in this case will include:

a. a set of lifetime observations

$$T_1, T_2, T_3, - - -, T_{N1}$$

for those valves which have been replaced after failing; and

b. a set of right censored observations

$$T_1^*, T_2^*, T_3^*, - - - , T_{N2}^*$$

for the valves that survived the flight time. Then the estimation is equivalent to fitting the parameters to the mixture distribution, so that the estimate $\theta = (\beta, \eta, \lambda, \gamma)$ is obtained as the value of θ that maximizes the log - likelihood expression

$$L(\theta) = \sum_{j=1}^{N1} \log f(T_j) + \sum_{i=1}^{N2} \log\left[1 - F(T_i^*)\right].$$

In this case $L(\theta)$ is quite complicated because of two types of observations (T_i's and T_i^*'s), and excessive number of parameters in the model. This is an interesting problem. I plan to continue working on this problem and try to complete the problem during summer 96.

References

1. Anderson, J.E. and Louis, T.A., (1995), "Survival Analysis Using a Scale Change random Effects Model," Journal of American Statistical Association, 90, 669-679.

2. Anderson, J.E., Louis, T.A., Holm, N.V., and Harvald, B. (1992), "Time-Dependent Association Measured for Bivariate Survival Distributions," Journal of the American Statistical Association, 87, 641-650.

3. Barlow, R.E., and Proschan, F. (1975), Statistical Theory of Reliability and Life Testing : Probability Models, New York : Holt, Rinehart and Winston.

4. Carter, A.D.S. (1986), Mechanical Reliability, New York: John Wiley & Sons.

5. Cox, D.R. (1977), Analysis of Survival Data, London : Chapman & Hall.

6. Dalal, S.R., Fowlkes, E.B., and Hoadley, B., (1989), " Risk Analysis of the Space Shuttle: Pre-Challenger Prediction of Failure," Journal of the American Statistical Association, 84, 945 -957.

7. Heydorn, R.P., Blumentritt, W., Doran, L., and Graber, R., (1991), " A Model for Projecting Early Failures on Space Station Freedom", NASA/JSC internal report.

8. Heydorn, R.P. (1995), "Some Connections between Random Failure Rates and Early Failure," NASA/JSC preliminary internal report.

9. Martz, H.F. and Waller, R.A. (1982), Bayesian Reliability Analysis, New York: John Wiley & Sons.

10. Oakes, D. (1989), "Bivariate Survival Models induced by Frailties," Journal of The American Statistical Association, 84, 487-493.

11. Vaupel, J.W., Yashin, A.I. (1985), 'Heterogeneity's Ruses : Some Surprising Effects of Selection on Population Dynamics," The American Statistician, 39, 176-185.

AN OPTIMAL USER-INTERFACE FOR EPIMS DATABASE CONVERSIONS AND SSQ 25002 EEE PARTS SCREENING

Final Report
NASA/ASEE Summer Faculty Fellowship Program--1995
Johnson Space Center

Prepared By:	John C. Watson, Ph.D.
Academic Rank:	Visiting Assistant Professor
University and Department	University of Houston College of Technology Electrical-Electronics Tech. Dept. Houston, Texas 77204
NASA/JSC	
Directorate:	International Space Station Program Office
Division:	Vehicle Office
Branch:	Vehicle Effectiveness Branch
JSC Colleague:	Pat Pilola
Date Submitted:	August 15, 1995
Contract Number:	NGT-44-001-800

ABSTRACT

The Electrical, Electronic, and Electromechanical (EEE) Parts Information Management System (EPIMS) database was selected by the International Space Station Parts Control Board for providing parts information to NASA managers and contractors. Parts data is transferred to the EPIMS database by converting parts list data to the EPIMS Data Exchange File Format. In general, parts list information received from contractors and suppliers does not convert directly into the EPIMS Data Exchange File Format. Often parts lists use different variable and record field assignments. Many of the EPIMS variables are not defined in the parts lists received. The objective of this work was to develop an automated system for translating parts lists into the EPIMS Data Exchange File Format for upload into the EPIMS database. Once EEE parts information has been transferred to the EPIMS database it is necessary to screen parts data in accordance with the provisions of the SSQ 25002 Supplemental List of Qualified Electrical, Electronic, and Electromechanical Parts, Manufacturers, and Laboratories (QEPM&L). The SSQ 25002 standards are used to identify parts which satisfy the requirements for spacecraft applications. An additional objective for this work was to develop an automated system which would screen EEE parts information against the SSQ 25002 to inform managers of the qualification status of parts used in spacecraft applications. The EPIMS Database Conversion and SSQ25002 User Interfaces are designed to interface through the World-Wide-Web (WWW)/Internet to provide accessibility by NASA managers and contractors.

INTRODUCTION

Historically, NASA was able to acquire quality electrical, electronic, and electromechanical (EEE) parts through the military supply system. As defense contractors have reduced in number, it is becoming increasingly more difficult to identify parts suppliers which can provide parts which satisfy the performance specifications required for spacecraft applications. NASA has been forced to perform considerable parts screening in-house. The EEE Parts Information Management System (EPIMS) database provides an on-line system which NASA managers and contractors can use to screen parts used in spacecraft design. However, it has been difficult uploading parts list information into the EPIMS database since most parts lists maintained by suppliers and contractors do not conform to the requirements of the EPIMS Data File Exchange Format.

EPIMS DATABASE CONVERSION SYSTEM

The EPIMS database contains 79 unique variables which describe EEE parts. The purpose of the EPIMS Database Conversion System is to map information from a parts list into the EPIMS variables. In most cases, not all 79 variables will be assigned values for each part. However, the EPIMS Database Conversion System must provide the capability to accommodate all EPIMS variables when performing a parts list to EPIMS Data Exchange File Format conversion. A major challenge in developing an automated system for performing the parts list to EPIMS database conversions was correctly translating each EPIMS variable with the parts list field which most accurately describes the corresponding data. The first attempt at developing the EPIMS database translator was to select the assignments for each EPIMS variable based on the supplier or contractor which submitted the parts list. The flaw in this technique is that an incorrect assignment for an EPIMS variable could not be adjusted without modifying the conversion table for the specific supplier or contractor. It was decided that the parts list to EPIMS conversion mapping must be dynamic to support flexible changes to EPIMS variable assignments. The intent was to enable the user to easily modify EPIMS variable assignments without modifying the software interface which supports the conversion. The EPIMS variable assignments for each supplier and contractor were made accessible through an HTML form which can be viewed and modified on the World Wide Web (WWW). If an observer sees an error in the assignment of EPIMS variables for their respective parts list, variable assignments may be modified through the HTML form. An example WWW form used for translating parts lists into the EPIMS Data File Exchange Format has been included in Figure 1. Each entry in the form can accommodate any one of the 79 unique EPIMS variables supported in the EPIMS database. After the user views the EPIMS variable assignments for their parts list and corrects any entries, the form is submitted for EPIMS conversion. The final product will be the EPIMS Data Exchange Files required for upload into the EPIMS database. For security reasons, a user may not transfer parts list data without owning a valid account number and password. An HTML hotlink is provided to enable the user to log on to perform the transfer of parts data.

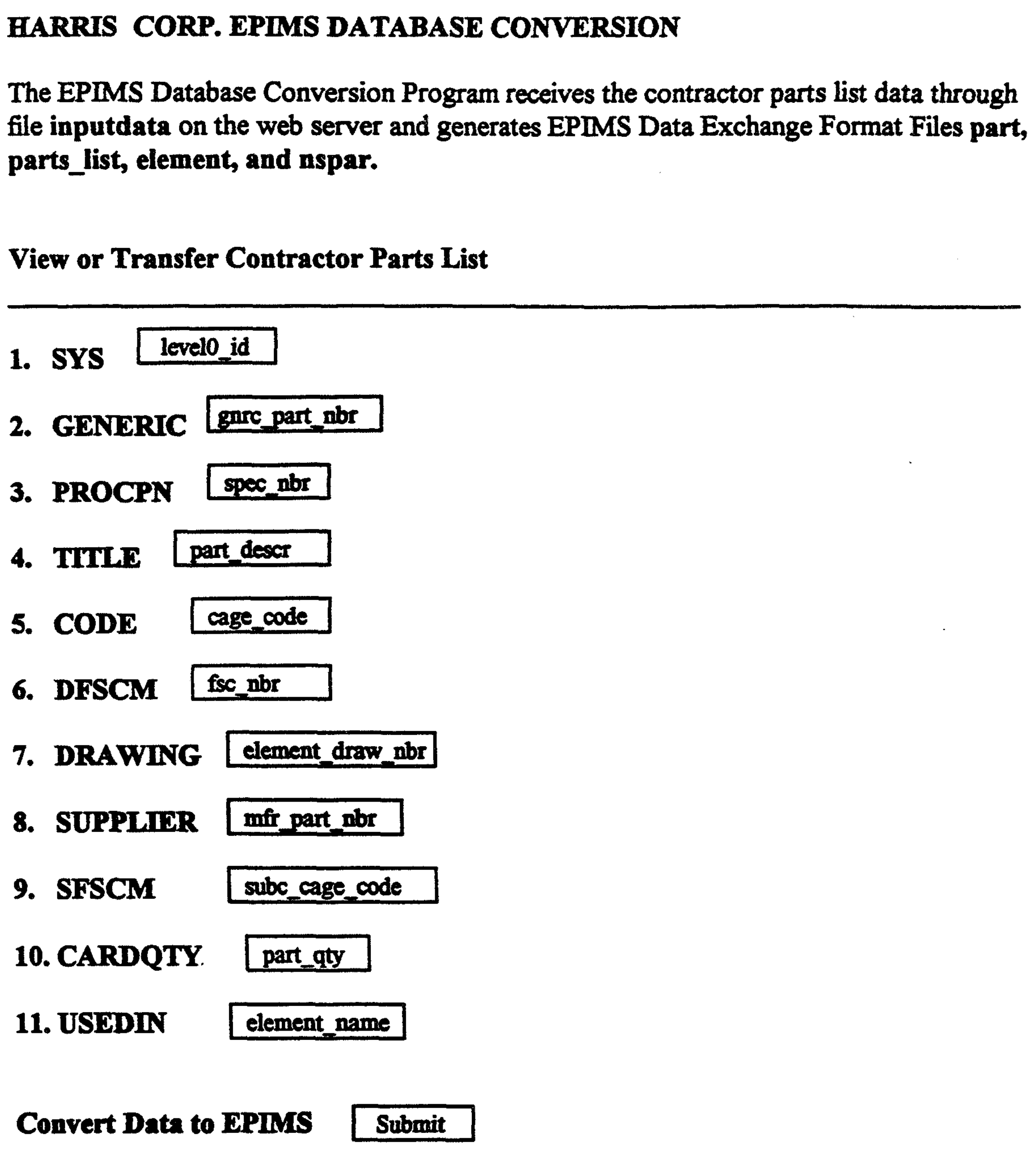

HARRIS CORP. EPIMS DATABASE CONVERSION

The EPIMS Database Conversion Program receives the contractor parts list data through file **inputdata** on the web server and generates EPIMS Data Exchange Format Files **part, parts_list, element, and nspar.**

View or Transfer Contractor Parts List

---

1. **SYS** level0_id
2. **GENERIC** gnrc_part_nbr
3. **PROCPN** spec_nbr
4. **TITLE** part_descr
5. **CODE** cage_code
6. **DFSCM** fsc_nbr
7. **DRAWING** element_draw_nbr
8. **SUPPLIER** mfr_part_nbr
9. **SFSCM** subc_cage_code
10. **CARDQTY** part_qty
11. **USEDIN** element_name

Convert Data to EPIMS Submit

Figure 1. Example of HTML Form for Converting Parts List Data to EPIMS

The most complex task of the EPIMS Database Conversion System development was creating the UNIX Bourne shell script required to process the entries received from each WWW form. The form processing software was written in UNIX Bourne shell script since this could be activated through the web server. The forms processor receives each entry from the form and creates an awk program that will map the parts list data to the desired variable fields for the EPIMS Data File Exchange Format files. Once the awk program has been created which satisfies the desired EPIMS variable assignments submitted by the user, the awk code will process the parts list data to create the required EPIMS Data File Exchange Format files used for upload of parts list data into the EPIMS database. The flowchart shown in Figure 2 describes the logic used to perform the mapping of EPIMS variables to the parts list data. The forms processor sequences through each EPIMS variable required to generate the EPIMS Data Exchange Files **part, parts_list, element,** and **nspar.** The Variable (*k*) shown in Figure 2 refers to each variable included in the contractor parts list data file containing *n* variables (column headers). The number of variables will vary with the particular contractor submitting parts list data to EPIMS. Each variable assignment received through the HTML form will be compared to each EPIMS variable used in the creation of the EPIMS Data Exchange Files. If a match is found, an awk code statement is created which will transfer the corresponding field of the contractor's parts list to the required field in the EPIMS Data Exchange File. The EPIMS variables *pl_number, version, ... reviewer_userid* shown in Figure 2 represent a sample of the 96 entries used to create the EPIMS Data Exchange Files. Although there are 79 unique EPIMS variables, some of these are repeated in the EPIMS Data Exchange Files.

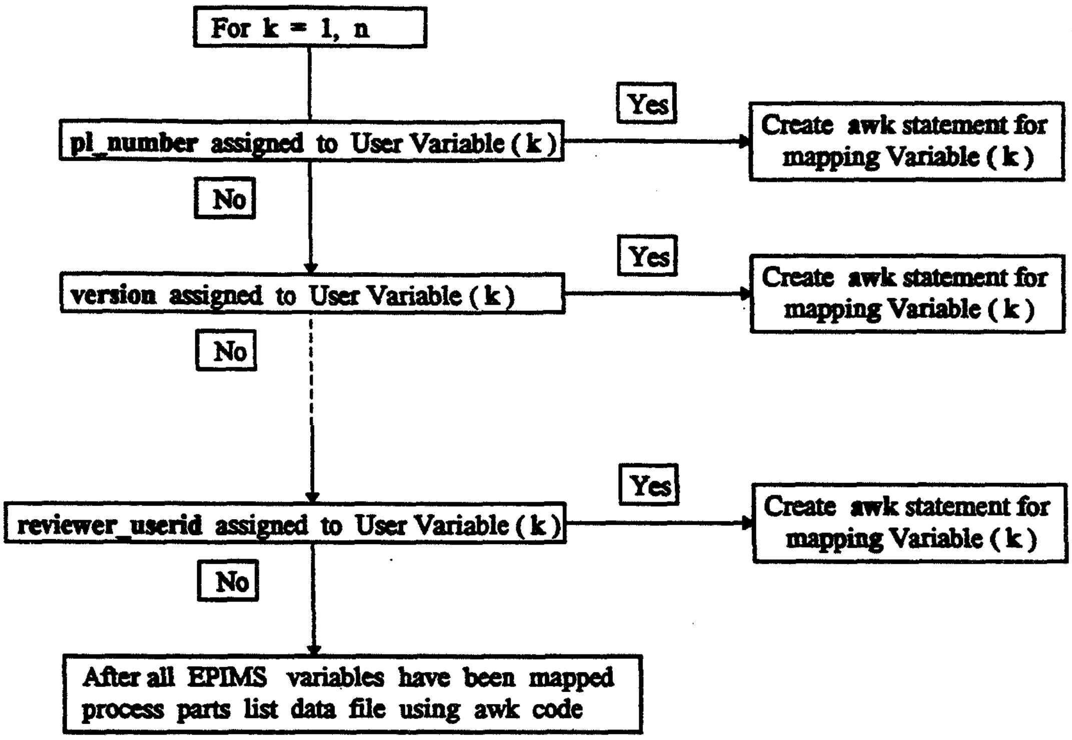

Figure 2. Flowchart for Performing EPIMS Variable Conversions

GENERIC EPIMS DATABASE CONVERSION FORM

Although HTML forms were created to accommodate current EEE parts suppliers and contractors, it would be desirable to create a Generic EPIMS Database Conversion Form which could be configured to translate parts list data from other parts list formats which may be submitted to NASA. The Generic EPIMS Database Conversion Form shown in Figure 3 lists all 79 EPIMS variables. The user indicates the appropriate column number which maps with the corresponding EPIMS variable. The forms processor for the Generic EPIMS Database Conversion Form generates the required awk code to map the field number of the submitted parts list with its corresponding EPIMS variable. The awk code then generates the EPIMS Data Exchange Files using data from the submitted parts list.

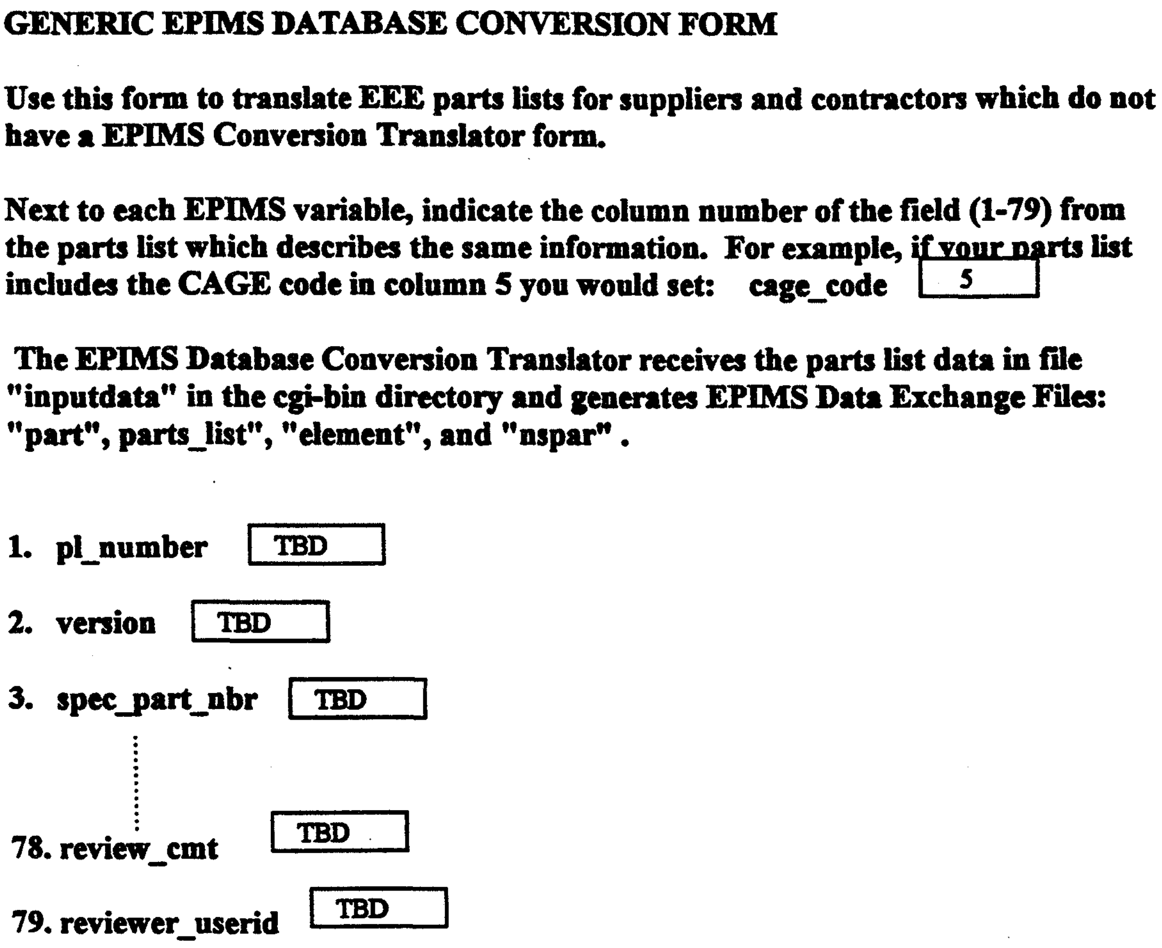

GENERIC EPIMS DATABASE CONVERSION FORM

Use this form to translate EEE parts lists for suppliers and contractors which do not have a EPIMS Conversion Translator form.

Next to each EPIMS variable, indicate the column number of the field (1-79) from the parts list which describes the same information. For example, if your parts list includes the CAGE code in column 5 you would set: cage_code 5

The EPIMS Database Conversion Translator receives the parts list data in file "inputdata" in the cgi-bin directory and generates EPIMS Data Exchange Files: "part", parts_list", "element", and "nspar".

1. pl_number TBD

2. version TBD

3. spec_part_nbr TBD

⋮

78. review_cmt TBD

79. reviewer_userid TBD

Figure 3. Generic EPIMS Database Conversion Form

SSQ 25002 EEE PARTS SCREENING

The SSQ 25002 Supplemental List of Qualified Electrical, Electronic, and Electromechanical (EEE) Parts, Manufacturers, and Laboratories (QEPM&L) is used to qualify EEE parts for spacecraft design. The SSQ 25002 includes appendices which identify the qualification status of EEE parts, manufacturers, and laboratories. The current version of SSQ 25002 contains the appendices listed in Table 1.

Appendix	Description
A	Type I SSQ Parts - Qualified
B	Type II SSQ Parts - Qualifications Pending
C	Type III SSQ Parts - Obsolete/Canceled
D	Type I Nonstandard Parts - Qualified
E	Type II Nonstandard Parts - Qualifications Pending
F	Type III Nonstandard Parts - Obsolete/Canceled
G	Type I Manufacturers - Qualified
H	Type II Manufacturers - Qualifications Pending
I	Type III Manufacturers - Disapproved
J	Type I Laboratories - Qualified
K	Type II Laboratories - Qualifications Pending
L	Type III Laboratories - Disapproved
M	List of Cage Codes

Table 1. SSQ 25002 Appendices Used for Screening EEE Parts

It is not uncommon for a parts list to contain thousands of parts so it would be preferable to automate parts list screening to identify parts which require investigation concerning their suitability for spacecraft design. It is especially important to identify EEE parts which are disqualified for use in spacecraft design applications. The SSQ 25002 EEE Parts Screening program was developed to automate the process of screening EEE parts lists. The EEE parts are screened by comparing each part number against the list of qualified, qualifications pending, and obsolete/canceled parts contained in appendices A through F. Should a part number match a part number listed in appendices A through F, information about the screened EEE part will be written in its respective display list which can be observed through the web browser. Each appendix listed in Table 1 has a corresponding parts list in the web browser for observation by the user. Each part is also screened by cage code to verify the qualification status of the manufacturer or laboratory which created the part. The flowchart shown in Figure 3 describes the SSQ 25002 EEE Parts Screening procedure for identifying parts which are placed in files QUAL_SSQ, PEND_SSQ, DISQUAL_SSQ, QUAL_NSTD, PEND_NSTD, and DISQUAL_NSTD for observation on the web browser.

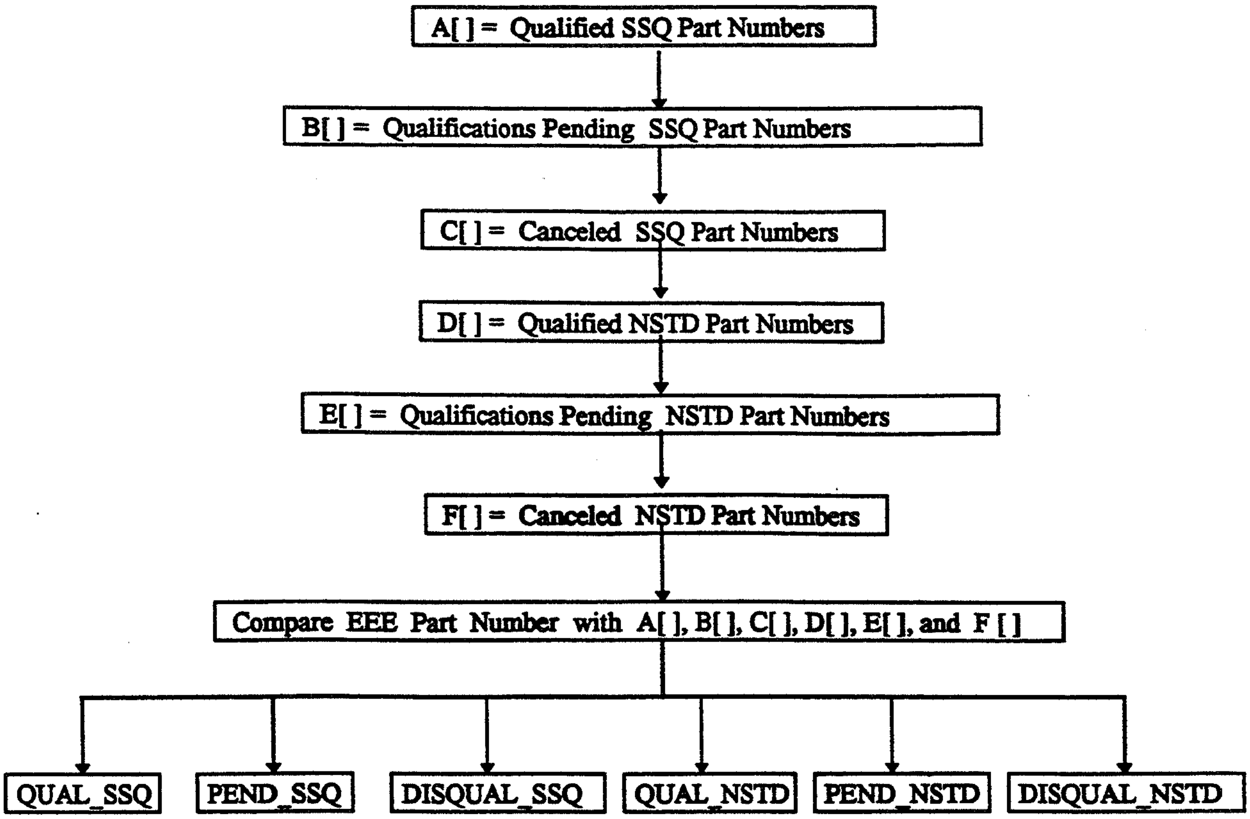

Figure 4. Flowchart for Screening EEE Parts by Part Number

Manufacturers and laboratories who develop EEE parts for spacecraft design are inspected to ensure parts are fabricated in accordance with design specifications. Each part record includes a CAGE code which identifies the manufacturer or laboratory that created the part. The SSQ 25002 EEE Parts Screening Program implements the flowchart shown in Figure 5 in which the CAGE code from each part in the submitted parts list is compared with the CAGE codes listed in appendices G through M. These appendices identify qualified, qualifications pending, and disqualified manufacturers and laboratories as well as valid and invalid CAGE codes. The SSQ 25002 EEE Parts Screening Program identifies parts produced by manufacturers and laboratories which have a Type I, Type II, or Type III qualification status and displays this information on files QUAL_MFGR, PENS_MFGR, DISQUAL_MFGR, QUAL_LAB, PEND_LAB, and DISQUAL_LAB for observation through the web browser. Parts which do not have a valid CAGE code are displayed in file UNLISTED_CAGE. It is essential that the user takes note of any parts which have been supplied by disqualified manufacturer or laboratory since these parts are not suitable for spacecraft applications.

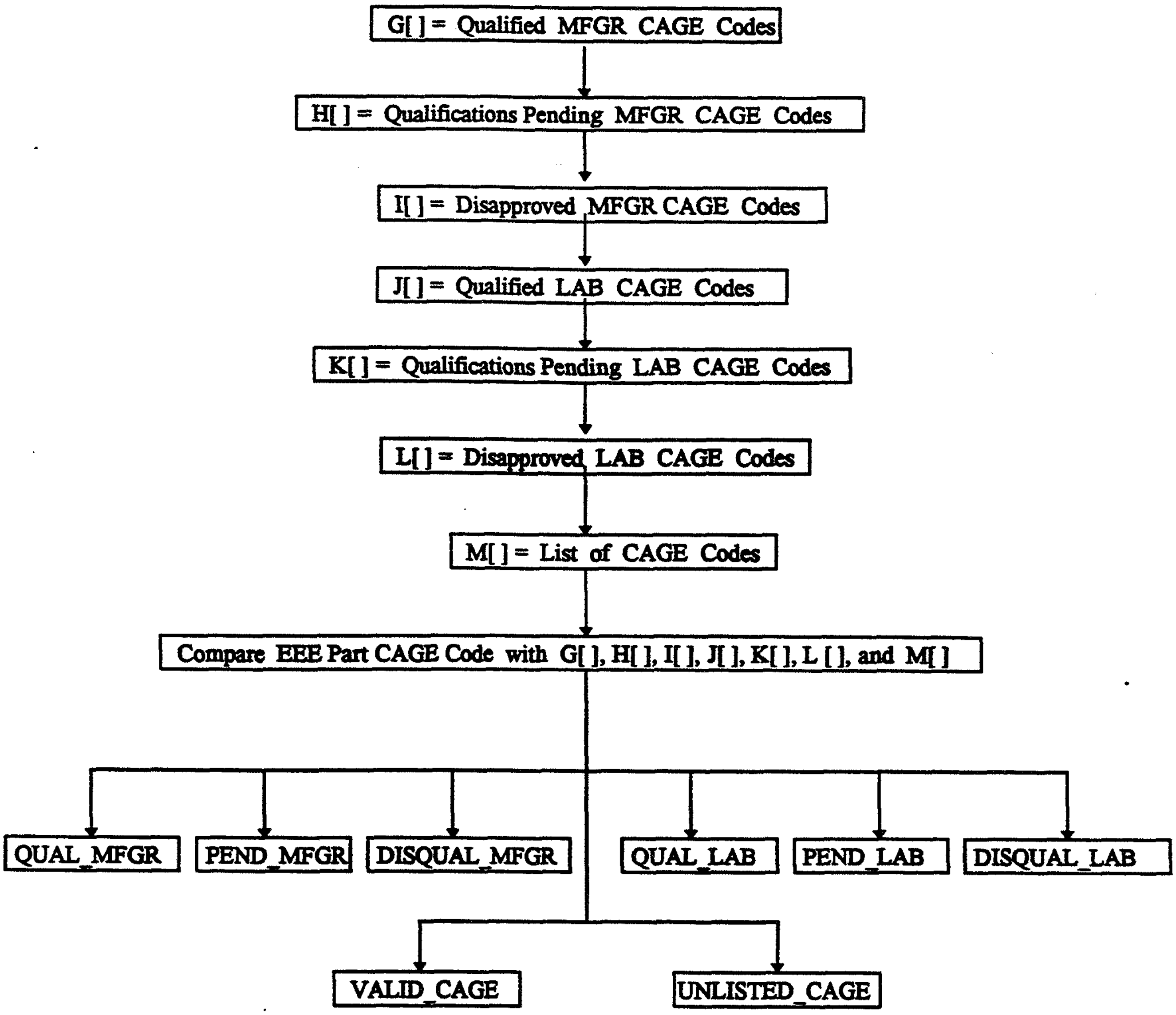

Figure 5. Flowchart for Screening EEE Parts by Cage Code

UPDATING SSQ 25002 APPENDICES

The information contained in the SSQ 25002 appendices must be updated whenever the qualification status of a EEE part, manufacturer, or laboratory changes. The SSQ 25002 appendices used in the screening program were acquired from downloading MS Excel Worksheets using the text format in files apxA_data through apxM_data on the UNIX fileserver. The capability of adding information for each of these appendices has been implemented on respective HTML forms which access data from each appendix. However, for security reasons, it may not be advisable to incorporate the update feature through the web server.

CONCLUSIONS

The primary objective for the EPIMS Database Conversion and SSQ 25002 EEE Parts Screening systems is to simplify the task of uploading parts information to the EPIMS database and screening parts for qualification for spacecraft design applications. The WWW/Internet provides accessibility of EEE parts information as well as flexibility in modifying EPIMS variable assignments for submitted parts lists. However, classified information, such as the qualification status of laboratories and manufacturers must be restricted to authorized viewers. A major challenge in developing EEE parts data processing systems is maintaining the desired security of information while simplifying the user interface. The general approach used in the development of the EPIMS Database Conversion and SSQ 25002 EEE Parts Screening systems was to establish designated files on the web server for processing EEE parts data but restricting file transfers to authorized users.

SUPPORT OF GAS FLOWMETER UPGRADE FINAL SUMMER FACULTY FELLOWSHIP REPORT

Final Report
NASA/ASEE Summer Faculty Fellowship Program--1995
Johnson Space Center White Sands Test Facility

512-35
76325
16P.
254360

Prepared By:	Dennis Waugaman
Academic Rank:	Associate Professor
Texas A&M University	Department of Engineering Technology College Station, TX 77843-3367
NASA/JSC	
Directorate:	White Sands Test Facility
Division:	Engineering Offices (RC)
Branch:	Not Applicable
JSC Colleague:	Mike Kirsch
Contract Number:	NGT-44-001-800

ABSTRACT

A project history review, literature review, and vendor search were conducted to identify a flowmeter that would improve the accuracy of gaseous flow measurements in the White Sands Test Facility (WSTF) Calibration Laboratory and the Hydrogen High Flow Facility. Both facilities currently use sonic flow nozzles to measure flowrates. The flow nozzle pressure drops combined with corresponding pressure and temperature measurements have been estimated to produce uncertainties in flowrate measurements of 2 to 5 percent. This study investigated the state of flowmeter technology to make recommendations that would reduce those uncertainties.

Most flowmeters measure velocity and volume, therefore mass flow measurement must be calculated based on additional pressures and temperature measurement which contribute to the error. The two exceptions are thermal dispersion meters and Coriolis mass flowmeters. The thermal dispersion meters are accurate to 1 to 5 percent. The Coriolis meters are significantly more accurate, at least for liquids. For gases, there is evidence they may be accurate to within 0.5 percent or better of the flowrate, but there may be limitations due to inappropriate velocity, pressure, Mach number and vibration disturbances.

In this report, a comparison of flowmeters is presented. Candidate Coriolis meters and a methodology to qualify the meter with tests both at WSTF and Southwest Research Institute are recommended and outlined.

INTRODUCTION

The NASA Johnson Space Center White Sands Test Facility (WSTF) currently conducts hydrogen and oxygen flow-rate measurements for the shuttle flow control valves (FCV's). Recent estimates have shown that these measurements have an uncertainty level of 2 to 5 percent, a level inadequate for certifying new FCV designs associated with using lightweight shuttle tanks. The new FCV's require flow measurements be performed to an uncertainty level of less than 1 percent. Currently, no facility is capable of qualifying the new shuttle FCV's without the use of costly gravimetric calibrations for hydrogen. A WSTF Center Director's Discretionary Fund (CDDF) project objective is to select an affordable flowmeter and method for testing the new FCV design.

In addition, the less accurate sonic-flow nozzles used for other calibrations in the WSTF Calibration Lab could be replaced by a Coriolis mass flowmeter (CMF) or calibrated on site using the CMF.

This CDDF project has an FY95 objective to complete a literature search and select a methodology for calibrating sonic gas flow meters. This Summer, this faculty fellow provided:

1. A review of the past work performed at WSTF on Coriolis gas meter testing
2. A literature review and summary
3. Communication with vendors to locate candidate flow meters
4. Identification of candidate Coriolis meters for testing in the WSTF High Flow Facility
5. Coordination of plans to test a candidate meter at Southwest Research Institute (SwRI) in San Antonio
6. A recommendation of relevant flow parameters to include in the test matrices for SwRI, the WSTF hydrogen test facility and the WSTF Flow Calibration Laboratory in the form of a preliminary test matrix. This is necessary to correlate the tests using different gases.
7. An extension of this Summer Faculty Fellowship project is being funded by the Center Director Discretionary Fund project. Its goals are to complete the test matrices, tour the SwRI's flow test facility and continue the search for applicable meters and testing facilities and literature.

REVIEW OF PAST WORK ON THE WSTF CORIOLIS FLOWMETER STUDY

Brandon Gabel's 1992 "A Study of the Use of a Coriolis Mass Flowmeter as a Gas Calibration Standard Calibrated in Liquid" (Gabel, 1992)

The WSTF Flow Calibration Laboratory has an EG&G liquid flowmeter, a Cox sonic gas nozzle flowmeter, and a Brooks Bell Prover gas flow measuring device. WSTF tested an ABB K-Flow model K-20 Coriolis flowmeter using these three available flow measuring devices. The goal was to test the Coriolis meter against other WSTF meters and evaluate the potential for the Coriolis meter as a calibration device for the Cox sonic meter and possibly other gas flow meters.

The K-20 meter was tested first against the Cox nozzle using GN_2 at 7 to 75 g/s. Nearly all the data points landed outside the ABB Company specifications for their Coriolis meter, but mostly remained within the Cox nozzle error bands. This is not surprising, since the uncertainty in the Cox system is about 1% and the specifications on the K-20 show accuracy of about 0.6 to 0.2 % in the tested range. No relevant conclusions regarding the Coriolis meter were made from this set of data, although the meters showed better agreement at the higher mass flow rates (45 to 75 g/s) than at the lower end of the scale.

Next, the Coriolis meter was compared to the Bell Prover, which is only capable of low flows (< 7 g/s). Again, all the data was outside the ABB company error specified accuracy. For instance, the specifications show an error of about 1% at 7 g/s, but the test showed 2 to 4% error.

Finally, the Coriolis meter was used with liquid water and compared to the EG&G calibration system. Only for the higher flow range (over 60 g/s) was the data within the ABB Company specified accuracy. Below 60 g/s, most of the data was outside the specified accuracy.

The conclusion was that the meter did not perform as specified in low liquid or low gas flow. The accuracy at higher flows could not be determined with available WSTF measuring devices. It was not proven that the meter does not give the same readings in liquid as it does in gas. However, it was also not proven that the Coriolis flowmeter could be calibrated in liquid and then used as a calibration standard in gas.

SUMMARY OF THE LITERATURE REVIEW

Genesi (April, 1991) focused on orifice-plate, segmental-wedge, venturi flow-nozzle, V-cone, target, and oscillating-vane flowmeters. In the following month (Genesi, May, 1991), he covered variable-area, vortex-shedding, magnetic, turbine, ultrasonic, Coriolis, and thermal-dispersion meters. Table 1 is a brief summary of his meter descriptions.

The Coriolis mass flowmeter consists of one or more tubes that are vibrated at a natural resonance frequency by electromagnetic drivers. Their harmonic vibrations impart Coriolis (angular) forces proportional to the product of fluid density and velocity that act against the wall. This results in a secondary movement that is superimposed on the primary vibration, which varies proportionally with mass flowrate. A sensor measures the phase difference between inlet and outlet caused by the magnitude of this secondary vibration. They supposedly are capable of an accuracy to 0.2% of the flowrate.

The Direct Measurement Corp. (DMC) has developed a Coriolis mass flowmeter that vibrates in the radial mode (Hahn, 1994). The flow path is a single straight tube with no intrusive elements. The vibration is induced at the center of the length and flattens the tube by about one thousandth of an inch. As fluid flows through, the combination of the fluid velocity relative to the tube and the rotational component of the vibration creates a Coriolis acceleration of the fluid. The reaction forces in the tube cause the tube to distort differently than the no-flow distortion. The difference in tube distortion is a measure of the flowrate. According to the company, the vibrational frequency (2000 Hz and above) is higher than most other Coriolis meters use and also higher than most noise vibration that may be produced by other flow effects, such as sonic nozzles in the line. The meter was designed specifically for gas metering. There will be a distinct advantage over other Coriolis meters that have been shown to lose accuracy because of noise and/or high velocity in gas.

TABLE 1.-FLOWMETER COMPARISON

Meter Type	Fluid Type	Accuracy (%)	Comments
Square Edge Orifice	Gas or Liquid	0.5 to 3 by volume	Edge and tap wear
Segment Wedge	Gas or Liquid	0.5 to 5 by volume	Good stability
Venturi Tube	Gas or Liquid	0.5 to 1.5 by volume	Good stability
Flow Nozzle	Gas or Liquid	1 to 2 by volume	Good stability
V-Cone	Gas or Liquid	0.5 to 2 by volume	Good stability
Oscillating Vane	Liquid	0.5 by volume	Sensor replacement
Target	Gas or Liquid	0.5 to 2 by volume	Wear
Variable Area	Gas or Liquid	0.5 to 5 by volume	Good stability
Vortex	Gas or Liquid	0.5 to 1.5 by volume	Corrosion, Erosion , & Reynolds no. limit
Ultra-sound Doppler	Liquid with Suspended Solids	1 to 5 by volume	Installation sensitivity
Ultra- sound Transit Time	Gas or Liquid	1 to 5 by volume	Installation sensitivity
Thermal Dispersion	Gas	1 to 5 by mass	Sensor buildup sensitivity
Magnetic	Liquid	0.2 to 1 by volume	Good stability
Turbine	Gas or Liquid	0.1 to 1 by volume	Bearing wear, viscosity, and installation sensitive
Coriolis	Liquid or Limited Gas Use	0.2 to 2 by mass	Re-zero for various fluids, one vendor for gas

Vogtlin and Txchabold (1994) gives a simple and clear explanation of Coriolis force and the principle applied to straight tube flowmeters. They also explain signal processing using photodiodes to measure change in frequency where the phase shift is proportional to mass flow. The drifts in the transmitters, receivers and amplifiers and are checked automatically at set intervals.

Vogtlin gives an interesting example of Coriolis forces: rivers flowing north to south exhibit heavier erosion on their western shores if in northern hemisphere and eastern shores if in southern hemisphere. Note in the northern hemisphere, the Coriolis acceleration of the river is toward the east but the corresponding reaction force (acting on shore) would be on west shore. They also derive the $F_{coriolis} = 2m\omega v$ based on two people standing on a rotating disk and one moving toward the other. Even though one moves through the original distance toward the other, the distance has changed because the innermost person on the disk does not move far as the outermos person in the tangential direction. This tangential distance requires a Coriolis acceleration to cover it in the required time to reach the radial distance.

Keita (1994) emphasized that Coriolis meters can be unduly influenced by fluid properties and process parameters. The linear approximation of the meter response as a function of the fluid velocity, legitimate for a liquid, remains to be ascertained for a gas. Like most mechanical systems, CMF's are truly non-linear. The meter sensitivity and resonance frequency can suffer from non-linear effects because of the stress induced by a process parameter, such as the line pressure. A list of the process parameters to consider in a liquid to gas comparison:

1. Temperature effect: elastic properties and thermal expansion render temperature correction necessary. All CMFs contain a temperature sensor and the correction algorithm is implemented in the instrument's software.
2. Pressure effect is due to the stress stiffening of the mechanical oscillator. Generally the manufacturers neglect this and no correction is applied. However, with gas under high pressure it must be accounted for. Fortunately, with straight pipe design, a theoretical estimate can be made.
3. The fluid velocity effect is a true non-linearity of the sensor. This is computable in a straight-pipe design.
4. It is common practice to calibrate a CMF with water. However, it is believed that for a gas the sound velocity or compressibility effect could be significant, as has been found for the vibrating element gas densitometer.

Keita concluded the following:

1. The main contribution to the shift in the meter factors is due to the pressure.
2. The compressibility effect can be smaller than the experimental uncertainty for a high-frequency CMF if the pipe diameter is small enough.
3. The pressure effect and compressibility effect partly compensate for each other.
4. Despite their high resonance frequency, straight pipe CMF's are suitable for gas measurement, and their behavior is predictable.

Carpron (1994) reported on tests that were performed at the Colorado Engineering Experiment Station, Inc. (CEESI) to compare discharge coefficients for ***sonic flow nozzles*** in ***GH_2*** to ***air***. Two systems were used to measure flowrates of air. One was a direct gravimetric scale reading (Primary B); the other was a volume-pressure-temperature calculation (Primary C) for mass of air. The GH_2 was only measured with the Primary C system. All three correlated mostly within their 95% confidence interval. The most deviation appeared to be for GH_2 at low and high Reynolds numbers.

Blickley (1990) focused on the shapes and specialty designs of Coriolis flowmeters to reduce the effects of fatigue stress in the meter tubes. Torsional twisting of the meter tube does not create localized high concentrations of stress that can result from pure bending. Instead, it distributes the stress along the whole length of tube. The effects of pipe vibration on the readings can be reduced by operating at higher oscillation frequencies (700-1100 Hz Vs 40-120 Hz) according to the Endress & Hauser, Inc., located in Greenwood, Indiana.

Babb (1992) reported that Exac Corporation had an SX series flowmeter that costs about the same as a good volumetric meter. The company surveyed customers and found most flow applications require about 0.5% accuracy. Exac Corporation has since merged with Micro Motion, Inc. and all their meters are sold under the Micro Motion name.

TESTING FACILITIES

The Institute of Gas Technology

The Institute of Gas Technology (IGT) has a multi-purpose meter testing facility capable of testing metering technologies for high flow rate and high-pressure natural gas applications (Rowley, et al). The testing and facility is supported by a consortium of utilities under IGT's Sustaining Membership Program (SMP). Meters are being evaluated that could, potentially, be applied to natural gas vehicles (NGV) at fueling station operating conditions. Two Coriolis meters have been evaluated:

1. The Micro Motion Model DH025S which is commonly used in NGV dispensing
2. The Micro Motion Model DH038S which has a higher flow capacity and is a modification of the DH025S.

The test facility consists of piping, control components and storage vessels mounted on a high-precision scale. The test loop is configured with two high-pressure storage vessels rated at 3600 psig and volume of 7 cu. ft. The loop is designed to accommodate flow rates up to 1700 scfm at 3000 psig. Before the test begins, the test stand piping on the scale is pressurized to the equilibrium pressure, and the scale is tared. The gas flow is directed through the meter and into high-pressure storage vessels mounted on the precision balance.

Micro Motion DH025S test results:
This meter was tested at 3000 psig and flow rates from 15 lb/min to 40 lb/min (875 scfm of NG). The meter was very unstable at flow rates over 25 lb/min but was very stable at flow rates of 23 lb/min and below. It appears to be have uncertainty of less than 0.3% at 23 lb/min and lower, but at 33 lb/min the uncertainty jumped to nearly 15% even though the meter is rated for as much as 40 lb/min.

Micro Motion DH038S test results:
Micro Motion developed a larger meter which has a 0 to 50 lbs/min and 5200 psig pressure capability. Tests were conducted at various line pressures and flow rates. The threshold flow rate at each pressure was determined based on the flow output stability from the meter and the overall error of the meter total compared with the high-precision scale. In general, the pattern of performance was similar to that of the DH025S.

In addressing the high flow rate problem, Micro Motion said the test results identified gas flow effects that disturb meter performance above some threshold flow rate. They determined that the threshold flow rate is closely related to gas velocity. Therefore, higher gas flow rates need to be measured at higher pressures. Note that the higher pressure increases the density, resulting in a corresponding decreased velocity.

IGT is currently expanding its facility to handle higher pressures and flow rates. The program has been accelerated by a recently awarded contract from the Gas Research Institute (GRI).

Chris Blazek, of IGT, said they have an 8000 cu ft scale for gravimetric analysis (about 3000 lbs). They can add 200 to 300 lbs N_2 gas. It can measure to 2 grams. Gases used are CNG and GN_2, says they can probably measure helium but have never done it. He thinks they can even measure H_2 but not classified for H_2 service. Blazek has 1000 psi H_2 experience. They have 40,000 cubic feet of gas storage capacity. Patricia Rowley said the scales are "Metler Scales" accurate to 0.05 lbs. used in their gravimetric analysis and the system may be adapted to H_2.

Southwest Research Institute (SwRI) in San Antonio

John Gregor at the Gas Research Institute said they are developing a flow calibration lab at SwRI. They have three test loops:

Distribution test loop: 0-40 psig, 2500 acfh (42 acfm)
Low pressure test loop: 0-210 psig, 36,000 acfh (600 acfm)
High pressure test loop: 185- 1440 psig, 120,000 acfh (2000acfm)

They can achieve a level of accuracy of 0.1% using a tank on a gyroscopic scale (made in Germany).

GRI is a private, not-for-profit membership organization that plans, manages, and develops financing for a cooperative research and development program in gaseous fuels and their use. SwRI is an independent, nonprofit, applied engineering and physical sciences research and development organization.

In 1987, GRI contracted with SwRI to develop a world-class Metering Research Facility (MRF) with the objective of improving the state-of-the-art in gas flow measurement at field installations. The MRF includes three independent, natural gas systems: a low-pressure loop (LPL), a high-pressure loop (HPL), and a distribution test stand (DTS). The research there has involved installation and pulsation effects for orifice and turbine meters as well as gas sampling, electronic flow measurement, ultrasonic meters, field meter provers, and distribution measurement using diaphragm, rotary, and compact gas meters. The MRF is available for third party use to perform metering research and development, equipment calibration and testing, and personnel training. The specifications for the MRF are shown in Tables 2 and 3.

The primary mass flow standard for each MRF test system is a gravimetric system that weighs the gas collected during a precisely measured time interval. The scales are gyroscopic balance systems and are considered the most sensitive weighing systems available for MRF applications. The scales are calibrated using mass standards traceable to the National Institute of Standard Testing (NIST). The HPL and LPL are re-circulating flow loops. Constant flow conditions in the test section during a primary calibration are maintained by adding gas to the re-circulating portion of the loop at the same rate it is drawn off to the weigh tank. Special fast-acting hydraulically powered diverter valves are installed in both the HPL and LPL to control the flow of gas to the weigh tank and from the makeup bottles. They are computer controlled and independently actuated, with a full stroke response time of less than 50 milliseconds. The DTS is a blowdown type or single-pass flow system, rather than a re-circulating system.

The secondary flow calibration standards in the HPL and LPL consist of ASME/ANSI MFC-7m critical flow nozzles and industrial turbine meters. The secondary flow calibration standards for the

DTS are laminar flow elements (LFEs). This secondary capacity ranges from 8 to 920 acfm of gas flow at considerably faster turn around time than the primary system.

The SwRI Coriolis meter experience is only with Natural Gas Vehicles and is useful because of the high velocity and pressures encountered in that application. SwRI is testing the meter in another of their test facilities.

In response to a request for a quotation, SwRI will prepare and submits a letter proposal to the client. The contractual arrangements can be tailored to meet the client's normal procedures for doing business. They serve in a consultant capacity for outside organizations. They cannot test H_2, but they are willing to develop the capacity. NOVA in Canada does some similar work, but probably not at our flow high flow rates; Astleford did not know if NOVA could test H_2. There are about a half-dozen other labs in world that do similar calibration work but none have the capacity of SwRI's HPL. The weigh scale is Vala Vagabaugh with a 24,000 lb tare on the tank. The gas weighs about 2200 pounds and the scale is accurate to 21 grams.

TABLE 2.-DESIGN PERFORMANCE SPECIFICATIONS OF THE MRF

	HPL	LPL	DTS
Flow Rate, scfm	115,000	7,700	42
Flow Rate, acfm	2,000	600	42
Pressure, psig	185 to 1440	0 to 210	0 to 40
Gas Temperature, °F	20 to 100	40 to 120	Ambient
Pipe Size, in.	6 to 16	1 to 8	up to 2
Specific Gravity	0.55 to 0.97	0.55 to 1.0	0.55 to 1.0
Test Fluid	Natural Gas/N2	NG/N2/Air	NG/N2/Air
Flow Standard	Weigh Tank	Weigh Tank	Weigh Tank

TABLE 3.-MRF CONTROLLABILITY AND ACCURACY

	HPL Controllability	LPL Controllability	DTS Controllability	Measurement Accuracy
Flow Rate	1.0%	0.5%	1.0%	0.1 to 0.25%
Pressure	1.0 psi	0.2%	0.2 psi	0.015%
Temperature	1 F	1 F	Ambient	0.1 F
Pipe size	Pipe Sch. 0.05 in.	Pipe Sch. 0.02 in.	Pipe Sch.	0.001 in.
Specific Gravity	0.005	0.005	0.005	0.001
Reynolds No.	1.0%	1.0%	2.0%	1.0%

Calibron Systems, Inc. in Scottsdale, AZ

Gary Cohrs (602/991-3550) was called on 6/30/95. He said they have used tanks on scales with 0.01 lb. resolution to test gas flow in the past at higher flow rates, but it is not a standard procedure. They calibrated the K- 20 meter on a 1.0-acfm bell prover. They cannot perform a gravimetric calibration at high flowrates.

POTENTIAL VENDORS

Krohne America; Peabody, MA; Warren Ellisin; 713/464-5454
Control Engineering referred to Krohne in an article: "Coriolis Flowmeter Measures Mass Flow Directly," in Jan., 1990. The claim by the Krohne America was that their "Corimass" system had a repeatibility of 0.1% of flowrate and an error of less than 0.2% of the value. The design used torsional stress, not bending stress. Rates are from 0.2 lb/min to 3600 lb/min. Average cost was $5000. The specs were for liquid. According to Warren Ellisin, Krohne America makes variable area flowmeters (rotameters) and Coriolis meters for liquids only (6/30/95).

Stork Ultrasonic Technologies, Inc.; Shelby Morley; 800/795-7512
Shelby Morley thinks his ultrasound meteres may have application in our H_2 flow control valve tests. Note: these ultrasound meters are not accurate enough for this project.

Daniel Flow Products, Inc.; Kevin Warner; 713/827-5067
Kevin Warner says ultrasonic meters for gas are less accurate than sonic nozzles (6.23/95).

Endress and Hauser Instruments (E & H) in Greenwood, IN; 800/428-4344
Marcel Woiton (a research engineer) said E & H makes Coriolis meters but they only have done limited gas testing with CNG. They usually calibrate with water and assume no change with gas. Their meter measures the phase shift. They have sent catalogs to WSTF.

Greg Harker, of E & H, said the M-point model is being replaced by Promass 60/63 models. The promass F is for higher temperatures (392F compared to 300F for the Promass M). The cost is about $6500. Delivery is as short as 3 days for a 1-in. Promass M. There are two tubes so the sensor can reference motion of one tube with respect to the other; this gives the measurement stability. Their velocity limitation is recommended mainly for viscous fluids that would produce too large of a pressure drop.

Woiton at E & H said it would cost about $1 million to develop a meter at 5000 psi and 980 F. The 1000/1 turndown refers to the electronics capability. They have a meter now being used for CNG at 3600 psi. High-pressure changes require new calibration for a meter. The high-pressure effect is to change the internal diameter (ID), thus the volume of the meter. Therefore, a new calibration is required. The pressure change does not affect the resonance frequency. The density influences the resonance frequency. For instance their meter resonates at 1000 Hz in air but at 700 Hz in water. The mass flow is measured by the delta time in the phase shift from inlet to outlet sensor.

According to Woiton, the mass flowrate errors at are probably due to sonic effects. They do not have much data to go on for gas, but in liquid a high upstream velocity causes interference in the meter. He recommended a 3/8 in. meter for calibration lab and a 1/2 in. meter for the high flow facility. He thinks the pressure drop may be too high at high flowrates to install two meters in series. They want to work with WSTF to get data. They will send us a meter to test but I think they need a purchase order and then for us to either return the meter or pay for it if we are satisfied.

Schlumberger-Neptune; Chandler, AZ; Marty Brickner

Schlumberger makes an omega shape for gas, but they cannot guarantee published accuracy for gas. They are quoting liquid accuracy. They are discontinuing their straight pipe version, which was used only for liquids.

Bailey-Fischer & Porter;

We have been unable to get the technical people here to talk to us to date (6.30/95 to 8/3/95).

The Direct Measurement Co. (DMC) in Longmont, CO; Dave Hahn

Within the last year, the Direct Measurement Corporation (DMC) has marketed a "radial mode meter" specifically for gaseous flow. The flow sensor is a single straight tube as opposed to the bent tubes found in most Coriolis flowmeters. The vibration is in the radial mode as opposed to the bending mode or torsional mode. Also, this arrangement can achieve higher frequencies (5000 Hz) than the bending mode. They claim 0.5% accuracy of the rate plus 0.025% at the upper range limit. Meters are available for 0 to 60,000 or 0 to 240,000 lbs/hr.

Dave Hahn discussed obtaining their 1-in. meter to test in our Calibration Lab. He said the problem is freeing up a meter. He expressed some concern about publicizing the results particularly at certain flowrates or in liquid. I faxed three proposed test matrices for his inspection. One was for Brooks Prover, another for Cox Sonic Nozzles, and the third was for liquid calibrations (7/5/95). He said they intend to test at SwRI when SwRI finishes with another customer. I mentioned we may cost share to get data. He seemed agreeable (7/8/95).

Don Cage it would take 10 weeks to deliver a 1-in. meter. I have a feeling it will be longer.

Hahn said their prototype 4000 psi meter is chromoly. There may be a provision for a one-time overpressure in the code B31.3 so that we could place it upstream of the FCV in Hydrogen flow facility. He has only investigated density and mass flow as opposed to effects of other variables and parameters. Angular velocity is function of frequency and geometry only. In the Coriolis force equation ($F_{cor}=2m\omega xV$), "m" is point mass, not mass flow. Therefore the "m" is unknown.

Foxboro Co. (Foxboro, MA); Carl Annromo

Foxboro Co. stated accuracy for their I/A series mass flowmeters is 0.2% over the top 90% of the entire range but only for liquids.

Carl Annromo has Coriolis experience testing a DMC meter at CEESI. He said Coriolis meters are just not made for gases because electronics are tuned for liquid flow ranges. We will be lucky to get 1% accuracy for gas flow in the DMC meter. Foxboro and other companies besides DMC only make them for liquids.

Jim Vignos (R&D at Foxboro: 508/549-2065) recommends Vortex meters no. 83F or 83D. The F-series is purely analog 4-20 mA output or pulse ouput; The D-series is a digital 4-20 mA or a total output, not flowrate. They come in flange or wafer. Specs are 1% in gas but 0.5% accuracy can be achieved. They just cannot calibrate that accurately. Summit Controls in Lubbock sent literature (Sheila 806/792-2072) (7/28/95).

Tables 4 and 5 summarize details regarding potential Coriolis flowmeter vendors.

TABLE 4.-CORIOLIS MASS FLOW METER COMPARISON (8/2/95)

Manufacturer and Model -->	**DMC Radial Mode CMF 303/535-4864 Dave Hahn**	**E & Hauser Promass M or Promass F 800/428-4344 Greg Harker MarcelWoiton**	**Krohne America Corimass 713/464-5454 Herb Wilson**	**Fischer & Porter Tru-mass 800/326-1786 Peter Belevich**	**Micromotion (Formerly Exac Corp) Model D 100 408/365-3300**
Construction material	316 SS	Ti Gr.6 or 904L SS		316L	316L SS or Hastelloy
Gas	yes	limited testing	no	?	?
Liquid	not tested	yes	yes	yes	yes
Nominal size	1 or 2"	3/8, 1/2, 1, 1.5, 2"		1/8 - 1.5"	1" and other sizes available
No. of tubes and diameter	1 straight @1" 1 straight @2"	Straight split into 2	1 straight or z-tube torsional vibration	1 Helix tube	Dual U- tubes
Accuracy (%)	0.5% +/- 0.025% of hi range in gas	0.2% +/- .005% of full scale in liquid	0.2%	.25%	0.5%
Rangeability	60:1	1000:1			
Cost ($)	7K	7K	5K		
Flow rate range (lb/s)	0-0.3 or 0- 17 0-1.1 or 0- 67	0-1.23 (3/8") 0-42.8 (2")	.003 - 60	.083 to 20.5	
Fluid Temp (F)	-238 to 302	-58 to 302 (Ti) -58 to 392(SS)		-40 - 400	
Pressure range (psig)	1440 std. 4000 prototype	580 (1450 opt.) 360 (580 opt.)		1450 - 1700	
Comments	10 week min. delivery. Designed for gas.	Some units available in 3 days			WSTF HFF used one:no success. IGT tests in CNG showed instab. at high veloc.

TABLE 5.-CORIOLIS MASS FLOW METER COMPARISON (CONT.) (8/2/95)

Manufacturer and Model -->	**Honeywell IA&C Phoenix 602-789-4040 Dick Verville**	**Foxboro Co. 508/549-6387 Carl Annromo 508/549-2065 Jim Vignos**	**Hersey Measurement Co. 803/574-8960 Strain Gage Mass Flowmeter (from KSC FAX)**	**ABB K-Flow "B-Tubes" 800/82k-flow**	**Schlumberger M-dot 2 tube 800/833-3357 Greg Nortz (engineering)**
Construction material				316L SS	316L SS and others
Gas		no	yes	yes	yes
Liquid		yes			yes
Nominal size				1/4 - 2"	1/8 to 8"
No. of tubes and diameter	Straight-split dual tubes	Inverted U-tube		B tubes 1 @ .078" to 2 @ 1.084"	Dual omega
Accuracy (%)				0.2%	0.15% M-dot
Rangeability					100:1 & 20:1
Cost ($)					
Flow rate range (lb/s)			400 SCFM - 5600 SCFM	.03 to 42	.003 to 250
Fluid Temp (F)				-140 to 356	-50 to 400
Pressure range (psig)			3000 - 5600	1000 - 1800	290 - 3600
Comments		Recommends Vortex meter for H2, N2. Mod. 83-F or Mod. 83-D Believe accurate to 0.5%	Apparently considered for use on FCVs by Rockwell FAX from KSC	WSTF cal lab tested K-20 by Gabel did not meet specs except for liq. at high flows	Accuracy is for liq. only

SUMMARY AND RECOMMENDATIONS

Table 1 shows that only thermal dispersion and Coriolis meters measure mass directly, and that using the thermal dispersion meter would be a step backwords in accuracy. Possible alternative meters for this project are turbine or vortex shedding meters, which measure volume flowrate. To obtain mass flowrate, the pressure and temperatures are required, which leads to additional error.

Based on the information collected during this Summer Faculty Fellowship, the following action is recommended to the project leaders:

#1. Obtain a 1-in. Coriolis Meter from DMC and calibrate it in CNG at SwRI using their high-pressure gravimetric primary calibration system. A test matrix should be developed to cover the appropriate range of parameters as described in the next section on "Test Matrices." The tests will identify the limitations of the meter within the chosen conditions in CNG.

#2. Test the same DMC meter against the EG&G liquid system and the Brooks Bell Prover. This will identify limitations as a liquid flowmeter, limitations in the very low range of the meter using GN_2.

#3. Obtain an Endress & Hauser Coriolis meter or Foxboro vortex shedding meter. Install it in series with the DMC meter in the Flow Calibration laboratory's GN_2 system and compare the readings. Another test matrix should be developed to cover the appropriate range of parameters as described in the next section on "Test Matrices." The purpose is to establish confidence in the Coriolis meter technology for gaseous flow.

#4. Based on the tests, WSTF could:

(a) cost share and work with the appropriate manufacturer to design a meter appropriate for the conditions of GH_2 in the WSTF high flow facility during the FCV tests, or

(b) install the appropriate meter in the hydrogen flow facility and calibrate it against the sonic flow nozzles to locate limitations and establish confidence as a calibration device for the FCV's.

Test Matrices

Experience with CMF's for measuring gaseous flowrates has revealed errors not found in liquid measurements. However, within certain limitations, some tests such as the CEESI testing of the DMC meter in air show uncertainties of less than 0.25%. The recommended approach here is to uncover the sources of error and the candidate meter limitations so that it is designed, sized, and used appropriately. Velocity, pressure, Mach number, and Reynolds number as well as flowrate are suspected limiting variables.

An example of the test matrix for pure methane is shown in the Appendix. The idea is to identify the GH_2 conditions, as shown in the first section of the table, used in the FCV tests. The following sections in the table will correlate relevant parameters for CNG, that will be used at the SwRI, or GN_2, that will be used at the WSTF Flow Calibration laboratory. The values in the table were computed based on ideal gas properties of hydrogen and methane. More accurate test matrices need to be developed based on real gas properties of the CNG mixture used at SwRI as the project progresses.

REFERENCES

Babb, Michael, "Simplicity of Design Reduces Cost of Coriolis Technology," *Control Engineering*, September, 1992:

Blickley, George, "Flowmeter Calibration Maintained by Design," *Control Engineering*, May, 1990:

Blickley, George, "Mass Flow Measurement Aided by Coriolis Methods," *Control Engineering*, April, 1990:

Control Engineering Editors, "Coriolis Flowmeter Measures Mass Flow Directly," *Control Engineering*, Jan., 1990

Corpron, Gary, "Correlation of Hydrogen and Air in Critical Flow Nozzles, Part 2: calibration Results Obtained with Air and Hydrogen," *1994 conference on Advanced Earth-to-Orbit Propulsion Technology*, NASA/Marshall Space Flight Center, Huntsville, AL, May, 1994

Gabel, Brandon, "A Study of the Use of a Coriolis Mass Flowmeter as a Gas Calibration Standard Calibrated in Liquid," A WSTF Flow Calibration Laboratory internal report, 1992

Genesi, D., "Choices Abound in Flow Measurement," Chemical Engineering, April, 1991

Genesi, D., "Flowmeters on Tap," *Chemical Engineering*, May, 1991

Hahn, David T., "New Technology Directly Measures Mass Flow of Gas," *Fluid Flow Measurement 3rd International Symposium*, 1994

Keita, N.M. (Endress & Hauser Flowtec AG), "Behavior of Straight Pipe Coriolis Mass flowmeters in the Metering of Gas: theoretical predications with experimental verification," *Flow Measurement Instrumentation*, vol. 5, no. 4, 1994

Rowley, Patricia, Butler, Marc, and Blazek, Christopher, "Evaluation of Mass Flow Meters for NGV Fueling Dispenser Applications," *Natural Gas Fuels*, August, 1994.

Vogtlin, B. and Txchabold, P., (FLOWTECH AG Flow Measurement, Reinach, Switzerland), "Direct Measurement of Mass Flow Using the Coriolis Force," (Endress and Hauser Publication):

APPENDIX

TABLE A1.-SAMPLE TEST MATRIX BASED ON PURE METHANE

Flowrate (lb/s)	Pressure (est. psia)	Temp. est. F	Molar mass	Viscosity (lb-s/sqft)	Density (lb/cuft)	Meter ID (in)	Flow (sqin)	Velocity (ft/s)	Sonic velocity	Reynolds no.	Mach no.	Vdot acfh
1"-DMC-HYDROGEN FACILITY FCV TEST RANGE												
0.21	93	102	2.016	2.20E-06	0.031262	1	0.78539	1232	4410	1.75E+09	0.28	24182
0.40	176	102	2.016	2.20E-06	0.058778	1	0.78539	1248	4410	3.33E+09	0.28	24499
0.60	262	102	2.016	2.20E-06	0.087743	1	0.78539	1254	4410	5.00E+09	0.28	24617
0.80	349	102	2.016	2.20E-06	0.116707	1	0.78539	1257	4410	6.67E+09	0.29	24677
1.08	470	102	2.016	2.20E-06	0.157258	1	0.78539	1259	4410	9.00E+09	0.29	24724
1.30	565	102	2.016	2.20E-06	0.189119	1	0.78539	1260	4410	1.08E+10	0.29	24746
DMC-METHANE TEST MATRIX 1-MASSFLOW & REYNOLDS NO. EQUIVALENCE												
0.21	200	102	16.04	2.60E-06	0.532296	1	0.78539	72	1563	1.48E+09	0.05	1420
0.40	200	102	16.04	2.60E-06	0.532296	1	0.78539	138	1563	2.82E+09	0.09	2705
0.60	262	102	16.04	2.60E-06	0.698117	1	0.78539	158	1563	4.23E+09	0.10	3094
0.80	349	102	16.04	2.60E-06	0.928569	1	0.78539	158	1563	5.64E+09	0.10	3102
1.08	470	102	16.04	2.60E-06	1.251202	1	0.78539	158	1563	7.62E+09	0.10	3107
1.30	565	102	16.04	2.60E-06	1.504700	1	0.78539	158	1563	9.17E+09	0.10	3110
DMC-METHANE TEST MATRIX 2-VELOCITY EQUIVALENCE												
3.58	200	102	16.04	2.60E-06	0.532296	1	0.78539	1232	1563	2.52E+10	0.79	24190
4.77	262	102	16.04	2.60E-06	0.697308	1	0.78539	1254	1563	3.36E+10	0.80	24622
6.37	349	102	16.04	2.60E-06	0.928856	1	0.78539	1257	1563	4.49E+10	0.80	24681
8.59	470	102	16.04	2.60E-06	1.250896	1	0.78539	1259	1563	6.06E+10	0.81	24720
10.33	565	102	16.04	2.60E-06	1.503736	1	0.78539	1260	1563	7.29E+10	0.81	24740
DMC-METHANE TEST MATRIX 3-MACH NO. EQUIVALENCE												
0.91	200	102	16.04	2.60E-06	0.532296	1	0.78539	313	1563	6.40E+09	0.20	6139
1.13	200	102	16.04	2.60E-06	0.532296	1	0.78539	391	1563	8.00E+09	0.25	7674
1.66	262	102	16.04	2.60E-06	0.697308	1	0.78539	438	1563	1.17E+10	0.28	8595
2.38	349	102	16.04	2.60E-06	0.928856	1	0.78539	469	1563	1.68E+10	0.30	9209
5.33	470	102	16.04	2.60E-06	1.250896	1	0.78539	782	1563	3.76E+10	0.50	15348
8.98	565	102	16.04	2.60E-06	1.503736	1	0.78539	1094	1563	6.33E+10	0.70	21487

53-46
76327
234361
20p.

Volcanism in Eastern Africa

Final Report

NASA/ASEE Summer Faculty Fellowship Program - 1995

Johnson Space Center

Prepared By:	Clay Cauthen and Cassandra R. Coombs, Ph.D.
Academic Rank:	Stundent
University & Department	College of Charleston Department of Geology Charleston, S.C. 29424

NASA/JSC

Directorate:	Space and Life Sciences
Division:	Solar System Exploration
JSC Colleague:	David McKay, Ph.D.
Date Submitted:	August 3, 1995
Contract Number:	NGT-44-001-800

Abstract

In 1891, the Virunga Mountains of Eastern Zaire were first acknowledged as volcanoes, and since then, the Virunga Mountain chain has demonstrated its potentially violent volcanic nature. The Virunga Mountains lie across the Eastern African Rift in an E-W direction located north of Lake Kivu. Mt. Nyamuragira and Mt. Nyiragongo present the most hazard of the eight mountains making up Virunga volcanic field, with the most recent activity during the 1970-90's.

In 1977, after almost eighty years of moderate activity and periods of quiescence, Mt. Nyamuragira became highly active with lava flows that extruded from fissures on flanks circumscribing the volcano. The flows destroyed vast areas of vegetation and Zairian National Park areas, but no casualties were reported. Mt. Nyiragongo exhibited the same type volcanic activity, in association with regional tectonics that effected Mt. Nyamuragira, with variations of lava lake levels, lava fountains, and lava flows that resided in Lake Kivu. Mt. Nyiragongo, recently named a Decade volcano, presents both a direct and an indirect hazard to the inhabitants and properties located near the volcano. The Virunga volcanoes pose four major threats: volcanic eruptions, lava flows, toxic gas emission (CH_4 and CO_2), and earthquakes. Thus, the volcanoes of the Eastern African volcanic field emanate harm to the surrounding area by the forecast of volcanic eruptions.

During the JSC Summer Fellowship program, we will acquire and collate remote sensing, photographic (Space Shuttle images), topographic and field data. In addition, maps of the extent and morphology(ies) of the features will be constructed using digital image information. The database generated will serve to create a Geographic Information System for easy access of information of the Eastern African volcanic field. The analysis of volcanism in Eastern Africa will permit a comparison for those areas from which we have field data.

Results from this summer's work will permit further study and monitoring of the volcanic activity in the area. This is of concern due to the large numbers of refugees fleeing into Zaire where they are being positioned at the base of Mt. Nyiragongo. The refugees located at the base of the volcano are in direct hazard of suffocation by gas emission and destruction by lava flow. The results from this summer study will be used to secure future funding to enable continuation of this project.

VOLCANISM IN EASTERN AFRICA

Introduction

Background

The African rift system extends 2200km down the continent of Africa from the coastal region of Ethiopia (Red Sea) to fault regions of Tanzania. The rift system is unique, for it is believed to be connected to the global mid-oceanic ridge system (Heezen and Ewing, 1963). The spectacular African rift system is divided into an eastern and a western portion. The Eastern African rift and/or the hotspots are responsible for the contents volcanoes in this area. This paper will focus on the eastern portion of the rift system, specifically regions in Zaire where Mt. Nyiragongo and Mt. Nyamuragira of the Virunga Mountains reside. (Baker et al., 1970)

In 1891, the Virunga Mountains of Eastern Zaire were first acknowledged as volcanoes, and since then, the Virunga Mountain chain has demonstrated its potentially violent volcanic nature. The Virunga Mountains lie across the Eastern African Rift in an E-W direction located north of Lake Kivu. Mt. Nyamuragira and Mt. Nyiragongo present the most hazard of the eight mountains making up Virunga volcanic field, with the most recent activity in 1982 at Nyiragongo and 1991 at Nyamuragira. (Tazieff, 1994)

In 1977, after almost eighty years of moderate activity and periods of quiescence, Mt. Nyamuragira became highly active with lava flows that extruded from fissures on flanks circumscribing the volcano. The flows destroyed vast areas of vegetation and Zairian National Park areas, but no casualties were reported. Mt. Nyiragongo exhibited the same type volcanic activity, in association with regional tectonics that effected Mt. Nyamuragira, with variations of lava lake levels, lava fountains, and lava flows that resided in Lake Kivu. Mt. Nyiragongo, recently named a Decade volcano (1991), presents both a direct and an indirect hazard to the inhabitants and properties located near the volcano. The Virunga volcanoes pose four major threats: volcanic eruptions, lava flows, toxic gas emission (CH_4 and CO_2), and earthquakes. Thus, the volcanoes of the Eastern African volcanic field emanate harm to the surrounding area by the forecast of volcanic eruptions.

Purpose

As an outcome of preliminary stages of this project, we will acquire and collate remote sensing, photographic (Space Shuttle images), topographic and field data. In addition, maps of the extent and morphology(ies) of the features will be constructed using digital image information. The database generated will serve to create a Geographic Information System for easy access of information of the Eastern African volcanic field. The analysis of volcanism in Eastern Africa will permit a comparison for those areas from which we have field data.

Results from this preliminary work will permit further study and monitoring of the volcanic activity in the area. This is of concern due to the large numbers of refugees fleeing into Zaire where they are being positioned at the base of Mt. Nyiragongo. The refugees located at the base of the volcano are in direct hazard of suffocation by gas emission and destruction by lava flow. The results from this summer study will be used to secure future funding to enable continuation of this project.

Also, another aspect of this study is to clear up any discrepancies that I and many others have come across when studying these volcanoes. Thus, throughout the paper, the reader will note times where I clarify or allude to another source with as slightly different results or data. I am not disregarding their validity, though, but rather formatting their data with a collective schematics.

Geographic Information Systems

Geographic Information Systems are means of efficient, quick access to information concerning a specific area. The GIS is computer system capable of capturing, analyzing and displaying 2D, 3D, or 4D information. The GIS database allows quick reference to areas of concern. This facilitates monitoring and further studies of the given areas. The assessment of Nyamuragira and Nyiragongo volcanoes using the GIS will include regional geography (rivers, hills, etc.), volcanic complexes, cinder and scoria cones, villages, refugee camps, cities, roads, geophysics (faults and fractures), seismic stations (i.e. instrumentation sites), areas of immediate concern (of Mazuku hazard, lava flow hazard, and mud slides), rainfall, drainage, and foliage patterns. See Appendix A at the end for the detailed steps of compiling the GIS. The figure below graphical displays the format of the GIS.

Figure 1. Courtesy of Cassandra Coombs

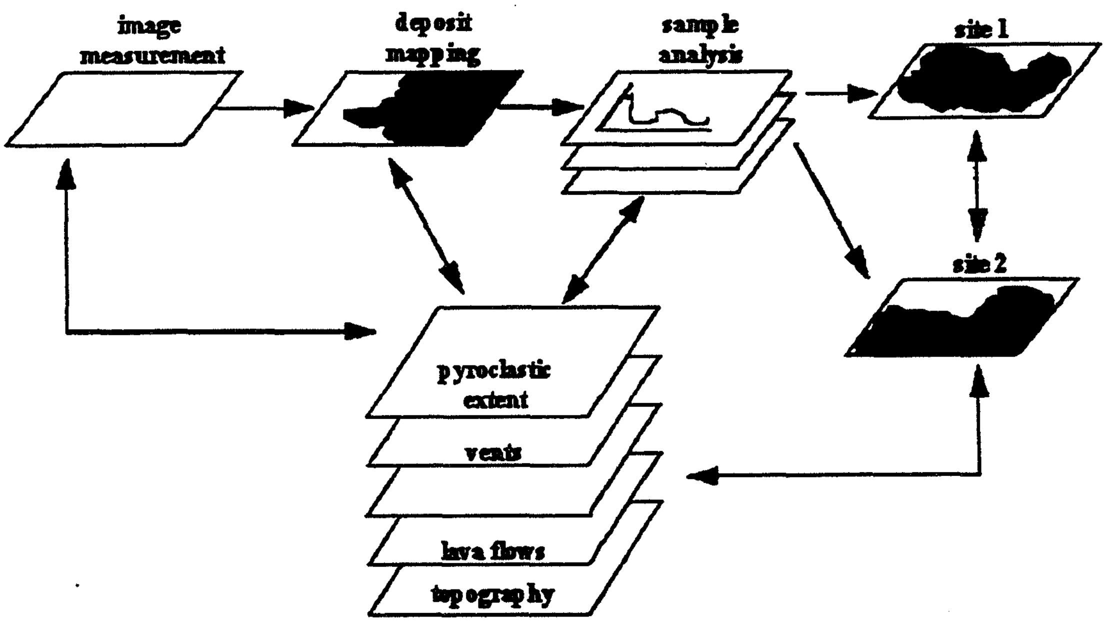

Nyiragongo

I. Introduction
II. Geography
III. Form and Structure
IV. Volcanic Activity
V. Petrography

I. Introduction

Mt. Nyiragongo lies at the southern region of the Western rift branch of the Eastern African rift system in the Virunga province. The volcano has been recorded as active since 1884 and more less, has been active up to the present, only with a brief period of quiescence of 1930-1935. Mt. Nyiragongo is a stratovolcano, and off and on throughout the recorded history of the volcano has had steady-state lava lake at the summit of the volcano. In January of 1977, Mt. Nyiragongo became highly active with the drainage of the lava lake at the summit and basaltic lava flows erupting from fissures semi-circumscribing the volcano. The eruption destroyed acres of land and took over 100 lives. Mt. Nyiragongo is one of the few volcanoes in recorded time that has taken so many lives. In 1982, the volcano reactivated consisting of lava fountains and continual feeding of the lava lake. The Nyiragongo volcano has been characterized with explosive behavior and extreme fluidity of the lava. Since 1990, Mt. Nyiragongo has been named a Decade Volcano by the International Association of Volcanology and Chemistry of the Earth's Interior (IAVCEI), but research concerning the volcano is constantly delayed because of the political unrest in Zaire.

II. Geography

Mt. Nyiragongo ($29^{o}15'$E, $1^{o}30'$S) is located 20km north of Lake Kivu and Goma, Zaire. It is also one of the eight volcanoes in the Virunga volcanic province that lies along the Western branch of the African Rift system. Mt. Nyiragongo's summit crater is 3465m above sea level and 2010m above Lake Kivu. Nyiragongo is south-east of it's more massive volcanic brother, Mt. Nyamuragira. Around the flanks of the volcano, fissures and scoria cones lie that are in a north western trend that highlight the evidence of the African Rift system. The major scoria cones (parasite vents) are Baruta (north flank), Shaheru (south flank), and Rashayo (south-west flank). These parasite vents attribute to a moderate amount of Nyiragongo's activity (this will be explain in detail later). Mt. Nyiragongo has an external gradient of 40^{o} on the southern flank and 55^{o} to 60^{o} on the eastern and western flanks.

At the summit of the volcano, a caldera of 1km in diameter sits. The caldera sinks 200m into the volcano with the slope gradient of the inner rim of 60^{o} to 80^{o}. At the base of the crater of the caldera, 500m wide, lies the permanent lava lake that has varied in volume and size over its recorded history of 1928.

III. Form and Structure

Mt. Nyiragongo is the result of tectonic activities of the western branch of the Eastern African rift system. The volcano has a general morphology of a stratovolcano which is evident by a central effusive pipe and radial eruptions. The Nyiragongo complex is composed of three overlapping volcanoes: (from north to south) Baruta, Nyiragongo, and Shaheru. All three have a pit crater at their respective summit. Nyiragongo is the youngest and the main cone of the volcanic complex. Over decades of activity, Shaheru has been, for the most part, obliterated by flows from the southern flank of Nyiragongo, while Baruta has remained well preserved and relatively undisturbed by Nyiragongo's flows. (Demant et al. 1994)

At the summit of the volcano, the pit crater (or caldera) is 1km in diameter and sinks 200 meters into the volcano. The pit crater dominated by lava lake, fluctuating in volume over the years with respect to its activeness.

The crater has been differentiated into three units: an upper, intermediate, and lower.

The Upper Unit (UU) is about 20m thick, composed of a succession of "thin decimetric to metric flows with scoriaceous basis" (Demant et al., 1994). The UU-lavas have an abundance of nepheline crystals, and observations denote that there is a series of progressions with little change between the lavas on the upper-most part of the crater wall and on the flanks. The observations reflect the periodic over flowing of the rim by the lava lake.

The Intermediate Unit (IU) is 50m thick composed of flows that are generally 1 meter thick, and dominated by leucite and nepheline megacrysts--usually forming aggregates. The flows indicate periodic over flowing " of a molten lava column from an open crater" (Demant et al., 1994). There are numerous vertical dikes on the crater wall which represents a relationship of the Lower Unit and the Intermediate Unit. Thus, Demant et al. reveal by the relationship of the IU and the LU that the collapse of the pit crater occurred towards the end of the Intermediate Unit.

The Lower Unit (LU) is dominated by 90 meters of pyroclastic deposits. In "Volcanological and petrological evolution of the Nyiragongo volcano, Virunga volcanic field, Zaire", Demant et al. offers a successional description of the LU starting from the bottom of the Lower Unit to the top:

1. Above the upper platform (157m from the rim of the crater), there is a thick layer of "chaotic" pyroclastic deposition with large round chunks of lava (up to a few meters in diameter). There are two facies of course-grained lavas with melilitite phenocrysts and clino-pyroxene rich, porphyritic in texture and prominent flow bands.

2. Between -142 and -108m of the inner wall there is finely stratified and non-welded cinders. Demant et al. notes that the color and the complex stratification are characteristic of a hydromagmatic style of eruption.

3. The top 30 meters of the LU reveal a succession of ten lava flows which are the result of rhythmic explosion phases from the open crater. The alternating flows of pyroclastic materials indicate the growth stages of the volcano which is typical of a stratovolcano (explosive and effusive).

Interruptions of volcanic activity are rep[resented by irregular contacts between the LU and the IU. The latter stages (IU and UU) are mainly effusive-type deposits and "correspond to the overflowing magma above the pit crater" (Demant et al., 1994). The UU is an artifact of these successional over-flows from the lava lake.

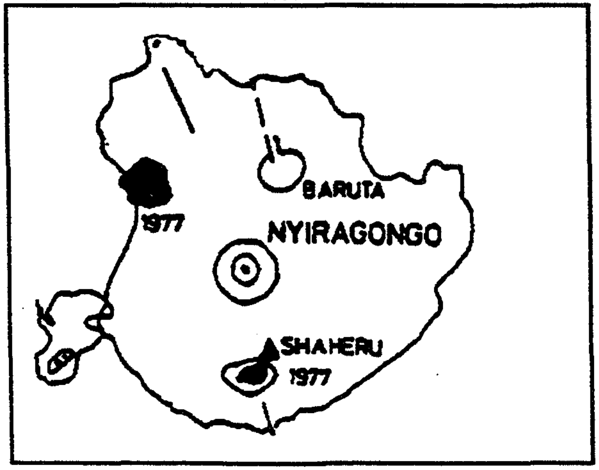

Figure 2. Map of Mt. Nyiragongo showing Baruta and Shaheru. Map is courtesy of N. Zana.

Baruta, Shaheru, and parasite cones. Baruta and Shaheru (See Figure 1) have been consider to be parasite cones, but for the classification schematics of this project and due to the Demant et al. 1994 research, Baruta and Shaheru are classified as long lived stratovolcanoes.

Baruta, north of the Nyiragongo caldera, has a crater 900m in diameter and is 250m deep. The Northwestern wall of the pit was destroyed during an undated eruption, producing a second crater in a NNW direction. Fracture trends of the Baruta stratovolcano are parallel to those of Nyamuragira and Nyiragongo. The lavas are composed mainly of nephelinites and melilitites which are genetically similar to those of Nyiragongo. The inner subvertical wall of the crater reveals a nice outcrop of alternating pyroclastic and massive lavas, which are dissected by a vertical dike.

Shaheru is the oldest of the Nyiragongo complex and flows from Nyiragongo have smothered the northern flanks of Shaheru. In 1977 eruption, flows from Nyiragongo partially filled the crater of Shaheru. The southern slopes of Shaheru seem to be the only uncontaminated portion of the volcano.

About 100 parasite cones surround the Nyiragongo complex. On the northeastern trend, Rashayo (a group of about 20 vents) extend 10km along the base of Nyiragongo. Hydroclastic tuffs around many of the parasitic cones reveals evidence of lacustrine eruptions. Many of the cones are a part of the complex fissure zone (elongated in shape). The cones are constantly recycled (destroyed and rebuilt) because of the high activity along the fissure zones.

IV. Volcanic Activity

Volcanologists have recorded and dated the volcanic activity of Mt. Nyiragongo from 1884 to the present. Tazieff describes the evolution of Nyiragongo and its siblings of the Virunga Mountain Chain: "Successive eruptions over the past one or two billion years have resulted in the build up of billions of cubic yards of lava; that immense volume of lava comprises the Virunga Mountain Chain" (Tazieff, 1977).

The following is a compilation of a brief history outline of Nyiragongo's activity:

Note that the name in parenthesis is the scientist, lay man, or missionary that documented the activity. In several instances, the person who cited the activity had no formal training as a volcanologist or even geology, but rather a mere spectator of the activity. Periods without a citation following usually means that a native tribe has dated the activity, and I could not find any names to associate with it. Also, I tried to be as specific as I could with regard to the research that I have done.

Table 1

1884	a normal explosion from the central crater of the southern portion of the pit (Linke)
1891	a central crater eruption and lava lake activity. Von Gotzen noted on his expedition to the summit of the crater that same year: "The volcano shines in the night like a column of fire" (Tazieff, 1976).
1898	a central crater eruption (Grogan)
1899	a central crater eruption (Moore)
1900	a central crater eruption (Sapper)
1901	a normal eruption of the central crater (Shwartz)
1902	a central crater eruption (Missionaries Herman and Kandt)
1905	a central crater eruption and lava lake activity
1906	a central crater eruption (Wollaston)

1908	? activity on the southern portion of the central crater
August-October,1911	a central crater eruption of the southern pit (Kirschstein and Meyer)
1918	a central crater eruption and lava lake activity
1920-1921	a normal explosion of the central crater
March-April, 1927	a central crater eruption, lava flows, and lava lake activity (Times and Barnes)
1928	a central crater eruption and dense clouds of smoke were emitted from the summit
1930-1935	the volcano had a brief period of dormancy
1935-1977	low to little activity except for variations of the lava lake level (I found little to no documentation concerning this forty-two year time period)
1977	an explosive central crater eruption, activity of regional fissures, lava lake activity, fatalities and damages.
1982	a phreatic central eruption, lava flows, and lava lake activity.
June 23,1994	a series of small eruptions within the central crater.

Table courtesy of Catalogue of Active Volcanoes

The following section is a more in depth look at the most recent volcanic activity, specifically the eruptions of 1977, 1982, and 1994.

The 1977 eruption was a simultaneous eruption with Mt. Nyamuragira. It is the shortest volcanic eruptive episode ever recorded. The, until then, semi-permanent lava lake drained more than $20x10^6$ cubic meters and spread over $20km^2$ in less than one hour. Lava flows exceeded $2km^2$ on the north and west flanks, while the main flows ran down the southern flank extending 10 km from their respective openings, covering an area of $18km^2$. The northern and western flows ran into jungle area, and the southern and eastern flows ran into populated areas. Several villages were wiped out and an estimated 30 to 300 hundred people were burned alive by the lava flows. The main road linking southern and northern Kivu province was cut off for about 10km. In the forest lava flows damaged an area of about 3-5 million m^2. The average thickness of the lava flow was a meter or less, except for flows that extended toward the Goma air field and the temperature of the fresh lava was 1100+-30°C (Bonnet). The flows were mainly high velocity melenites.

Tazieff, using an accepted value of 1m in thickness, calculated the volume of the flow to be 20-22 million m^3, which matches the estimated volume of the lava lake and the feeding pipe. Tazieff concluded that the lava lake and feeding pipe was drained by a set of vertical fissures that opened on the northern (2,200m in altitude), western (2400m in altitude), and on the southern side (2700m in altitude) of the Nyiragongo complex. The fissures drained the lake complex in less than one and a half hours (note: that was the time extent of the whole volcanic episode). The up-down motion of the lava lake over time has caused the inner walls of the volcano to weaken and the fact that the lava lake had disappeared heightened the chance of an outbreak along the base of Nyiragongo; both of which allowed an episode of that sorts to occur. Ten days after the eruption, the lava lake was 800 meters deep and the platform(s) had disappeared which reveals the collapsing nature of the volcano.

On June 21, 1982, fresh lava began to flow into the 800 meter deep crater of the 1977 eruption, producing a molten pond at the base of the crater and a spatter cone seemingly near the bottom of the crater. On July 11, the spatter cone had vanished because of the rising lava lake, but fountains remained in the same position and magnitude. By August 4, the lava lake was entirely crusted over except for two fountains which corresponded to the initial vents (spatter cones). The surface of the lava lake was 3050m a.s.l, 370,00m^2 in area, and had an estimated volume of 44x10^6. For a week or two the activity of the lava lake had seem to have stopped. On October 3, the level rose to 440m of the rim of the crater and was approximately 500m across in diameter, and the fountaining had resumed. In late October, the outflows continued but were of degassed, short-lived, and cooler (960+-30 ^{o}C) lavas near the main outer portion of the lake. At this point the lava lake is at a steady-state where the volume of the lake is hypothetically not varying because the cooler magma on top will be degassed, therefore the heavier, and will sink to the bottom which allows fresh magma to rise. "The persistence of such an extraordinary large steady-state lava lake may be due to the equally exceptional fluidity of the magma rising at the intersection of four different tectonic trends of fractures in the subvolcanic basement" (Tazieff, 1982).

The most recent eruption of Nyiragongo occurred on June 23, 1994 with a small series of eruptions within the crater. Over a five month period there was an accumulation of a 500m deep lava lake that is now almost half filled. Lockwood and Casadevall recorded eruptive episode on June 23-27, August 10-13, August 25-28, and September 5-8. Their observations suggest a recycling of molten lava as noted by Tazieff in 1982 and 1977. Casadevall and Lockwood believe that Nyiragongo's present activity reveals that the volcano may be returning to the steady-state status observed before the 1977 eruption.

V. Petrography

The lavas of Nyiragongo are strongly silica-undersaturated feldspar-free lavas. The mineralogy of the walls of the pit crater have been differentiated into three units. The data table is supplied by Demant et al.

Table 2

Upper Unit	Melilite, nephelinite
Phenocrysts	nephiline, melilite+-leucite
Matrix	glassy or fine grained; nepheline, melilite, clino-pyroxene and titanomagnetite
Accessory Phase	apatite
Aggregates	nephiline with interstitial clinopyroxene + titanomagnetite + apatite
Intermediate Unit	Nephelinites
Phenocrysts	nephiline, leucite, and clinopyroxene
Matrix	same as Upper Unit
Accessory	same as Upper Unit
Aggregates	Leucite, titanomagnetite, clinopyroxene, and interstitial nepheline
Upper Lower Unit	heterogeneous melilitites
Phenocrysts	Clinopyroxene + melilitite
Matrix	glassy or fine-grained; nepheline, clinopyroxene, and titanomagnetite; abundant calcite +- zeolites
Aggregates	melililtite + olivine + perovskite + titanomagnetite + interstitial nepheline
Lower Lower Unit	Melilites

Phenocrysts	melilitite, nepheline and kalsilite, scarse clinopyroxene, and olivine
Matrix	fine-grained; nepheline, nepheline, greenish poikilitic clinopyroxene, and olivine
Accessory phase	persokite and apatite
Aggregates	kalsilite + melilite + titanomagnetite

Table courtesy of Demant et al., 1994

These three units of the crater are the main building components of the volcano.

Nyamuragira

I. Introduction
II. Geography
III. Form and Structure
IV. Volcanic Activity
V. Petrography

I. Introduction

Of the two volcanoes, Mt. Nyamuragira has had the lesser amount of research and documentation on it, but the volcano has had more eruptions (22 eruptions since 1901) than Nyiragongo. Nyamuragira is a shield volcano and is the most active of the Virunga complex. Before the massive volcano emerged, the Nile river ran through the area, and Nyamuragira is now a natural dam separating the Nile and Lake Kivu, which is the offspring of the Nile river. Nyamuragira has many synonyms that are derived from natives tribes of the area, such as Nyamlagira and Namlagira.

II. Geography

Mt. Nyamuragira is located 40km north of Lake Kivu (1o25'S, 29o12'E). It rises 3056m above sea level and 1593m above Lake Kivu. The position of the volcano follows the NW-SW trend of the African rift system and is NW of Nyiragongo. The massive volcano has a basal extension on its longest axis of 60km. Along the exterior of the volcano, Nyamuragira has an external gradient of 8-10%.

The summit of the volcano is occupied by a large crater caldera system, 2km in diameter, with openings in the SW sector of the crater. The crater is terraced by platforms on the N, NE, and E that are separated into two by a point of land jutting into water.

The volcano is dotted by active parasite cones and satellite cones along the base of the volcano. Mikombe is located 15km NE of the summit caldera and extends to a height 60-70m. Mikombe is about 10km away from the road to Tongo. Satellite eruptions, such as Tshambe of 1938 and Muhuboli of 1948, commonly take place along fissure zones without the formation of a cone. Active parasite cones that circumscribe the flanks of the volcano are: Singiro (East flank), Nahimbi (SW flank), Rumoka (SW flank), Tshambene (SW flank), Gituro (SW flank), Muhuboli (SW flank), Shabubembe-Ndakaza (NNW fissure zone), Mihaga (SSE fissure zone), Murara (SSW flank), Kitsimbanyi (North flank), Gakararanga (North flank), Rugarama (SE flank), Harakindi (SSW flank), Gafuranindi (North flank), and Mikombe (NE flank). These parasite cones are responsible for the majority of flows and activity of Nyamuragira. The locality of refugee camps are positioned near Katale, Mugungu and Kituku.

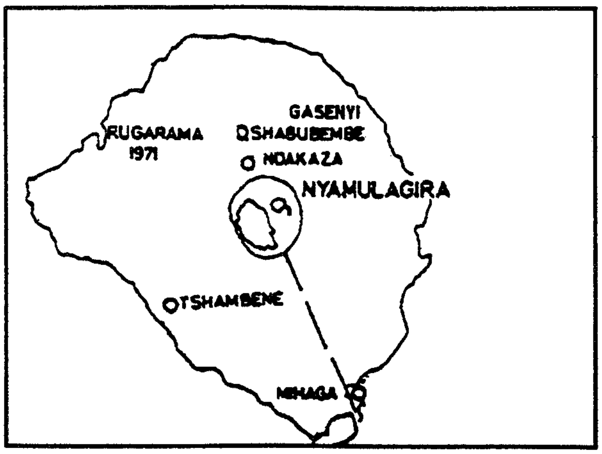

Figure 3. Map of Mt. Nyamuragira showing the crater and the satellite cones surrounding the volcano. Map is courtesy of N. Zana

III. Form and Structure

The general morphology is that of a shield volcano with fissure zones positioned in a NW trend of the shield. The most outstanding features of the volcano is the vast amount of satellite eruption zones on the flanks of the volcano and the surrounding area. Mainly, the eruptive zones attribute to the drainage of the lava lake at the summit caldera. Frequently, small cones have been observed with the effusion of large volumes of lava and/or sulfurous gases.

The lavas consist mainly of the Pleistocene age, and evidence dictates that the release of primary basalts are from the lower to upper mantle regions. Like Nyiragongo, these emission are relatively rare and indicative of mid-oceanic ridges. These conditions are accepted as being caused by a mantle plume below the subcrustal to upper mantle region of the Earth.

IV. Volcanic Activity

Over the past century, Mt. Nyamuragira has been the most active volcano of the Virunga Mountain chain with thirty eruption dating from 1882 to the present. The following abbreviate volcanic activity table displays the frequency and consistency of activity of Nyamuragira.

Table 3

1882	venting of the northern flank
1894	normal explosive eruption of the central crater and lava flows
1896	normal explosive eruption from the central crater
1899	flank venting, radial fissures, normal explosive eruption, lava flows of the NNW fissure zones
1901	explosive eruption and lava flows of the East flank (Singiro)
1902	flank and fissure zone venting of the SSE fissure zone
1904	flank venting, explosive eruption, and lava flows of the SW flank (Nahimbi)
1905	flank venting, explosive eruption, and lava flows of the East flank (Kanamaharagi)
1906	explosive eruption of the central summit caldera

1907	explosive eruption of the central summit caldera (there were two episodes documented that year, but no specific dates were given)
1908	explosive eruption of the central summit caldera
1909	explosive eruption of the central summit caldera, ? phreatic
1912	explosive eruption and lava flows of the central summit caldera and of the SW flank (Rumoka). Fatalities and damages
1920	?explosive eruption of the SSW flank (Lake Kivu), radial fissures, and lava lake activity at the summit caldera.
1921	explosive eruption, lava flows, and lava lake activity of the central summit caldera.
1938	explosive and phreatic eruption of the central summit caldera, venting of SE and SW flanks (Tshambene), regional fissures, lava flows, and a Tsunami.
1938-1940	eventual drainage of the lava lake of the central crater.
1948	explosive eruption of the SW flank (Gituro) and N flank (Muhuboli), flank and regional fissures, lava flows, and lava lake activity.
1951	explosive flank venting of the SW flank (Gituro)
1951	explosive eruption of the NNW fissure zone (Shabubembe-Ndakaza), lava flows, and lava lake activity
1954	explosive venting of the SSE fissure zone (Mihaga) and lava flows
1956	explosive eruption of the central summit caldera and NNW fissure zone, and lava flows associated with both.
1957	eruption of the central summit caldera and SSE fissure zone with lava flows associated with both
1958	explosive eruption of the Northern flank (Kitsimbanyi) and NNW rift with lava flows associate with both
1967	explosive eruption of the Northern flank (Gakararanga) with lava flows
1971	explosive eruption of the WNW flank (Rugarama), lava flows, and damages
1976-1977	explosive eruption of the SSW flank (Murar and Harakandi), lava flows, and lava lake activity. The activities mentioned persisted until the 1977 eruption of Nyiragongo.
1980	explosive eruption of the Northern flank (Gasenyi), lava flows, and damages
1981	explosive eruption of the SE flank (Rugarambiro), lava flows, and damages
1984	explosive eruption of the NW flank (Kivandimwe), lava flows, and damages
1986	explosive eruption of the Southern flank (near Kitazungurwa), lava flows, lava lake activity, and damages
1987	explosive eruption of the Northern radial fissure (Gafuranindi) with lava flows
1989	explosive eruption of the central summit caldera, SE and Eastern flanks with lava flows

1991	explosive eruption of the NE flank (Mikombe), lava flows, and damages
1994	eruption of the central summit caldera and western flank, lava fountains, and volcanic ash

Table courtesy of Catalogue of Active Volcanoes.

The most resent major eruptions of Mt. Nyamuragira were in 1977, 1982, and 1994. These eruptions were associated with activity of Mt. Nyiragongo.

On December 11 1976, intense magma movement beneath the surface was recorded with a multitude of volcanic earthquakes. On December 23 of the same year, there was an eruption on the north eastern end of a fissure zone and explosive activity centered on three locations of the fissure zone which produced three new cinder cones. The following day Murara was created. On January 18 1977, Murara grew to 150 meters high and had a flow rate of 10m/min.; by the next day, it had slowed to 2-4m/min. Murara's activity resumed on the north end of Murara ten days later. In February, an eruption from a new flank 8m south west of the summit produced lava fountains scaling 150-180m high which formed a 70m spatter cone around the vent. The lava flows extended 1km to the west and 3km to the south west.

During the January of 1982, an eruption on the south east flank of Nyamuragira produced lava rates recorded at 20-24km/hr to 6km/hr. Observers noted the vigorous fountaining from the scoria cones and a large cloud of SO^2 emitted during the eruption.

The most recent activity was on July 4, 1994 which lasted until July 17. The eruption took place within the summit of volcano and on the western flank of the volcano. Lava fountains shot several hundred feet into the air from openings on the western flank, producing vast quantities of Pele's hair. A new line of cinder cones were produced on the western flank. Lava flows of the western flank extend 10km in a western fashion that eventual smothered a small lake. There were no reported human casualties, but cattle were reported to have died by ingesting volcanic ash.

V. Petrography

Mt. Nyamuragira, as with Nyiragongo, are chemically exceptional volcanoes. The lavas are mainly leucite basanites, leucite theralites (Finckh, 1912), basanitiods, olivine hyalobasalts (Pullfrey and Richard, 1950), and occasionally basanitiod limburgites from the Nahimbi eruption of 1904. The lavas have a very low viscosity with SIO$_2$ averages of 44-45 and range from 34.72 to 57.64, and are, for the most part, highly potassic. The low viscosity indicates the source is tapped from an upper chamber (Blake and Ivy, 1986). Blake and Ivy have also noted temporal changes of lava flows with respect to time and chemical composition that trends increasingly become more mafic. Hayashi et al.'s geochemical analysis further the Blake and Ivy studies and indicate that there is a magma zonation where the upper portion of the chamber is more mafic than the lower portion of the chamber.

Volcanic Hazard of Nyamuragira and Nyiragongo

The volcanic hazards associated with an eruption and perpetual volcanic-related activity are of short and long-term concern. Moreover, there are four major concerns that threaten 100,000 population of Goma and over a million Rwandan refugees: Mazukus, lava flows, earthquakes, ash flows and the degassing of Lake Kivu. This section combines the hazards of both volcanoes, but Mt. Nyamuragira poses less of a threat because of its locality in relation to populated areas.

Mazuku is the Swahilian equivalent for "evil winds"; the "evil winds" that the Swahili's refer to are the gas emissions associated with dry gas vents. Dry gas vents are vents that emit harmful gases into the atmosphere (i.e. CO_2) These vents are created when there is insufficient amounts of ground water to absorb the gas, thus a dry gas vent. From freshman chemistry, we learned that CO_2 is heavier than air; thus, a cloud of CO_2 will accumulate in areas that serve as a natural cup for the gas. The gas, though has the potential to migrate due to winds or other natural causes. Mazukus are silent and dangerous hazards that must be monitored. (Lockwood and Casadevall, 1994)

The lava flows associated with Mt. Nyiragongo are typified by silica-poor composition, making the lava of high fluidity. The lava flows would be of high velocity (1977 over 100Km/hr on the steeper slopes); therefore, it would allow little time for evacuation of the populated areas. Lockwood and Casadevall offer a recent analysis of the foundation of the highly populated Goma reveal "textures of very rapid emplacement, and is about 700 years old" (Lockwood and Casadevall, p.5), which highlights the potential destructive nature of the lava flow. Human causalities would be unexpected in areas around Goma because of the lava flow tendency (i.e. more gentle slope and the lower temperature of the lava). Damages and fatalities from lava flows of Mt. Nyamuragira are highly unlikely because the extremely gentle slope of the volcano, thus causing the lava to move slower and to a lesser extent.

Earthquakes will be associated with any major volcanic activity. An earthquake could be associated with one of the many faults surrounding the area or with the magma moving beneath the surface. Although I have yet to find any sufficient amount of information concerning the urbanization of the areas surrounding the area, Goma will run the highest risk of destabilization of edifices and other large structures that potentially would place people in harm's way. Also, an earthquake could cause the possible upwelling of Lake Kivu which allow vast amounts of CO_2 and CH_4 into the atmosphere.

Volcanic ash (Pele's hair) presents a potential threat, for the ash can cause human discomforts such as eye damage and has been documented to kill livestock if it is ingested. On the July, 1994 eruption, volcanic ash covered an area exceeding $30km^2$.

Because of the positioning of Lake Kivu, Lake Kivu has acquired large quantities of CO_2 and CH_4 have been dissolved into the deep water of the lake. Currently, the lake is at steady level and degassing without a major force is unlikely, Lockwood and Casadevall note that "large subsurface landslide or lava flow into the lake" or even an earthquake could cause the fatal upwelling and the degassing of the lake.

A major eruption of Mt. Nyiragongo could be devastating because of the highly populated areas of Goma and the refugee camps. A major eruption could cause indirect hazards such as the degassing of Lake Kivu and Mazukus and the direct hazards of lava flows and earthquakes.

Appendix A

The GIS Compilation Process

The following is a detailed analysis of the steps and tools taken while compiling the GIS.

Software and Tools:
Adobe Photoshop
Dimple
Shuttle image STS 005-42-1470
Radar image downloaded from JPL
U-MAX Scanner
Machintosh IIfx
Rodime Systems Hard-drive
Machintosh Power PC

1. The first portion of my research was text research. After compiliing an adequate amount of abstracts and papers concerning the Mt. Nyiragongo and Nyamuragira volcanoes and the mechanisms of volcanism, I constructed a detailed outline that included a date-line of activity and generalities of the volcanoes.
2. Soon, after I received the STS 005-42-1470 and STS 005-42-1470 images that were formated IBM-PC's and in the tiff picture format.
3. I converted the IBM-PC tiff files to Machintosh format by ftp'ing them to a Machintosh computor.
4. Since I would be using Dimple as the mainframe for the GIS, the tiff files had to be converted into pict files. I opened the tiff file in Adobe photoshop, and chose Save As... from the File menu. I saved the tiff file as a 32-bit pict file.
5. While in Dimple, I opened the pict file shown as a Raster. I chose Color Components from the Transform file menu. This separated the picture in a Red-Green-Blue fashion. Being in the RGB, this will allow a multiband to be formed and allow the picture to be munipulated.
6. From the Image file menu, I chose New Multiband, and saved the RGB and the color components in the Multiband.
7. From there, I wanted to establish Ground Control Points (GCP). From the Image menu, I selected Image Details, and mark the box entitled

Modify Details. I change the coordinate system from pixles to Geo. This will allow the multiband to be formatted in Longitude and Latitude, as opposed to pixel, x-y coordinates.

8. From the Image file menu, I chose New GCP model. Using the cross symbol from the cursor selection box at the top left of the screen, I selected a pre-designated point that I had exact coordinates. After pin-pointing the spot, I selected Add GCP. The computor, then, ask to record the point with it's specific longitude and latitude.

9. Once I designated three (minimum amount required for a linear calculation) points, I chose the model box that from the GCP screen to calculate the coordinate system.

The following steps involve scanning specialized maps of roads, lava flows, siesmic stations, seismic activity, and general maps of the area.

10. From Adobe Photoshop, I selected Aqure=> Pulg-in Scan 3.4 from the File menu. I place the image to be scanned on the scanner and selected preveiw with the mouse. After seeing the preveiw, I selected scan with the mouse.

11. I, then, chose Save as... from the file menu saving the image as a pict file. From Adobe Photoshop, I selected Aqure=> Pulg-in Scan 3.4 from the File menu. I place the image to be scanned on the scanner and selected preveiw with the mouse. After seeing the preveiw, I selected scan with the mouse. After scanning each image, I would selected Save As... from the file menu to save the image as a 32-bit pict file.

12. After opening each image in Dimple (Open as a Raster), I overlayed each image by selecting Join Images from the Image file menu. The process of joining images is such: Join two images, then join another to the joined image, and so on. Because this combined image of all of the previously scanned images appeared to be too cluttered, I joined another image complex with only a selected bunch of the images with each other, thus making two complexes of joined images.

The Classification of the maps didn't run as smoothly as we had hope; nonetheless here are the steps that I employed while trying to classify the images.

1. I opened the multiband, and then chose the RGB composite by clicking the mouse to the right of the images name. This allowed only one picture to open.

2. I chose the tracer cursor from the box on the right hand portion of the screne. I outlined a distinct area of the map, in this case Lake Kivu. I then chose collect statistics from the Image menu. After the stats has been collected, I chose edit training sets from the Image menu. I named the new training set Lake Kivu, and chose the color that I wanted the classified portion of the map to convey on the new image. I, then, classified the are by chosing the Superfied Classification from Image menu. When you are only classifiing one portion of the map, it will not take long, but when you combine more than classification, it will take thirty minutes to an hour. So for each individual classification, run an initial seperate classification of that one area, so that you may see the results before running a lengthy full scale classificaiton.

3. For the two images that I classified, I couldn't classify anymore than two training sets without an extreme drop off in precision.

References

Burt M.L., G. Wadge, and W.A. Scott. Simple stochastic modeling of the eruption history of a basaltic volcano: Nyamuragira, Zaire. Bull Volcanol. (1994) 56:87-97.

Demant, A., P. Lestrade, R.T. Lubala, A.B. Kampunzu, and J. Durieux. Volcanological and petrological evolution of Nyiragongo volcano, Virunga volcanic feild, Zaire.Bull. Volcanol. (1994) 56:47-61.

Ebinger, C.J. Tectonic developement of the western branch of the Eastern African rift system. Geological Society of American Bulletin. July (1989) 101: 885-903.

Hamaguchi, H., T. Nishumura, and N. Zana. Process of the 1977 Nyriagongo eruption inferred from the analysis of long-period earth uakes and volcanic tremors.Tectonophysics. (1992) 209:241-254

Hayashi, S., M. Kasahara, K. Tanaka, H. Hamaguchi, and N. Zana. Major element chemistry of recent eruptive products from Nyamuragira volcano, Africa (1976-1989). Tectonophysics (1992) 209:273-276.

Kasahara, M., H. Hamaguchi, K. Tanaka, N. Zana, and M. Kabnwik. Recent horizontal crustal movements in and around volcano Nyamuragira, Zaire. Tectonophysics (1992) 209: 267-272.

Lockwood, J. and T. Casadevall. Status of active volcanoes in the Goma area, Eastern Zaire, and associated hazards to residents and refugees. U.S. Geological Survey Open-file Report 94-581. Sept. 20, 1994.

Lukaya, N., M. Ciraba, T. Mavonga, and W. Wafula. Main pattern of waveforms observed in the Virunga volcanic zone, Western rift valley of Africa. Tectonophysics (1992) 209: 261 -265.

Marcelot, G., C. Dupuy, J. Dostal, J.P. Rancon, and A. Pouclet. Geochemistry of mafic rocks from the Lake Kivu (Zaire and Rwanda) section of the western branch of the African rift. J. Volcanol. Geotherm. Res. (1989) 39: 73-88.

Tazieff, H. Recent activity at Nyiragongo and lava-lake occurences. Bull. of the Geological Society of Finland. Num. 57, part 1-2.

Tazieff, H. Mt. Niragongo: renewed activity of the lava lake. J. Volcanol. Geotherm. Res., (1984) 20: 267-280.

Tazieff, H., An exceptional eruption: Mt. Niragongo, Jan 10th, 1977. Bull. Volcanol. (1976-77) 40-3:189-200.

Tilling, R. and J.J. Dvork. Anatomy of a basaltic volcano. Nature. May 13, 1993. 363:125-133.

Wafula, M., N. Zana, T. Mavavonga, and M. Sassa. Recent Seismicity of the Virunga volcanic zone, Western rift, Zaire. Tectonophysics., (1992) 209:259-260.

Zana, N. K. Tanaka, and M. Kasahara. Main geophysical features related to the Virunga zone, Western rift, and their volcanic implications. Tectonophysics (1992) 209:255-257.

Other references: Catalogue of Active Volcanoes 1951-1958. 2,3-2 and 2,3-3

MEASURING THE SPECTRAL EMISSIVITY OF THERMAL PROTECTION MATERIALS DURING ATMOSPHERIC REENTRY SIMULATION

S14-18
76329
10P
234362

Final Report

NASA/ASEE Summer Faculty Fellowship Program--1995

Johnson Space Center

Prepared By:	Elizabeth Marble
Academic Rank:	Undergraduate
University & Department:	University of Houston-- Clear Lake Campus Division of Natural Sciences Houston, Texas 77058

NASA/JSC

Directorate:	Engineering
Division:	Aeroscience and Flight Mechanics
Branch:	Aeroscience
JSC Colleague:	Carl D. Scott
Date Submitted:	September 6, 1995
Contract Number:	NGT-44-001-800

ABSTRACT

Hypersonic spacecraft reentering the earth's atmosphere encounter extreme heat due to atmospheric friction. Thermal protection system (TPS) materials shield the craft from this searing heat, which can reach temperatures of 2900° F.

Various thermophysical and optical properties of TPS materials are tested at the Johnson Space Center Atmospheric Reentry Materials and Structures Evaluation Facility, which has the capability to simulate critical environmental conditions associated with entry into the earth's atmosphere. Emissivity is an optical property that determines how well a material will reradiate incident heat back into the atmosphere upon reentry, thus protecting the spacecraft from the intense frictional heat. This report describes a method of measuring TPS emissivities using the SR5000 Scanning Spectroradiometer, and includes system characteristics, sample data, and operational procedures developed for arc-jet applications.

INTRODUCTION

Background

Hypersonic spacecraft reentering the earth's atmosphere encounter extreme heat due to atmospheric friction. As the speeding craft rips through the air, its movement agitates and compresses the gaseous molecules in the upper atmosphere, surrounding the craft with a shock wave and converting the vehicle's kinetic energy to thermal energy. The resulting heat is so acute that it tears electrons away from the air molecules, producing a plasma of hot particles. Reentry temperatures, which can reach 2900° F, are thwarted by Thermal Protection System (TPS) materials developed to absorb and reradiate the heat, keeping the aluminum airframe of the spacecraft below its threshold of 350° F.

The Atmospheric Reentry Materials and Structures Evaluation Facility (ARMSEF) at the Johnson Space Center is a convective (plasma arc-jet) heating facility, capable of simulating critical environmental conditions associated with entry into the earth's atmosphere. While undergoing reentry simulation, TPS materials are tested for a variety of thermophysical and optical properties, evaluated for mission life and operational limitations and investigated for flight anomalies.

Tests have been conducted to obtain thermophysical and optical properties of two TPS materials that have been proposed for use on the single-stage-to-orbit ACRV/X35[1] vehicle. The proposed materials are the Silicon Impregnated Reusable Ceramic Ablator (SIRCA) developed by the Ames Research Center and the ACUSIL 1 ablator developed by the Aerotherm Corporation. The test objectives were to obtain the relevant properties of the materials, provide correlations to thermal math models, and provide qualitative evaluation of the materials at the flight conditions expected during the ACRV/X35 reentry flight.

An important optical property governing the effectiveness of a TPS is that of emissivity. Roughly speaking, emissivity is a measure of how well a material will reradiate incident heat back into the environment. A TPS material of high emissivity is desired as it will better protect the spacecraft from incineration during atmospheric reentry.

In 1992 an improved technique for determining the spectral emissivities of TPS materials was implemented at the ARMSEF. This technique utilizes the SR5000 rapid scanning spectroradiometer procured from CI Systems. The instrument was supplied with a custom built filter to record emissions of TPS surfaces within the range from 0.7 microns to 8.0 microns, this range providing the most useful data for the temperatures encountered in the Shuttle and ACRV/X35 programs.[2]

The emissivities of the ACRV/X35 experimental ablators were measured at the ARMSEF using the PC-based scanning spectroradiometer and its accompanying software. This report describes the method of obtaining emissivity measurements with the spectroradiometer and does not report data pertaining to the proprietary materials that were scanned.

THEORETICAL

Blackbody Radiation

Every object in the universe continuously emits and absorbs energy in the form of electromagnetic radiation. The radiated energy originates from the internal energy associated with atomic and molecular motion and the accompanying accelerations of electrical charges within the object. For an object to maintain thermal equilibrium its rates of emission and absorption of energy must be equal. This equality leads to *Kirchhoff's Law* that, if $M_\lambda(T)$ (spectral radiant emittance) is the power emitted per unit area per unit of wavelength at the wavelength λ , and $\alpha_\lambda(T)$ (spectral absorbtance) is the fraction of the incident power per unit area per unit of wavelength, all objects in thermal equilibrium at the same absolute temperature T have the same ratio of $M_\lambda(T) / \alpha_\lambda(T)$. It follows that an object having the maximum possible absorbtance $[\alpha_\lambda(T) = 1]$ also has the maximum possible spectral radiant emittance $[M^b{}_\lambda(T)]$. Such a perfect absorber and perfect emitter is called a *blackbody* and the electromagnetic energy it emits is called *blackbody radiation.* (Theoretically, a blackbody TPS material would reradiate all of the absorbed heat back into the atmosphere). No true blackbody exists, but a small hole through which radiation escapes from an isothermal enclosure is an excellent approximation. Any real substance is characterized by a spectral emissivity $\varepsilon_\lambda(T)$ $[0 < \varepsilon_\lambda(T) < 1]$ expressing its spectral radiant emittance as some fraction of that of a blackbody at the same temperature, $M_\lambda(T) = \varepsilon_\lambda(T)\, M^b{}_\lambda(T)$. With this, Kirchoff's Law becomes $\varepsilon_\lambda(T) = \alpha_\lambda(T)$. This is an important result--a good emitter of thermal radiation is also a good absorber. It follows also that a good reflector is a poor emitter.[3]

Emissivity:

$$\varepsilon_\lambda(T) = \frac{M_\lambda(T)}{M^b{}_\lambda(T)}$$

Graybody Radiation

As shown, the spectral emissivity of a material is the ratio between the radiation emitted of it and the radiation emitted of a blackbody at the same temperature, in all wavelengths. For the most part, $\varepsilon_\lambda(T)$ varies only slowly with temperature, but rather more with wavelength. For a large number of materials, however, $\varepsilon_\lambda(T)$ is approximately constant over a fairly wide wavelength range. These are called *graybodies* . Many TPS materials radiate as graybodies. Their emissivities can be determined by measuring their spectral radiant emittance with the scanning spectroradiometer, then dividing the specimen scan by a blackbody scan of the same temperature. The emissivity of a graybody TPS material is a measure of how well it approximates a blackbody, and therefore, how well it reradiates incident heat back into the atmosphere.

EXPERIMENT

Reentry Simulation Chamber

The reentry simulation tests were conducted in Test Position 2 of the ARMSEF (Fig. 1). A segmented, constricted arc heater is used to generate a high temperature plasma flow. Test gases (23%O_2 and 77% N_2 by mass) are heated by an electrical arc discharge within the constrictor column of the arc heater. The highly energized gas is then injected into an evacuated chamber through a water-cooled conical nozzle that has a 15° half-angle. TPS test specimens, located inside the chamber, were subjected to constant surface heating cycles. By varying the current to the arc heater, the surface temperature of the test specimens was kept constant, as recorded by the optical pyrometer.

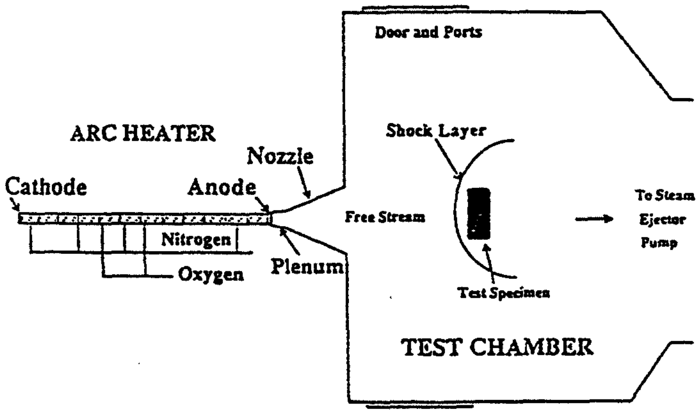

Figure 1.--General setup of arc heater and evacuated reentry simulation chamber.

Scanner Setup

The scanning spectroradiometer was mounted on a tripod and placed just outside the atmospheric reentry simulation chamber (Fig. 2), where it could collect TPS radiation through a 5" diameter zinc selenide transmission window installed in a porthole of the chamber door. A gold first surface Pyrex mirror was mounted near the nozzle exit to reflect the TPS specimen radiation into the instrument's optical system. To minimize directional effects the specimen distance to the nozzle exit diameter was selected to permit viewing at 45° or less from the normal to the test surface. This distance was set at 14". An aluminum tunnel was used to enclose the optical path between the chamber door window and the scanner detector head to allow a nitrogen purge, thus removing the atmospheric attenuation due to water and carbon dioxide.

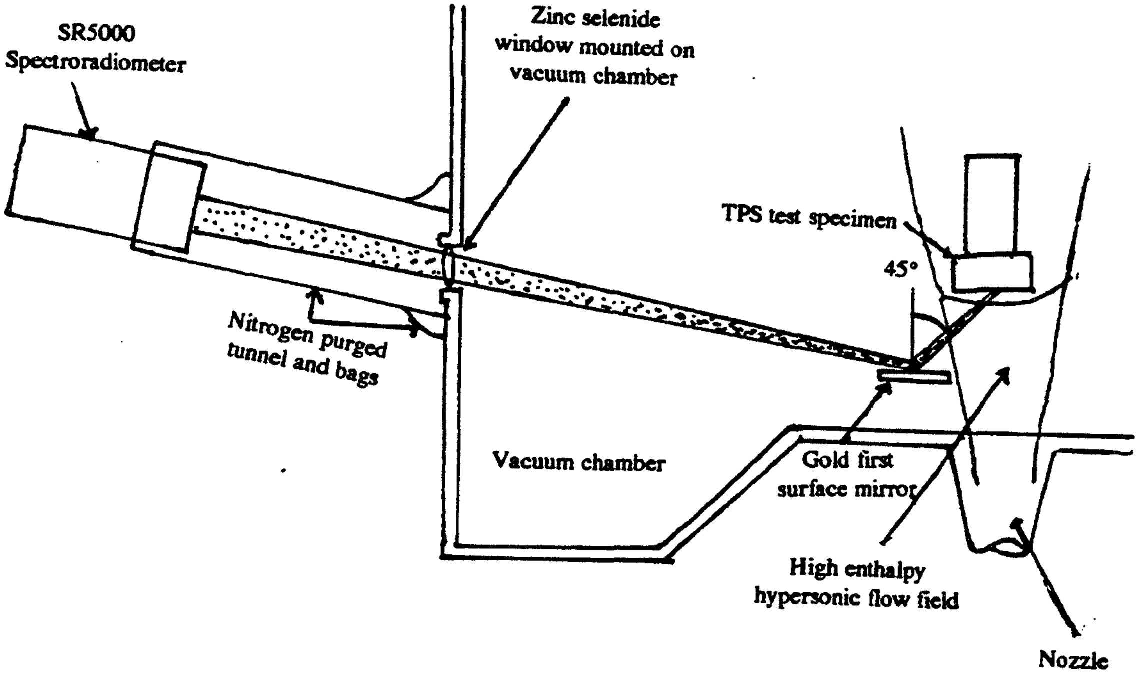

Figure 2.--Scanning spectroradiometer experimental setup.

Calibrating the system by scanning a blackbody in the chamber was not possible because of the facility's demanding test schedule. Instead, a blackbody was scanned alongside of the chamber at the correct tripod to TPS test specimen distance (141") with a gold first surface mirror and a zinc selenide transmission window in the optical path. Because of the severe atmospheric attenuation due to water and carbon dioxide, an aluminum enclosure was built to permit the optical path from the detector head to the blackbody to be purged by nitrogen. In this way, the system could be calibrated in a humidity-free optical path as required by the evacuated chamber. A smaller aluminum enclosure was used when running the experiment so that the path between the detector head and chamber window could be purged.

OBTAINING EMISSIVITY MEASUREMENTS

Design Theory

The SR5000 Scanning Spectroradiometer is used to measure the spectral radiant emittance of a TPS material undergoing atmospheric reentry simulation. The radiation emitted by this material is directed toward the instrument, where it is collected, focused on the first focal plane and chopped by a precision rotating wheel with blades (Fig. 3). After entering the field stop it is refocused by an ellipsoidal mirror onto the detector, which outputs an amplified AC signal. This signal and the synchronous reference signal from the chopper are processed through a synchronous detection circuit. Now a DC signal, it is further amplified, digitized and transferred to the computer for additional processing and display.

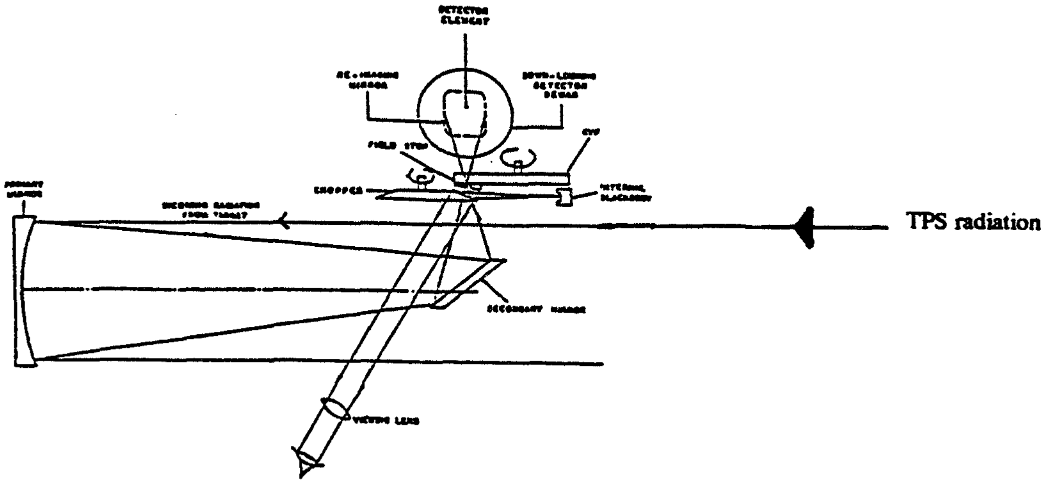

Figure 3.--Optical layout for the scanning spectroradiometer.

So that a quantitative result may be obtained, the precise amount of radiation seen by the detector when the chopper obstructs the TPS radiation must be known. For this reason, when the chopper obstructs the field of view, it exposes the detector to the radiation of a reference blackbody. The blackbody temperature is continuously and precisely monitored digitally by the computer in order to be used in the calibration procedure and in the calculation of the spectral radiant emittance.

Through a combination of calibration procedures and mathematical processing of the instrument signal output, the spectral radiant emittance is converted to the *spectral radiance.*[4] Spectral radiance is measured in units of watt/sterad.micron.cm^2, as a function of wavelength.

Data Processing

Emissivity data was obtained with the accompanying SR5000 software, run on a 386 PC. Plots of TPS spectral radiance vs. wavelength were superimposed on blackbody curves of the same temperature (Fig. 4). Plots of TPS emissivity vs. wavelength were then obtained by dividing the specimen plot by the blackbody plot (Fig. 5).

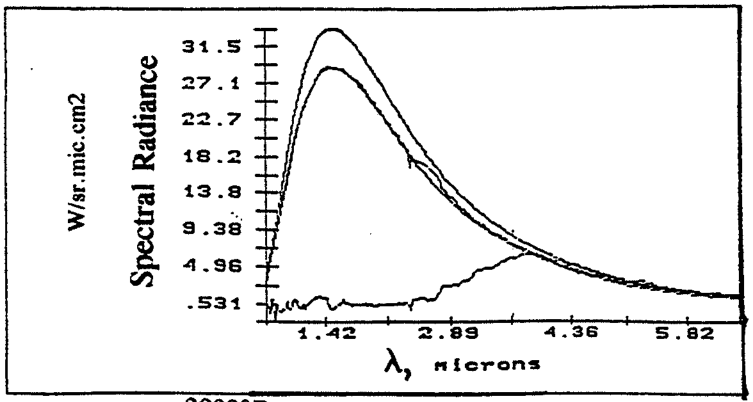

TOP CURVE- 3000°F PLANK FUNCTION
MIDDLE CURVES- SPECIMEN EMISSION AND .86 GRAYBODY OVERLAYED
LOWER CURVE- SPECIMEN EMISSION WITHOUT COATING

Figure 4.--(Above) A sample monitor display of spectral radiance vs. wavelength for a Planck blackbody curve (generated by SR5000 program), a TPS graybody curve (obtained with scanner) and a TPS non-graybody curve (obtained with scanner).

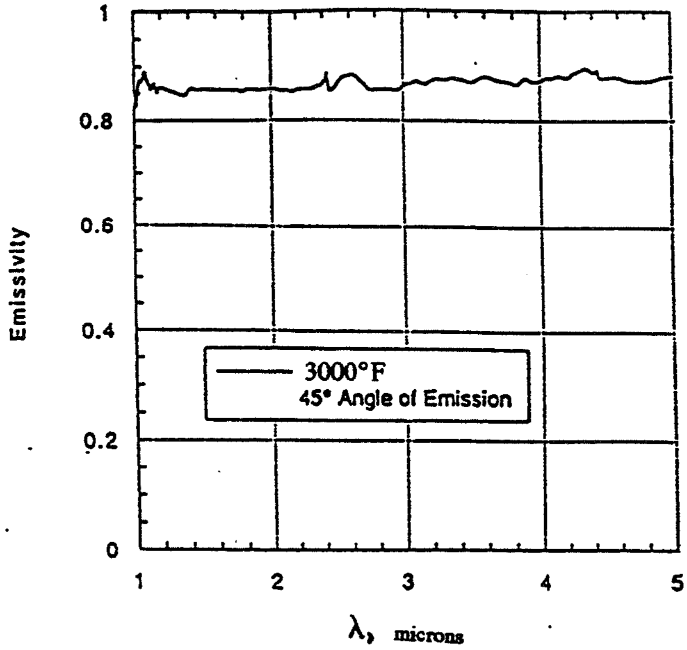

Figure 5.--A sample plot of TPS emissivity vs. wavelength, as obtained by dividing the TPS graybody plot by the Planck blackbody plot.

DISCUSSION

Currently, estimates of emissivities and temperatures for uninstrumented test articles are made manually by trial and error fitting of graybody curves for various emissivities and temperatures to the test data. The ARMSEF plans to eventually incorporate a program that will select the best fit based on iterative minimization of the area between the graybody curve and the test data.

REFERENCES

1. Note: The ACRV/X35 is a reusable single-stage-to-orbit launch vehicle currently under development as part of the National AeroSpace Plane (NASP) program. It combines a liquid hydrogen/liquid oxygen Linear Aerospike rocket with a lifting body shape, allowing the vehicle to take off vertically and land horizontally like the Space Shuttles.

2. J. D. Milhoan, "A Technique for Measuring Spectral Emissivities of Thermal Protection Materials During Reentry Simulation Testing," NASA/JSC/ARMSEF, Bldg. 222 Memo, (1992).

3. R. E. Bedford, "Blackbody Radiation," Encyclopedia of Physics, 2nd Edition, VCH Publishers, Inc. (1991).

4. CI Systems, "The SR5000 Scanning Spectroradiometer: User's Manual," NASA/JSC/ARMSEF, (1990).

515-51
76330
234363
16P.

AN INTELLIGENT CROP PLANNING TOOL FOR CONTROLLED ECOLOGICAL LIFE SUPPORT SYSTEMS

Final Report
NASA/ASEE Summer Faculty Fellowship Program -- 1995
Johnson Space Center

Prepared By:	Laura O. Whitaker
Academic Rank:	Graduate Student
University & Department:	Texas A&M University Department of Industrial Engineering College Station, Texas 77843-3131
Prepared By:	Dr. Jorge Leon
Academic Rank:	Assistant Professor
University & Department:	Texas A&M University Department of Industrial Engineering & Department of Engineering Technology College Station, Texas 77843

NASA/JSC	
Directorate:	Engineering
Division:	Automation, Robotics, & Simulation
Branch:	Intelligent Systems
JSC Colleague:	Mariata McCamy
Date Submitted:	August 11, 1995
Contract Number:	NGT-44-001-800

ABSTRACT

This paper describes a crop planning tool developed for the Controlled Ecological Life Support Systems, CELSS, project which is in the research phases at various NASA facilities. The Crop Planning Tool was developed to assist in the understanding of the long term applications of a CELSS environment. The tool consists of a crop schedule generator as well as a crop schedule simulator. The importance of crop planning tools such as the one developed is discussed. The simulator is outlined in detail while the schedule generator is touched upon briefly. The simulator consists of data inputs, plant and human models, and various other CELSS activity models such as food consumption and waste regeneration. The program inputs such as crew data and crop states are discussed. References are included for all nominal parameters used. Activities including harvesting, planting, plant respiration, and human respiration are discussed using mathematical models. Plans provided to the simulator by the plan generator are evaluated for their "fitness" to the CELSS environment with an objective function based upon daily reservoir levels. Sample runs of the Crop Planning Tool and future needs for the tool are detailed.

INTRODUCTION

In order for the success of long duration manned missions into space, the concept of closed ecological life support systems (CELSS) are being explored by the National Aeronautics and Space Administration. Development of life support systems relatively independent of resupply are necessary for a reduction of launch weight and resupply penalties. Long duration missions will require autonomous systems capable of maintaining any series of internal environments, as well as regenerating wholesome food and air from waste materials (1). Within CELSS, gases such as oxygen and carbon dioxide and food can be described as reservoirs which must be maintained within some boundaries for the survival of both human and plant life. As well as maintaining adequate reservoirs, a CELSS has rigid system constraints such as space and time constraints. A CELSS environment contains physiochemical as well as biological functions such as food production. With these functions and the rigid system constraints of a CELSS, the long term dynamics of the system must be explored.

One primary concern of a system which relies on plant growth for food and gas reservoir balance is the long term planning and scheduling of crop planting. What crops to plant, when to plant, and how much to plant can affect the reservoir levels and the system constraints of a CELSS system weeks, months, or even years in the future. A Crop Planning Tool has been developed which addresses these long term implications of the CELSS environment. The Crop Planning Tool is comprised of a crop schedule generator developed by V. J. Leon (2) coupled with a crop schedule simulator. The purpose of the Crop Schedule Simulator is to provide a proof of concept simulator which will allow the Crop Schedule Generator to produce plans which are flexible and adaptable while providing maximum probability of survival for the crew. The Crop Schedule Simulator will be discussed here in detail while the algorithm for the Crop Schedule Generator will be touched upon briefly.

CROP PLANNING TOOL

The importance of crop planning for a CELSS is important for two reasons. First, what will be planted today will affect the crew's probability of survival tomorrow. Second, limited reservoirs and buffers in the CELSS environment make crop planning an important decision. The crop schedule decision is a difficult one because of the system constraints affecting a CELSS environment. These constraints can be grouped into the following areas: nutrient constraints, processing constraints, space and time constraints, and reservoir requirements. Nutrient requirements for both plants and humans must be met and balanced. This process requires proper food requirements and regeneration systems such as recycling of inedible biomass in order to recover valuable minerals and nutrients for plants. Obeying constraints on processes such as harvesting and planting by humans or robots is necessary while taking into account other daily maintenance and research activities on the part of the crew. Space and time constraints are vital to the balance of a CELSS because limited planting space and storage buffers exist. While satisfying these constraints, a CELSS environment must maintain adequate reservoirs of gases such as oxygen and carbon dioxide, water, and amounts of fresh and stored edibles.

SIMULATOR

The Crop Schedule Simulator, which will be referred to as the Simulator, requires the initial state of the system as well as a crop planting schedule provided by the Crop Schedule Generator (2), which will be referred to as the Planner. The initial state of the system includes information pertaining to the crew, crops, and the environment. The plan which is obtained from the crop planner module is integrated with the initial state to simulate the activities of the CELSS over some ΔT time period. The outcome of the simulation is then evaluated to obtain an objective function for the overall fitness of the plan. The

Simulator also calculates any adjustments required by the CELSS system. For example, the Simulator might suggest increased efficiency in the waste regeneration systems. These changes will be reflected in the waste processing parameters.

Assumptions

In developing this proof of concept Crop Planning Tool, several assumptions have been made.

- The Simulator developed here tracks solely oxygen and carbon dioxide levels. Other vital resources such as water and nutrients have not been modeled.
- Two crop models are utilized and therefore, two planting options exist, either wheat or lettuce.
- Within a time slice (1 day for this implementation) average growth rates of plants and activity levels of crew members are assumed. It is assumed that there exists a constant hour to hour monitoring and control system which maintains target gas concentrations in the air.
- With the existence of a monitoring and control system, the Planner and Simulator will consider only tank levels and not in air concentrations.

INPUT -- INITIAL STATE

Capturing the initial state of the CELSS is vital for two reasons. One, the outcome of the system depends on the initial state of that system. Futhermore, detailing an initial state allows dynamic planning capabilities. The initial state can be categorized in five main areas: Reservoir Levels, Crew Information, Crop States, Crop Historical Data, Waste Processing Parameters.

Reservoir Levels

Reservoir levels are required for gases and crops in the system. Inputs include the initial storage level of each type gas or crop, the minimum reservoir level, the nominal reservoir level, and the maximum reservoir level. These values can vary for design purposes.

Crew Information

Crew data requirements include:

- Average Metabolic Rate (BTU per hour)
- Respiratory Quotient
- Food Requirement (kg per person per day)
- Menu Desires: Rating factor for the proportion of each type of crop which the crew desires for consumption
- Average Oxygen Generation and Carbon Dioxide Production Rates (kg per person per day)
- Crew Member Profile: Number of crew members per day

Table 1 indicates the values used for each crew data requirement above and the associated reference.

TABLE 1. CREW DATA REQUIREMENTS

DATA	VALUE	REFERENCE
Average Metabolic Rate	619 (BTU/hour)	3
Respiratory Quotient	.90	3
Food Requirement	.800 (kg/person - day)	4 (based on wheat as only provider)
Average Oxygen Generation and Carbon Dioxide Production Rates	1.096 Oxygen 1.356 Carbon Dioxide (kg/person - day)	3
Crew Member Profile	See Reference	5

Crop States
The Simulator is also given the initial state of crops which are in planting. The Simulator tracks the state of trays in "batches". Each batch of plants is of a particular plant type and the batch was planted or is scheduled to be planted at the same time. The information required of each batch in planting is the following: number of trays associated with the batch, time the batch was planted, plant type of the batch. These batches can then be preprocessed with general parameters utilized for a plant of its particular plant type. For instance, plant density (plants/m^2), temperature of the biom (°C), and edible/inedible biomass ratios are associated with each batch. General plant model parameters are discussed in (6).

Crop Historical Data
Each crop model utilized in the simulation produce rates of oxygen production and carbon dioxide use as well as biomass production rates. Using these models, historical data is compiled by the Simulator to be used in long term planning by the Planner. Table 2 summarizes this data. A storage conversion is also necessary to check storage limits of edible food.

TABLE 2. HISTORICAL CROP PARAMETERS

DATA	Wheat	Lettuce	REFERENCE
Edible Biomass at Harvest	0.424 (kg/m^2)	2.115 (kg/m^2)	6, 7, 8
Inedible Biomas at Harvest	2.230	0.235	6, 7, 8
Total Biomass at Harvest	2.654	2.350	6, 7, 8
Growth Cycle	80 days	30 days	7
Storage Conversion	0.001 m^3/kg edible	0.003 m^3/kg edible	7

Total biomass at harvest data was obtained from the Wheat and Lettuce Crop Growth Models in (6). The amount of edible biomass obtained from the total biomass at harvest for wheat varied widely from 16% in (8) to 45% in (4). For the general wheat plant, 16% was used.

Waste Processing Parameters
Waste processing parameters are necessary from the system to determine how efficiently the waste regeneration system performs. Human waste processing rates and plant waste processing rates were derived from (4). During the simulation, reservoirs of oxygen and carbon dioxide must be adjusted to account for waste processing.

The amount of oxygen used for waste processing and the amount of carbon dioxide generated by human and plant waste processing can be broken down into human waste and plant waste requirements using the ratio of human or plant waste to the total waste from both sources. These ratios can then be used to breakdown the amount of oxygen and carbon dioxide used and given off respectively from waste processing due to plant waste and human waste. Gas generation and utilization rates due to the processing of human and plant wastes were found using (4). For example:

Carbon dioxide given off due to processing human wastes:

$$\left(\frac{(.16136)}{(.16136+1.04475)}\right)2.33452 = 0.313 kg/p-d$$

(All numbers are in units of kg / p - d which refers to kilograms per person per day)

Carbon dioxide given off due to processing plant wastes:

$$\left(\frac{(1.04475)}{(.16136+1.04475)}\right)2.33452 = 2.023 kg/p-d$$

Similarily, oxygen utilized due to human waste processing was found to be 0.288 $kg\ /\ p\ -\ d$. Oxygen utilized due to plant waste processing was found to be 1.866 $kg\ /\ p\ -\ d$. In order to look at the mass flows concerning plants, the mass units can be converted into kilograms per meter squared (in order to take into account a specific area of plants). Using these values, the amount of carbon dioxide generated in waste processing due to plants can be found using the following ratios:

$$\left(\frac{2.023kg/p-d(CO_2forplantwaste)}{1.045kg/p-d(plantwaste)}\right)=1.936\frac{kg(CO_2forplantwaste)}{kg(plantwaste)}$$

Similarily, the amount of oxygen utilized by the waste processing of inedible plant mass is found using the following ratios:

$$\left(\frac{1.866kg/p-d(O_2forplantwaste)}{1.045kg/p-d(plantwaste)}\right)=1.786\frac{kg(O_2forplantwaste)}{kg(plantwaste)}$$

These values were found based on amounts of inedible biomass at harvest. Therefore, the model discussed here will adjust reservoir levels of oxygen and carbon dioxide when plants are harvested.

INPUT -- A PLAN

A plan consists of the following: What crop to plant, How much to plant, When to plant. The plan is generated by the Crop Schedule Generator and is delivered to the Simulator in the form of an event list.

SIMULATOR OUTLINE

The simulation updates critical reservoirs daily. Activities required daily which effect these reservoirs include: harvesting, planting, plant respiration, human respiration, human consumption, and adjustments to reservoirs. Figure 1 depicts the overall model of a CELSS with average data abstracted from the human and plant models used in the Simulator. Figure 2 depicts the simulation flow. Any harvesting or planting required in each time period are simulated. At harvest, edible and inedible biomass ratios are utilized to calculate the amount of food and wastes in kilograms obtained from each harvested batch. The food level of the crop is then adjusted, and oxygen and carbon dioxide tank levels are appropriately adjusted for waste processing of inedible biomass resulting from each harvest.

PLANT RESPIRATION

Plant respiration simulates plants producing oxygen and using carbon dioxide. For these purposes, the biomass rate models for wheat and lettuce developed in (4) are used. The plant respiration function therefore, not only simulates the respiration of plants, but also simulates their growth. In this manner, biomass is accumulated over each plant's growth cycle.

Wheat Model

Miller, McFadden, and Sirko (4) developed the biomass production model utilized by the Simulator. The wheat model is valid for a specific range of environmental parameters documented in (4). The first step in the wheat model is to determine the development rate in terms of crop age and

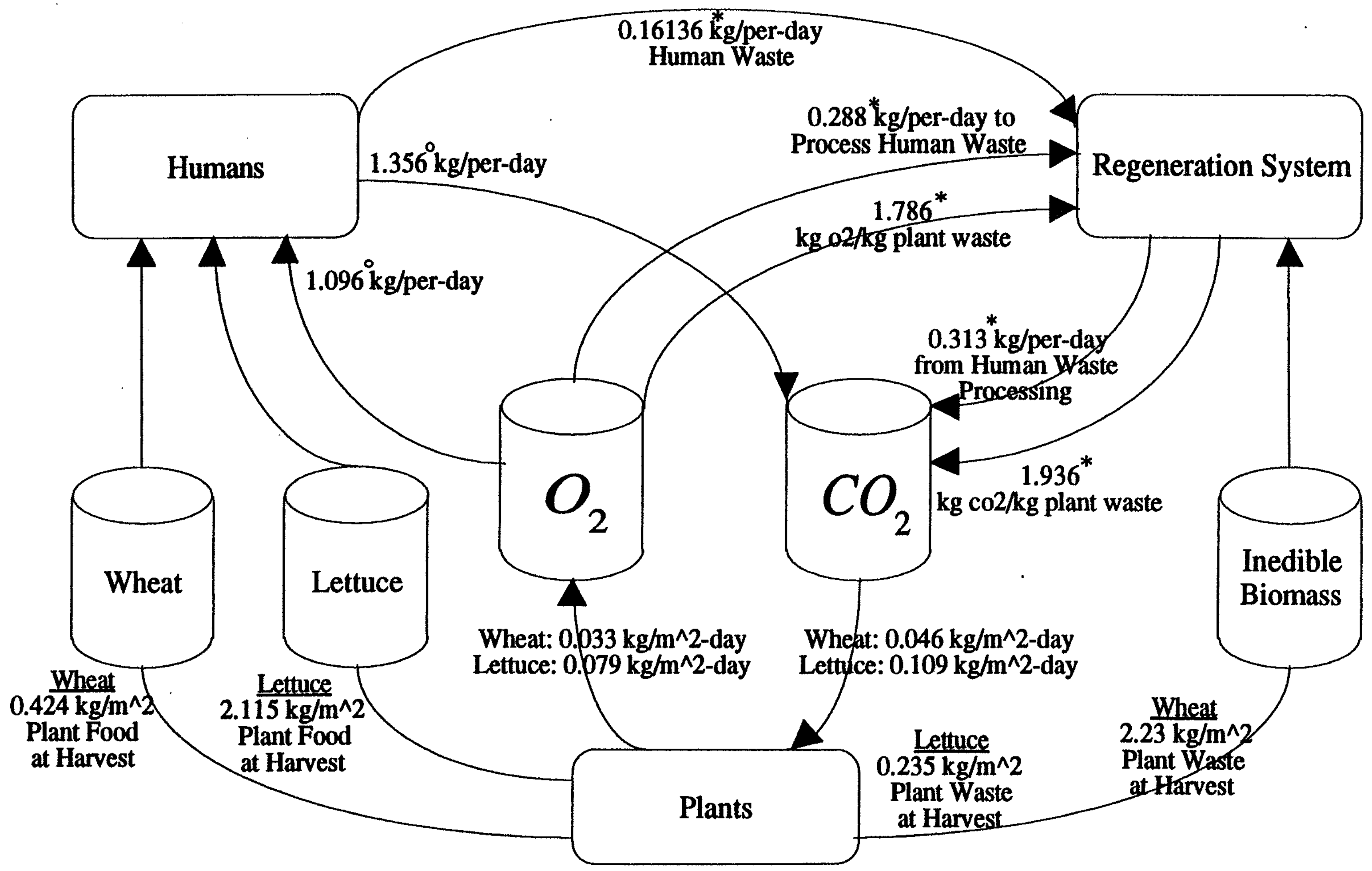

° (3)
* (4)
All others (6)

Wheat: Eb = .16 IEb = .84 (8)
Ave. Biomass at Harvest = 2.65 kg/m^2
Lettuce: Eb = .90 IEb = .10 (7)
Ave. Biomass at Harvest = 2.35 kg/m^2

Figure 1. CELSS World Model with Plant Model Data

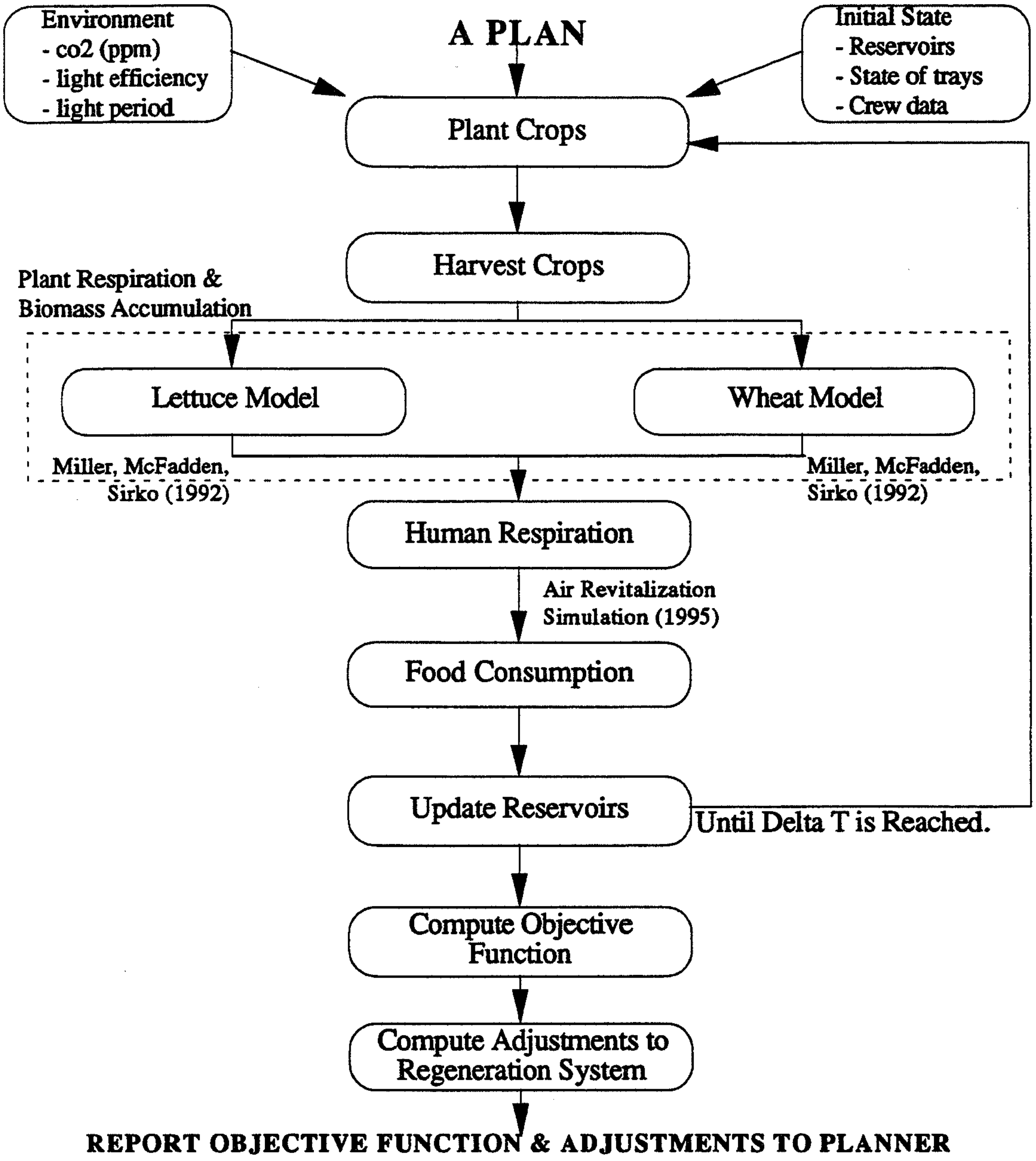

Figure 2. Simulator Block Diagram

temperature. In order to introduce the effect of photoperiod, the development rate is adjusted by a ratio of the nominal photoperiod (hours) to the daily daylight interval (hours). The age, temperature, and photoperiod dependent crop development rate can then be written:

$$r(T,\tau;t) = a_1 + \frac{a_2(t)(\tau)}{\tau_N} + \frac{a_3(t_l)^2(\tau)^2}{\tau_N^2}$$

$a_1 = -3.782 + 0.3.56T$

$a_2 = 0.24696 + 0.2515T$

$a_3 = 0.06175 - 0.006866T$

where $\tau =$ Daily Daylight Interval, $\tau_N =$ Nominal Photoperiod (20 hr), and t = Crop Age. Other effects such as light intensity and carbon dioxide concentration are taken into account. The average biomass rate *B(A)* is found where *A* is the photosynthetic active radiation provided by the lights. The photosynthetic active radiation is scaled by the canopy's age. The average biomass rate is then written:

$$\begin{aligned}
&B(A_L) = -7.6146 + 0.11114A_L - 0.00002149A_L^{\,2} \\
&A = ((160)(Eff)(Conv)(Y))/a \\
&A_L = A - (1.167(H))
\end{aligned}$$

where *Eff* = Electrical efficiency of the lights (0.095 nominally), *Conv* = µmol/J for lights (4.59 for cool white fluorescent lights), *a* = Area of each plant growth tray(m^2), and *H* is the height of the lights above the crop canopy(cm). The crop development rate is then scaled to take the average biomass production rate into account by:

$$r(T,\tau,A;t) = r(T,\tau;t)\frac{B(A_L)}{B(A_N)}$$

where A_N = 1204µmol/m^2-sec and $B(A_N)$ = 95 grams/m^2-day. In order to incorporate the effect of carbon dioxide concentration, the net photosynthesis *C(p)* in µmol/m^2-sec is found and then integrated into the crop development rate. Finally, to account for varying plant density a scaling factor is integrated into the crop development rate. The crop development rate is found in grams/m^2-day.

$$C(p) = 72.0 - 78.89/e^{p/400}$$

$$r(T,\tau,A,p,d;t) = r(T,\tau,A;t)\frac{C(p)}{C(p_N)}\frac{d}{d_N}$$

where p = Carbon dioxide concentration in the air, p_N = Nominal carbon dioxide concentration(2000 ppm), $C(p_N)$ = 71.47 µmol/m^2-sec, d = Plant density (plants/m^2), and d_N = Nominal plant density (2000 plants/m^2). The corresponding carbon dioxide and oxygen rates were found by Miller, McFadden, and Sirko using a generalized photosynthetic equation. From these equations, it was determined that for 1 gram of biomass produced 0.727 grams of oxygen are produced and 1.381 grams of carbon dioxide are assimilated.

Lettuce Model

Miller, McFadden, and Sirko (4) developed a mathematical model for carbon dioxide assimilation for Waldman's green lettuce. The model developed is a function of the carbon dioxide concentration in the air, *x*, the light intensity, *y*, and crop age, *t*. The carbon dioxide assimilation can be written:

$$r_{CO_2}(t,x,y) = r(t)g(x,y)$$

If $t < 11$ days,

$$r(t) = 0.31752$$

Else if $11 < t < 30$,

$$r(t) = 26.72 - 5.45t + 0.341t^2 - 0.0059t^3$$

$$CO_2N = -3.333 + 0.00333x$$

$$LTN = -3.0 + 0.5y$$

$$g(x,y) = 1.0 + 0.12CO_2N + 0.354LTN - 0.0732LTN^2$$

where $r(t)$ is the nominal carbon dioxide assimilation as a function of crop age in grams per hour, $g(x,y)$ is the off-nominal carbon dioxide assimilation as a function of carbon dioxide concentration in the air and light intensity in grams per hour, and CO_2N and LTN are normalized carbon dioxide concentration and light intensity, respectively. The model only applies within specific parameter ranges (4). Moreover, prior to day 11 in the growth cycle of a lettuce plant, a constant rate of carbon dioxide assimilation is used which is equal to the nominal assimilation rate for an 11 day old lettuce plant, 0.3175 grams per hour. The corresponding biomass production and oxygen production rates were found by Miller, McFadden, and Sirko using a generalized photosynthetic equation. From these equations, it was determined that for 1 gram of carbon dioxide assimilated 0.727 grams of oxygen are produced and 0.723 grams of dry biomass are produced.

HUMAN RESPIRATION

The human respiratory model used in the Simulator was developed at the Johnson Space Center for an Air Revitalization Simulation for a CELSS environment (3). The model utilizes the human respiratory quotient, RQ, and metabolic rate, MR, to produce an oxygen use rate in kilograms per person per day and a carbon dioxide generation rate in kilograms per person per day. An average metabolic rate is utilized to calculate average gas rates daily. It is assumed that a real time control and monitoring system would account for hourly metabolic profiles.

$$O_2(lb/person-hour) = [0.1708 - (RQ - 0.707)/0.293)(0.0123)](MR)$$
$$O_2(kg/person-day) = (10.88)O_2(lb/person-hour)$$
$$CO_2(kg/person-day) = (44/32)(RQ)(O_2(kg/person-day))$$

HUMAN CONSUMPTION

In order to simulate the depletion of food reservoirs through human consumption, the idea of menus was introduced. Delivered to the Planner and Simulator are menu preferences by the crew. The menu is a ranking of what portions of each type crop would be desired for the crew's daily food requirement. The consumption function is called daily by the Simulator. The consumption function follows the outline below:

(A) Calculate the total daily food requirement for the crew.
(B) While all food reservoirs are not depleted and the total daily requirement is not met:
    (i) Update menu desires. Recalculate where needed for depleted reservoirs.
    (ii) Deplete each reservoir according to daily requirements and preferences.

The Simulator not only keeps track of food levels for each crop but in addition, tracks how much edible storage remains of each harvested batch. Therefore, as food levels are depleted, batches are depleted accordingly. The Simulator depletes batches on a first-in, first-out (FIFO) basis. With FIFO in mind, initial food reservoirs are depleted first.

UPDATING RESERVOIRS

Every time period or time slice (1 day in this implementation), reservoirs of gases and food must be updated to reflect the planting, harvesting, respiration, and consumption processes. Food levels are adjusted accordingly as plants are harvesting and food is consumed. Gas levels are adjusted at the end of each time period. The following equation is used to update oxygen and carbon dioxide reservoirs.

Gas Level (*t*) = Gas Level (*t* - 1) +/- Gas to Process Human Waste +/- Gas to Process Plant Waste + (Gas Generated - Gas Used)

ADJUSTMENTS

After the Simulator completes the emulation of a plan, various parameter adjustments can be computed. Currently, the Simulator recalculates the waste processing needs for plant wastes. Looking at the trends in oxygen and carbon dioxide tank levels, the Simulator can calculate what waste processing needs would be required in order to obtain nominal gas levels. In order to calculate these adjustments to waste processing parameters, the following formulation is used for each gas:

$$Change = \left(\frac{\sum_{t=t_S}^{t_F} Gas(t) - Gas(t-1)}{t_F - t_S} \right) \left(\frac{t_F - t_S}{\sum_{t=t_S}^{t_F} Harv(t)} \right)$$

where *Gas(t)* is the gas level at time t, t_F is some specified finish time to end summing deviations, t_S is a specified start time to begin summing deviations, and *Harv(t)* is the amount of inedible biomass obtained from harvesting in time period *t*. The start and finish times are used to establish a "warm up" period for data collection.

OBJECTIVE FUNCTION

In order to establish the overall "goodness" of a plan, an objective function was developed which is a function of the vital reservoir levels in the CELSS. Currently, the Simulator considers oxygen, carbon dioxide, wheat, and lettuce levels in these calculations. In order for crew and plant life to be maintained in a CELSS, reservoir levels must be maintained within certain desirable limits. Because levels too low or too high could put the CELSS environment in jeopardy, the objective function penalizes reservoir levels above and below the nominal reservoir levels. First, average deviations from nominal levels are calculated and they are then scaled by the deviation of the maximum and nominal limits. Large deviations are then penalized by a power. The objective function is written as follows:

For $R = 0$ to the number of critical reservoirs, N:

$$D_R = \left(\frac{\left[\sum_{t=0}^{M} \left[\frac{RL(t) - RL_N}{RL_{MX} - RL_N} \right]^{PW} \right]}{M} \right)^{1/PW}$$

$$ObjectiveFunction = \left(\frac{\sum_{R=0}^{N} (D_R)^{PR}}{N} \right)^{1/PR}$$

where D_R is the deviation for each reservoir, M is the amount of time simulated, $RL(t)$ is the reservoir level at time t, RL_N and RL_{MX} are the nominal and maximum reservoir levels, and PW and PR are variables used to penalize large deviations from nominal.

CROP SCHEDULE GENERATOR

The Crop Schedule Generator was implemented following the approach suggested by V. J. Leon (2). The procedure *Planner()* is summarized in the following pseudo-algorithm:

```
Procedure Planner():
    do{
        tnow = tnow + Next_time_incr();
        Update_reservoir();
        Get_donothing_levels(LOOKAHEAD);
        Diagnose_situation();
        Get_desire_probability();
        Repeat for NTRIALS{
            What_to_plant();
            Local_evaluation();
            Save_best();     }
        } while (tnow < PLANNING_HORIZON)
```

Next_time_incr(). This function determines when the next scheduling decision will be made. In the current implementation this time is determined by the following events: (1) next crop ready for harvest, (2) the pre-specified cycle (e.g. WHEAT_CYCLE or LETTUCE_CYCLE) for a given crop when there are empty trays.

Update_reservoir(). This function updates all reservoir levels based on the previous planting decision and the time increment determined in *Next_time_incr().*

Get_donothing_levels(). This function determines the reservoir levels for the next LOOKAHEAD time units if no planting takes place at time tnow.

Diagnose_situation(). Given the *do-nothing* alternative, this function is used to alert the user on the possible problems in the near future. This information can be used for schedule explanation and during schedule decision making.

Get_desire_probability(). This function computes the desirability probability distribution by assuming that a single crop will be planted on all available trays. The impact of this decision is evaluated from time 0 to the next LOOKAHEAD time units. The *do_nothing* action is considered as one of the possible actions. The output of this function is a probability distribution which reflects how desirable it is to plant a given crop type or do-nothing.

The following three procedures are a simplistic approach to search for a good alternative:

What_to_plant(). Using the desirability probability distribution, empty trays are randomly assigned crop-types (including *do_nothing*). Care is taken not to exceed the maximum allowable batch size, (e.g. MAX_WHEAT, MAX_LETTUCE) - if a maximum is reached, the tray is left empty and rescheduled for consideration at the next crop cycle (e.g. WHEAT_CYCLE time units later).

Local_evaluation(). The planting decision made in *What_to_plant()* is evaluated from time 0 up to tnow + LOOKAHEAD time units.

Save_best(). The best decision found in the NTRIAL trials is added to the partial schedule and used to continue the generation process.

Clearly, better solutions can be searched for using more elaborated search procedures. This however is out of the scope of the project and is an interesting direction for future research.

EXAMPLE RUNS

Using the Crop Planning Tool, several runs were made which illustrate the applications of the Crop Planning Tool. A sample of the different scenarios analyzed include:

- Comparing the effects of different amounts of growing area available
- Comparing different crew profiles over a mission life
- Comparing baseline waste processing parameters to the parameters as suggested by the Simulator after an initial run
- Comparing light intensities available to wheat by changing the number of light bulbs per tray
- Comparing different inedible and edible biomass ratios for wheat

Several of these scenarios are depicted in Figures 3 - 6. The food and gas levels are illustrated for each scenario. These examples illustrate the design implications of the Crop Planning Tool. The tool could be utilized to plan for future missions or in the design of a CELSS. The baseline scenario is based on the crew profile outlined in (5), 300 trays for growing at 0.88 m^2 (264m^2 growing area), nominal values for wheat and lettuce parameters, nominal waste processor values, and nominal crew data values as outlined in INPUT -- INITIAL STATE above.

FUTURE NEEDS

Future needs for the Crop Planning Tool include:

- A friendly user interface for parameter changes and the corresponding outcomes to be viewed quickly by the user.
- Additional crop models including more advanced crop models which illustrate gradual harvest crops.
- Integration of the tool with a control and monitoring system as well as a low level task sequencer and resource allocater.
- Critical reservoirs such as water, nutrients, etc. should be included for a more robust world model.
- Model robustness could be improved with real time data from NASA experiments currently in process.
- Processes such as the waste processing system should be modeled explicitly to gain a deeper understanding of the CELSS waste regeneration requirements.

All of these needs stated and more would improve the Crop Planning Tool as a design tool and an evaluation tool for current CELSS environments.

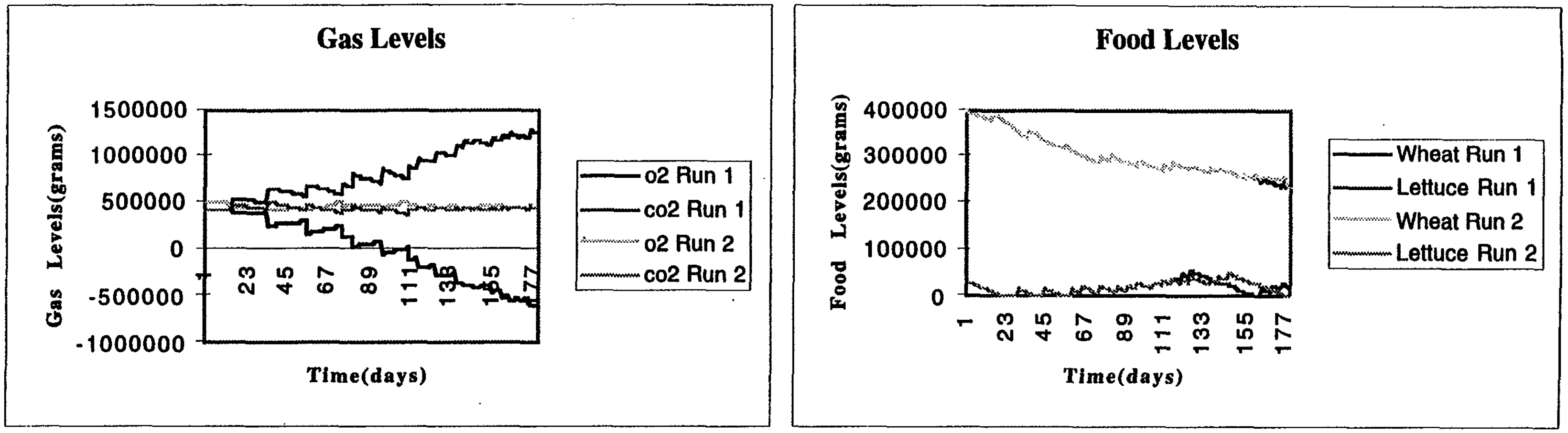

Figure 3 and Figure 4. Gas Levels and Food Levels for Baseline vs. Waste Processing Parameter Change.
Run 1: Baseline with waste processing parameters: 0.288 kg o2/kg-pers-day, 0.313 kg co2/kg-pers-day, 1.786 kg o2/kg plant waste, 1.936 kg co2/kg plant waste.
Run 2: Simulator suggested waste processing parameters: 0.288 kg o2/kg-pers-day, 0.313 kg co2/kg-pers-day, 0.619 kg o2/kg plant waste, 1.011 kg co2/kg plant waste.

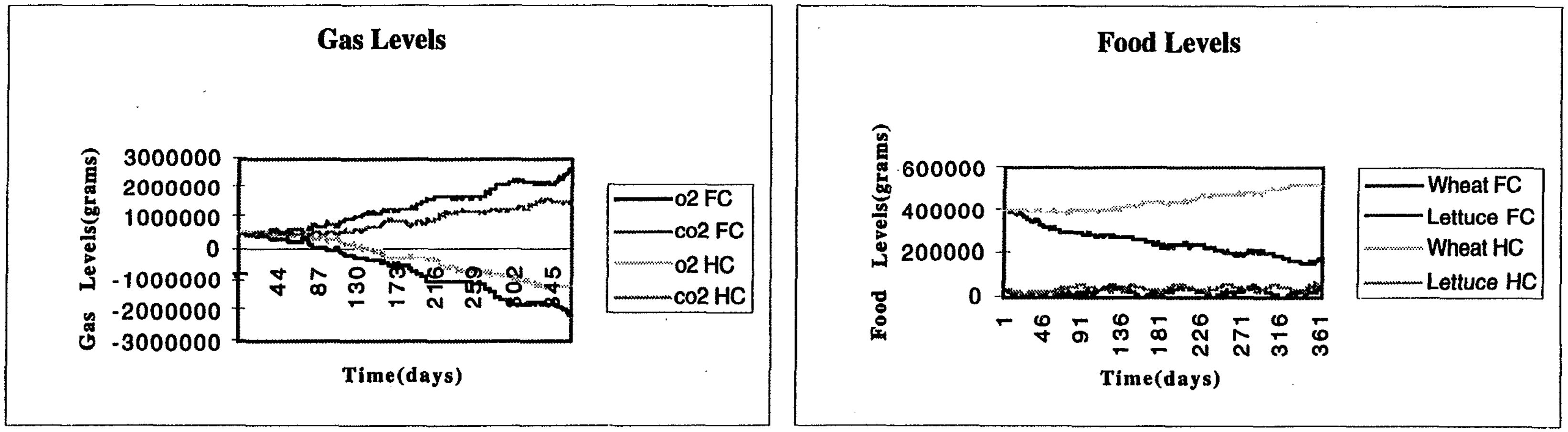

Figure 5 and Figure 6. Gas and Food Levels for Baseline with Full Crew vs. Half Crew Profile.
Run 1: Baseline scenario with full crew profile as stated in (5) for 364 days.
Run 2: Baseline Scenario with half crew profile (2 crew members for 364 days.

REFERENCES

1. MacElroy, R. D., "Current Concepts of the CELSS Program", presented at First Principal Investigators Meeting, NASA Conference Publication 2247, Conference held at University of New Hampshire, Durham, New Hampshire, May 1981.

2. Leon, V. J., "Intelligent Planning and Scheduling of Controlled Ecological Life Support Systems", 1995 Summer Faculty Fellowship Program, NASA - Johnson Space Center, Houston, Texas, Summer 1995.

3. Air Revitalization Simulation, Automation, Robotics, & Simulation Division, NASA - Johnson Space Center, Houston, Texas, June 1995.

4. Rummel, J.D. and Volk, T., 1987, "Mass Balances for a Biological Life Support System Simulation Model", Advanced Space Research, 7(4):141-145.

5. Henniger, D. L., Tri, T. O., Winkler, H. E., Behrend, A. F., and Ellis, W. E., "Advanced Life Support Project Plan", JSC #38092, NASA - Johnson Space Center, Houston, Texas, June 1994.

6. Miller, A. M., McFadden, C. D., and Sirko, R. J., "Regenerative Life Support System Testing, Modeling, and Database Development", Prepared for NASA under Contract NAS 9-17885, September 1992.

7. Personal Communication with Rick Eckelkamp, Automation, Robotics, & Simulation Division, NASA - Johnson Space Center, Houston, Texas, June 1995.

8. EHT-1 Data of Wheat Biomass Recovery, Crew and Thermal Systems Divsion, NASA - Johnson Space Center, Houston, Texas, June 1995.

9. Automation and Robotics Division, "Status of Advanced Life Support System Simulation", Reported to Crew and Thermal Systems Division, NASA - Johnson Space Center, Houston, Texas, January 1994.

10. Rummel, J. D. and Volk, T., 1987, "A Modular BLSS Simulation Model", Advanced Space Research, 7(4):59-67.

REPORT DOCUMENTATION PAGE

Form Approved
OMB No. 0704-0188

1. AGENCY USE ONLY (Leave Blank)	2. REPORT DATE August 1996	3. REPORT TYPE AND DATES COVERED NASA Contractor Report

4. TITLE AND SUBTITLE

National Aeronautics and Space Administration (NASA)/American Society for Engineering Education (ASEE) Summer Faculty Fellowship Program - 1995 (Volumes 1 and 2)

5. FUNDING NUMBERS

NGT 44-001-800 ~Vol-2

6. AUTHOR(S)

William A. Hyman* and Donn G. Sickorez, Editors

7. PERFORMING ORGANIZATION NAME(S) AND ADDRESS(ES)

Lyndon B. Johnson Space Center
Office of Public Affairs
Houston, Texas 77058

8. PERFORMING ORGANIZATION REPORT NUMBERS

9. SPONSORING/MONITORING AGENCY NAME(S) AND ADDRESS(ES)

National Aeronautics and Space Administration
Washington, D. C. 20546-0001

10. SPONSORING/MONITORING AGENCY REPORT NUMBER

CR-201377 ~ Vol-2
1826: -V -2

11. SUPPLEMENTARY NOTES

*Texas A&M University, College Station, Texas

12a. DISTRIBUTION/AVAILABILITY STATEMENT

Unclassified/Unlimited
Available from the NASA Center for AeroSpace Information (CASI)
800 Elkridge Landing Road
Linthicum Heights, MD 21090-2934
(301) 621-0390

Subject Category: 99

12b. DISTRIBUTION CODE

13. ABSTRACT *(Maximum 200 words)*

The JSC NASA/ASEE Summer Faculty Fellowship Program was conducted at JSC, including the White Sands Test Facility, by Texas A&M University and JSC. The objectives of the program, which began nationally in 1964 and at JSC in 1965, are (1) to further the professional knowledge of qualified engineering and science faculty members; (2) to stimulate an exchange of ideas between participants and NASA; (3) to enrich and refresh the research and teaching activities of the participants' institutions; and (4) to contribute to the research objectives of the NASA centers. Each faculty fellow spent at least 10 weeks at JSC engaged in a research project in collaboration with a NASA/JSC colleague. In addition to the faculty participants, the 1995 program included five students. This document is a compilation of the final reports on the research projects completed by the faculty fellows and visiting students during the summer of 1995. The reports of two of the students are integral with that of the respective fellow. Three students wrote separate reports.

14. SUBJECT TERMS

information transfer, research, research projects, engineering, science, university program

15. NUMBER OF PAGES

428

16. PRICE CODE

17. SECURITY CLASSIFICATION OF REPORT	18. SECURITY CLASSIFICATION OF THIS PAGE	19. SECURITY CLASSIFICATION OF ABSTRACT	20. LIMITATION OF ABSTRACT
Unclassified	Unclassified	Unclassified	Unlimited

NSN 7540-01-280-5500

Standard Form 298 (Rev 2-89)
Prescribed by ANSI Std. 239-18
298-102